Universidad de Valladolid


**DOCTORAL PROGRAM BY THE UNIVERDIDAD DE VALLADOLID**

DOCTORAL THESIS:

# EMPLOYING ARTIFICIAL INTELLIGENCE TECHNIQUES FOR THE ESTIMATION OF ENERGY PRODUCTION IN PHOTOVOLTAIC SOLAR CELLS BASED ON ELECTROLUMINESCENCE IMAGES

Thesis submitted by Héctor Felipe MATEO-ROMERO as part of the requirements for the degree of DOCTOR by the University of Valladolid with mention of INTERNATIONAL DOCTORATE

Supervised by:

Dr. Luis HERNÁNDEZ-CALLEJO
Dr. Valentín CARDEÑOSO-PAYO, Dr. Miguel Ángel GONZÁLEZ-REBOLLO

Valladolid, 2024

Universidad de Valladolid


**PROGRAMA DE DOCTORADO EN INFORMÁTICA**

TESIS DOCTORAL:

# USO DE TÉCNICAS DE INTELIGENCIA ARTIFICIAL PARA LA ESTIMACIÓN DE LA PRODUCCIÓN ENERGÉTICA DE CÉLULAS SOLARES FOTOVOLTAICAS A PARTIR DE IMÁGENES DE ELECTROLUMINISCENCIA

Presentada por Héctor Felipe MATEO-ROMERO para optar al grado de DOCTOR por la Universidad de Valladolid con MENCIÓN DE DOCTORADO INTERNACIONAL

Dirigida por:

Dr. Luis HERNÁNDEZ-CALLEJO
Dr. Valentín CARDEÑOSO-PAYO, Dr. Miguel Ángel GONZÁLEZ-REBOLLO

Valladolid, 2024

# Abstract

The investment in renewable energies has increased significantly in recent years, with photovoltaic solar energy emerging as one of the most prominent sources. The shift towards sustainable energy solutions is driven by the urgent need to mitigate climate change, reduce greenhouse gas emissions, and achieve energy independence. Photovoltaic (PV) technology, which converts sunlight directly into electricity using semiconductor materials, has seen substantial advancements in efficiency and cost reduction, making it a viable and attractive option for large-scale energy production.

Traditionally, the maintenance of photovoltaic plants has relied on manual labor to inspect the conditions of numerous solar modules. This involves technicians physically examining each module, looking for defects such as cracks, hot spots, and dirt accumulation that can impair performance. While effective for small installations, this manual approach becomes impractical for large-scale installations comprising thousands or even millions of modules. The sheer scale of these operations requires a more efficient and comprehensive method to ensure optimal performance and longevity of the PV systems.

The integration of artificial intelligence in this field has offered a pathway to optimize production and maintenance. AI technologies, including machine learning and computer vision, can automate the inspection process, providing rapid and accurate detection of defects. Presently, detecting problems on the surface of photovoltaic cells involves identifying patterns of defects using various technologies such as infrared thermography, electroluminescence imaging, and aerial drone inspections. However, this method has limitations because it does not directly correlate these issues with energy production, leading to a potential gap in understanding the actual impact of detected defects on the overall performance of the PV modules.

This thesis proposes a novel approach to analyzing the state of photovoltaic cells, serving as the initial step toward developing a system applicable to entire modules. The analysis involves developing an AI model capable of estimating the energy production of a photovoltaic cell using its electroluminescence image. Electroluminescence imaging is a powerful diagnostic tool that can reveal otherwise invisible defects by capturing the emitted light when a current is applied to the cell. By correlating these images with the cells performance data, specifically the current-voltage (I-V) curves, the AI model can predict the energy output and identify cells that may underperform due to defects.

The research has led to the creation of several datasets featuring various types of photovoltaic cells, encompassing different technologies and defect types. These datasets are crucial for training and validating the AI models, ensuring they can generalize across different conditions and cell types. Different proposals have been explored to address the problem, analyzing the advantages and disadvantages of each. For instance, various machine learning algorithms, including Convolutional

Neural Networks or Random Forest. These algorithms have been tested to determine the most effective approach for image-based energy prediction.

Additionally, secondary achievements of the thesis include analyzing data imbalance using synthetic datasets and investigating the issue of series resistance observed in various cells. Data imbalance can bias the AI model, leading to poor performance on rare defects. By generating synthetic datasets, the research mitigates this issue, ensuring a balanced representation of all defect types. Series resistance, which affects the flow of current through the cell, is another critical parameter influencing performance. The investigation into series resistance provides insights into its impact on energy production and how it can detected with the EL images.

This thesis contributes by introducing an innovative AI-based approach for the precise estimation of energy production from electroluminescence images. This work not only enhances the efficiency of maintenance and monitoring of PV cells but also sets the stage for implementing it at module level or even in large-scale PV installations.

***Keywords*:** Solar Photovoltaic Energy, machine learning, deep learning, Artificial Vision, Max Power Point.

# Resumen

La inversión en energías renovables ha aumentado significativamente en los últimos años, con la energía solar fotovoltaica emergiendo como una de las fuentes más prominentes. El cambio hacia soluciones energéticas sostenibles está impulsado por la necesidad urgente de mitigar el cambio climático, reducir las emisiones de gases de efecto invernadero y lograr la independencia energética. La tecnología fotovoltaica, que convierte la luz solar directamente en electricidad utilizando materiales semiconductores, ha visto avances sustanciales en eficiencia y reducción de costos. Esto lo hace una opción viable y atractiva para la producción de energía a gran escala.

Tradicionalmente, el mantenimiento de las plantas fotovoltaicas ha dependido del trabajo manual para inspeccionar el estado de numerosos módulos solares. Esto implica que los técnicos examinen físicamente cada módulo, buscando defectos como grietas, puntos calientes y acumulación de suciedad que pueden perjudicar el rendimiento. Aunque este enfoque es efectivo para instalaciones pequeñas, se vuelve impracticable para instalaciones a gran escala que comprenden miles o incluso millones de módulos. La magnitud de estas operaciones requiere un método más eficiente y completo para asegurar el rendimiento óptimo y la longevidad de los sistemas fotovoltaicos.

La integración de la inteligencia artificial en este campo ha ofrecido una forma para optimizar la producción y el mantenimiento. Las tecnologías de IA, incluyendo el aprendizaje automático y la visión por computadora, pueden automatizar el proceso de inspección, proporcionando una detección rápida y precisa de defectos. Actualmente, la detección de problemas en la superficie de las celdas fotovoltaicas implica identificar patrones de defectos utilizando varias tecnologías como la termografía infrarroja, la imagen electroluminiscente y las inspecciones con drones aéreos. Sin embargo, este método tiene limitaciones porque no correlaciona directamente estos problemas con la producción de energía, lo que lleva a una posible brecha en la comprensión del impacto real de los defectos detectados en el rendimiento general de los módulos fotovoltaicos.

Esta tesis propone un enfoque novedoso para analizar el estado de las celdas fotovoltaicas, sirviendo como el paso inicial hacia el desarrollo de un sistema aplicable a módulos completos. El análisis implica desarrollar un modelo de IA capaz de estimar la producción de energía de una celda fotovoltaica utilizando su imagen de electroluminiscencia. La imagen de electroluminiscencia es una herramienta de diagnóstico poderosa que puede revelar defectos invisibles capturando la luz emitida cuando se aplica una corriente a la celda. Al correlacionar estas imágenes con los datos de rendimiento de la celda, específicamente las curvas corriente-voltaje (I-V), el modelo de IA puede predecir la producción de energía e identificar las celdas que pueden tener un rendimiento inferior debido a defectos.

La investigación ha llevado a la creación de varios conjuntos de datos que presentan varios tipos de celdas fotovoltaicas, abarcando diferentes tecnologías y tipos de defectos. Estos conjuntos de datos son cruciales para entrenar y validar los modelos de IA, asegurando que puedan generalizarse en diferentes condiciones y tipos de

celdas. Se han explorado varias propuestas para abordar el problema, analizando las ventajas y desventajas de cada una. Por ejemplo, se han probado varios algoritmos de aprendizaje automático, incluyendo Redes Neuronales Convolucionales o Random Forest para determinar el enfoque más efectivo para la predicción de energía basada en imágenes.

Además, los logros secundarios de la tesis incluyen el análisis del desequilibrio de datos utilizando un conjunto de datos sintéticos y la investigación del problema de la resistencia en serie observada en varias celdas. El desequilibrio de datos puede sesgar el modelo de IA, llevando a un rendimiento pobre en defectos raros. Al generar conjuntos de datos sintéticos, la investigación mitiga este problema, asegurando una representación equilibrada de todos los tipos de defectos. La resistencia en serie, que afecta el flujo de corriente a través de la celda, es otro parámetro crítico que influye en el rendimiento. La investigación sobre la resistencia en serie proporciona información sobre su impacto en la producción de energía y cómo puede ser detectada con las imágenes de electroluminiscencia.

Esta tesis contribuye al introducir un enfoque innovador basado en IA para la estimación precisa de la producción de energía a partir de imágenes de electroluminiscencia. Este trabajo no solo mejora la eficiencia del mantenimiento y la monitorización de las celdas fotovoltaicas, sino que también sienta las bases para su implementación a nivel de módulo o incluso en instalaciones fotovoltaicas a gran escala.

*Palabras clave*: **Energía Solar Fotovoltaica, Aprendizaje Automatico, Aprendizaje Profundo, Vision Artificial, Punto de Maxima Potencia**

# Acknowledgements

En primer lugar quiero dar las gracias a mi familia por todo el apoyo durante estos años, en especial a mi madre, que en paz descanse y a mi padre. Ellos lo han dado todo para proveerme de una buena educacion, que ha sido vital para llegar a este punto. Tambien agradezco mucho tambien el labor de mis amigos durante estos años apoyandome cuando lo necesitaba.

En segundo lugar agradecer el apoyo de mis directores de tesis, guiandome en el proceso de realizacion de los experimentos y de la redacción del documento. Gracias por vuestro apoyo durante estos años.

Tambien agradecer a todo las personas que han colaborado en el desarrollo de la tesis: los compañeros que estabamos todos los dias en Soria, la gente que colaboraba desde Valladolid, a varios estudiantes de Erasmus que colaboraron durante su estancia y a todos los coautores de los distintos trabajos que se han llegado a publicar.

Durante el desarrollo de la tesis he realizado varios viajes y estancias. Destacar a todos los compañeros cientificos maravillos con los que coincidí en los congresos y al TEC de Costa Rica y a la Universidad de Murcia por acogerme durante las estancias que realicé.

Finalmente agradecer a la propia Universidad de Valladolid y al banco Santander por financiar mi contrato durante la realizacion de la tesis. Agradecimientos adicionales a la propia UVA por las ayudas provistas para viajes y estancias.

# Contents

# List of Figures

# List of Tables

# List of Acronyms and Abbreviations

| | |
|---|---|
| **ABC** | **A**rtificial **B**ee **C**olony |
| **ACO** | **A**nt **C**olony **O**ptimization |
| **AI** | **A**rtificial **I**ntelligence |
| **ANFIS** | **A**daptive **N**euro **F**uzzy **I**nference **S**ystem |
| **CNN** | **C**onvolutional **N**eural **N**etwork |
| **EL** | **E**lectro**L**uminescence |
| **FA** | **F**irefly **A**lgorithm |
| **FID** | **F**réchet **I**nception **D**istance |
| **FL** | **F**uzzy **L**ogic |
| **GA** | **G**enetic **A**lgorithm |
| **GAN** | **G**enerative **A**dversarial **N**etwork |
| **GBR** | **G**radient **B**oosting **R**egressor |
| **IS** | **I**nspection **S**core |
| **I-V Curve** | Current (**I**) - **V**oltage (V) Curve |
| **LR** | **L**ineal - **R**egressor |
| **ML** | **M**achine **L**earning |
| **MAE** | **M**ean **A**bsolute **E**rror |
| **MSE** | **M**ean **S**quared **E**rror |
| **MPP** | **M**ax **P**ower **P**oint |
| **MPPT** | **M**ax **P**ower **P**oint **T**racking |
| **PL** | **P**hoto**L**uminescence |
| **PSO** | **P**article **S**warm **O**ptimization |
| **PV** | **P**hoto**V**oltaic |
| **P-V Curve** | Power (**P**) - **V**oltage Curve |
| **RFR** | **R**andom **F**orest **R**egressor |
| **RMSE** | **R**oot **M**ean **S**quared |
| **RNN** | **R**ecurrent **N**eural **N**etwork |

# Capítulo R1

# Resumen en español de la Tesis Doctoral

Este capítulo presenta la versión traducida al Español del capitulo de Introducción y Resultados de la tesis.

## R1.1 Introduccion

Optimizar la producción y reducir los costes de mantenimiento de los Sistemas Fotovoltaicos (PV) son desafíos críticos para mejorar la viabilidad y la confiabilidad de las inversiones en Energía Fotovoltaica. Se han empleado nuevas tecnologías para abordar diversos problemas en esta área, siendo particularmente importante la detección de defectos en los paneles solares.

La mayoría de los estudios en este tema se enfocan en analizar la superficie de los paneles solares dividiéndola en células PV individuales y luego aplicar diversas técnicas para identificar patrones de defectos.

Sin embargo, un enfoque alternativo implica considerar directamente la producción energética del propio modulo. La monitorización de los datos de producción puede ayudar a detectar cuándo los paneles no están funcionando como se esperaba.

Desarrollar un modelo que pueda estimar la producción únicamente a partir de una imagen de un panel sería altamente ventajoso, ya que proporcionaría una medida confiable del rendimiento sin la necesidad de medir la curva I-V.

### R1.1.1 Motivación

Actualmente, habitamos en una sociedad con una demanda sustancial de energía, alcanzando los 177,000 TWh en 2022 [1] (ver Fig. 1.1). Este persistente aumento en la demanda requiere una inversión continua en generación de energía, influenciada además por factores como los objetivos de reducción de gases de efecto invernadero y la escasez de recursos fósiles. Esto promueve la inversión en formas alternativas de energía que no solo mitigan los efectos de los gases invernadero, sino que también reducen la dependencia en recursos limitados, es decir, las energías renovables. El crecimiento de las energías renovables ha aumentado constantemente en los últimos años, con una expansión anticipada de hasta 100 GW en producción para 2030 [2], consolidando la energía solar como la forma más predominante de energía renovable.

Entre las distintas fuentes de energía renovable, los sistemas Fotovoltaicos han ganado una relevancia significativa en los últimos años debido a una considerable reducción en los costes asociados [3]. Esto, sumado a su fácil instalación que facilita la democratización de la energía, ha provocado que actualmente sea la forma de energía con mayor crecimiento [3].

La energía solar fotovoltaica se basa en la instalación de paneles solares que absorben la energía solar para generar electricidad. Cada panel solar está compuesto por numerosas unidades conocidas como células solares, responsables del proceso de producción de energía. Las grandes instalaciones solares consisten en una gran cantidad de paneles solares, y también se instalan en entornos urbanos o en áreas donde el suministro de otras formas de energía eléctrica puede no ser factible [3]. Diferentes tecnologías se emplean en la creación de paneles y células, mostrando variaciones en eficiencia energética, vida útil, costo y otras características [4].

El mantenimiento de grandes granjas solares está influenciado por gran cantidad de factores. Se ha observado un aumento en la investigación e inversión en áreas relacionadas con la optimización de la producción y la reducción de costes de mantenimiento [5]-[7].

Estos métodos de inspección son capaces de detectar una parte significativa de los defectos presentes en células o paneles fotovoltaicos. Para mantener eficazmente grandes instalaciones, es imperativo automatizar el proceso de inspección. La utilización de inteligencia artificial facilita la detección de defectos u otras anomalías en los paneles, eliminando la necesidad de personal dedicado a estas tareas.

Existen varios enfoques para lograr esta tarea, pero el más comúnmente empleado en la literatura es la detección directa de defectos [8]-[11]. Este enfoque permite la identificación de fallas pero no considera el impacto de estas fallas en la producción de energía de los paneles o células. Para evaluar la producción de energía, es necesario medir la Curva I-V, un proceso que puede realizarse a nivel de panel en el campo o a nivel de celda en un laboratorio.

Actualmente, no hay muchas propuestas que consideren la detección de problemas en células o paneles basándose en la curva IV [12], [13]. Este enfoque propuesto proporcionará una estimación mucho más precisa del estado de los paneles y sus células constituyentes, ya que una disminución en la producción de energía servirá como una clara prueba de que el panel necesita ser verificado o incluso reemplazado.

### R1.1.2 Hipótesis de Investigación

La hipotesis de investigacion de la tesis es la siguiente: *Las imágenes de Electroluminiscencia de las células fotovoltaicas proveen información suficiente para estimar la producción de las propias células utilizando algoritmos de Inteligencia Artificial*

### R1.1.3 Objetivos

El objetivo global de esta tesis es **mejorar la producción y reducir el costo de mantenimiento de los Sistemas Fotovoltaicos mediante la creación de modelos de Inteligencia Artificial (IA) capaces de predecir la producción energética de las células Fotovoltaicas (PV), utilizando imágenes de Electroluminiscencia (EL) de esas células**.

Para lograr este objetivo global se utilizará la curva IV de las células fotovoltaicas, que proporciona información sobre su producción energética. El desarrollo de

un modelo capaz de estimar la producción de energía de las células basándose en patrones aprendidos durante la fase de entrenamiento sería una herramienta vital en la optimización de los grandes sistemas fotovoltaicos. Una vez aplicado, también podría usarse a nivel de panel, permitiendo una estimación precisa de la producción de cada panel del que se disponga de una imagen de electroluminiscencia.

En base a esto, se proponen los siguientes objetivos específicos:

- SO1: Crear conjuntos de datos adecuados para los experimentos. Estos conjuntos de datos deben estar compuestos por imágenes EL y la curva I-V de las células PV.
- SO2: Analizar el desbalance de los datos y crear imágenes sintéticas para resolverlo.
- SO3: Estimar el rendimiento de las células PV basándose en su imagen de electroluminiscencia y su curva I-V utilizando modelos de IA.
- SO4: Realizar experimentos con otras tecnologías y enfoques en el problema.
- SO5: Realizar un análisis de los efectos de los problemas relacionados con la resistencia en serie presente en las células PV apartir de la imagen EL y la curva I-V.
- SO6: Mejorar el estimador de la potencia de salida de las células para que sea capaz de ser utilizado con diferentes tecnologías de células PV.

## R1.2 Contribuciones Principales

Esta tesis ha llevado a varias contribuciones al campo que se explicarán durante el documento, también se pueden encontrar en la bibliografía o consultando al autor:

- Se han creado varios conjuntos de datos compuestos por imágenes EL de células fotovoltaicas y su curva I-V. Estos conjuntos de datos son importantes ya que la mayoría de los conjuntos de datos de imágenes EL encontrados en la bibliografía no proporcionan la curva I-V de las células analizadas. Se han utilizado varios tipos de células fotovoltaicas para crear estos conjuntos de datos.
- Se ha presentado un Conjunto de Datos Ampliado compuesto por imágenes sintéticas creadas por GANs. Este conjunto de datos funciona como una extensión del Conjunto de Datos de Policristalino.
- Se han propuesto varios modelos para resolver este problema:
  - Modelo basado en la extracción de características. Este modelo extrae características que describen las imágenes en lugar de utilizar directamente las imágenes.
  - Modelo Clasificador Difuso. Este modelo proporciona una consideración alternativa del problema, abordándolo como una clasificación en lugar de una regresión, lo que lo hace más simple. El enfoque difuso del modelo proporciona una lógica comprensible para los humanos.
  - Modelo Regresión ANFIS. Este modelo proporciona un híbrido entre la Lógica Difusa con su conocimiento comprensible para los humanos y las Redes Neuronales con su alta capacidad de cálculo.

– Mezcla Convolucional de Expertos. Este modelo proporciona una solución convolucional al problema, siendo capaz de tratar directamente con la imagen. También tiene la capacidad de manejar varios tipos de células fotovoltaicas gracias a la implementación de la Mezcla de Expertos.

### R1.2.1 Estructura del Documento

Este documento está estructurado en seis partes. El capítulo 1 presenta y explica el tema principal de esta tesis y sus objetivos. En el capítulo 3 , se presenta una revisión profunda del trabajo relacionado en el estado del arte. También proporciona una introducción al tema fotovoltaico para los lectores que no conocen ese campo. El capítulo 4 presenta los materiales utilizados durante la tesis.

Los detalles sobre el esquema de la metodología se presentan en el capítulo 5. La sección 5.2 explica la recopilación, el preprocesamiento y el etiquetado de los datos para crear los conjuntos de datos originales.

Los detalles sobre cada parte de la experimentación se explican en el capítulo 6 de la tesis. En particular, la sección 6.1 explica los detalles sobre la construcción del conjunto de datos sintéticos y el diseño de Redes Generativas Adversarias (GANs) para crear datos sintéticos.

En la sección 6.2 se evalúan diferentes técnicas de Machine Learning (ML) tratando de estimar la potencia de salida de las células PV basándose en características extraídas de las imágenes. En las secciones 6.3 y 6.4 se proponen dos enfoques utilizando lógica difusa.

El problema de la resistencia en serie se analiza en la sección 6.5. Finalmente, la sección 6.6 presenta un enfoque convolucional capaz de manejar diferentes tipos de células fotovoltaicas.

Una discusión sobre los resultados de los diferentes modelos se proporciona en el capítulo 7, abordando el problema del desbalance (sección 7.1), el problema de la resistencia en serie (sección 7.2) y el rendimiento de los modelos propuestos (sección 7.3).

En el capítulo 8 se resumen las conclusiones de la tesis, presentando también algunas posibles líneas de trabajo futuro. Finalmente, se enumeran las publicaciones, logros y atribuciones obtenidas durante esta disertación.

## R1.3 Discusión de los resultados

Este capítulo explica las conclusiones obtenidas a partir de los experimentos realizados y explicados en el Capítulo 6. Este análisis se divide en tres problemas diferentes: el desbalance en los datos observado durante la recopilación de datos, analizando cómo afecta al problema; el problema de la Resistencia en Serie que también fue observado; y, finalmente, se realiza una comparación de los rendimientos de los diversos modelos propuestos.

### R1.3.1 Efectos del Desbalance en los Datos

El problema del desbalance en los datos se observó durante la recopilación de los mismos (Capítulo 5.2). Se detectó que un alto porcentaje de las etiquetas de los datos estaban entre 0.6 y 0.8, dando una baja representación a otros valores del dominio.

La creación de datos sintéticos (Capítulo 6.1) se concibió para resolver este problema, proporcionando nuevos ejemplos de valores subrepresentados. Se ha demostrado que estas imágenes son similares a las originales mediante el análisis del histograma y con métricas de similitud como la Inspection Score (IS) y Fréchet Inception Distance (FID).

A pesar de que se comprobó que las imágenes sintéticas eran de alta calidad, se ha observado en los experimentos del regresor basado en características (Capítulo 6.2) que su inclusión no tiene una mejora crítica en el rendimiento de los modelos. Se encontró que el mejor modelo (Gradient Boosting) proporcionó un ECM de 0.00265 utilizando solo los datos originales frente a un ECM de 0.00282 al incluir los datos sintéticos. Esto evidenció dos hechos importantes: es posible crear un modelo que proporcionara un buen rendimiento para el problema (esto se detallará en la Sección 7.3) y la inclusión de datos sintéticos implica una mejora muy limitada en el rendimiento de los modelos.

Existen varias razones plausibles para esta falta de mejora. En primer lugar, estos modelos son bastante capaces de resolver el problema ya que proporcionan métricas de error bajas, esto muestra que el problema del desbalance de los datos no les impide realizar un buen desempeño en el problema. Otra razón de la falta de mejora es que las GAN crean datos basándose en los datos de entrada [14], tratando de encontrar los patrones para replicarlos lo más exactamente posible. Esto implica que este tipo de método no es adecuado para generar nuevos patrones, creando datos sintéticos demasiado similares a los originales, lo que no proporciona nueva información en los procesos de entrenamiento de los modelos.

La falta de mejora mostró que no era necesario considerar el problema del desbalance en los siguientes experimentos, por esta razón, los otros modelos no utilizan el conjunto de datos sintéticos. Sin embargo, se planea volver a este problema en el futuro, para probar otras tecnologías capaces de generar datos.

### R1.3.2 Efectos del Problema de Resistencia en Serie

Durante la recopilación de datos (Capítulo 5.2), se observaron valores inesperados de la potencia de salida en varias células, ya a pesar de no presentar defectos ni sombras mostraban valores inusualmente bajos. Tras realizar el análisis presentado en el Capítulo 6.5, se concluyó que este problema se debía a que esas células fotovoltaicas presentan una resistencia en serie más alta de lo habitual, lo que estaba produciendo una reducción en su rendimiento.

El análisis usando Wavelet proporcionó una nueva forma de analizar las imágenes, ya que fue capaz de detectar problemas que no eran directamente visibles en la imagen EL. Se observó que tanto el análisis continuo como el análisis discreto también proporcionan información sobre la densidad espectral de potencia en cada barra busbar. Las células con bajo Punto de Máxima Potencia (MPP) exhibieron barras de busbar con zonas de baja densidad electrónica.

También se descubrió que el problema de resistencia en Serie en nuestros conjuntos de datos fue provocado por algunas soldaduras incorrectas entre las células fotovoltaicas y sus barras de busbar. Este tipo de defectos se presentó en las células desde su fabricación, ya que algunas células nuevas también presentaban este problema.

Sin embargo, este problema no es extremadamente crítico, ya que solo se presenta en unas pocas células. En ese punto de la investigación, se decidió que no era factible incluir este nuevo problema en los modelos que intentaban resolver el problema, ya que requeriría cambiar completamente la planificación de los experimentos. No obstante, será importante volver a este problema en el futuro, tratando de agregar información sobre la resistencia a los modelos para mejorar su rendimiento.

### R1.3.3 Comparación de los resultados de los diferentes Modelos

La estimación de la potencia de salida de las células fotovoltaicas fue el objetivo principal de la tesis, y todos los objetivos específicos se han elegido para completarlo. Se han abordado dos enfoques diferentes: considerando el problema como una clasificación (Capítulo 6.3) y como una regresión (Capítulos 6.2, 6.4, 6.6).

#### Enfoque de Clasificación

El enfoque de clasificación difusa fue propuesto para resolver el problema tratandolo como una clasificacion. De los dos modelos propuestos con este enfoque, el modelo de Policristalino mostró una precisión del 99 % y el modelo de Monocristalino una precisión del 98 %. Sus resultados son claramente superiores a otros métodos de Machine Learning probados, como los clasificadores en conjunto o los árboles de decisión. Este modelo también ha proporcionado varias reglas comprensibles que pueden ser utilizadas por los trabajadores para realizar una inspección visual manual. Es importante destacar que el enfoque de clasificación reduce considerablemente la complejidad del problema. La cantidad de información proporcionada por la clasificación es bastante limitada en comparación con la información proporcionada por una estimación completa de la potencia de salida. Sin embargo, este modelo sigue siendo útil debido a sus buenos resultados y su lógica transparente.

#### Enfoque de Regresión

El enfoque de regresión fue el enfoque principal de la investigación. Los primeros modelos que lo abordaron fueron los modelos basados en características, que utilizaron características configuradas manualmente obtenidas de las imágenes para estimar la potencia de salida. El mejor modelo presentó un MAE de 0.0341 y un MSE de 0.0021. Esto demostró que era posible resolver el problema con un buen rendimiento, ya que un MAE de 0.0341 presenta un error de alrededor del 3.4 %, lo cual es un valor aceptable en nuestro contexto. Sin embargo, este modelo solo se probó en el conjunto de datos de Policristalino, ya que era el único disponible en ese momento.

La segunda ola de modelos propuestos se basó en el concepto ANFIS, combinando las capacidades de las Redes Neuronales y la lógica transparente de los Modelos Difusos. También se basó en características configuradas manualmente pero limitadas a tres características. El mejor modelo obtuvo un MAE de 0.0535 y un MSE de 0.0073. Aunque su rendimiento es considerablemente menor que el del modelo anterior, es importante tener en cuenta que ese modelo utilizó la primera propuesta de etiquetado (ver Capítulo 5.2). La primera propuesta tenía los valores extremadamente enfocados en ciertos valores, lo que redujo el dominio real del problema. Este modelo y los siguientes utilizan la segunda propuesta, que proporciona una mejor distribución de salida. Este modelo también proporcionó información importante que puede ser útil para la inspección manual o para encontrar nuevos patrones

de error en las células. Similarmente al caso anterior, solo se utilizó el conjunto de Policristalino.

La última ola de modelos propuestos se basó en Redes Neuronales Convolucionales (Capítulo 6.6), analizando el rendimiento de los modelos dependiendo de los datos utilizados para entrenarlos. Los resultados mostraron que los modelos no eran capaces de obtener buenos resultados con tipos de células PV diferentes a los utilizados en el proceso de entrenamiento. Por ejemplo, un modelo entrenado solo con el conjunto de datos de Monocristalino obtuvo un MAE de 0.0194 en su conjunto de prueba, pero obtuvo un MAE de 0.2159 en el conjunto de Policristalino. Este comportamiento se presentó con todos los diferentes tipos de células PV, mostrando que era necesario entrenar un modelo en un tipo de tecnología para obtener buenos resultados con esa tecnología. El enfoque de Mezcla de Expertos presentado en el mismo capítulo, que combina modelos entrenados con cada tipo de células PV, fue capaz de obtener un MAE de 0.0262 en el conjunto de datos Mono+Poli. Esto mostró cómo este modelo era capaz de resolver el problema para cada una de las tecnologías presentadas de células PV, y tenía la ventaja de ser fácilmente reentrenable si se incluían nuevas tecnologías de células PV.

El enfoque CNN ha sido encontrado como el método de mejor rendimiento, sin embargo, los otros enfoques no son inútiles. El método basado en características proporciona un buen rendimiento con un bajo costo computacional en comparación con los enfoques basados en las propias imágenes. El enfoque ANFIS no proporciona un rendimiento al nivel de los otros enfoques, pero proporciona la base de su lógica con reglas comprensibles. Estas reglas pueden ser utilizadas para analizar directamente cómo las sombras y los defectos impactan en la producción de las células PV. También es menos exigente en términos computacionales que el enfoque CNN.

La Tabla 7.1 proporciona una comparación del tiempo de entrenamiento para cada uno de los modelos. Aunque el número de muestras no es exactamente el mismo en cada modelo, muestra cómo los modelos convolucionales necesitan una cantidad considerable de tiempo en comparación con los modelos que utilizan solo características. La lógica difusa no incluye un número ya que el entrenamiento debe realizarse manualmente, con el conocimiento de los expertos. ANFIS necesita un tiempo considerablemente mayor que otros modelos basados en características, ya que utiliza redes neuronales, pero aún es extremadamente rápido en comparación con CNN.

# Chapter 1

# Introduction

Optimizing production and reducing maintenance costs of Photovoltaic (PV) systems are critical challenges for enhancing the feasibility and reliability of investments in photovoltaic energy. New technologies have been employed to address various issues in this area, with the analysis of the surface of solar modules being particularly important.

The majority of studies focus on analyzing the surface of solar modules by dividing it into individual PV cells and then applying various techniques to identify patterns of defects that appear in the cells.

However, an alternative approach involves directly considering the production process of the each cell. Monitoring production data can help detect when modules are not performing as expected.

Developing a model that can estimate production based solely on an image of a module would be highly advantageous, as it would provide a reliable measure of performance without the need to measure the Current-Voltage (I-V) curve.

In this chapter, an in-depth discussion is provided on various pertinent topics, offering comprehensive context and motivation for the thesis. It elaborates on the specific problem being addressed and clearly delineates the objectives of the research. Additionally, the chapter outlines the structure of the remaining sections of the documents.

## 1.1 Motivation

Presently, we inhabit a society with a substantial demand for energy, reaching 177,000 TWh in 2022 [1] (see Fig. 1.1). This persistent escalation in demand necessitates continuous investment in energy generation, further influenced by factors such as greenhouse gas reduction goals and the depletion of fossil resources. This prompts investment in alternative forms of energy that not only mitigate greenhouse effects but also alleviate dependence on limited resources, namely, renewable energies. The growth of renewable energies has steadily increased in recent years, with an anticipated expansion of up to 100 GW in production by 2030 [2], solidifying solar energy as the most predominant form of renewable energy.

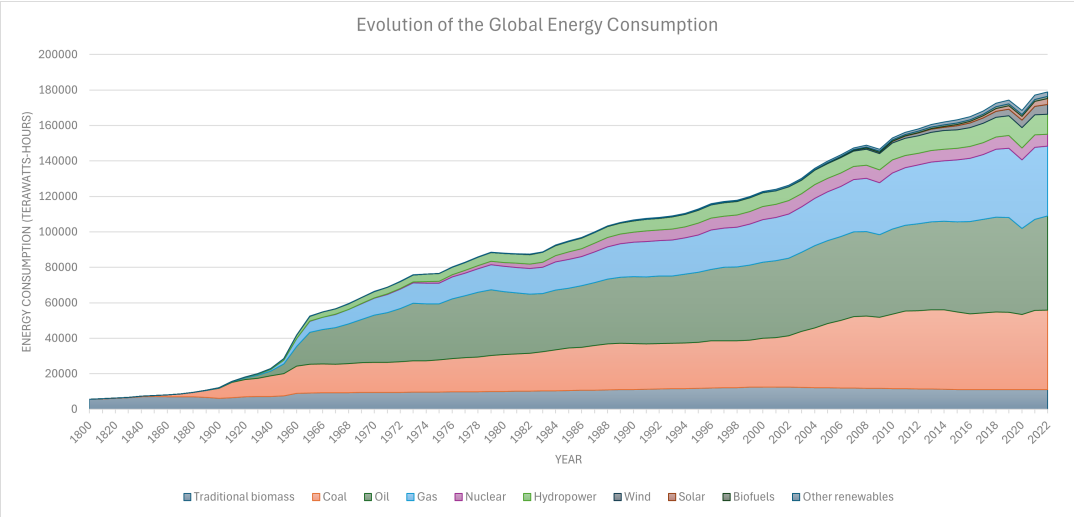


FIGURE 1.1: Evolution of the Energy Consumption. Data adapted from [1].

Among the various renewable energy sources, Photovoltaic systems have gained significant prominence in recent years due to a substantial reduction in associated costs [3]. This, coupled with their ease of installation facilitating the democratization of energy, has made them the fastest-growing form of energy currently [3].

Photovoltaic solar energy is based on installing solar modules that absorb solar energy to generate electricity. Each solar panel is composed of numerous units known as solar cells, responsible for the energy production process. Large solar installations consist of a vast number of solar modules, and they are also installed in urban environments or areas where supplying other forms of electrical energy may not be feasible [3]. Different technologies are employed in the creation of modules and cells, exhibiting variations in energy efficiency, lifespan, cost, and other characteristics [4].

The maintenance of large solar farms is influenced by various factors. An increase in research and investment has been observed in areas related to production optimization and maintenance cost reduction [5]–[7].

The inspection methods are capable of detecting a significant portion of the defects present in photovoltaic cells or modules. To effectively maintain large installations, it is imperative to automate the inspection process. The integration of artificial intelligence greatly enhances the process of identifying defects or anomalies within modules. By automating these detection tasks, AI eliminates the necessity for human personnel to manually inspect and monitor for issues. This not only improves efficiency but also reduces the potential for human error, allowing employees to focus on more complex and value-added activities while ensuring consistent and accurate detection. Additionally, AI systems can operate continuously, providing real-time feedback and enabling faster corrective actions, further optimizing the overall workflow.

Various approaches exist for accomplishing this task, but the most commonly employed in the literature is direct defect detection [8]–[11]. This approach enables the identification of faults but does not take into consideration the impact of these faults on the energy production of the modules or cells. To assess energy production,

it is necessary to measure the Current-Voltage (I-V) Curve, a process that can be conducted at the panel level in the field or at the cell level in a laboratory.

Currently, there are not many proposals considering the detection of issues in cells or modules based on the IV curve [12], [13]. This proposed approach will provide a much more accurate estimation of the state of the modules and their constituent cells, as diminished energy production will serve as a clear indication that the module needs to be replaced.

## 1.2 Research Hypothesis

Previous starting to work on the thesis and its objectives. It is important to settle the hypothesis of the thesis, which will be the founding of the research. The research hypothesis of the thesis is the following: *Electroluminescence images of photovoltaic cells provide sufficient information to estimate the production of the cells themselves using Artificial Intelligence algorithms*.

## 1.3 Objectives

The global objective of this thesis is **to improve the production and reduce the maintenance cost of Photovoltaic Systems by creating Artificial Intelligence (AI) models capable of predicting the energetic production of the Photovoltaic (PV) Cells, using Electroluminescence (EL) images from those cells**.

To achieve this global objective, the IV curve of photovoltaic cells is used, which provides information about their energy production. The development of a model capable of estimating the energy production of cells based on patterns learned during the training phase would be a vital tool in optimizing large photovoltaic systems. Once applied, it could also be used at the module level, allowing for the precise production estimation of each module for which an electroluminescence image is available.

Based on this, the following specific objectives are proposed:

- SO1: Create datasets suitable for the experiments. These datasets need to be composed of EL Images and the I-V Curve of the PV cells.
- SO2: Analyze the unbalance of the data and create synthetic images to solve it.
- SO3: Estimate the performance of PV Cells based on their Electroluminescence image and their I-V Curve using AI models.
- SO4: Perform experiments with other technologies and approaches
- SO5: Perform an analysis of the effects of the problems related to Series Resistance presented in the PV cells using the EL and the I-V curve.
- SO6: Improve the estimator of the output power of the cells to be suitable for different technologies of PV cells.

## 1.4 Main Contributions

This thesis has led to various contributions to the field that will be explained during this document, they can also be found in the bibliography or by asking the author:

- Various datasets composed of EL images of PV cells and their I-V curve has been created. These datasets are important since most of the datasets of EL images found in the bibliography does not provide the I-V curve of the analyzed cells. Various kinds of PV cells has been used for creating these datasets.
- An Expanded Dataset composed of synthetic images created by GANs has been presented. This dataset works as an extension of the Polycrystalline Dataset.
- Various models have been proposed to solve this problem:
  - Feature-Extraction base model. This model extracts features that describe the images instead of using directly the images.
  - Fuzzy Classifier Model. This model provides an alternative consideration of the problem, tackling it as a classification instead of a regression, which makes it simpler. The fuzzy approach of the model provides a human-understandable logic
  - ANFIS Regressor Model. This model provides a hybrid between Fuzzy Logic with its human-understandable knowledge and Neural Networks with its high-computing power.
  - Convolutional Mixture of Experts. This model provides a Convolutional Solution to the problem, being capable of dealing with the image directly. It also has the capacity of deal with various kinds of PV cells thanks to the Mixture of Experts implementation.

## 1.5 Outline

The document is organized into eight chapters.

Chapter 1 introduces and explains the main topic of this thesis along with its objectives. Relevant concepts are provided in Chapter 2. A comprehensive review of related work in the state-of-the-art is presented in Chapter 3. The materials used throughout the thesis are detailed in Chapter 4.

The methodology employed in this research is outlined in Chapter 5. Section 5.2 describes the processes of gathering, preprocessing, and labeling the data to create the original datasets.

Experimental procedures are elaborated in Chapter 6. Specifically, Section 6.1 explains the creation of the synthetic dataset and the design of Generative Adversarial Networks (GANs) for generating synthetic data. Section 6.2 evaluates various Machine Learning (ML) techniques for estimating the output power of PV cells based on features extracted from images. Sections 6.3 and 6.4 propose two approaches using Fuzzy Logic. The issue of Series Resistance is examined in Section 6.5. Finally, Section 6.6 presents a Convolutional Approach designed to handle different types of Photovoltaic cells.

A discussion on the results of the various models is provided in Chapter 7, addressing the issue of Unbalance (Section 7.1), the Series Resistance Problem (Section 7.2), and the performance of the proposed models (Section 7.3).

The conclusions of the thesis are summarized in Chapter 8, which also suggests potential future research directions. Lastly, the publications, achievements, and attributions resulting from this dissertation are listed.

# Chapter 2

# Theoretical Concepts

This chapter serves to introduce fundamental concepts relevant to the thesis topic, providing readers with essential context to comprehend the document and the underlying research.

The thesis is closely tied to the field of Photovoltaics, as its goal is to estimate the production of PV cells. Consequently, Section 2.1 presents key concepts pertinent to this domain.

Throughout the thesis, various Machine Learning algorithms have been employed in experiments to achieve specific objectives. Section 2.2 details the Traditional Machine Learning Algorithms utilized in these experiments.

In Section 2.3, Deep Learning techniques considered during the study are presented, alongside an exploration of Generative Adversarial Networks (GANs) used for generating synthetic data.

Section 2.4 delves into the fundamentals of Fuzzy Logic, explored as an alternative approach within the research. Similarly, Section 2.5 introduces the basics of the Adaptive Neuro-Fuzzy Inference System (ANFIS), another alternative approach examined in the study.

Lastly, Section 2.6 elucidates the principles of Wavelet Transform, which was employed for analyzing images to address problems not directly visible via Electroluminescence images.

## 2.1 Photovoltaics

As explained before, the radiation emitted by the sun is one of the most important energy sources available. There are different ways of using that energy, one of them is known as Solar Thermal which harnesses solar energy to generate thermal energy. This energy can be used in industry, residential areas, or for commercial sector [15].

Another one, known as Photovoltaic Energy transforms the light produced by the sun into Electric Power. PV systems employ PV modules, each composed of high amounts of small units known as PV cells [16]. These cells are in charge of producing the conversion between solar energy and electricity.

The traditional PV cells are made with crystalline silicon but different technologies are being created to improve the performance of the PV cells[16]. The following technologies have been used in the experiments of this research:

- Monocrystalline Cells: These cells are made with a single silicon crystal. They have a high efficiency but they present a high price in comparison to other technologies
- Polycrystalline Cells: These cells are mode with multiple fragments of silicon crystal. The impurities reduce the efficiency of the cells but also reduce their cost.

The surface of a silicon-based cell is composed of the following elements (Fig. 2.1

- Electrical Bus Bars: Metallic thin rectangular strips presented in the front and the back of the PV cells. The number depends on the manufacturer of the cell. They function is to conduct the current generated in the cells.
- Fingers: Silver conductive strips perpendicular and thinner than the busbars. They collect and send to the busbars the electric current generated in the areas around them.

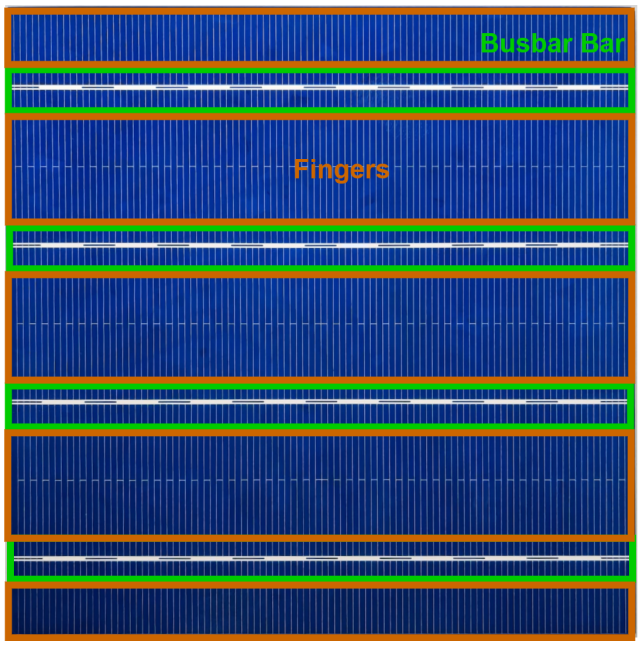


FIGURE 2.1: A Polycrystalline PV cell. The green line corresponds to horizontal big bars, the busbar. The orange line corresponds to the perpendicular thin lines, the fingers. Extracted from [17]

As mentioned before, different techniques have been designed in order to inspect the surface of the modules or cells, in order to find defects or others problems:

- Visual Inspection: This method directly utilizes the visible spectrum, enabling the detection of faults that are visible to the human eye or conventional cameras. Its primary limitation is its inability to detect faults that are not visible under these conditions, remaining imperceptible to the human eye [18].
- Thermography [19]: This technique analyzes the infrared radiation emitted by cells, induced by their heat emissions, to identify faults in the panel. It requires an infrared camera.
- Electroluminescence (EL) [20]: This method involves capturing a photograph of the photons emitted by cells when subjected to electrical current injection.

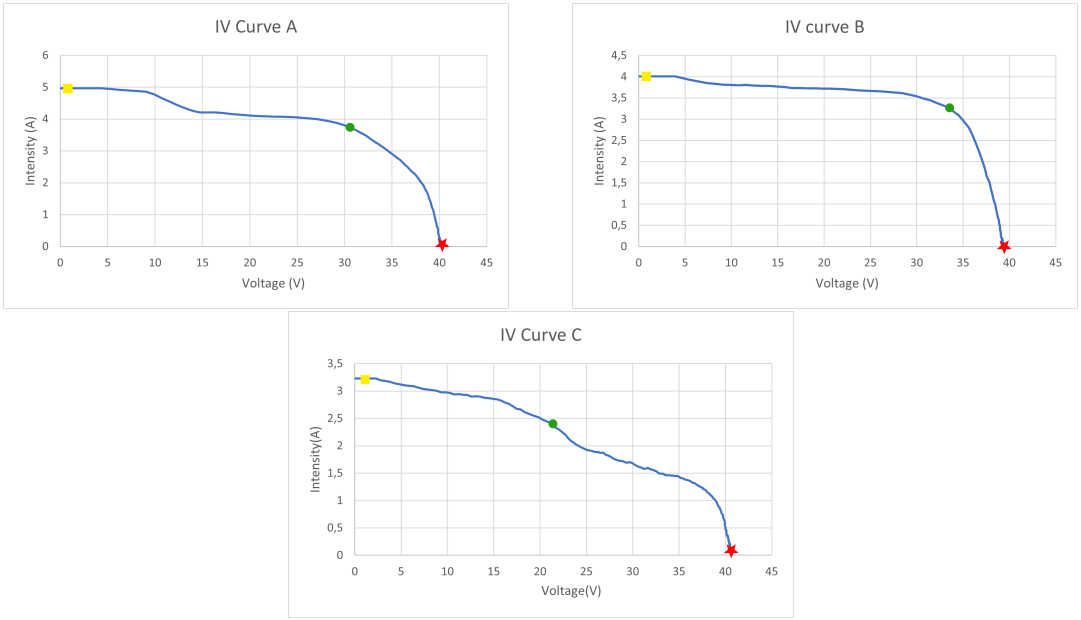


FIGURE 2.2: Different IV curves. Green circle: Max Power Point, Red Star : Open-Circuit Voltage ($V_{OC}$), Yellow Square: Short-Circuit Current ($I_{SC}$). Extracted from [11]

The emitted radiation is around the 1150 nm wavelength, allowing the detection of faults that are not visible in other spectra. A drawback of this technique is that EL radiation can only be efficiently detected by InGaAs cameras, which are considerably expensive.

- Photoluminescence (PL) [21]: Photovoltaic cells are capable of emitting EL radiation even in the absence of injected current, as a response to the absorption of solar photons. However, this technique shares the same limitation as EL, requiring an InGaAs camera.

The previous inspection methods provide information about the condition of the cell but they are not suitable for estimating the performance of the modules or cells. It is necessary to measure the levels of Current and Voltage (I-V Curve)2.2 to find the amount of electricity that they are producing. Usually, this process is performed at module level in the solar installations but it is also possible to perform it at cell level in the laboratory. The I-V Curve also depends on many external factors such as temperature, pressure, irradiance, weather, etc.

## 2.2 Traditional Machine Learning Algorithms:

This section presents the Traditional ML algorithms that have been used during the thesis

### 2.2.1 Support Vector Machines

Support Vector Machines (SVM) were conceived within the framework of statistical learning theory [22]. The primary objective of SVMs was to develop a robust and adaptable machine learning algorithm capable of effectively managing both classification and regression tasks by maximizing the margin of separation between distinct classes of data points.

#### Architecture and Operational Principles

The architecture of SVM revolves around identifying an optimal hyperplane that can best separate data points of different classes with the maximum margin [23]. This is accomplished by transforming the input data into a higher-dimensional feature space using a kernel function. The essential components of SVM include the hyperplane, support vectors (data points closest to the hyperplane), kernel function (used for computing inner products in the transformed space), and margin (the distance between the hyperplane and the nearest data points of each class). The optimization task involves maximizing this margin while simultaneously minimizing the classification error [24].

#### Applications

Support Vector Machines find applications in various domains, including text categorization and sentiment analysis [25], image recognition and object detection [26], bioinformatics for protein classification and gene expression analysis [27], finance for stock market prediction and risk assessment [28], and medical diagnosis and disease classification [29]. SVMs excel in scenarios where a clear separation between classes is essential.

#### Advantages and Limitations

Support Vector Machines offer several advantages such as effectiveness in high-dimensional spaces [30], versatility with different kernel functions [31], and regularization to avoid overfitting. However, they can be computationally expensive for large datasets [32], require careful selection of kernel and hyperparameters, and are originally designed for binary classification (though extensions exist for multi-class tasks) [33].

### 2.2.2 Gaussian Process Regression

Gaussian Process Regression (GPR) originates from the field of Bayesian inference and non-parametric statistics, aiming to offer a flexible and probabilistic framework for regression tasks while enabling uncertainty estimation alongside predictions [34]. Unlike traditional parametric models, GPR does not assume a specific functional form for the relationship between input and output variables, making it suitable for capturing complex patterns in data without overfitting [35].

GPR is rooted in the theory of Gaussian processes, where a Gaussian process defines a distribution over functions, allowing GPR to model the entire space of possible functions consistent with observed data, providing a rich representation for regression tasks.

#### Architecture and Working Principles

The architecture of Gaussian Process Regression involves defining a prior over functions using a Gaussian process. Given a set of observed input-output pairs $(X, \mathbf{y})$, where $X = \{x_1, x_2, \ldots, x_n\}$ are input points and $\mathbf{y} = \{y_1, y_2, \ldots, y_n\}$ are corresponding outputs, the predictive distribution for a new input $x_*$ is computed as a Gaussian distribution:

$$p(y_* \mid x_*, X, \mathbf{y}) = \mathcal{N}(\mu_*, \sigma_*^2)$$

where

$$\mu_* = k(x_*, X)[K + \sigma_n^2 I]^{-1}\mathbf{y}$$
$$\sigma_*^2 = k(x_*, x_*) - k(x_*, X)[K + \sigma_n^2 I]^{-1}k(X, x_*)$$

Here, $k(\cdot, \cdot)$ is the chosen covariance (kernel) function, $K = k(X, X)$ is the covariance matrix of observed inputs, $\sigma_n^2$ is the observation noise variance, and $I$ is the identity matrix [34].

#### Applications

Gaussian Process Regression finds applications in diverse domains such as Bayesian optimization [36], spatial modeling and geostatistics [37], machine learning and pattern recognition [34], and time-series prediction [38]. GPR is particularly useful in scenarios where uncertainty estimation and flexibility in modeling are essential.

#### Advantages and Limitations

Gaussian Process Regression (GPR) offers several advantages. It provides uncertainty estimates along with predictions, making it suitable for decision-making under uncertainty. GPR is flexible and can capture complex patterns in data without explicitly defining a fixed functional form. Additionally, it offers a principled framework for incorporating prior knowledge into the modeling process [34].

However, GPR has certain limitations. It can be computationally expensive for large datasets due to the need to invert large covariance matrices. The choice of kernel function and hyperparameters can significantly impact performance and must be carefully selected based on the characteristics of the data. GPR is not well-suited for very high-dimensional data due to computational constraints associated with large covariance matrices.

### 2.2.3 Random Forest

Random Forest is a popular ensemble learning method developed by Leo Breiman and Adele Cutler, aiming to enhance the predictive performance and robustness of decision trees [39]. Decision trees often overfit on training data, leading to poor generalization to new data. Random Forest addresses this by leveraging an ensemble approach with multiple decision trees.

#### Architecture and Working Principles

The architecture of Random Forest comprises an ensemble of decision trees. Each tree is trained on a random subset of the training data and a random subset of features. During prediction, the output of each individual tree is aggregated to produce the final prediction. Aggregation involves averaging the predictions for regression tasks or voting for classification tasks [39].

#### Applications

Random Forest is applied across various domains due to its effectiveness in handling complex datasets and providing robust predictions. It has been successfully used in bioinformatics, remote sensing, finance, and other fields. For example, in

bioinformatics, Random Forest is employed for gene expression analysis and protein structure prediction [40]. In finance, it is used for credit scoring and stock market prediction [41].

#### Advantages and Limitations

Random Forest offers several advantages. It is robust against overfitting due to the ensemble approach, which reduces variance and improves generalization performance. Additionally, Random Forest can handle high-dimensional data and large datasets effectively, making it suitable for complex real-world applications. It also provides feature importance ranking, aiding in feature selection and model interpretation.

Despite its advantages, Random Forest has limitations. It can be computationally expensive, especially with a large number of trees and features, requiring significant computational resources. It may introduce bias if the majority class dominates the dataset, resulting in skewed predictions. Lastly, the model can be less interpretable compared to simpler models like individual decision trees, making it challenging to understand underlying relationships.

### 2.2.4 Gradient Boosting

Gradient Boosting is a powerful machine learning technique developed to create a robust predictive model by combining the predictions of multiple weak learners [42]. The motivation behind Gradient Boosting is to sequentially enhance the performance of a base learning algorithm by focusing on the mistakes made by preceding models, thus reducing the overall prediction error.

#### Architecture and Working Principles

The architecture of Gradient Boosting involves building an ensemble of weak prediction models, typically decision trees. Each subsequent model corrects the errors of its predecessor by fitting to the residual errors (the differences between observed outcomes and existing ensemble predictions). The final prediction is obtained by aggregating predictions from all models in the ensemble.

#### Applications

Gradient Boosting is widely applied across various domains, excelling in regression, classification, anomaly detection, fraud detection, natural language processing, ranking, and recommendation systems [42]–[44].

#### Advantages and Limitations

Gradient Boosting offers highly accurate predictions by sequentially improving the model and effectively handling complex variable interactions [42], [45]. It automatically manages missing data and provides feature importance ranking for interpretability.

Despite its advantages, Gradient Boosting has limitations. Careful tuning of hyperparameters is required to avoid overfitting, and it can be computationally expensive and time-consuming, especially with large datasets [46]. Gradient Boosting

may also struggle with noisy data or outliers, and it is generally less interpretable compared to simpler models like linear regression.

## 2.3 Deep Learning Methods

This section presents the Deep Learning methods that have been used during the thesis. It starts explaining the basis of the Multilayer Perceptron since it provides a overview of the basis of all the ANNs. After that, it provides the basis of Recurrent Neural Networks and Convolutional Neural Networks. Finally it presents the basis of the Generative Adversarial Neural Networks

### 2.3.1 Multilayer Perceptron

The Multilayer Perceptron (MLP) is a fundamental architecture in deep learning, designed to overcome the limitations of simple perceptrons by modeling complex and nonlinear relationships in data, such as pattern recognition and natural language processing [47].

#### Architecture and Operating Principles

The MLP consists of an artificial neural network (ANN) with multiple layers of interconnected neurons. It typically includes an input layer, one or more hidden layers, and an output layer. Neurons apply nonlinear activation functions (e.g., sigmoid or ReLU) to introduce nonlinearities and approximate complex functions [48], [49].

MLP operates through forward and backward propagation. During forward propagation, inputs propagate through the network, and neuron outputs are computed by weighted input summation and activation. Backward propagation adjusts weights to minimize the loss function via optimization algorithms like stochastic gradient descent (SGD) [47].

#### Training Techniques and Areas of Application

Training an MLP involves iteratively adjusting network weights using labeled training data to minimize prediction errors. Success depends on data quality, quantity, and proper selection of architecture and hyperparameters [47].

MLP finds applications in image recognition, text classification, time series prediction, and speech processing due to its ability to model complex relationships [50].

#### Advantages and Disadvantages

Advantages of MLP include modeling complex relationships, adaptability, and automatic feature learning. Techniques like L1/L2 regularization, dropout, and batch normalization enhance generalization [50].

MLP limitations include computational demands and overfitting risks with small datasets. Proper architecture and hyperparameter selection are critical but challenging [50].

### 2.3.2 Recurrent Neural Networks

Recurrent Neural Networks (RNNs) were developed to address the limitations of feedforward neural networks in processing sequential data [51]. The motivation behind RNNs is to model temporal dependencies within sequences, making them well-suited for tasks such as time series prediction, speech recognition, and natural language processing. RNNs are designed to maintain a state or memory of previous inputs, allowing them to capture context and sequential patterns.

#### Architecture and Working Principles

The architecture of Recurrent Neural Networks consists of recurrent connections that enable them to exhibit dynamic temporal behavior [52]. Unlike feedforward networks, RNNs have connections that form directed cycles, allowing information to persist over time. At each time step, an RNN processes an input vector along with its current internal state, producing an output and updating its internal state based on both the current input and the previous state. This recurrent nature enables RNNs to model sequences and learn dependencies.

#### Applications

Recurrent Neural Networks have been applied extensively across various domains due to their ability to handle sequential data. They are commonly used for language modeling and text generation. For instance, Sutskever, Vinyals, and Le [53] proposed sequence-to-sequence learning with neural networks, which has been pivotal in natural language processing tasks like machine translation. Additionally, RNNs are employed in speech recognition and synthesis, as demonstrated by Graves, Mohamed, and Hinton [54].

Moreover, RNNs find applications in time series analysis and forecasting, where they excel in capturing temporal dependencies and patterns. In music generation and composition, Recurrent Neural Networks have been utilized to generate novel musical sequences based on learned patterns. They are also employed in video analysis and action recognition tasks, leveraging their capability to model sequential data effectively.

Recurrent Neural Networks are particularly suited for tasks where the input and output are sequences, and context or temporal information is essential.

#### Advantages and Limitations

Recurrent Neural Networks offer several advantages. They excel in handling input sequences of variable length and are capable of capturing long-range dependencies within data sequences [55]. RNNs are particularly effective in tasks requiring context awareness and sequential pattern recognition, such as language modeling, speech recognition, and time series analysis. Additionally, RNNs can automatically adapt to input sequences of different lengths, making them versatile for various applications.

However, RNNs also have limitations. They can be prone to issues like vanishing or exploding gradients during training, especially in deep architectures. This can hinder their ability to effectively capture long-term dependencies in data sequences. Additionally, RNNs may struggle with retaining relevant information from earlier

time steps, which can impact their performance on tasks requiring memory over long sequences.

Despite these limitations, Recurrent Neural Networks remain a powerful tool for sequence modeling and have been instrumental in advancing research across domains requiring sequential data processing.

### 2.3.3 Convolutional Neural Networks

Convolutional Neural Networks (CNNs) were developed with the motivation to improve the learning of hierarchical representations from raw input data, particularly in the context of image recognition and computer vision tasks [47]. The primary goal was to address the challenges of traditional neural networks in processing high-dimensional data efficiently while leveraging spatial relationships within images.

#### Architecture and Working Principles

The architecture of Convolutional Neural Networks is inspired by the visual processing mechanism of the human brain. CNNs consist of multiple layers, including convolutional layers, pooling layers, and fully connected layers. The key idea behind CNNs is to learn local feature representations through convolutions and hierarchical abstractions through layer-wise processing [56]. Convolutional layers apply filters (kernels) across input data to extract spatial features, while pooling layers downsample feature maps to reduce dimensionality. The extracted features are then processed by fully connected layers for classification or regression.

#### Applications

Convolutional Neural Networks have revolutionized various applications in computer vision, image recognition, and pattern analysis. They are widely used for language modeling and text generation. For instance, Simonyan and Zisserman [57] demonstrated the effectiveness of very deep convolutional networks for large-scale image recognition, achieving state-of-the-art performance on image classification tasks. CNNs are also applied in medical image analysis, where they play a critical role in automated diagnosis and disease detection [58]. Additionally, CNNs are employed in facial recognition systems, autonomous vehicles, and augmented reality applications.

#### Advantages and Limitations

Convolutional Neural Networks offer several advantages. They can automatically learn hierarchical representations from raw pixel data, eliminating the need for handcrafted feature engineering. CNNs exhibit translational invariance, allowing them to recognize objects regardless of their position in an image. Additionally, CNNs can efficiently process large-scale image data using shared weights and sparse connectivity, enabling scalability.

However, Convolutional Neural Networks have limitations. They require substantial computational resources, especially during training and inference on large datasets. Overfitting can occur, particularly with insufficient data or complex architectures. CNNs may struggle with handling rotation, scale, and occlusion variations in images, requiring additional techniques for robustness.

### 2.3.4 Generative Adversarial Networks

The explanations of this section have been adapted and extended from [59], [60].

Generative Adversarial Networks (GANs) [61] stand as pivotal and widely utilized technologies across various domains [62], offering applications in both semi-supervised and unsupervised learning. A GAN typically comprises a pair of neural networks engaged in a competitive dynamic.

#### Architecture and Working Principles

The Generator network is tasked with generating realistic new data to deceive the other network, known as the Discriminator. The Discriminator, on the other hand, is responsible for distinguishing between real and forged data.

Notably, the Generator lacks access to real data, a critical aspect of these algorithms. Instead, it learns to create data based on feedback from the Discriminator. The Discriminator, in contrast, has access to both real and generated data but remains unaware of their origins during prediction. The networks adjust their weights based on the outcomes of this adversarial interaction: the Generator refines its forgery techniques, while the Discriminator endeavors to enhance its ability to discern forgeries. Figure 2.3 provides a diagram illustrating the behavior of this algorithm.

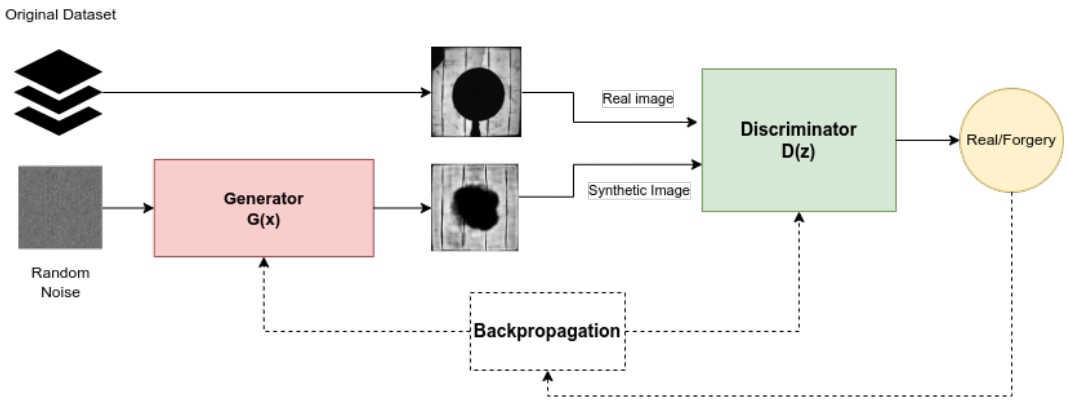


FIGURE 2.3: Diagram of a GAN. Extracted from [59].

The fundamental operational principle of a GAN can be articulated as a two-player minimax game involving players D and G, characterized by a value function $V_{GAN}(G, D)$, as formulated in the seminal work by Goodfellow et al. [61]. This value function typically employs a binary cross-entropy function, a common choice for binary classification problems:

$$\min_G \max_D V_{GAN}(G, D) = \mathbb{E}_{\mathbf{x}\sim p_{data}(\mathbf{x})}[\log D(x)] + \mathbb{E}_{\mathbf{z}\sim p_z(\mathbf{z})}[\log(1 - D(G(z)))]. \quad (2.1)$$

In Equation 2.1, the first term represents the expected value of entropy computed by the Discriminator over real data, while the second term corresponds to the entropy calculated by the Generator over the generated (fake) data.

While GANs typically consist of Deep Feed-forward Networks, more sophisticated architectures, such as Convolutional Neural Networks (CNNs), are often employed to enhance the generative capabilities of the algorithm and the quality of the synthesized data.

### Applications

Generative Adversarial Networks have found diverse applications in computer vision, image synthesis, and generative modeling. They are widely used for language modeling and text-to-image synthesis. For instance, Karras, Laine, and Aila [63] proposed a style-based generator architecture for GANs that enables high-quality image synthesis with fine-grained control over generated images. GANs are also applied in medical image synthesis, data augmentation, and video generation tasks.

### Advantages and Limitations

Generative Adversarial Networks offer several advantages. They can generate highly realistic and diverse samples that capture intricate patterns and details present in the training data. GANs excel in tasks requiring image synthesis and data generation, outperforming traditional generative models. Additionally, GANs can learn from unlabeled data and are capable of discovering complex data distributions without explicit supervision.

However, Generative Adversarial Networks have limitations. GAN training can be unstable and sensitive to hyperparameters, often requiring careful tuning and monitoring. Mode collapse, where the generator produces limited varieties of samples, is a common issue. GANs may also suffer from vanishing gradients or training divergence, affecting their convergence and quality of generated outputs. Furthermore, GANs are prone to problems such as vanishing gradients, where the gradients become too small for the model to learn effectively. Overcoming these challenges often requires specialized techniques and fine-tuning, adding to the complexity of working with GANs.

### Deep Convolutional GAN

Research on GANs has yielded novel and compelling architectures that significantly enhance network performance and the quality of generated data [64]. For this study, we implemented the architecture known as Deep Convolutional GAN (DCGAN) [65]. DCGAN is founded on convolutional layers and introduces a series of constraints aimed at stabilizing training and improving output quality. The key guidelines for DCGAN implementation are as follows:

- Use of batch normalization in the Generator and the Discriminator.
- Removal of fully connected hidden layers in both networks.
- Usage of convolutional transposed layers instead of the stridden convolutional layers. This is only applied in the Generator network.

## 2.4 Fuzzy Logic

Fuzzy Logic was introduced by Lotfi Zadeh in 1965 [66] as a mathematical approach to deal with uncertainty and imprecision in human reasoning. Traditional logic is based on binary (true/false) values, which are often inadequate for representing the complexity of human decision-making. The motivation behind Fuzzy Logic was to develop a system that could handle approximate reasoning and linguistic variables by allowing degrees of truth instead of strict binary values.

### Architecture and Working Principles

Fuzzy Logic extends traditional logic [67] by allowing values to range from completely true to completely false, thus overcoming the binary limitations of traditional logic. Unlike classical logic, which operates in a binary manner, where propositions are either true or false, Fuzzy Logic extends this paradigm by allowing for degrees of truth between 0 and 1. This flexibility enables Fuzzy Logic to model complex systems where precise inputs and outputs are difficult to define. Fig 2.4 presents the difference between representing the temperature in both types of logics

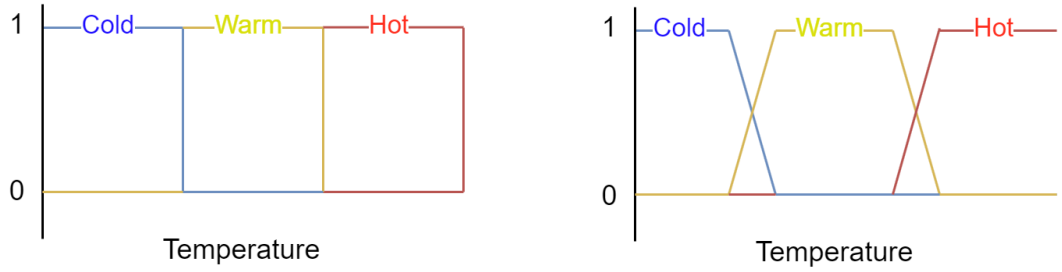


(A) Representation of the property Temperature with traditional logic

(B) Representation of the property Temperature with fuzzy logic

FIGURE 2.4: Comparison of the representation of the property Temperature with Traditional Logic and Fuzzy Logic

The foundation of Fuzzy Logic lies in Membership Functions, which assign membership grades to elements of a universe of discourse. These functions capture the fuzzy boundaries of linguistic variables and enable the representation of human-like reasoning in computational systems. They yield values in the domain of [0, 1], where 0 indicates no membership to the category, and 1 signifies full membership.

One of the key strengths of Fuzzy Logic is its ability to handle uncertain and ambiguous information in a natural and intuitive manner. This capability makes it particularly valuable in situations where traditional approaches fail to capture the nuances of real-world problems. Furthermore, Fuzzy Logic systems offer interpretability, as their rules and decisions can be understood and validated by domain experts, fostering trust and acceptance in practical applications.

At the heart of Fuzzy Logic lies its inference algorithms, which facilitate the translation of vague, qualitative rules into precise, quantitative decisions. These algorithms enable Fuzzy Logic systems to emulate human-like reasoning processes, allowing them to navigate complex, real-world scenarios with ease.

There are several Fuzzy Logic inference algorithms, each with its own strengths and applications. One of the most widely used is the Mamdani inference method [68], which employs fuzzy sets and linguistic variables to model human expertise and intuition. Mamdani systems combine fuzzy rule bases with fuzzy inference engines to generate crisp, actionable outputs from fuzzy inputs. This algorithm is renowned for its simplicity and interpretability, making it ideal for applications where transparency and user understanding are paramount.

Another prominent inference algorithm is the Takagi-Sugeno method [69], which differs from Mamdani in its treatment of the consequent part of fuzzy rules. Instead of using linguistic variables, Sugeno systems utilize mathematical functions to

represent the output of each rule. This approach simplifies the inference process and can lead to more computationally efficient systems, especially in control applications where precise numerical outputs are desired.

In addition to Mamdani and T-S, there are hybrid approaches that combine elements of both methods to leverage their respective advantages. These hybrid algorithms offer flexibility and adaptability, allowing designers to tailor inference systems to specific problem domains and application requirements.

#### Applications

Fuzzy Logic has been applied in various domains where decision-making involves uncertainty and ambiguity. It is widely used in control systems, such as fuzzy logic controllers for industrial processes and robotics. Fuzzy Logic is also employed in pattern recognition, image processing, natural language processing, and information retrieval. Consumer electronics like washing machines and air conditioners utilize fuzzy control for efficient and adaptive operation.

#### Advantages and Limitations

Fuzzy Logic offers several advantages. It can model and control nonlinear systems effectively, allowing for flexible and robust decision-making under uncertainty. Fuzzy Logic systems are interpretable and can handle imprecise and incomplete information more naturally than traditional binary logic. Fuzzy Logic has been successfully applied in diverse engineering and scientific fields.

However, Fuzzy Logic also has limitations. Designing fuzzy systems requires expert knowledge to define appropriate fuzzy sets and rules, which can be time-consuming and subjective. Fuzzy Logic may struggle with complex decision-making tasks involving high-dimensional data or dynamic environments. Additionally, tuning fuzzy systems for optimal performance can be challenging due to the subjective nature of linguistic variables and rules.

## 2.5 ANFIS

Adaptive Neuro-Fuzzy Inference Systems (ANFIS) were introduced by Jang in 1993 [70] as a hybrid approach that combines the adaptive capabilities of neural networks with the interpretability of fuzzy logic systems. The motivation behind ANFIS was to develop a framework for building adaptive fuzzy systems that can learn from data and make accurate predictions in complex environments. ANFIS aims to provide a flexible and efficient way to model nonlinear systems using fuzzy rules.

#### Architecture and Working Principles

The Adaptive Neuro-Fuzzy Inference System (ANFIS) [71], [72] serves as a bridge between Artificial Neural Networks and Fuzzy Logic. Rooted in Takagi-Sugeno fuzzy logic with IF-THEN rules, this integration imparts the model with adaptability to different scenarios, facilitated by the learning capacities of the ANN. The essential architecture of the network, outlined in Fig. 2.5, encompasses five distinct layers:

- **Fuzzification Layer:** In this layer, the determination of parameters occurs, encompassing factors such as the count, range, and kind of each input membership function (such as triangle, trapezoid, generalized bell, or Gaussian). What is more, each node demonstrates adaptability, functioning as an information processing point.
- **Rules Layer:** The main function of this layer is to generate knowledge rules that establish connections between inputs and outputs within the system. It consists of static nodes that correspond with the firing power of each rule.
- **Normalization Layer:** This layer normalizes the firing strength of each rule. It accomplishes this by dividing the firing strength of each rule by the total sum of the firing strengths of all rules.
- **Defuzzification Layer:** The computed normalized firing strength of the rules is multiplied by its consequent parameters, obtaining the weighted output for each rule.
- **Output Layer:** The last step of the ANFIS model combines all the individual rule contributions into one final result. This is done by adding up all the rule outputs. This sum is the model's prediction.

.

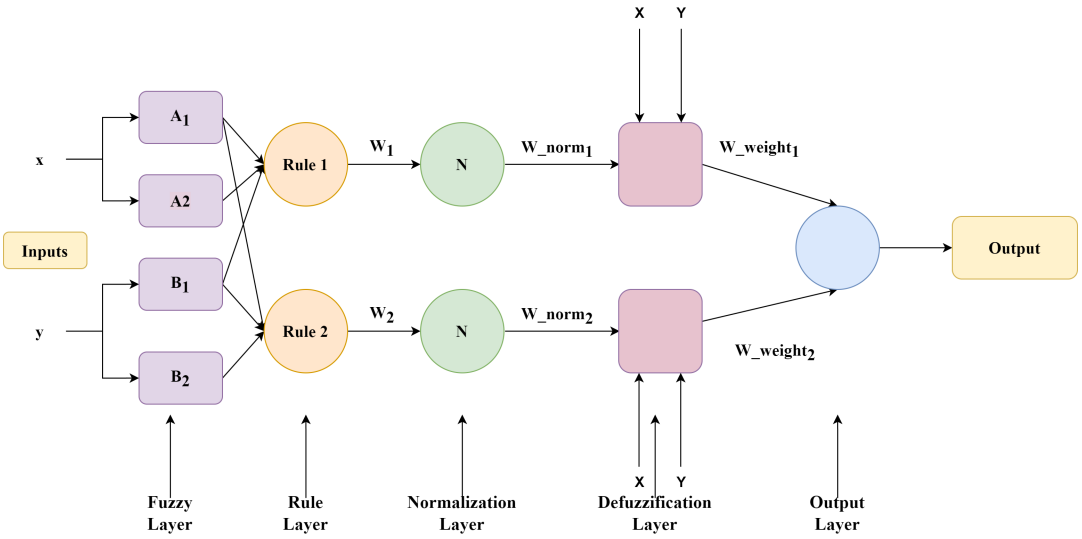


FIGURE 2.5: Diagram of the structure of an ANFIS model. Extracted from [73].

### Applications

ANFIS has been applied in various domains where complex nonlinear relationships exist between input and output variables. Some common applications include time series prediction and forecasting, system identification and control, pattern recognition, classification tasks, and financial modeling [74], [75]. ANFIS provides a versatile framework for building adaptive systems that can learn from data and make accurate predictions in real-world scenarios.

### Advantages and Limitations

ANFIS offers several advantages. It can effectively model complex nonlinear systems using fuzzy rules and neural network learning, combining the strengths of both approaches. ANFIS is interpretable due to its fuzzy rule-based structure, allowing users to understand and modify the system's behavior. Additionally, ANFIS can adapt to changing environments and learn from data, making it suitable for dynamic applications.

However, ANFIS also has limitations. Designing ANFIS models requires expertise in defining appropriate fuzzy rules and membership functions, which can be challenging and subjective. ANFIS may struggle with high-dimensional data or noisy inputs, and training complex ANFIS models can be computationally expensive. Additionally, ANFIS models may not generalize well to unseen data if not properly validated and tuned.

## 2.6 Wavelet Transform

Wavelet Transform is a mathematical tool that originated in the late 20th century [76], [77]. The motivation behind the development of wavelet analysis was to address the limitations of traditional Fourier methods in analyzing signals with localized features. While Fourier Transform provides frequency-domain representation, it lacks time localization, which is crucial for analyzing non-stationary signals. Wavelet Transform was designed to offer both frequency and time localization, making it suitable for a wide range of signal processing applications.

### Working Principles

The two-dimensional wavelet analysis [78], [79] serves as a mathematical tool for image processing, enabling examination across various frequencies and resolution scales, a principle known as multi-resolution. This facilitates the simultaneous detection of spatial and frequency attributes within the image. This analysis is accomplished through the application of the Two-Dimensional Discrete Wavelet Transform (2D DWT), which partitions the image pixels into two discrete approximation components and two detail components using high-pass and low-pass filters.

Numerous wavelet filters, including Haar, Daubechies, and Symmlet, have been developed for discrete image processing [80]. However, our primary focus will be on the Biorthogonal wavelet (Bior) filter, chosen for processing the electroluminescence images analyzed in this research work. The key characteristic of this filter is its flexibility, as it consists of two wavelets with distinct regularity characteristics. This enables each wavelet to handle different tasks effectively in image processing [81].

Wavelet analysis can be expanded to incorporate the utilization of the Continuous Wavelet Transform in two dimensions (2D CWT), representing a logical extension of the one-dimensional CWT. In comparison to traditional spectral analysis methods [82], the 2D CWT stands out by providing localized spectral information across various scales. This is achieved by acting as a local scale and position filter on spatial domain data. The 2D CWT excels in offering detailed spectral insights at specific positions and orientations within the data, conducting a continuous analysis across the entire spatial domain. This distinguishes it from the Two-Dimensional Discrete

Wavelet Transform (2D DWT), which generates a condensed representation of the analyzed dataset [79].

Different wavelets are proposed in the literature, and some can be real, complex, isotropic, anisotropic, etc [83], [84]. The Cauchy wavelet was chosen for the analysis of EL images in this research due to its minimal uncertainty and adaptable nature, enabling effective examination of information at various angles .

### Applications

Wavelet Transform has found widespread applications in various domains, including signal and image processing, data analysis, and biomedical engineering. In signal and image processing, Wavelet Transform is used for denoising, compression, edge detection, and feature extraction. In data analysis, it facilitates time-frequency analysis, pattern recognition, and machine learning tasks. In biomedical engineering, Wavelet Transform is applied to EEG analysis, MRI reconstruction, and biomedical signal processing.

Wavelet Transform provides a versatile framework for analyzing and processing signals efficiently across different scales and resolutions.

### Advantages and Limitations

Wavelet Transform offers several advantages over traditional Fourier methods. It provides time-frequency localization, allowing for the analysis of non-stationary signals with localized features. Wavelet-based methods are computationally efficient and offer good time-frequency resolution compared to Fourier Transform. Additionally, Wavelet Transform is adaptable to different applications and data types, providing robustness in handling real-world signals.

However, Wavelet Transform also has limitations. The choice of wavelet basis and decomposition parameters can significantly impact the analysis results, requiring careful selection and tuning. Wavelet-based methods may introduce artifacts, especially in image compression applications. Interpreting wavelet coefficients and selecting appropriate scales for analysis can be challenging in practice.

# Chapter 3

# State of the Art

The explanation of the State of the art is divided into three different topics: An overview of how Artificial Intelligence is applied to Photovoltaics, the AI techniques used to analyze the PV cells to find defects or to estimate their condition and the techniques used to generate synthetic data, focused in the generation of synthetic images of PV cells.

## 3.1 Artificial Intelligence applied to Photovoltaic Systems

The contents of this section have been extracted from [11]. A more detailed review of this topic can be found in that article.

Maintenance problems in PV systems have historically been addressed through either straightforward automatic supervision methods [85] or resource-intensive human oversight.

However, a shift has occurred in recent years with the emergence of AI-based solutions. AI techniques are now being utilized across diverse research domains and industries to enhance services or tackle challenges that traditional methods struggle to address [86].

These techniques can also be applied to address the challenges encountered in PV systems. In this review, we will analyze the application of AI in the PV sector. PV systems encounter various issues during installation and operation, as the PV modules are susceptible to climate conditions and unpredictable events.

Several analysis of problems encountered in PV plants can be found in bibliography[87], [88]. Additionally, the maintenance of modules is crucial for maximizing production and enhancing installation security [89]. To narrow the scope of this review, only the four most critical problems related to energy optimization and maintenance have been considered:

- **Max Power Point Tracking (MPPT)** plays a crucial role in optimizing production.
- **Output power Forecasting** is critical for predicting potential production issues related to climatic conditions.
- **Parameter Estimation** that is also extremely important for optimizing the production of the PV modules.

- **Defect Detection** is crucial for identifying underperforming modules or faults that could significantly impact overall system performance and security. This topic will be elaborated upon in Section 3.2.

### 3.1.1 Max Power Point Tracking

PV cells exhibit a complex relationship between their environment and the power they generate. Along the IV curve of solar cells, there exists a point where power is maximized, known as the Maximum Power Point (MPP). This point typically varies depending on conditions such as irradiation, temperature, or the state of the PV cell. These conditions can alter the curve's shape, rendering the problem nonlinear and time-varying due to atmospheric and load condition changes.

Tracking the maximum power point is crucial for optimizing PV systems and is arguably the most intriguing research problem. Various techniques have been employed to address this issue, as depicted in Figure 3.1. Classical methods include Incremental Conductance and Perturb & Observe [90], [91]. Recent trends indicate the use of AI techniques to tackle this problem. Metaheuristics and Neural Networks have emerged as the most commonly utilized techniques based on literature surveys.

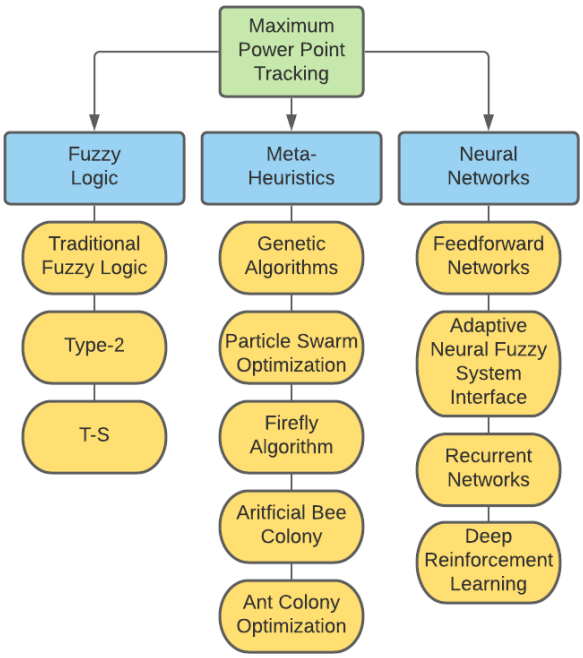


FIGURE 3.1: Taxonomy of most used IA method for MPPT. Extracted from [11].

Table 3.1 presents a summary of reviewed AI methods applied to solve the MPPT problem. The details of each article can be found in the original review[11].

TABLE 3.1: AI used Methods for MPPT. Adapted from [11].

| Classification | Method | Features |
|---|---|---|
| Fuzzy | Fuzzy Logic (FL) [92][93][94] [95][96] | FLC systems offer rapid responses to changes and minimal oscillations near the MPPT, thereby reducing power losses compared to traditional systems. Combining FL with Fuzzy Cognitive Networks [97] or initializing the estimation of the MPP voltage further enhances the results. |
| | Type-2 [98][99][100][101] | Type-2 FL offers techniques for modeling and managing uncertainties, thereby enhancing the robustness of the system and, consequently, its outcomes. |
| | Takagi-Sugeno (T-S) [102][103][104] | The parallel distributed control offered by T-S FL enhances the performance of FL systems, resulting in acceptable settling times, reduced oscillations, and accurate outputs. |
| | Combined with other methods [105][106][107][108][109][110] | Other methods can leverage the advantages of FL systems to enhance their outcomes in MPPT. |
| Metaheuristics | Genetic Algorithms (GAs) [111][112][113] | Genetic Algorithms enhance the outcomes of other methods such as ANN or FL |
| | Particle Swarm Optimization (PSO) [114][115] | PSO is utilized to optimize the learning process of Neural Networks |
| | Firefly Algorithm (FA) [116] | This algorithm is directly employed to solve the MPPT, ensuring rapid convergence with minimal oscillations. |
| | Artificial Bee Colony (ABC) [117][118][119] | For MPPT, this algorithm delivers rapid convergence and accuracy in tracking. |
| | Ant Colony Optimization [120] | It is utilized in the learning process to adjust the weights and biases of neural networks, thereby enhancing its results. |
| Neural Networks | FeedForward Neural Network | Two networks, each with a single hidden layer consisting of 20 nodes. [121]<br>Five nodes on a single layer, with data preprocessed by a Genetic Algorithm. [111]<br>Three hidden layers with 8, 7, and 7 nodes respectively, utilizing Bayesian Regulated Backpropagation for training. [122]<br>A single hidden layer with 13 neurons, with data generated by a Gaussian Support Vector Machine. [123]<br>Structured as 2-3-3-1, with the Neural Network optimized by FPSOGSA. [106]<br>The topology and optimal weights are optimized using a PSO algorithm. [124]<br>ACO is employed to optimize the neural network. [125] |
| | Adaptive Neural Fuzzy System Interface | The Bat Algorithm is employed for training the network. [107]<br>The Crowded Plant Height Optimization algorithm is responsible for conducting the learning process of the network. [126]<br>It combines Fuzzy Logic and Neural Networks, incorporating three intermediate layers where the output is determined by fuzzy rules.[127] |
| | Recurrent Neural Network | A hidden layer, a context layer storing the results of the previous outputs of the hidden layer. A metaheuristic is used to optimize the structure and weights. [105] |
| | Deep Reinforcement Learning | There are four networks involved: one for computing the policy, one for the critic, and two referred to as targets, which are utilized to stabilize the learning procedure. [128] |

The tracking of the maximum power point has been approached in various ways,

ranging from traditional and straightforward methods to those employing sophisticated technologies such as neural networks. Simple methods still hold significance, as many systems do not require complex MPPT algorithms to optimize production. However, in large-scale power plants with complex configurations of PV arrays, more intricate algorithms are necessary for efficient MPP tracking.

Comparing the different techniques, it's evident that the most commonly utilized technologies are FeedForward Neural Networks and FLC systems (Fig. 3.2). While Neural Networks outperform Logic Systems, they come with certain drawbacks. Neural Networks are computationally intensive compared to FL systems and require substantial amounts of data, although this is less of an issue due to the widespread availability of data nowadays. Another challenge is the complexity in optimizing hyperparameters, given the multitude of parameters involved in neural networks. This challenge has been addressed through the use of optimization algorithms, such as metaheuristics, to find the best parameter combinations or optimal architectures.

Despite advancements, there is ongoing interest in improving the efficiency and performance of complex systems. To achieve this objective, exploration of newer technologies applied in other sectors is warranted, as evidenced by previous studies demonstrating their effectiveness in this domain. FL methods and metaheuristics are commonly implemented using MATLAB, while Neural Networks can also be implemented using Python, leveraging libraries like Tensorflow [129].

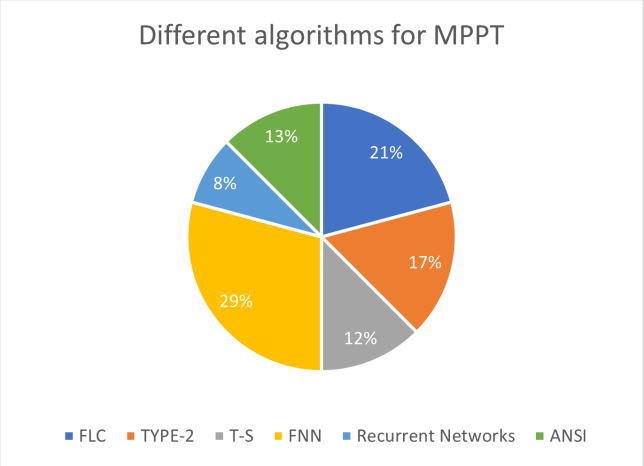


FIGURE 3.2: Diagram of sectors of most used IA methods for MPPT. Extracted from [11].

### 3.1.2 Output power Forecasting

Forecasting energy production in PV systems encompasses several variants of the forecasting problem, including weather forecasting, solar irradiance forecasting, and energy production forecasting, which estimates the energy output of the system. This is crucial for optimizing the real-time management of systems that rely on this type of energy, such as smart cities and villages. Electric companies prioritize this issue as they seek a more robust and reliable system to anticipate changes in energy loads and demands.

The time horizon for forecasting varies:

- Short-term forecasting typically ranges from 1 hour to a week ahead and is utilized for scheduling energy transfer, economic load dispatch, and demand response.
- Mid-term forecasting spans from 1 month to 1 year ahead, often used for planning near-term power plans and illustrating system dynamics within that timeframe.
- Long-term forecasting extends from 1 year to 10 years and serves to plan power generation plants to meet future requirements efficiently.

The amount of information and data available is crucial for precise forecasting models. However, excessive data can sometimes introduce noise or provide misleading information, impacting model performance. Each type of forecasting is typically treated as a distinct problem due to differences in data volume and precision requirements. For more detailed information on forecasting, refer to [130].

Energy production forecasting has long been a significant challenge, even in traditional systems, and it has been addressed using various techniques, as depicted in Fig. 3.3.

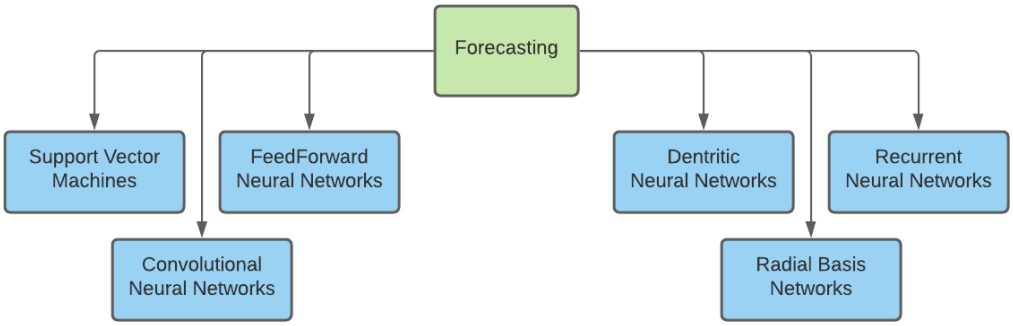


FIGURE 3.3: Taxonomy of most used IA method for forecasting. Extracted from [11].

Table 3.2 presents a summary of the reviewed AI methods applied to solve the forecasting problem. The details of each article can be found in the original review [11].

TABLE 3.2: Models for forecasting. Adapted from [11]

| Type | Features |
|---|---|
| FeedForward Neural Network | 9 inputs, with 20 hidden nodes on a single layer. [131]<br>9 inputs, with two hidden layers having 6 and 4 nodes respectively. Trained using a hybrid PSO GA algorithm. [132]<br>Utilizes 2 inputs, creating ensembles of neural networks. [133]<br>Incorporates 2 inputs, with 1 hidden layer and Conjugate Gradient as the learning rule. [134]<br>Employs 3 neural networks, each designed for a specific type of weather. Utilizes Extreme Learning to optimize the parameters and architecture. [135]<br>Applies Fuzzy Logic as a filter to the input data. Features 7 inputs, with 2 hidden layers consisting of 9 and 5 nodes respectively. Trained using a hybrid of PSO and GA. [136]<br>Utilizes Big Data. Implements a multi-step methodology to decompose the problem into sub-problems. [137] |
| Convolutional Neural Networks | Utilizes 2 inputs, with parameters selected by testing different combinations. [138] |
| Dendritic Neural Networks | Aided by Wavelet Transform, providing better convergence speed and better fitting ability. [139] |
| Radial Basis Network | Utilizes 2 inputs, aided by Wavelet Transform to preprocess the input data. [140]<br>Employs high-resolution time series as input, aided by Wavelet Transform for data preprocessing and PSO for neural network optimization. [141] |
| Recurrent Neural Network | Aided by Wavelet Transform to address fluctuation in time series input data. [142]<br>Utilizes preprocessed and normalized high-resolution time series as input, with two hidden layers consisting of 35 neurons. [143]<br>Tests different RNN architectures, with LSTM using previous time steps found to be the best. [144]<br>Utilizes Echo State Networks aided by Restricted Boltzmann Machine, Principal Component Analysis, and DFP quasi-Newton Algorithm for network optimization. [145] |
| Support Vector Machines | Utilizes 2 inputs, with a parameter to tune the number of SVM during training. [146]<br>Compares SVM with KNN, with SVM found to be better. [147]<br>Implements multi-input SVM, with different combinations of inputs tested, and 3 inputs found to be the best. [148] |

Forecasting poses a significant challenge in PV systems, with the estimation of energy production from Solar Plants predominantly treated as a regression problem in the literature. Given the abundance of data available, neural models have emerged as highly suitable solutions for this task (Fig. 3.4). There is a notable trend towards employing the latest neural architectures while optimizing their parameters and architecture using methods such as metaheuristics. While an increase in network complexity has been observed to enhance results, it is not the sole avenue for performance improvement. Integration with other systems, such as Wavelet Transform, has shown to enhance reliability. Moreover, alternative network systems like Recurrent Networks or Dendritic Networks have demonstrated further enhancements over traditional Neural Networks. However, there remains ample room for improvement in this field, given the inherent complexity of forecasting, which relies on a multitude of variables. For future research, exploring novel combinations of parameters, enhancing datasets, or leveraging innovative technologies used in similar domains could yield promising results. While much of the research is conducted using MATLAB, there is a growing presence of Python in recent years, attributed to the availability of Deep Learning Libraries.

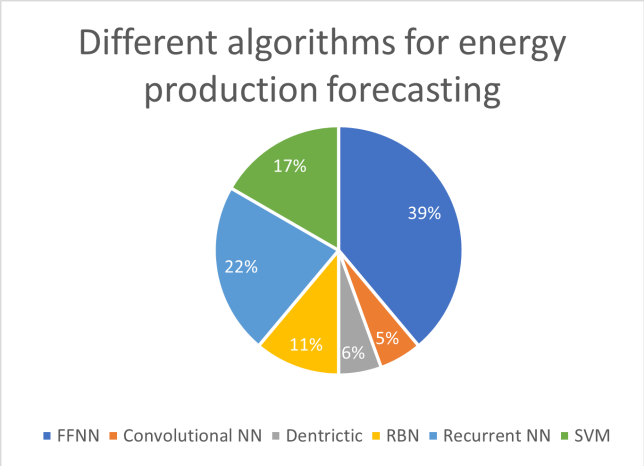


FIGURE 3.4: Diagram of sectors of most used IA methods for forecasting. Extracted from [11].

### 3.1.3 Parameter Estimation

The simulation of PV systems plays a crucial role in optimizing their production in real-world applications. It's widely acknowledged that any PV system can be effectively modeled and represented by an equivalent electric circuit, where the parameters govern the predicted or estimated operation of the PV cell or module [149], [150].

Determining the parameters of PV models is crucial for simulating their behavior and optimizing production. This task, characterized by the identification of unknown parameters to optimize output power, has been tackled using various techniques, predominantly metaheuristics, as depicted in Figure 3.5.

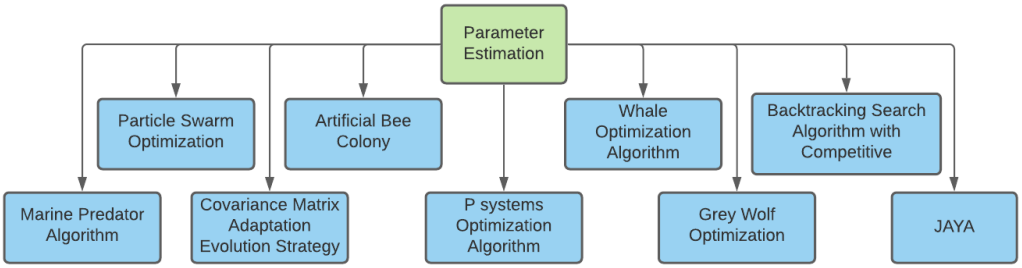


FIGURE 3.5: Taxonomy of most used metaheuristics for Parameter Estimation.

Table 3.3 presents a summary of the reviewed AI methods applied to estimate the parameters of the models. The details of each article can be found in the original review [11].

TABLE 3.3: Models for Parameter Estimation. SD: Single Diode, DD: Double Diode, MC: Monocrystalline, PC: Polycrystalline. Adapted from [11].

| Type | Features | Error |
|---|---|---|
| ABC and CE | This method combines Extremal Optimization with ABC. When the global optimum is not improving, Extremal Optimization is introduced in ABC. However, EO has a high computation cost. [149] | RMSE: SD: $1.1678 \cdot 10^{-3}$ DD: $1.1479 \cdot 10^{-3}$ |
| CMA-ES | This evolutionary algorithm achieves a good balance between exploration and exploitation, making it competitive with other methods. [151] | RMSE: SD: $9.8603 \cdot 10^{-4}$ DD: $9.8402 \cdot 10^{-4}$ |
| WOA and LM | A variant of RLWOA changes the parameter update rule and relies on the Logistic Model to balance exploration and exploitation. [152] | RMSE: SD: $9.8602 \cdot 10^{-4}$ DD: — |
| CBSA | Combines the exploratory capacities of WOA with the convergence capacities of Social Group Optimization. [153] | RMSE: SD:$9.8602 \cdot 10^{-4}$ DD: |
| GWO | This method improves basic GWO with a new bridging mechanism and opposition-based learning. [154] | MAE: SD-MC: $4.65 \cdot 10^{-13}$ DD-MC: $1.07 \cdot 10^{-12}$ SD-PC: $8.50 \cdot 10^{-12}$ DD-PC: $1.95 \cdot 10^{-12}$ |
| GWO and PSO | This method combines the social capability of PSO with the local search ability of GWO. [155] | RMSE: SD: $3.06 \cdot 10^{-3}$ DD: — |
| CSO | CSO is improved by a Spiral Movement Strategy to enhance the results. [156] | RMSE: SD: $1.1678 \cdot 10^{-3}$ DD: — |
| JAYA | This method enhances basic JAYA with an improved evolution operator, control of the population size, and generalized opposition-based learning. [157] | RMSE: SD: $9.8602 \cdot 10^{-4}$ DD: $9.8248 \cdot 10^{-4}$ |
| MPA | The algorithm extracts the parameters faster and with high reliability and robustness. [158] | RMSE: SD: $7.73 \cdot 10^{-4}$ DD: $7.65 \cdot 10^{-4}$ |
| POA | Proposes an extension of standard POA. The results show that the method produces high-quality solutions. [159] | RMSE: SD: $9.8606 \cdot 10^{-4}$ DD: $9.8256 \cdot 10^{-4}$ |
| GA,PSO, DE and others | Compares different algorithms and crossover between them, with Differential Evolution assisted by Tabu Search found to be the best. [160] | RMSE: SD: — DD: — |

Estimating the parameters of PV models has been approached using a plethora of different algorithms, with a majority belonging to the family of metaheuristics (Fig. 3.6). Interestingly, the results exhibit similarity across these algorithms in terms

of error (Fig. 3.7), suggesting that further minimizing the error may not yield significant benefits. Some of the most promising works combine various metaheuristics, leveraging different algorithms to address the limitations or weaknesses of each other. Moving forward, the focus of research should shift towards identifying algorithms with lower computational costs while maintaining comparable error levels. It's worth noting that the majority of these methods are implemented in MATLAB[161].

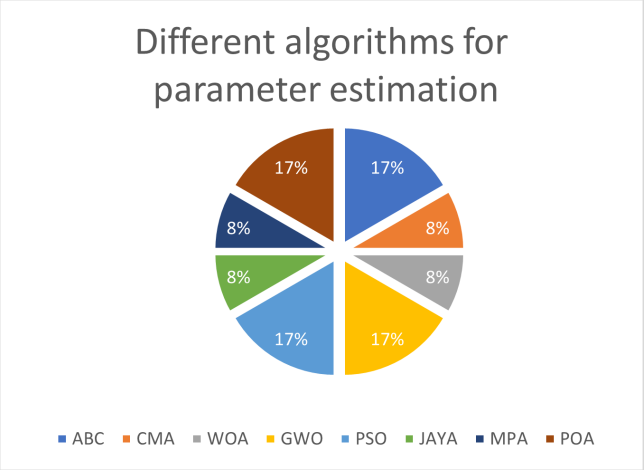


FIGURE 3.6: Diagram of sectors of most used IA methods for parameter estimation. Extracted from [11].

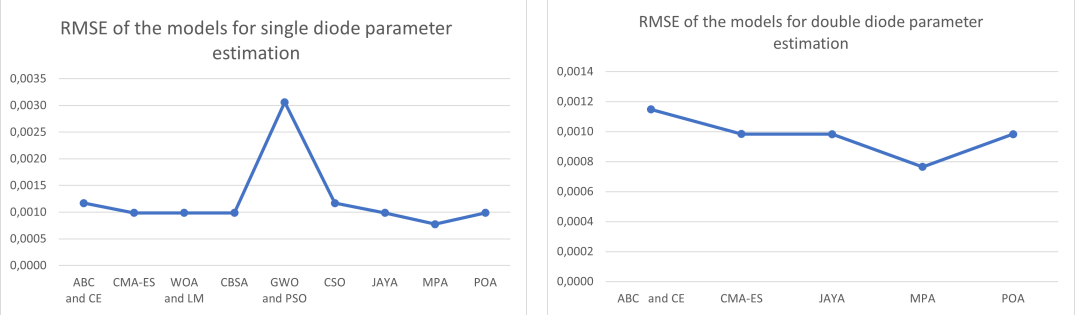


(A) Single Diode (B) Double Diode

FIGURE 3.7: RMSE of the different models for parameter estimation. Extracted from [11]

## 3.2 Analysis of the state of the PV cells of modules

The contents of this section have been adapted from [11], [17], [162].

The analysis of the surface of the PV modules or cells is another key problem in the photovoltaic field. Analyzing the state of the PV cells is one of the most discussed problems, due to the complexity of the problem. This is usually aided by using different techniques to obtain more information about the surface such as Thermography or Electroluminescence or Photoluminescence (Section 2.1)

### 3.2.1 Defect Detection

Most of the works tackle this issue by finding patterns of defects in the surface of the modules. Fig 3.8. presents the most used IA techniques used for this topic.

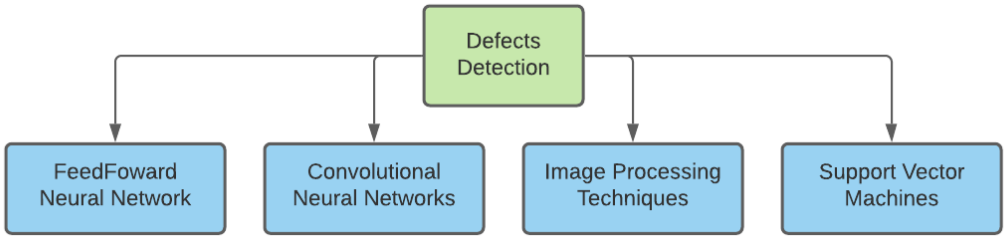


FIGURE 3.8: Most used IA method for Defect Detection. Extracted from [11].

Classical methods, as described in [163], aimed to identify defects in solar modules using image processing techniques. They employed the first derivative of the statistical curve to locate division lines between individual chips, followed by the Otsu method to generate a binary image. Subsequently, the algorithm analyzed the geometry of the resulting image to determine the module's state. This approach yielded promising results, with recognition rates of 80% for cracked modules, 95% for fragmented modules, and 99% for modules in good condition. Notably, the algorithm demonstrated efficient processing. The implementation and application of these algorithms were carried out using MATLAB.

Another method, outlined in [164], integrated image processing techniques with SVMs. The dataset consisted of 13,392 EL images of solar cells, which underwent preprocessing to reduce spatial noise and highlight crack pixels. Subsequent binary processing was performed, followed by feature extraction. Various SVMs were employed to classify the cells, with the SVM utilizing penalty parameter weighting identified as the best performer, achieving a correct detection rate of 91% with specificity and accuracy exceeding 97%. The experiments were conducted using MATLAB.

In [165], a comparison between CNN and SVM was conducted. The SVM was trained on data from the ELPV dataset, consisting of 2624 EL images of solar cells, with features extracted using various descriptors. Meanwhile, a pre-trained VGG19 CNN, with its upper layers modified and trained on provided examples, was employed. Both classifiers were assessed on mono-crystalline and poly-crystalline modules, showing effectiveness in visual inspection with an average accuracy of 82.4%. The algorithms were implemented in Python, using Keras for the Neural Network.

Similarly, [166] adopted a comparable approach, employing SVM and CNN. The CNN architecture included two convolutional layers with leaky ReLU and max-pooling, augmented by two leaky ReLU dense layers and an output layer. The SVM was trained on diverse image features extracted from a dataset of 90 images of full-size commercial modules, segmented to obtain 540 cells. Both methods exhibited similar performance, achieving an accuracy of 98%. Additionally, the study

explored unsupervised learning by attempting to cluster images based on two features, resulting in a model capable of correctly assigning labels in 66% of cases. The algorithms were implemented in Python, utilizing TensorFlow and OpenCV.

The study in [167] introduces a Convolutional Neural Network (CNN) featuring 13 convolutional layers, adapted from the VGG16 architecture. Data for training was acquired by capturing images of solar modules measuring 6x12 cells using an EL camera. The network underwent training with oversampling and data augmentation techniques to mitigate errors. Results indicated optimal performance when both oversampling and data augmentation were applied, achieving a Balance Error Rate of 7.73% in binary classification tasks, along with rapid convergence. The method was implemented using Keras, with preprocessing conducted using OpenCV.

Meanwhile, authors in [168] propose new models trained not only on images of cracked modules but also those exhibiting corrosion. Images were captured using EL techniques, and segmentation was performed to obtain a dataset comprising 5400 images. The models employed include Support Vector Machines (SVM) and CNN, with the latter comprising two convolutional layers. SVM parameters were optimized through a Grid Search. Results showcased a precision of 99%, representing an enhancement over previous methodologies. The experiments were conducted using Keras and TensorFlow.

In [169], a novel approach is presented with a Multi-channel Convolutional Neural Network (CNN). This network employs distinct convolutional layers for various types of inputs, accommodating inputs of different sizes. After each convolutional layer, a dense layer is applied, and a final dense layer amalgamates all preceding data to classify the image. This Multi-channel CNN enhances feature extraction compared to single-channel CNNs. The dataset comprises 8301 distinct EL images of cells, yielding an accuracy of 96.76%, significantly higher than the 86% achieved by single-channel CNNs. The algorithms were implemented using Python, with Keras.

The model introduced in [170] consists of six convolutional layers employing various regularization techniques such as batch optimization. Utilizing the ELPV dataset containing 2624 images, the resulting network, despite its lightweight architecture, achieved high performance with an accuracy of 93%. The experiments were conducted using TensorFlow.

In an effort to further enhance results, [171] proposes a new approach utilizing Fully Convolutional Neural Networks (FCNN). An FCNN, unlike traditional CNNs, lacks dense layers. The model employed, namely the U-net, previously applied in biomedical image problems with limited data, operates with a dataset comprising 542 EL images. It consists of 21 convolutional layers of varying sizes. Results suggest accepting a slight performance decrease to improve system speed. The algorithms were implemented using Python, with Keras and TensorFlow.

Wavelet Transform (WT) is applied in [172], combining Discrete WT and Stationary WT to extract textural and edge features from preprocessed solar cell images. The dataset consists of 2300 EL images. Two classifiers, Support Vector Machine (SVM) and Feedforward Neural Network (FFNN), are employed, with FFNN achieving the best performance at 93.6% accuracy, surpassing the 92.6% accuracy of SVM.

In [173], the authors introduce the Complementary Attention Network (CAN), comprising a Channel-wise attention sub-network and a spatial attention sub-network.

CAN can be integrated with any Convolutional Neural Network (CNN), with Fast R CNN chosen for experimentation. Two datasets, one comprising 2029 images and another of 2129 EL images, are utilized for classification and detection tasks, yielding an accuracy of 99.17% for classification and a mean average precision of 87.38%. The network demonstrates faster processing and similar parameter number compared to other methods. The algorithms were implemented using Python.

A notable approach is presented in [174], termed Deep Feature-Based, which extracts features via convolutional neural networks (CNNs) and subsequently classifies them using SVM, KNN, or FNN. This method integrates features from different networks, combining them with minimum redundancy and maximum relevance for feature selection. Utilizing the ELPV dataset with 2624 images, CNNs such as ResNet-50, VGG-16, VGG-19, and DarkNet-19 are employed for feature extraction. The SVM model, incorporating 2000 selected features, achieves an accuracy of 94.52% in binary classification and 89.63% in four-class classification scenarios.

TABLE 3.4: Models for detection of faults. Extracted from [11].

| Type | Features | Accuracy | Dataset Size |
|---|---|---|---|
| Technique | Description | Accuracy (%) | Dataset Size |
| Image Processing Techniques | Segmentation + Obtention of binary Image + Classification. [163] | 80% to 99% | — |
| SVM + Image Processing Techniques | Images are preprocessed and features are extracted. Used with an SVM with penalty parameter weighting. [164] | 97% | 13392 |
| SVM and CNN | Pre-trained VGG19 with different feature descriptors. Similar results for both methods. [165] | 82.4% | 2624 |
| | CNN composed of 2 layers using leaky-relu. SVM trained with different features. Similar behavior in both models. [166] | 98% | 540 |
| | CNN with 2 convolutional layers. SVM parameters optimized by search grid. [168] | 96% | 2840 |
| CNN | 13 convolutional layers, adaptation of VGG16. Uses oversampling and data augmentation. [167] | Uses a different measurement | 5400 |
| | Multi-channel CNN. Accepts inputs of different sizes. Improves feature extraction. [169] | 96.76% | 8301 |
| | 6 convolutional layers. Regulation techniques like batch optimization. [170] | 93% | 2624 |
| | Fully Convolutional Neural Network. Pretrained u-net, composed of 21 convolutional layers. [171] | Uses a different measurement | 542 |
| | CNN aided by a Complementary Attention Network. Usable with different CNN architectures. [173] | 99.17% | 2300 |
| WT + SVM and FFNN | Combines discrete WT and stationary WT to extract features. SVM and FFNN classify them. [172] | 93.6% | 2029 |
| CNN + SVM, KNN,... | Extracts features from different networks, combines them for feature selection. Uses Resnet-50, VGG-16, VGG-19, and DarkNet-19. [174] | 94.52% | 2624 |

Analyzing the state of modules or cells has always been important for optimizing production since damaged modules are not as productive as they should be. This problem has primarily been applied at the cell level, involving the segmentation of images taken of solar modules. Only few authors have provided open datasets to test models with a more regular amount of data. The main challenge of this problem lies in its nature. Most models are trained with unbalanced datasets, as the number of damaged modules is usually considerably smaller than that of good-state modules.

To improve neural models, researchers have explored the use of pre-trained neural networks like VGG-19 to leverage patterns found in other datasets. Despite their challenges, a considerable number of models have been presented in the literature and have achieved good results (Fig. 3.10), with Convolutional Neural Networks being the most commonly used (Fig. 3.9). However, there is still much to be done in

this area. Most models only utilize Electroluminescence images, but the incorporation of other techniques such as Thermography could provide additional information and improve model performance.

Another promising approach could involve addressing the imbalance in the data. Some studies have attempted to use simple methods such as flips or rotations, but more complex algorithms are needed to generate images that can effectively train the models.

Deep learning methods are predominantly implemented with TensorFlow, while OpenCV is commonly used for image preprocessing. MATLAB is utilized for traditional methods.

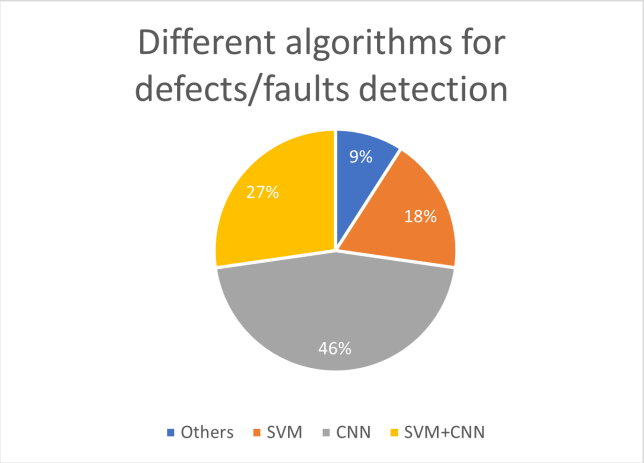


FIGURE 3.9: Diagram of sectors of most used IA methods for Defect Detection. Extracted from [11].

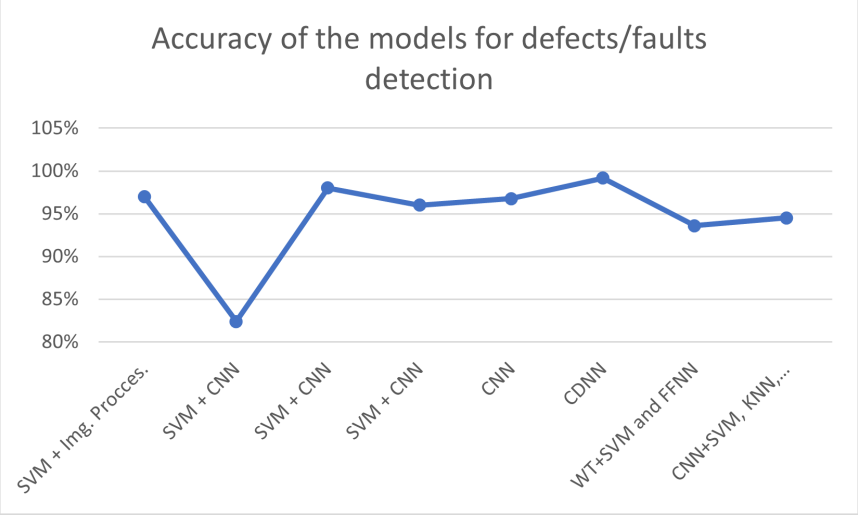


FIGURE 3.10: Accuracy of the different models for detection.Extracted from [11].

### 3.2.2 Estimation of the performance

Another way of tackling this problem is to directly consider their performance when analyzing the PV cells of modules. As explained before in the introduction

(Chapter 1), this is the main approach of this thesis since the datasets have information about the I-V curve of each sample.

Only a few studies have addressed this issue. The works by Hoffman aim to predict the Module Power using EL images [13] or PL [12].

In these studies, Hoffman et al. employed Deep Learning techniques, particularly Residual Neural Networks, to develop predictive models. Despite the complexity of the task, their models achieved promising results. Specifically, they reported mean absolute errors (MAE) of 4.4% and 3.7% for predicting Module Power from EL and PL images, respectively.

However, it's important to note that these works focus primarily on predicting at module-level rather than individual cell-level. While their results demonstrate the effectiveness of Deep Learning in analyzing solar module images, the proposed approach differs in its finer granularity, targeting cell-level analysis.

## 3.3 Synthetic Data Generation

The contents of this section have been adapted from [59], [60].

Data augmentation serves as the predominant approach for addressing image data scarcity, involving the introduction of slight modifications (such as rotations, flips, and minor deformations) to original images to generate new ones [171], [174], [175]. However, recent research has advocated for the adoption of more advanced AI techniques, notably Generative Adversarial Networks (GANs), to produce synthetic images [176], [177]. GANs are regarded as state-of-the-art algorithms for data generation [178], and their application extends to various domains, including photovoltaic (PV) systems, where they have been employed to tackle diverse challenges [179].

The concept of generating synthetic EL images of PV cells using GANs has also been explored in other studies [176], [177]. These investigations introduce synthetic datasets created with different GAN architectures trained on EL images of cells exhibiting various defects. Although the datasets from these studies have not been publicly released, it is apparent that the synthetic images are labeled based on visual inspection to train standard defect/normal classifiers. However, it is important to note that the synthetic cell's energy output performance cannot be measured, as it is simulated.

The work presented in [180] also tackles the issue of generating images but in their case, they use a commercial software known as "Griddler-Pro". However, the generation is based in the creation of new defects in the original ones since the study is focused in defect detection.

## 3.4 Main Findings

The application of AI in addressing various challenges within the PV sector has been extensively demonstrated. One of the most significant topics in this field is the analysis of PV modules or cells through their images, as evidenced by the substantial number of research papers focusing on this issue.

Most studies use EL images as their primary input because these images provide more detailed information about the modules compared to other techniques. However, as will be explained in its section, it has been observed that EL images are not capable of directly showing all kinds of problems in PV cells (Objective SO5). The predominant approach to analyzing PV modules involves identifying defects on the surface of PV cells, treating this as a classification task. Depending on the study, this may involve binary or multiclass classification. Additionally, some research also addresses the detection of defect locations.

There are only a few studies that do not focus on defect detection. These studies align with the main objective of this thesis: to estimate the performance of PV modules based on their images (Objective SO3). However, most of these studies concentrate on the module level rather than individual PV cells. This scarcity of research may be attributed to the difficulty in obtaining IV curves of PV cells, which are necessary to label data for training AI models. While most research relies on deep learning methods, this thesis will explore alternative approaches that could also be suitable for solving this problem (Objective SO4).

Another limitation of the majority of works is that the models created for one kind of PV module or cell are not tested with other kinds. This limitation reduces the utility of the models since they could underperform with other technologies. Therefore, testing with various kinds of PV cells is essential (Objective SO6).

The lack of research is further highlighted by the absence of a public dataset of EL images that includes information about the energy production of each sample. Existing datasets are primarily designed for defect detection, providing only defect-related information for each sample. This issue can be addressed by creating public datasets comprising both measured and synthetic data (Objective SO1).

GANs have been previously utilized to generate synthetic EL images of PV cells and represent the state of the art in synthetic data creation across various fields. However, there is no public dataset available that includes labels related to the theoretical performance of these synthetic PV cells (Objective SO2).

# Chapter 4

# Materials

The main work of the thesis has been performed by manually collecting the data, creating various datasets, and developing the models for problems. This divides the materials needed into four different categories: The PV cells and masks used, the materials needed for measuring the I-V curve of the cells, the ones needed for capturing the EL image of the cells, and the materials used in the processes of creating the models.

## 4.1 Photovoltaic Cells and Masks

The PV cells used in the experiments can be classified according to their technology and number of busbar bars. Fig. 4.1 presents a sample of each kind of PV cell.

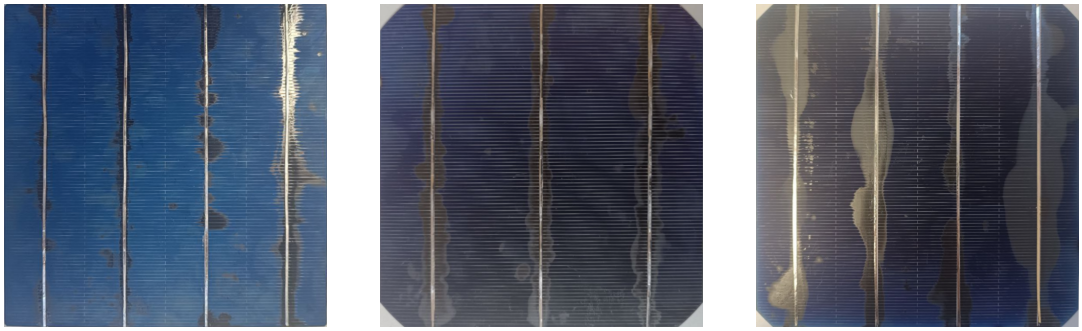

(A) Polycrystalline with 4 busbar (Poly-4).

(B) Monocrystalline with 3 busbar (Mono-3).

(C) Monocrystalline with 4 busbar (Mono-4).

FIGURE 4.1: Different Kinds of PV cells used in the experiments.

The cells that were measured were originally brand-new cells, most of them did not present any defects. To improve the data, it was necessary to create artificial masks that imitated defects or shadows presented in cells installed in operating farms. These masks are capable of absorbing sun irradiation since they were created by combining cardboard with foil.

## 4.2 Materials for measuring the I-V curves of the cells

The measuring of the I-V curves was performed using a Three Quadrants I-V tracer capable of measuring at the Cell Level. According to its specifications, it has a resolution of 25 mA in current and 1 mV in Voltage. More details can be found in its original paper [181].

The PV cells were illuminated by LED array composed of 42 infrared LEDs. (Fig. 4.2)

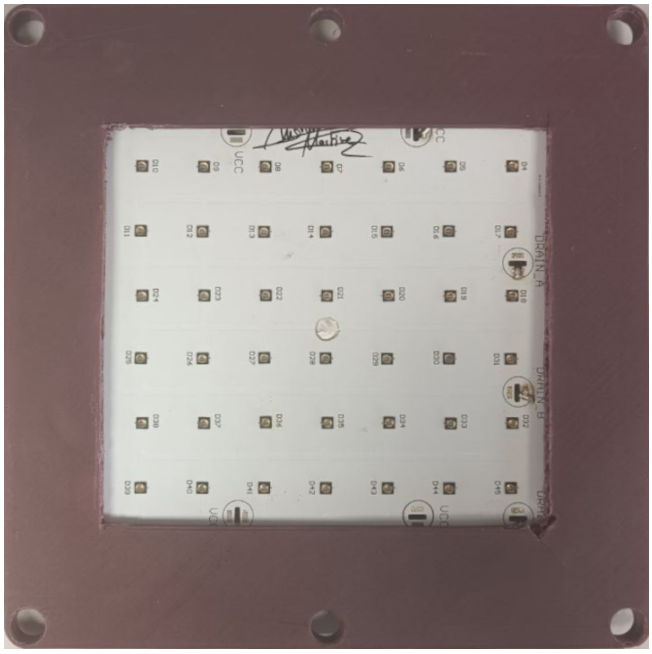

FIGURE 4.2: Led Array used in the experiments

Fig. 4.3 presents the setting used for these measurements.

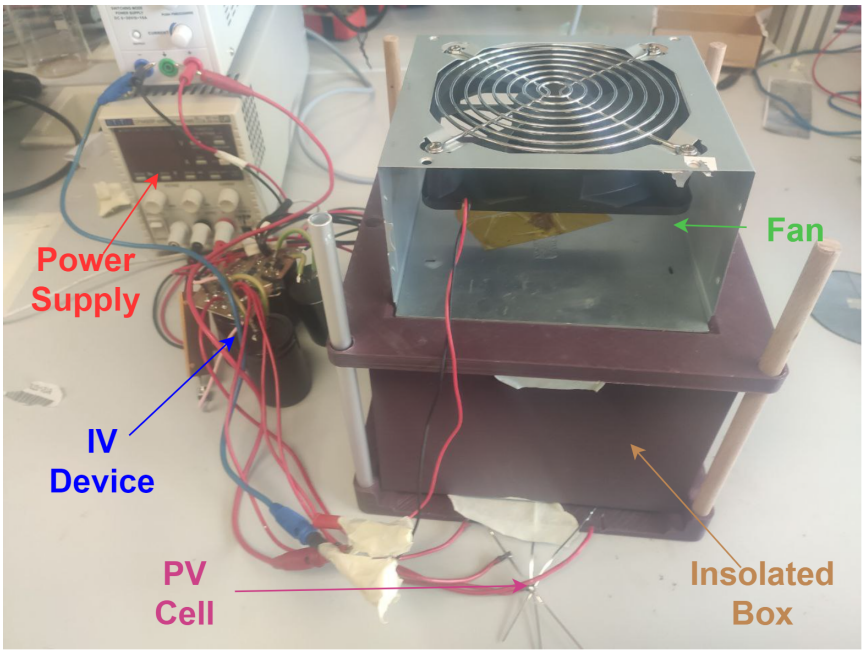


FIGURE 4.3: Setting used to measure the I-V Curves of the PV cells. Extracted from [59].

Some additional tools were needed to perform correctly the measurements:

- Insulated Box
- Power Supplies for the LED Array and the I-V tracer.
- Multimeters.
- Wire.
- Soldering station for connecting the I-V tracer with the PV cells with wire.
- Fan used to cool the LED array and the PV cell.
- A computer used to communicate with the I-V tracer.

## 4.3 Materials for Capturing the EL image of the cells

The EL images were obtained using a silicon detector camera, specifically the *InGaAs C12741-0*, equipped with an 8 mm focal length lens and an *f number* of 1.4. Fig 4.4 presents the setting used for obtaining these images.

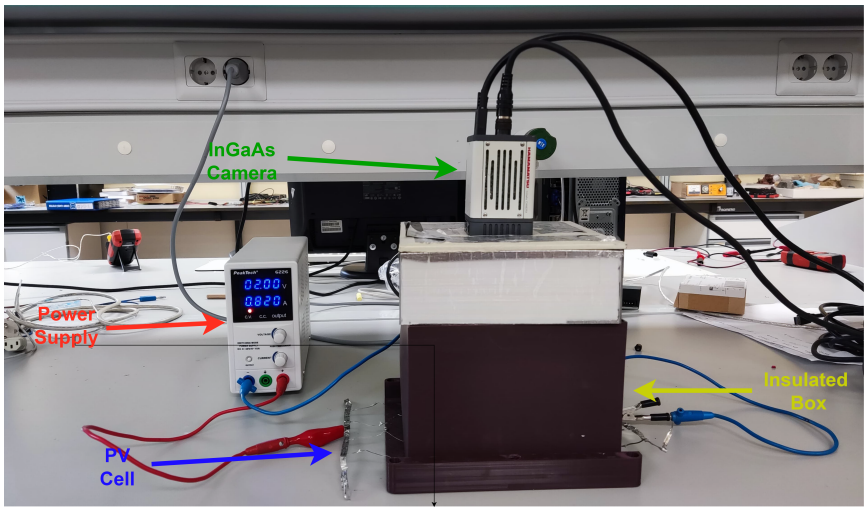


FIGURE 4.4: Setting used to capture the EL image of the PV cells. Extracted from [182].

Some additional tools were needed to perform correctly the measurements:

- Power Supplies for the PV cells and the camera.
- Multimeters.
- Wire.
- Soldering station for connecting the Power Supply with the PV cells with wire.
- A computer to communicate with the camera.

## 4.4 Materials used in the processes of creating the models

The experiments were run in a laptop with an AMD Ryzen 7 5800H CPU, 16 GBs of RAM memory, and a Nvidia Geforce GTX 1650 as GPU.

The preprocessing and labeling of the Data have been conducted using Python, using scientific libraries such as Matplotlib, OpenCV, Numpy and SkImage.

The experiments and analysis of the results have been performed using Python with libraries such as Tensorflow, Sklearn and Matlab with applications such as Fuzzy Designer, Wavelet Image Analyzer, Regression Learner, and Classification Learner.

# Chapter 5

# Methodology

To achieve the objectives outlined in the thesis, an experimental research methodology inspired by classical methodologies [183], [184] has been adopted. This methodology is divided into several phases:

1. Identifying the Research Problem: The process initiates with pinpointing the issues that need to be addressed.
2. Literature Review: A comprehensive review of state-of-the-art research about the identified issues is conducted to grasp the context and establish a robust theoretical foundation.
3. Objective Setting: Specific objectives are defined to steer the research and guide the experiments that will be undertaken.
4. Experiment Design: Experiments are meticulously designed to fulfill the established objectives, adhering to an appropriate methodological approach.
5. Data Collection: The methodology for acquiring the necessary data is carefully planned and implemented.
6. Execution of Experiments: The experiments are conducted according to the designed protocols.
7. Analysis of Results: The outcomes of each experiment are scrutinized to evaluate their alignment with the objectives. In cases where expectations are not met, adjustments are made to the experimental approach, and experiments may be repeated.
8. Publication of Findings: The most significant results are disseminated and published in scientific journals or presented at conferences.

## 5.1 Methodology Overview

After defining the global objective and the first analysis of the State of the art was performed, it was necessary to start the procedure of obtaining of the data since there were not any available datasets suitable for the experiments. This procedure was divided into two different processes: capturing the EL images and measuring the I-V curves of the Polycrystalline PV cells. They will be explained in Section 5.2. This completed objective SO1, however, the gathering of data continued during all the whole thesis.

During the creation of the dataset, it was evident that the nature of the problem provoked an unbalance in the data. It is known [62], [185], [186] that underrepresented classes have problems when they do not have enough samples of the data. To solve this issue, a review of the state of synthetic images was performed and it was found that Generative Adversarial Networks are capable of creating synthetic images while maintaining the characteristics of the original images. The following experiment was planned:

- Creation of a Synthetic Dataset using Generative Adversarial Networks (Explained in chapter 6.1) :
  - Objective: Improve the amount of available data (Objective SO2)
  - Expected Result: A synthetic dataset with labeled data similar to the original dataset.

After creating the synthetic dataset, the next step was the creation of the first working model capable of fulfilling the objective SO3. After researching the topic, an approach based on features extracted from the images was proposed with the following experiment:

- Creation of a estimator based on features (Explained in chapter 6.2) :
  - Objectives: Creation of models capable of estimating the output power of PV cells (Objective SO3). Analysis of the unbalance of the data in the problem (Objective SO2).
  - Expected Result: Models capable of providing an estimation with low error.

The obtained models were capable of solving the problem and fulfilling the objective SO3. However, objective SO4 required the creation of additional models in order to explore new approaches and methods for the problem. The following experiments were planned:

- Creation of a Classifier based on Fuzzy Logic (Explained in chapter 6.3) :
  - Objective: Test other technologies or approaches for the problem (Objective SO4). FL systems provides the rules of the reasoning made by the algorithm
  - Expected Result: A Fuzzy Logic model capable of solving the problem as a classification.
- Creation of an estimator based on Adaptive Neuro Fuzzy Inference System (ANFIS) 6.4) :
  - Objective: Test other technologies or approaches for the problem (Objective SO4). This technology combines FL and NN and is capable of solving problems and providing easy-to-understand rules.
  - Expected Result: An ANFIS model capable of solving the problem as a classification.

These two proposals provide two different alternatives that while do not provide the same performance as the original models, they have other advantages instead, completing the objective SO4.

Another issue observed in the analysis of the data is that some cells presented a clear discrepancy between their EL images and their I-V curve. A study about this problem was performed with the following experiment.

- Analysis of the connection Failures(Explained in chapter 6.5) :
  - Objective: Analyze the causes of the problems presented by several PV cells that are not visible directly with their EL image (Objective SO5).
  - Expected Result: A technique capable of detecting these kinds of defects and how they are presented in the PV cells.

This experiment revealed that certain cells exhibited a sequence of resistance defects that were not directly observable in EL images but became apparent when applying wavelet transform to the EL image. This analysis fulfills the objective SO5.

To achieve objective SO6, a new dataset consisting of Monocrystalline PV cells was created concurrently with the experiments described in the preceding paragraph. Following the creation of this dataset, a novel model was developed to accommodate various types of PV cells with the following experiment:

- Improve the estimation with various kinds of PV cells. (Explained in chapter 6.6) :
  - Objective: Analysis of the effects of various kinds of PV cells in the performance of the models. (Objective SO6).
  - Expected Result: Create a model capable of dealing with various kinds of PV cells.

This model successfully met the criteria outlined in objective SO6, fulfilling the final objective that was planned for the thesis. Fig. 5.1 presents a diagram of the workflow used during this thesis.

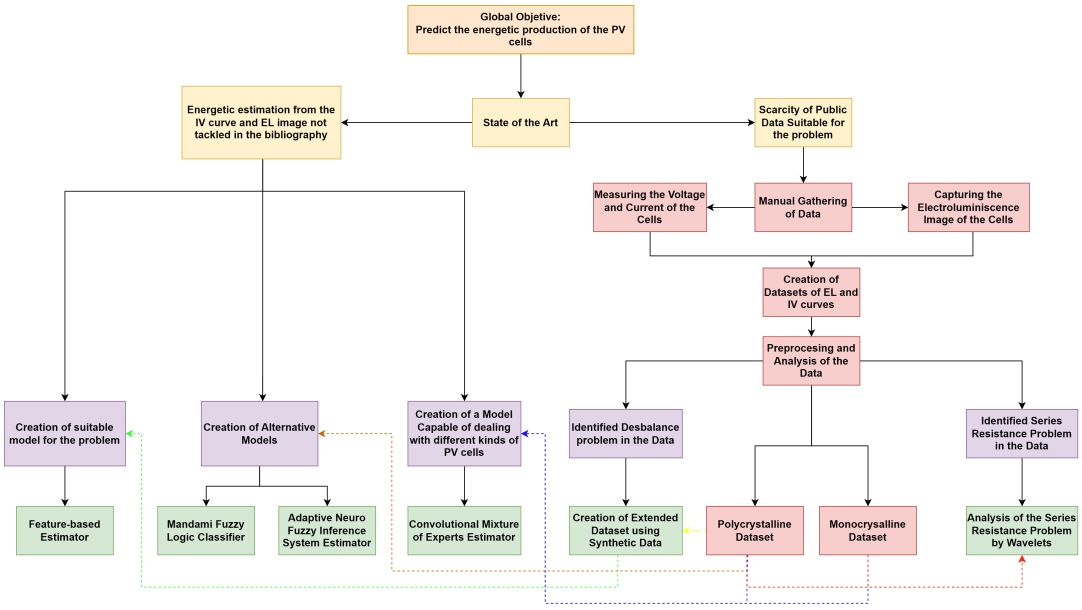


FIGURE 5.1: Diagram of the methodology used during the thesis.

## 5.2 Dataset preparation

This section explains the processes (gathering of the data, preprocessing, feature extraction) that have been performed to create the datasets.

### 5.2.1 Data Gathering

As explained before, it was necessary to obtain two different things from the PV cells: the EL image and the IV curve. Each one needed a different process.

#### Calibration of the currents for the LED array and the PV cells

Before taking the measurements it was necessary to determine the irradiance values that were going to be used and what current were needed to be supplied to the LED array and the PV cells to obtain the ideal conditions.

- Current for the LED array: An analysis of the injected current was performed, trying different values of current while measuring the irradiance produced by the LED array. This experiment was conducted using the Insulated Box created for the measurements. All the measurements were taken with a similar temperature in the LED array since its internal heating can reduce its light production. Fig 5.2 presents the tendency line obtained from the measurement, with an irradiance of 1000 W/m$^2$ when using 2.53 A.

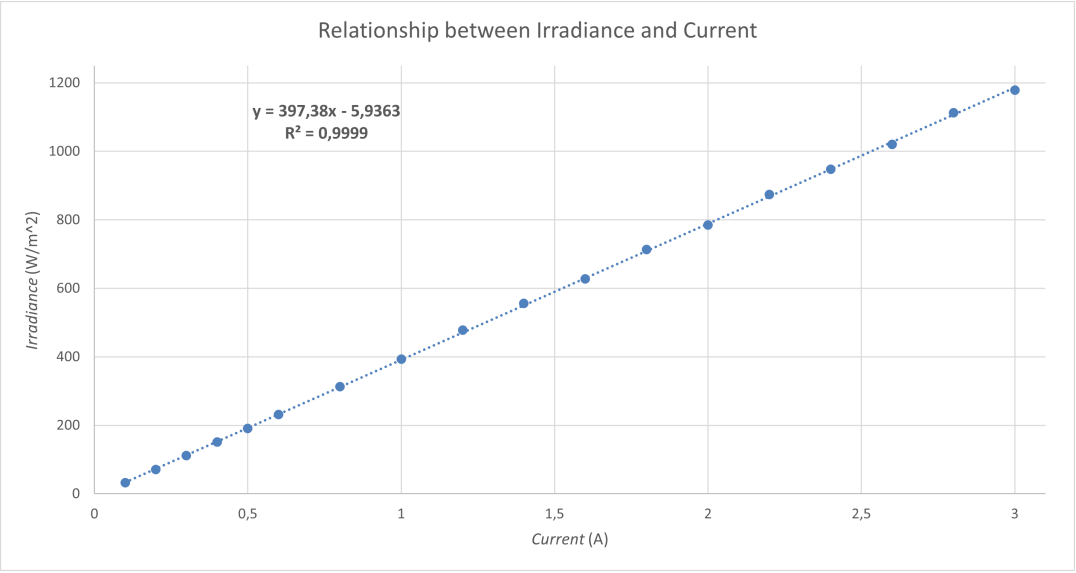


FIGURE 5.2: Relationship between the current provided to the LED array and the produced irradiance

Since 1000 W/m$^2$ is considered the standard condition, the following values have been considered.

- 1.27 A: Corresponds with an irradiance of 500 W/m$^2$ (50%)
- 1.52 A: Corresponds with an irradiance of 600 W/m$^2$ (60%)
- 1.78 A: Corresponds with an irradiance of 700 W/m$^2$ (70%)
- 2.03 A: Corresponds with an irradiance of 800 W/m$^2$ (80%)

  - 2.28 A: Corresponds with an irradiance of 900 W/m$^2$ (90%)
  - 2.53 A: Corresponds with an irradiance of 1000 W/m$^2$ (100%)

- Current for the PV cell for the EL image: These values were chosen based on the Short Circuit Current Value of the cells (7.5 A) that was provided by the manufacturer: 7.5 A (100%), 6.75 A (90%), 6 A (80%), 5.25 A (70%), 4.5 A (60%) and 3.75 A (50%).

**EL images**

The EL images were captured using the InGaAs Camera and the setting presented in Section 4.3. The images were taken in the same conditions of pressure and temperature, varying the values of current injected (7.5 A, 6.75 A, 6 A, 5.25 A, 4.5 A and 3.5 A) in the PV cells to simulate different values of irradiance. Three different kinds of PV cells have been used, Fig. 5.3 presents a sample of an EL image of each one.

(A) Polycrystalline with 4 busbar (Poly-4).

(B) Monocrystalline with 3 busbar (Mono-3).

(C) Monocrystalline with 4 busbar (Mono-4).

FIGURE 5.3: EL Images of the PV cells used in the experiments.

The various masks (More information in Section 4.3) were applied to the surface of the PV cells to simulate various kinds of defects or shadows that appear in real installations on the surface of the PV modules. These masks mostly intend to simulate soiling defects [18]. Fig 5.4 presents a sample of each type.

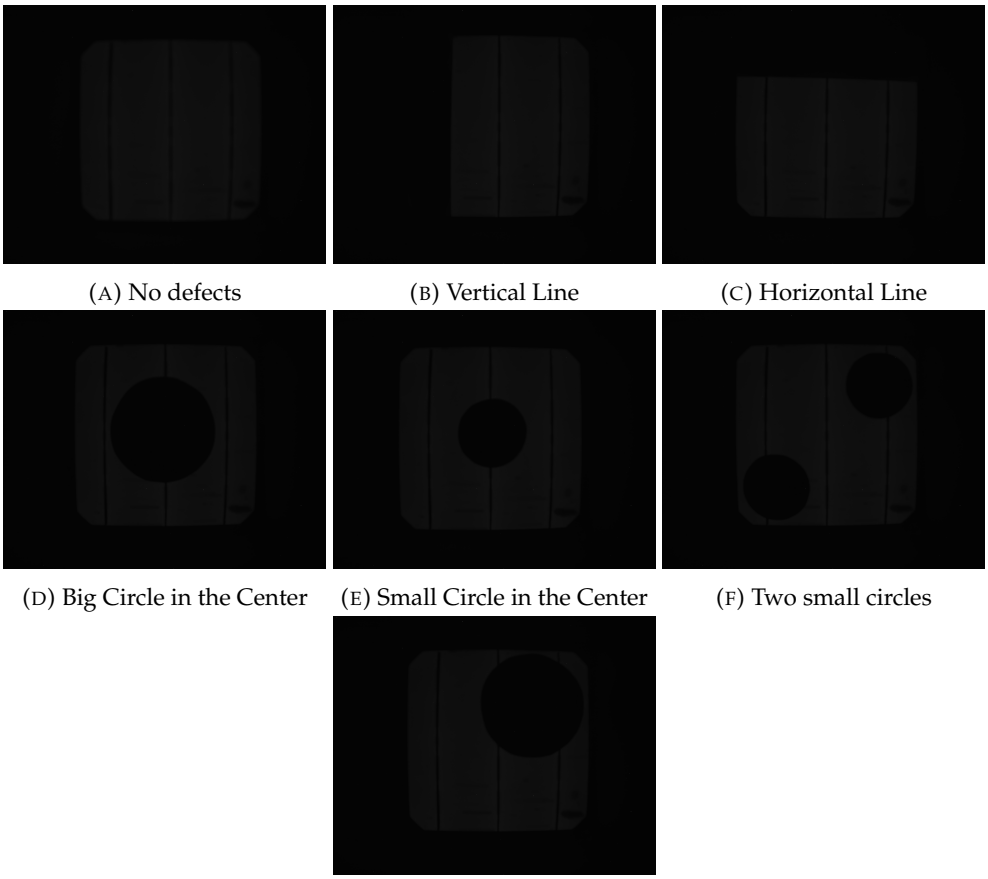

(A) No defects (B) Vertical Line (C) Horizontal Line

(D) Big Circle in the Center (E) Small Circle in the Center (F) Two small circles

(G) Big Circle in a corner

FIGURE 5.4: Samples of EL images with each kind of shadow or defect presented in the dataset

As it can be seen. The obtained images suffer from various problems that will be fixed in the preprocessing.

### I-V Curves

The I-V curves were measured with the IV tracer and the setting presented in Section 4.2. The measurements were taken in the same conditions of pressure and temperature, varying the current injected (1.27 A, 1.78 A, 2.03 A, 2.28 A, 2.53 A) in the LED array to simulate different values of irradiance.

These various values of irradiance were applied along the several masks that have been explained before. Fig. 5.5 presents the various I-V curves of a single cell, it can be seen how the values depend on the kind of mask used and the current used in the LED array.

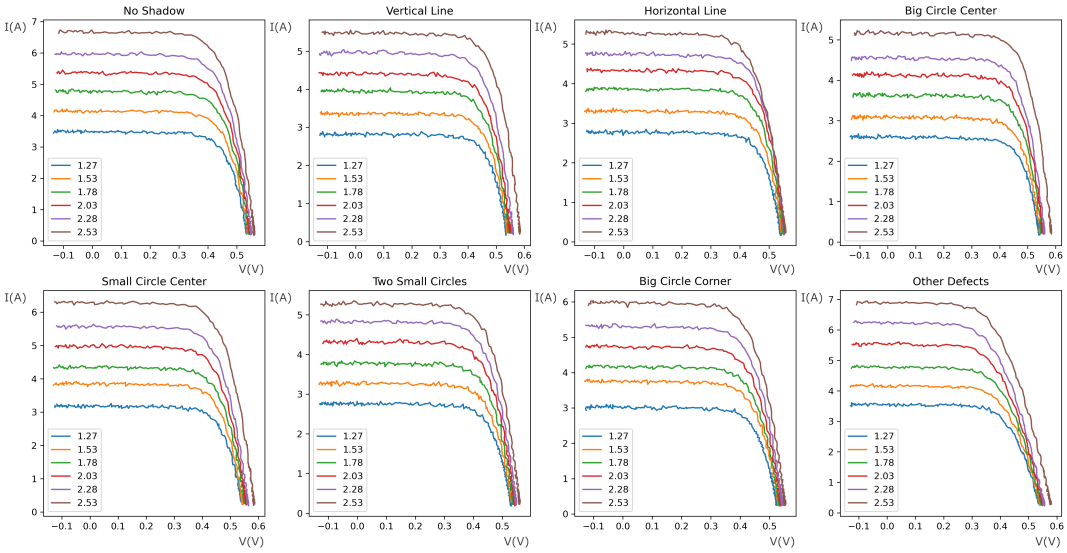


FIGURE 5.5: All the I-V curves of a single PV cell. (Polycrystalline Cell 5)

### 5.2.2 Image Preprocessing

#### Removing the luminous noise and dead pixels of EL images

The images present some pixels that present lighter colors due to light leaks produced by limitations of the insulated setting that was used and Dead pixels of the lens of the camera (See Fig. 5.6). These pixels reduce the quality of the captured EL images since they provide bright pixels that do not exist in the real cell.

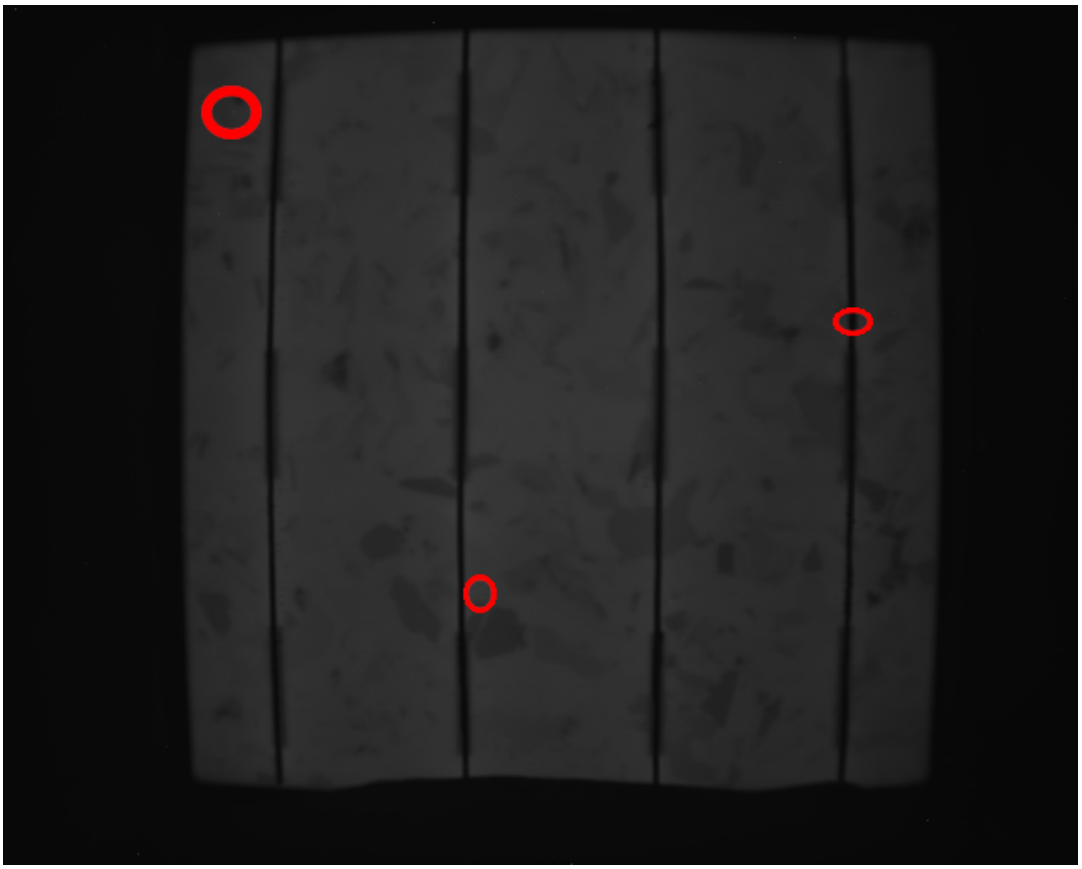

FIGURE 5.6: EL image with some strange pixels. The red circles indicate where are samples of these pixels.

To solve this problem, it has been necessary to capture an image with the camera before capturing each EL image. This image captures the light leaks and the dead pixels of the lens (See Fig. 5.7).

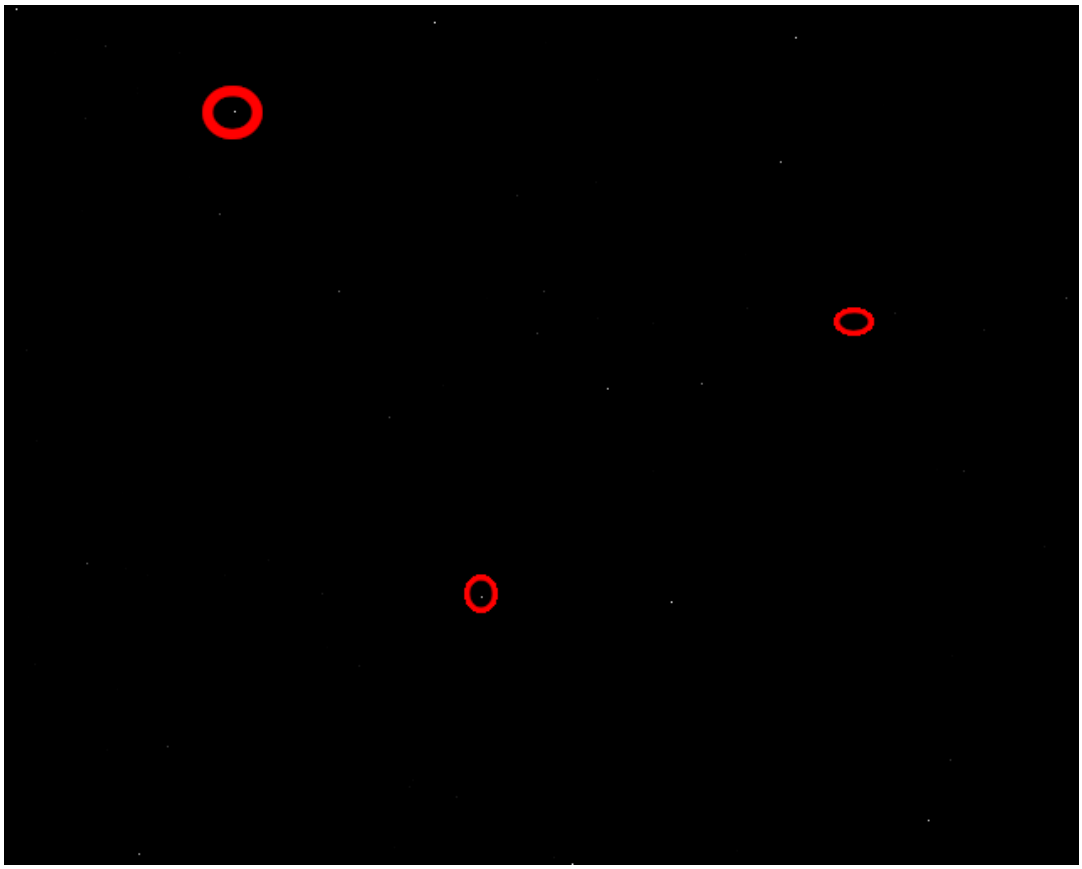

FIGURE 5.7: Image taken before the EL image. The red circles indicate zones with dead pixels or light leaks.

After that, a subtraction between the EL image and the previous image is performed, this removes any bright pixel that appears on the "dark" image from the EL image (See Fig. 5.8).

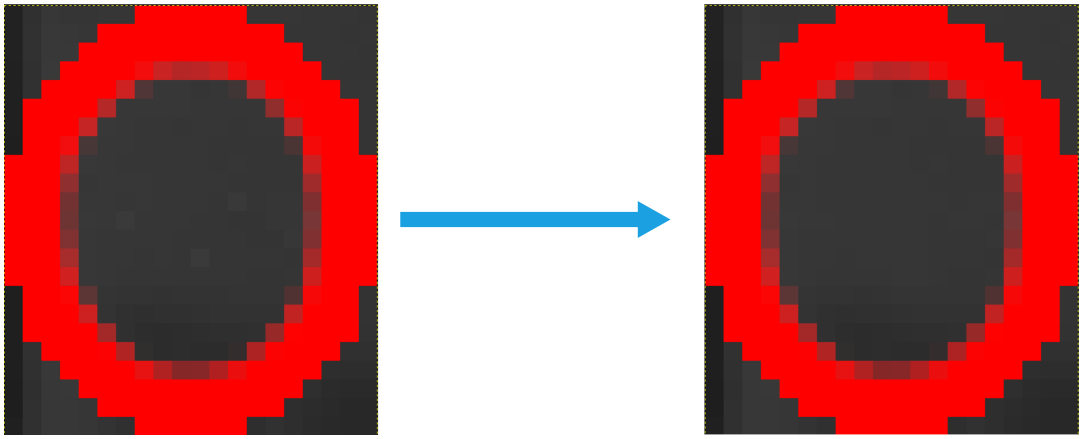

FIGURE 5.8: A zone of an EL image before and after the noise removal

### Fixing the Luminosity

Another critical issue of the images is that images are extremely dark. It can be seen in Fig. 5.9 how the histogram of the image is stacked to the left since it only uses a range (from 0 to 256) of the values available (from 0 to 65536).

(A) An EL Image before the luminosity fix


(B) The luminous histogram of the same EL image cell.

FIGURE 5.9: An EL image and its histogram before the luminosity fix

This is fixed by performing a histogram standardization of the images, widening the histogram to all of the available values. Fig. 5.10 presents an EL image and its histogram after performing the explained standardization.

(A) An EL Image after the luminosity fix

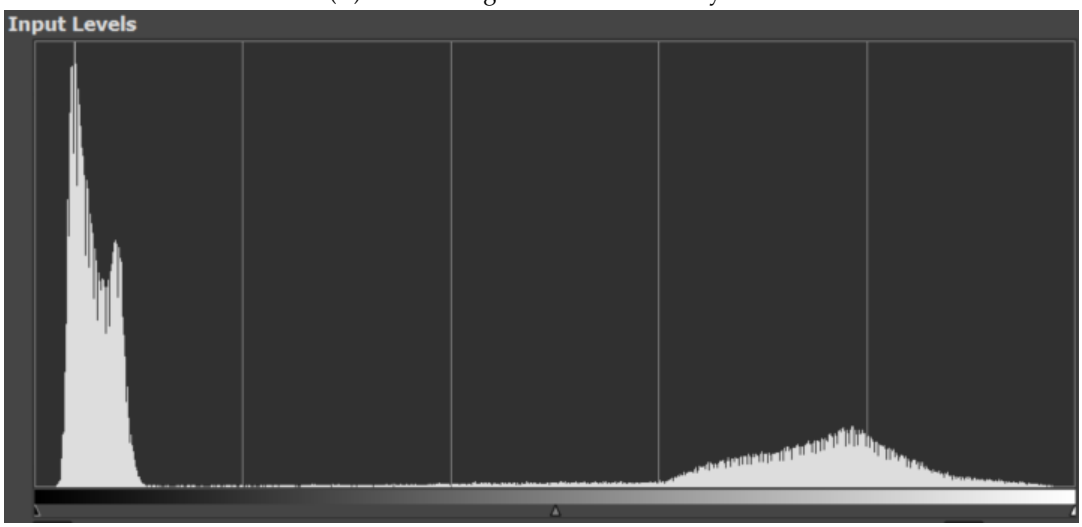


(B) The luminous histogram of the same EL image cell.

FIGURE 5.10: An EL image and its histogram after the luminosity fix

**Removing the black surrounding areas**

The final problem presented by these images is that the images have black areas surrounding the PV cells. These areas correspond to the walls of the box that was created for insulating the PV cells, however, they do not provide any kind of information about the PV cells.

To solve this issue, it is necessary to be able to detect the cell in the images and remove the other areas. This is obtained by following these steps:

- Binarize the image using several filters to remove the details from the images, leaving only the most important characteristics. The filters used are Sharpen Filter, Denoise Filter, Gaussian Filter, Color Reducer, and Closing (See Fig. 5.11). More information about these kinds of processes can be found in the bibliography [187].

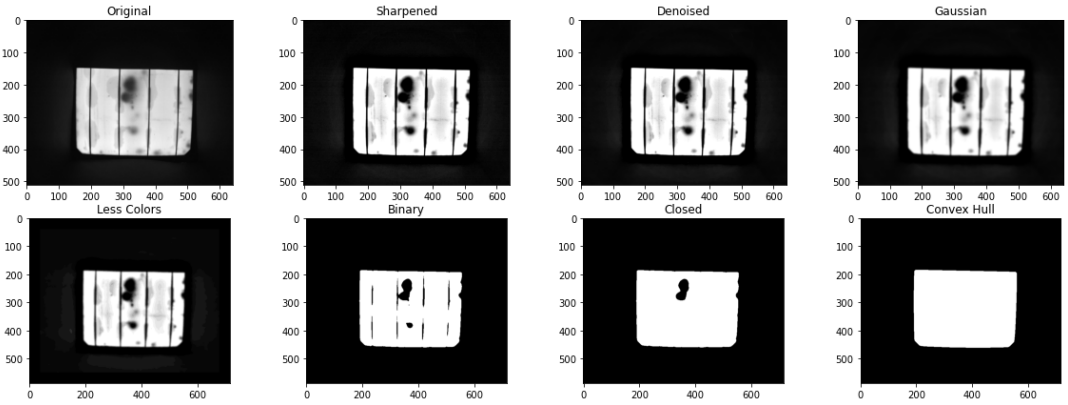


FIGURE 5.11: An EL image during the process of applying the filters to binarize the image and calculate the Convex Hull

- Calculate the Convex Hull of the binarized image. (See Fig. 5.11).
- Detect the slope and extreme points of the borders of the Convex Hull by using Hough Lines. (Fig. 5.12)
- Find the corners of the cell by finding the intersection between the detected borders. (Fig. 5.12)

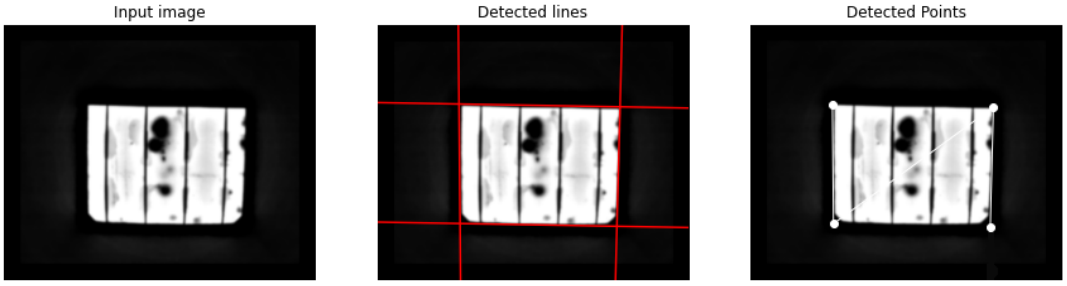


FIGURE 5.12: An EL image during the process of detecting the borders and the corners

- Perform a fix in the position corners depending on the kind of shadow presented in the EL image.
- Fix the perspective of the image according to the corner points.
- Crop the surrounding areas of the PV cell according to the points

After finalizing this algorithm, the images have been reduced only to the surface of the cell. (Fig. 5.13) presents to original input and the output for one EL image.

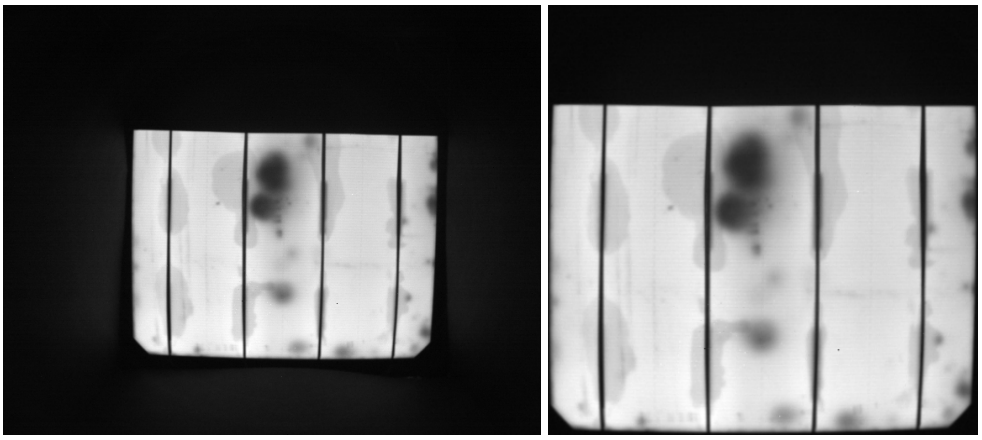

(A) EL image before the border removal (B) EL image after the border removal

FIGURE 5.13: An EL image before and after the removal of the surrounding areas.

The obtained images are suitable for AI models and visual inspection. Fig. 5.14 presents a sample of each kind of shadow that appears in the dataset after applying the preprocessing.

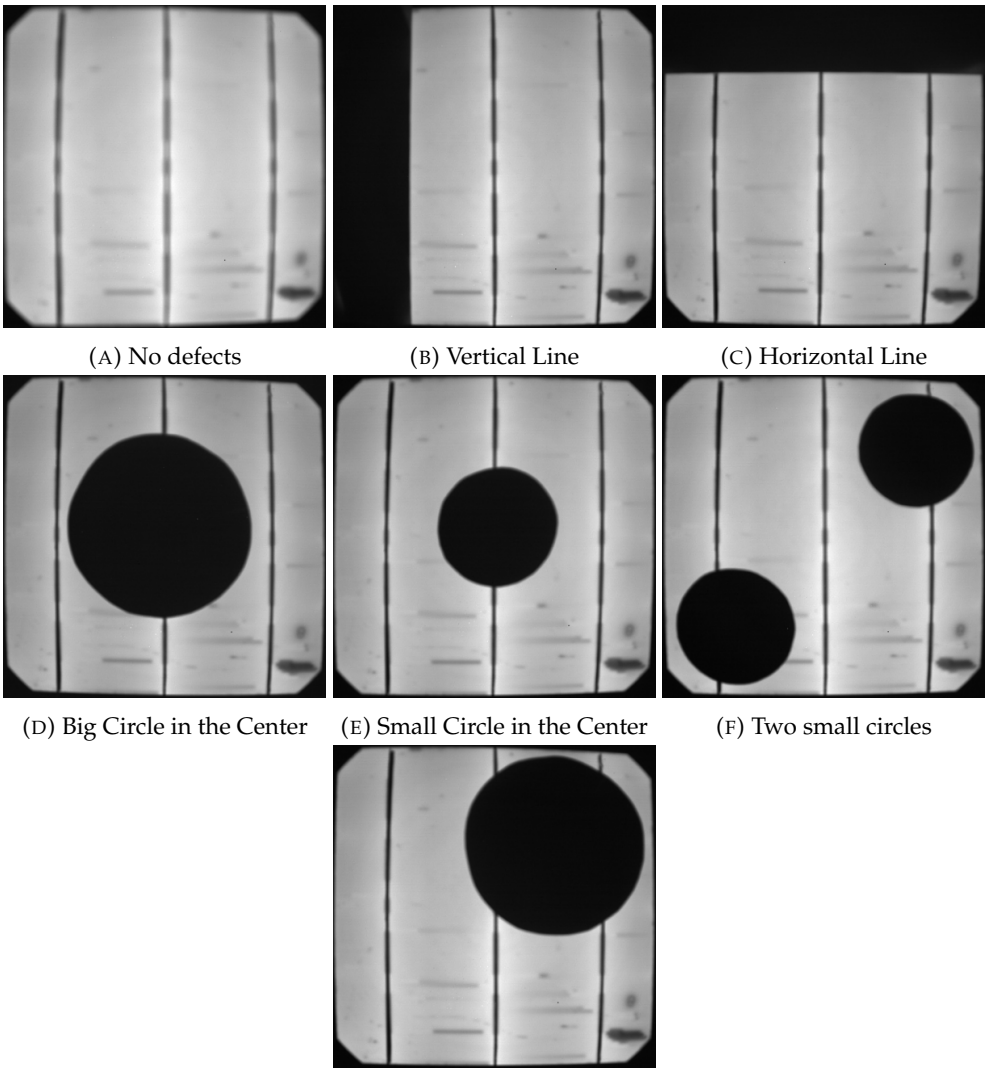

(A) No defects (B) Vertical Line (C) Horizontal Line

(D) Big Circle in the Center (E) Small Circle in the Center (F) Two small circles

(G) Big Circle in a corner

FIGURE 5.14: Samples of EL images with each kind of shadow or defect presented in the dataset after being preprocessed

### 5.2.3 Feature Extraction

One of the most important limitations of traditional AI methods such as FL lies in their inability to process images directly. To overcome this limitation, it is imperative to identify and extract pivotal features from the images. This extraction process involves discerning the most relevant characteristics that effectively represent the information contained within the images. The forthcoming section delves into the selection of such features and elucidates the methodologies employed for their extraction.

Two different methods for Feature Extraction have been developed, a manual feature extraction based on the histogram and an automatic extraction based on a Resnet Network [188]. Not every experiment has used all the available features, as will be explained in each corresponding section.

### Manual Extraction

The features, after being selected manually, have been extracted automatically from each image. The features chosen are the following:

- Mean, Median, Mode, and Variance values. These values are obtained by taking into account all the values of the pixels of each image.
- Number of dark pixels, gray pixels, and white pixels presented in the images. The process for obtaining these features involves partitioning the histogram into several subgroups and calculating the pixel count within each subgroup (see Fig. 5.15):
  - The color histogram of each image is obtained and accumulated into the general histogram of all images.
  - The minimum point between the first and second peaks is used to separate the black area from the gray area.
  - The minimum point between the second and third peaks is used to separate the gray area from the white area.
  - The mean between all of the values of each minimum point is computed. These values are rounded an used for the limit of each group (0.35 and 0.7). Fig 5.15 presents a cell and its histogram where the 3 different peaks can be seen, the divisions between the three groups are also presented.
  - The amount of pixels of each group is divided by the total amount of pixels of each image.

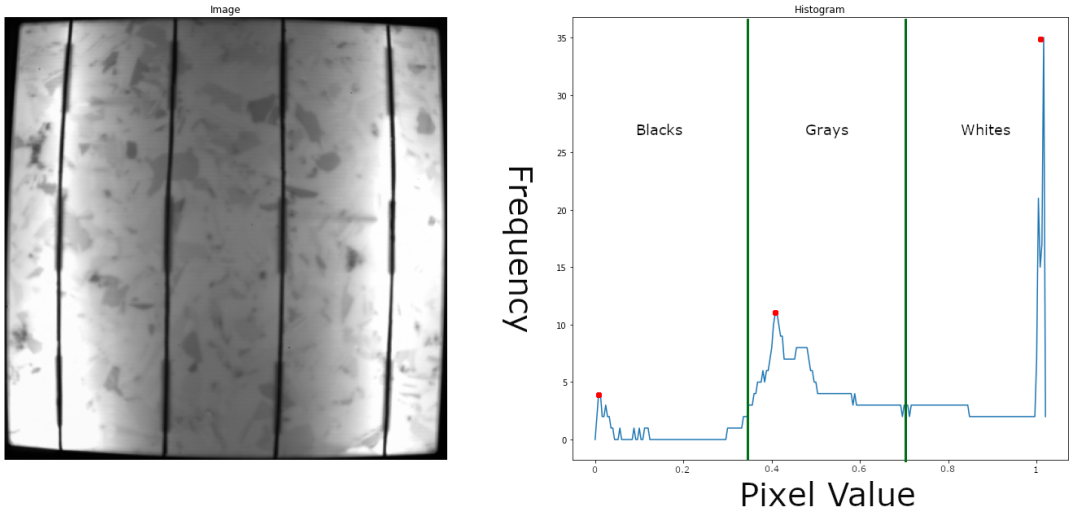


FIGURE 5.15: A PV cell and its histogram. Red dots represent the peaks. The green lines represent the division between the groups for calculating the features. Extracted from [189].

- Roughness of the histogram of the image, computed by taking into account the Inflection Points found in the histogram.
- Number of Peaks in the histogram. Only the important important peaks are considered, The curve has been softened to avoid false peaks provoked by the irregularities of the histogram.

- Distance between the two highest peaks. These two peaks correspond with the peaks of black pixels and the peak of white pixels in the majority of the images
- Height and Width of the two previously explained highest peaks

**Resnet Extraction**

Pre-trained convolutional networks are widely utilized for feature extraction across various domains, showcasing excellent performance. In the context of EL images of solar cells, they have demonstrated promise. Research indicates that models trained on datasets like ImageNet [190] offer significant advantages due to their remarkable ability to extract features from diverse images and address different problems [191], [192]. Among the popular architectures, ResNet [188] stands out, featuring configurations ranging from 18 to 152 layers. For the specific problem at hand, ResNet50 was chosen, leveraging its implementation available in the TensorFlow Library [129]. To extract features, the measurements were converted into RGB images and resized to align with the network's specifications.

### 5.2.4 Data Labelling

The I-V curves of the cells provide information about their values of current and voltage. However, this does not provide direct information about the performance of the cells.

The Max Power Point (MPP) of the cell provides the best indicator about the performance its performance, this point corresponds with the maximum value of power in the Power-Voltage (P-V) Curve. This curve can be computed with the values of current and Voltage ($Power = Voltage * Current$), Fig. 5.16 presents a Current-Voltage curve of a PV cell and the Power-Voltage with the MPP remarked.

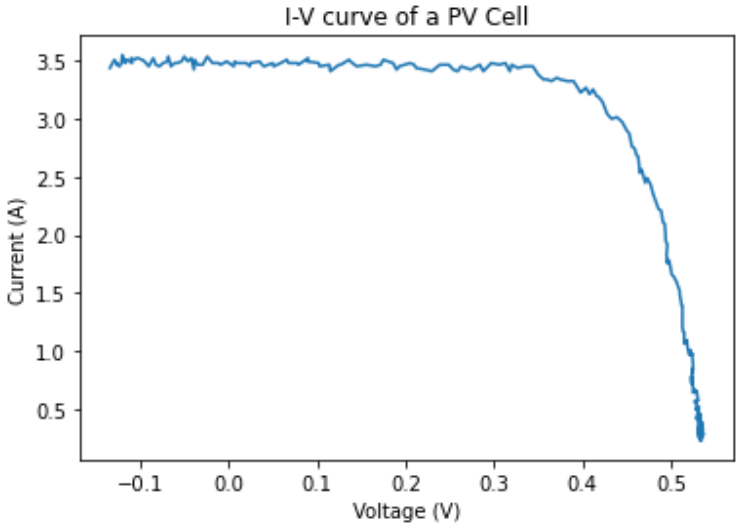


(A) I-V curve of a PV cell

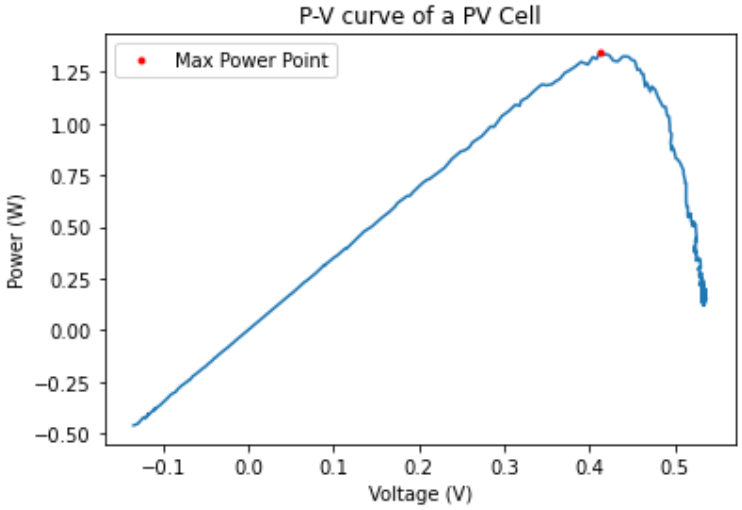


(B) The correspondent P-V curve computed from the values of the I-V curve. The MPP is marked with a red dot.

FIGURE 5.16: I-V and P-V curves of a PV cell.

However, the MPP depends on the irradiance presented in the measuring of the I-V curves. It has been seen in Fig. 5.5 how higher values produce higher values of Current which results in higher values of Power. This is an issue since the problem needs a value that is independent of external conditions of the cell such as irradiation. The solution to this issue embarks on standardizing the values of MPP, making them independent of the irradiance. Two different proposals have been tackled for this standardization:

- First Proposal: Min Max Normalization with the 5 highest values. This proposal provides an output with a domain $[0, 1.1]$ since there are cells that can outperform the computed MPP ideal value.
  - The MPP values for each measurement are computed.
  - The MPP values are divided into six different groups depending on the irradiance used to take the measures. The following steps will be repeated for each one.
  - The mean of the 5 highest values is considered, this value will represent the ideal MPP of the cell of that group.
  - Each MPP value is divided by the ideal value.
- Second Proposal: Combination of Z-normalization and Min-Max normalization. This proposal provides an output with a domain of $[0, 1]$ independent of the irradiance.
  - The MPP values for each measurement are computed.
  - The MPP values are divided into six different groups depending on the irradiance used to take the measures. The following steps will be repeated for each one.
  - A Z-normalization using the mean and the standard deviation is performed on the MPP values.
  - A min-max normalization is performed in the z-normalized values.

The processes were performed for each one of the three different kinds of PV cells that were available. The domain of the output value for each one of the proposals has been divided into three different intervals (See Table 5.1), this made it possible to tackle the problem as a classification problem (Chapter 6.3).

TABLE 5.1: Intervals of each one of the classes that have been used to tackle the problem as a classification

| | Cells with good performance (Class 0) | Underperforming Cells (Class 1) | Severely underperforming Cells (Class 2) |
|---|---|---|---|
| First Proposal | $[1.1, 0.825]$ | $(0.825, 0.725)$ | $[0.725, 0]$ |
| Second Proposal | $[1, 0.75]$ | $(0.75, 0.65)$ | $[0.65, 0]$ |

The first proposal was proposed with the idea of comparing the MPP values of each cell with an ideal MPP value that a cell in good condition should have. The idea of computing the mean of the best values also reduced the problems of extreme values due to measuring errors. However, it was found that this proposal had some

drawbacks: The domain was not completely settled, since some cells could have values bigger than 1. Another problem is that the majority of the values were concentrated between 0.6 and 1. (Fig. 5.17). This proposal was used in the experiments explained in Sections 6.1 and 6.2.

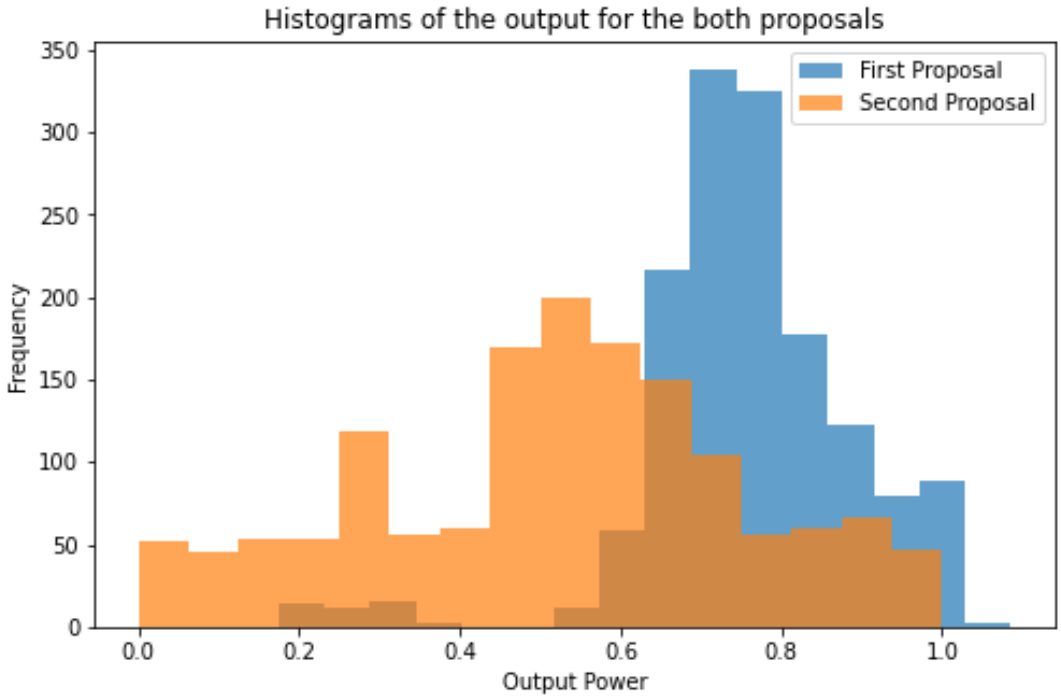


FIGURE 5.17: Histogram of distribution of the output values for both proposals

The second proposal fixed the problems of the first proposal, since it provides a domain of $[0, 1]$ with values distributed along all the domain (See Fig. 5.17). This proposal was used in the experiments explained in Sections 6.3, 6.4, 6.56.6

### 5.2.5 Obtained Datasets

The processes of gathering of data, preprocessing and labeling the data have resulted in the following datasets composed of the EL images and the output power values of each sample:

- Poly-4: Composed of 785 samples of Polycrystalline Cells with 4 busbars.
- Mono-3: Composed of 398 samples of Monocrystalline Cells with 3 busbars.
- Mono-4: Composed of 168 samples of Monocrystalline Cells with 4 busbars.
- Mono-Combined: Composed of the 566 samples of Monocrystalline cells (Mono 3 + Mono 4).
- Poly-4 Reduced: Poly 4 reduced to the size of Mono-Combined (566 samples). The objective of this dataset is simple, having a dataset of the same dimensions of the Mono-Combined provides a more valid comparison between the models trained with them.

- Mono + Poly: Composed of all the 1351 samples available (Poly-4 + Mono-Combined)
- Mono + Poly Balanced: Dataset comprising all the images from Mono-Combined and an equivalent number from Poly-4 (Poly-4 Reduced).

Fig. 5.18 shows each one of the explained datasets and the relationship between them.

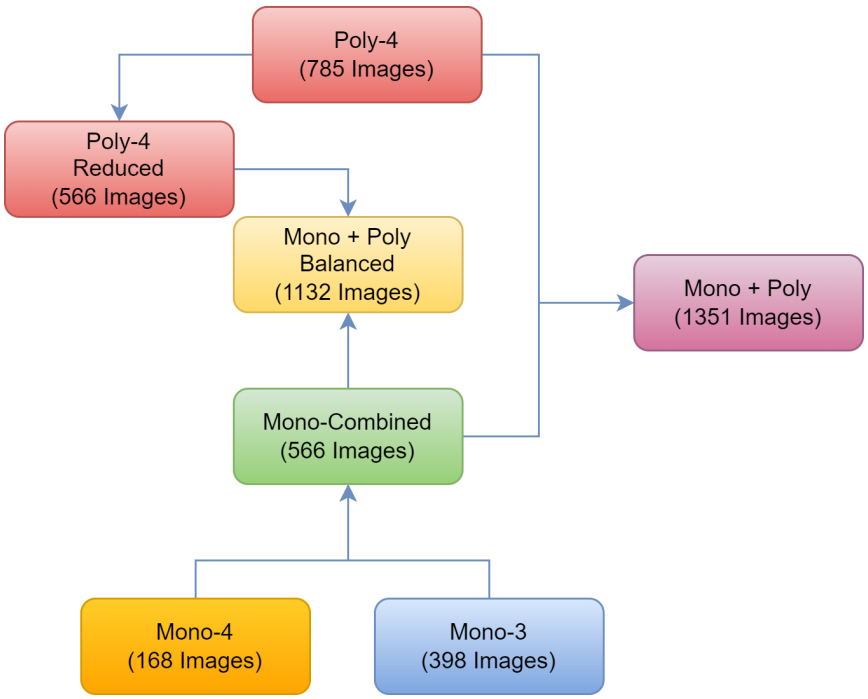


FIGURE 5.18: Diagram of the datasets used in the experiments during developing of the thesis

The datasets are divided into three distinct sets in most of the experiments described in the following sections. The allocation percentages for each set are determined to ensure sufficient samples for training the models to capture all patterns in the data while retaining enough data for meaningful validation and testing of the models.

# Chapter 6

# Experiments

This chapter presents the experiments conducted throughout the thesis, detailing the objectives, the data used, model specifications, and outcomes of each experiment. Additionally, a concise summary accompanies each experiment, encapsulating its key findings and implications.

## 6.1 GAN generated dataset

The work explained in this section has derived into two publications: one in the Congress **V ICSC-CITIES 2023** in the article [60] and another in the Journal JCR Q2 Sustainability [59].

### 6.1.1 Objective

The limitation of data is one of the biggest problems with DL models since these kinds of algorithms need high amounts of data to obtain a good performance. Moreover, it was observed that our datasets had another limitation: they were unbalanced. This unbalance of the data was shown in a high amount of cells with an output power of 0.6-0.8 (based on the first proposal of labeling) (5.2).

This section presents the solution to these two problems: An synthetic dataset. This dataset increases the number of samples available to train the models (Objective S01). It also can be used to reduce the difference in number of samples between the different values. The creation of this Synthetic Dataset was produced using a Deep Convolutional Generative Adversarial Network (DCGAN) [65].

### 6.1.2 Structure

The section is structured in the following manner: initially, it provides an introduction to the data employed for training the GAN network. Following this, it delineates the architectures of both the generative and discriminator networks. Lastly, it describes the training and labeling process and conducts several analyses to demonstrate their quality.

### 6.1.3 Data

The GAN model was trained using the polycrystalline Dataset with the first labeling method presented in Chapter 5.2 since it was the only one available at that moment.

### 6.1.4 Model

This section presents the architecture and hyperparameters of the two networks composing the GAN model. It also presents the obtained synthetic images.

#### Generative Network

The generative network was developed adhering to the principles of the DCGN. It incorporates three distinct Convolutional Transpose Layers (Deconvolutional) to generate patterns. The utilization of these layers in conjunction with batch normalization [193] enhances the generative capabilities of the network and improves the stability of the training process. Leaky Relu [194] is employed as the activation function, as it typically yields superior performance compared to standard Relu. The architecture of this network is illustrated in Fig. 6.1. The input to the network (Fig. 6.2a) comprises a random noise array sampled from a normal distribution, while the output is a 200 $\times$ 200 image (Fig. 6.2b). This size selection aims to reduce the computational burden of the algorithm while still producing images with a substantial amount of information. Further crucial hyperparameters can be found in Table 6.1.

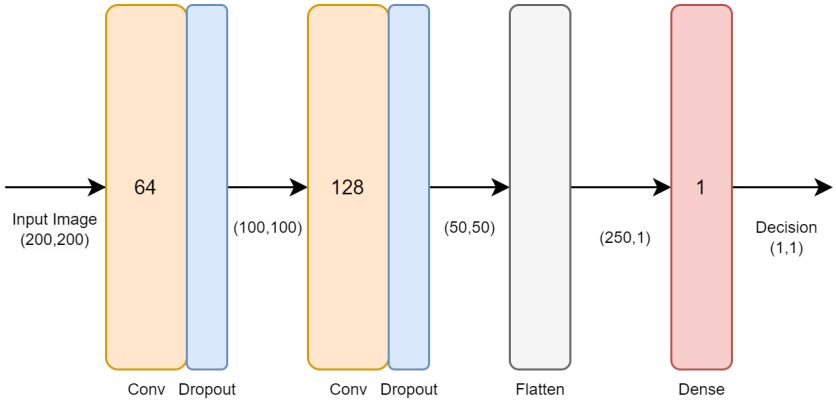


FIGURE 6.1: Architecture of the generative network. Extracted from [59].

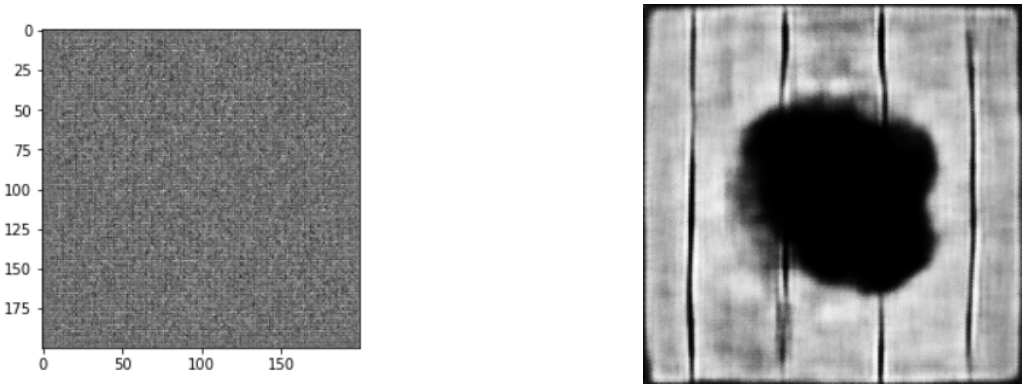


(A) Output image before training.

(B) Output image after training.

FIGURE 6.2: Images generated by the GAN before and after training. Extracted from [59].

TABLE 6.1: Hyperparameters for both networks. Extracted from [59].

| Activation Function | Loss Function | Learning Rate | Epochs | Batch Size | Output Size |
|---|---|---|---|---|---|
| Leaky Relu | Cross Entropy | $5 * 10^{-5}$ | 800 | 4 | 200x200 |

### Discriminator Network

The Discriminator network also adheres to the principles of DCGAN. Utilizing various Convolutional Neural Networks, the network identifies patterns within the images. The conventional feed-forward component of the network is omitted, leaving only the output layer. Dropout layers and batch normalization are incorporated to enhance the network's generalization capacity and stabilize the training process. The architecture is depicted in Fig. 6.3. Input consists of a 200 $\times$ 200 image, while the output yields a binary value indicating whether the image represents a real cell or a forgery. The remaining important hyperparameters are consistent with those of the Generator and can be found in Table 6.1.

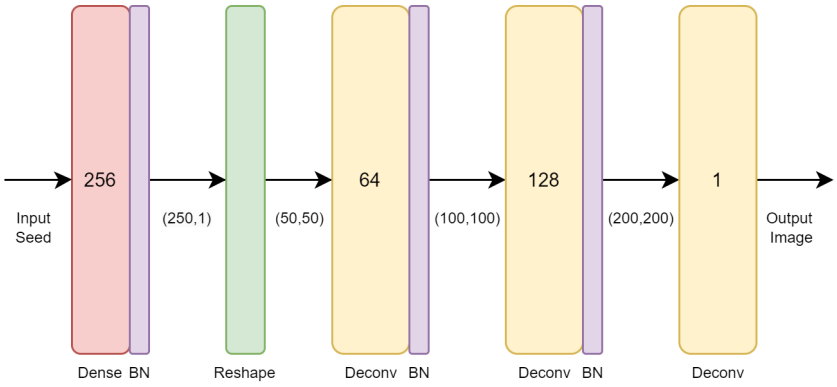


FIGURE 6.3: Architecture of the Discriminator network. Extracted from [59].

### Training

The training was conducted concurrently in both networks using all available samples. The training process initiates with the Generator Network creating synthetic images using random seeds. Subsequently, a mix of real and synthetic images is presented to the Discriminator for training. The loss is computed for each network based on the Discriminator's evaluation results. The evolution of loss for both networks is depicted in Fig. 6.4. Initially, the loss of the Discriminator network is notably high during the first epochs as it has not yet learned the patterns of the original images, thus unable to distinguish between real and forged images, even when the forged images closely resemble noise. As the Discriminator gradually learns to differentiate real images, its loss decreases, leading to an increase in the Generator's loss. Subsequently, the Generator's loss steadily diminishes as it learns to generate images akin to the originals. By epoch 400, both networks reach critical points in their loss evolution. Further changes in values are negligible thereafter, indicating the optimal conclusion of training at that point.

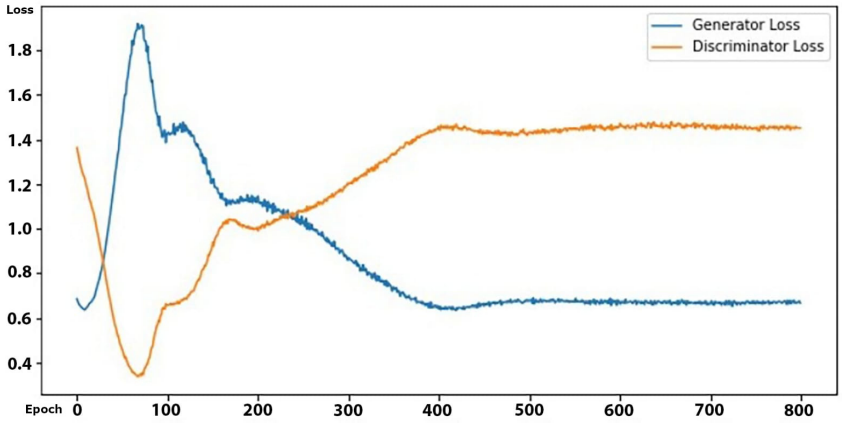


FIGURE 6.4: Evolution of the Generator and Discriminator loss. Extracted from [59].

The training was performed with a CPU AMD Ryzen 7 5800H, 16 GB of RAM, and a GPU Nvidia Geforce GTX 1650. It took 2 hours and 41 min to complete the training.

Following the conclusion of training, the Generator network was employed to generate the synthetic dataset. A total of 10,000 distinct images were generated, each utilizing a unique random seed. Fig. 6.5 showcases a selection of these generated images.

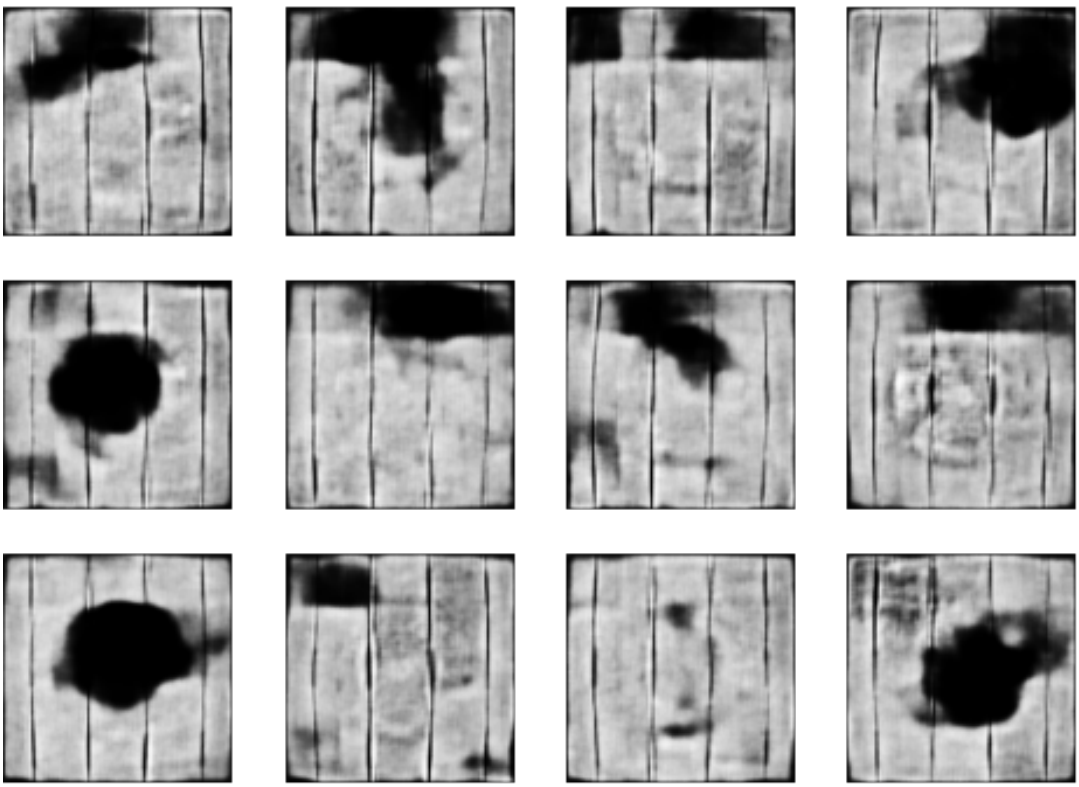

FIGURE 6.5: Samples of the synthetic images generated by our GAN-based method. Extracted from [59].

### 6.1.5 Labelling of the Synthetic Images

Labeling the synthetic dataset presented a unique challenge. As previously explained, the values of the original images were determined based on their IV curve, a process unattainable for synthetic images due to their lack of real-cell representation, thereby rendering measurement impossible.

To overcome this obstacle, the problem was reframed as a regression task solvable through a machine-learning model. The model was trained using the complete dataset of original images alongside their normalized power (MPP) derived from IV curves, as detailed in the preceding subsection (comprising 602 samples). The Random Forest model was selected for its demonstrated low error rate on the original dataset and remarkable generalization capabilities in associating MPP with synthetic images.

The implementation of the algorithm leveraged the Sklearn library for this purpose. Hyperparameter tuning for the RF model was conducted utilizing the Grid Search method available in the Sklearn library (GridSearchCV), resulting in the determination of optimal values outlined in Table 6.2.

TABLE 6.2: Estimation of Random Forest hyper-parameters using GridSearchCV. Extracted from [59].

| **Parameter** | **Range** | **Optimum value** |
|---|---|---|
| n_estimators | [20, 500] | 200 |
| max_depth | [0, 10] | 10 |
| min_samples_split | [1, 10] | 1 |
| min_samples_leaf | [1, 10] | 1 |
| min_weight_fraction_leaf | [0, 0.8] | 0 |

Since Random Forest is not suitable to work directly on raw images, some features were extracted from the images. The features are based on typical statistics (mean, standard deviation, etc.) and other characteristics directly extracted from the histogram (amounts peaks, peaks width, peaks height, amount of colors, etc.) (More information in Chapter 5.2). A complete list can be found in Table 6.3.

TABLE 6.3: Features for Random Forest Regressor. Extracted from [59].

| | | | | |
|---|---|---|---|---|
| mean | median | mode | variance | std |
| roughness | blacks | burned whites | others | peaks_number |
| peaks distance | peak 0 height | peak 0 width | peak 1 height | peak 1 width |

Feature selection (FS) is an important step in the preparation of machine learning models. We used correlation-based FS. As depicted in Fig. 6.6, the cross-correlation between all the original sets of features shows that almost no feature is highly correlated with the others, except for the standard deviation and the variance, which are completely dependent on each other, meaning one of them can thus be safely removed from the final set of features.

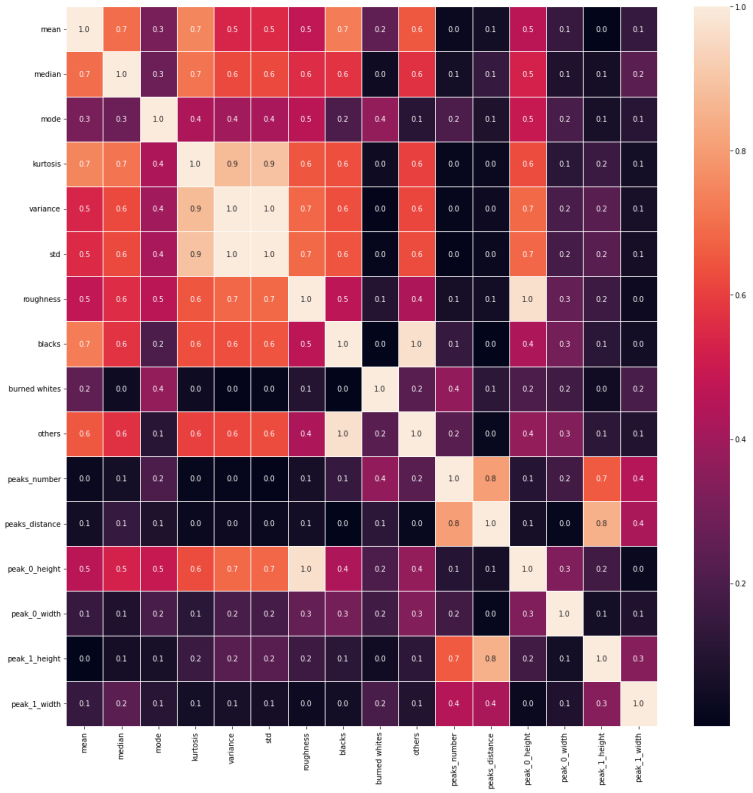


FIGURE 6.6: Correlation Heatmap of the initial set of features. Extracted from [60].

The dataset underwent division into two subsets: training (67%) and validation (33%). This decision was made owing to constraints stemming from data limitations, necessitating a simplified approach. The target variable was defined as the relative power of each cell, which was standardized to fall within the range of 0 to 1.

The model obtained a Mean Absolute Error (MAE) of 0.041 and a Mean Squared Error (MSE) of 0.0038 in the validation dataset. The distribution of the predictions of the model can be found in Fig. 6.7. The low error and the similarity in the distribution confirm the validity of the model. It can also be observed the distribution of the prediction for the synthetic dataset. Finally, the images were divided into two groups, according to their predicted power (class 0 $>$ 0.8 and class 1 $<=$ 0.8). 6963 images were classified as class 0 and 3037 as class 1.

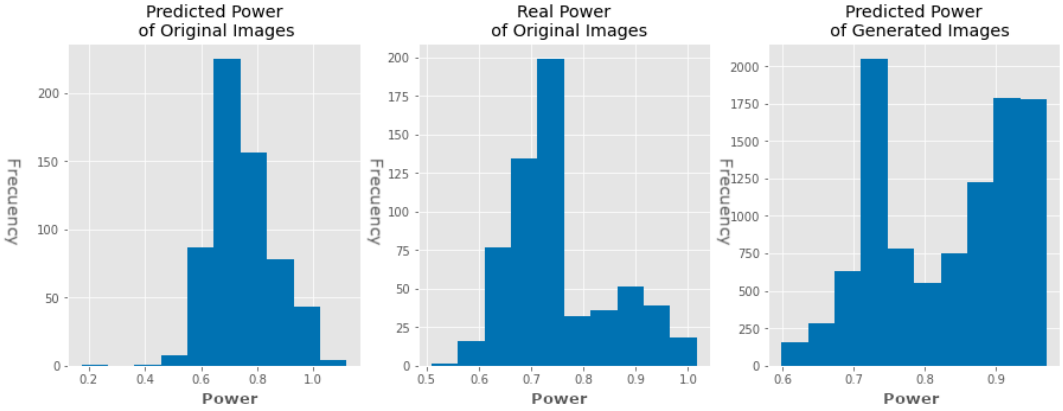


FIGURE 6.7: Histograms of real and predicted normalized power of the original and generated dataset. Extracted from [60].

### 6.1.6 Results

The resulting dataset was divided into two different folders, one for each class: Class 0 (6963 samples, Fig. 6.8a) represented the images whose relative power is at least 0.8, and the images in that class can be considered as functional PV cells. Class 1 (3037 samples, Fig. 6.8b) represented the images with a power of less than 0.8, and the images in that class can be considered as underperforming PV cells.

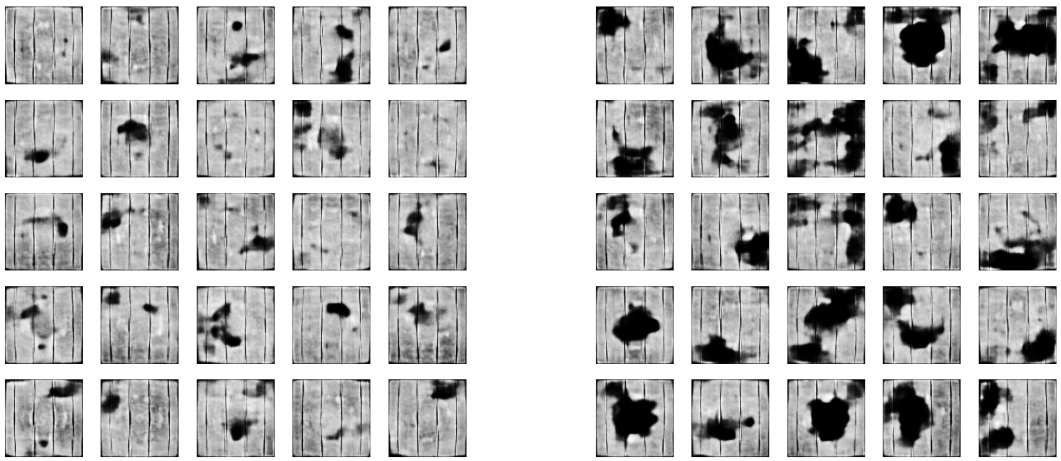

(A) Sample of images of class 0

(B) Sample of images of class 1

FIGURE 6.8: Sample of images of both classes. Extracted from [60].

#### Visual Analysis

To ensure the quality and similarity of the images, two distinct methods are proposed: an analysis based on visual characteristics and histograms in this section, and an analysis based on different metrics in the subsequent section.

As illustrated in Fig. 6.8, the generated images exhibit a comparable structure while introducing new patterns of shadows different from the original ones. This notable feature is a consequence of the generative capacity of the GAN, enabling it to amalgamate various types of shadows observed in the original images to create novel patterns, thereby enhancing the diversity of shadows within the dataset.

Fig. 6.9 illustrates the distribution of previously selected features for labeling (refer to Table 6.3). For each feature, the relationship between its values and the relative power of the cell is presented. Synthetic images are denoted by orange dots, while original images are represented by blue dots. In most features, the original dataset images appear as a subset of the synthetic dataset, with exceptions primarily arising from underrepresented cases. This suggests that synthetic images not only encapsulate the characteristics of the original images but also introduce new instances of defects or shadows while preserving the most significant attributes. This phenomenon is primarily attributed to the generative capabilities of the GAN, which can generate novel patterns by combining input data patterns, thereby enhancing dataset diversity. This augmentation potentially leads to improved performance in machine learning methods leveraging this dataset.

Another noteworthy observation is the absence of the most underrepresented cases in the original data within the synthetic data. This occurrence is also induced by the properties of the GAN, as it necessitates a substantial volume of samples to discern patterns.

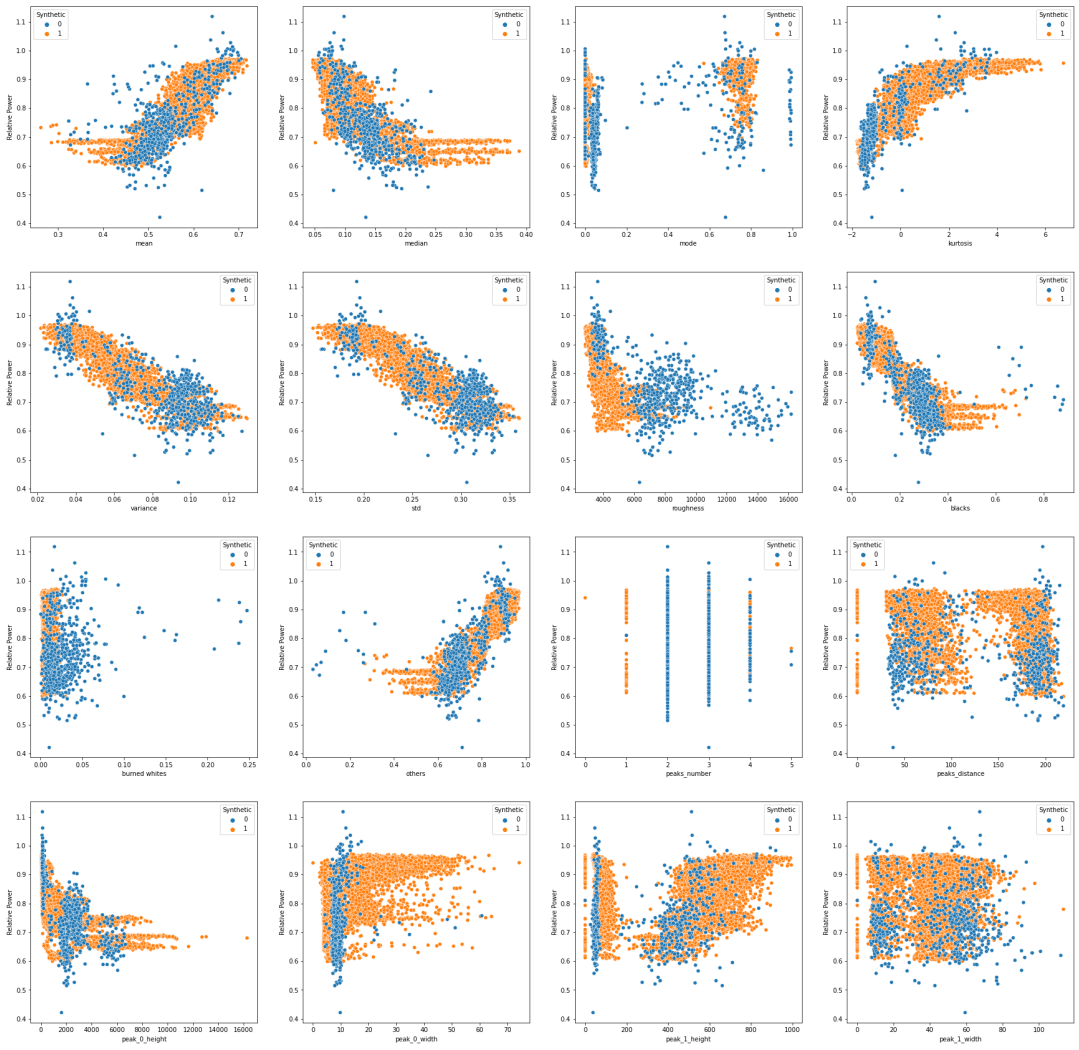


FIGURE 6.9: Distribution of the Relative power generated by a cell as a function of the value of each of the sixteen features used to characterize the images Orange dots: Synthetic Images, Blue dots: Original Images. Extracted from [60].

### Histogram Analysis

The histogram of images provides valuable insights into their characteristics. Fig. 6.10a displays the mean histogram of all images belonging to class 0 in the original dataset, alongside the mean for all images of class 0 in the synthetic dataset.

Observing class 0 images, it's evident that they predominantly consist of light gray to white pixels (values near 200), with occasional minor defects or shadows indicated by the presence of black pixels (values near 0). Notably, a discrepancy between the two datasets is apparent: the synthetic dataset's images exhibit higher but narrower peaks and sometimes appear slightly shifted to the left.

Similarly, Fig. 6.10b presents analogous information for images in class 1. These images are characterized by a significant presence of dark pixels attributable to defects and shadows, with fewer lighter pixels. In the synthetic images, the peak of black pixels is higher, but its width is narrower. The light pixels in synthetic images closely resemble those in the original dataset.

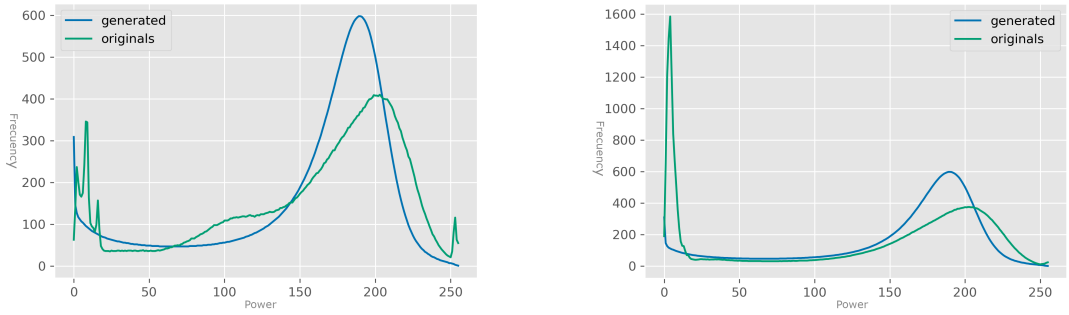


(A) Histogram of the images of class 0

(B) Histogram of the images of class 1

FIGURE 6.10: Histograms of the images of each class. Extracted from [60].

As observed, the histograms of both datasets exhibit a strikingly similar appearance. Any minor disparities are primarily attributable to the augmented variety of patterns of defects and shadows.

Fig. 6.11 showcases two different cells from class 1: one original and one synthetic, both displaying similar characteristics. Upon visual examination of their histograms, it's evident that they share a comparable structure, featuring the same number of peaks and even positioned similarly. However, synthetic images tend to exhibit a more symmetrical histogram and a shift from maximum to lower intensities, as extreme intensity values are less prevalent than in real images.

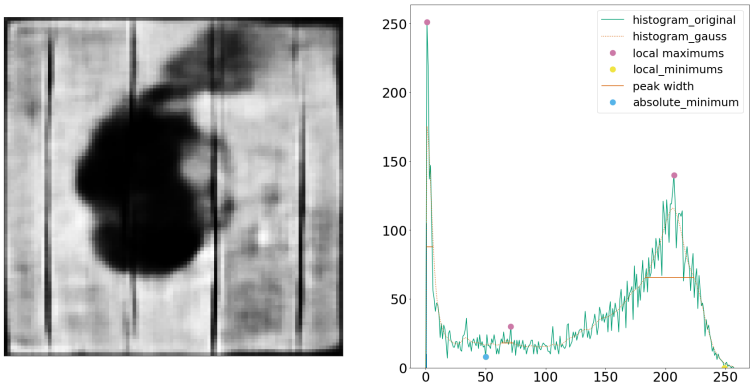


(A) A defective synthetic cell with its histogram

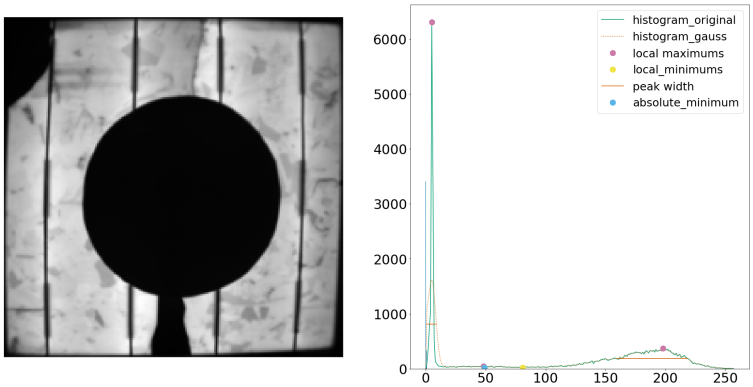


(B) A defective original cell with its histogram

FIGURE 6.11: Comparison of a defective synthetic cell and a defective original cell. Extracted from [60].

Fig. 6.12 depicts the same comparison for two images belonging to class 0. These images exhibit minimal apparent defects. Their histograms share similar shapes, evident from the comparable number of peaks and their placement.

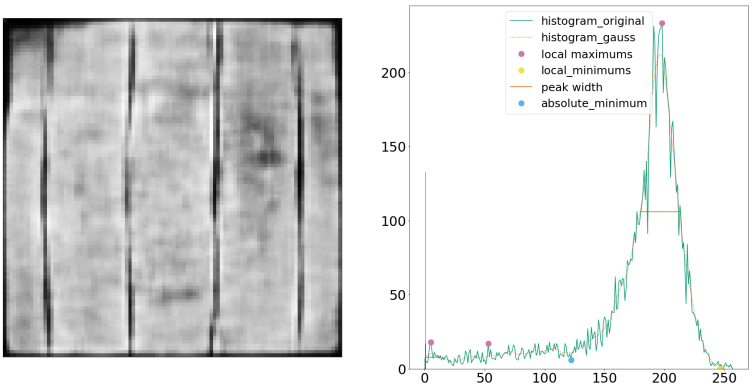


(A) A good synthetic cell with its histogram

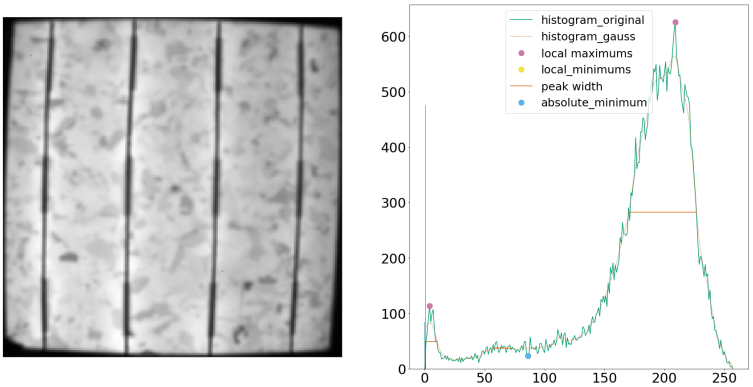


(B) A good original cell with its histogram

FIGURE 6.12: Comparison of a good synthetic cell and a good original cell

Fig. 6.13b illustrates a comparison of histograms depicting the position of the maximum, predominantly found in the right half of the histograms (gray/white colors). Both histograms exhibit a similar shape, indicating consistency between the datasets.

In Fig. 6.13b, histograms of the number of pixels with low values (up to 10% of the maximum values) are presented. Notably, synthetic images do not entirely replicate the distribution observed in the original images.

Similarly, Fig. 6.13c displays histograms of the number of pixels in the last decile, showcasing a similarity in shape with a slight shift to the left. This observation suggests that while the overall patterns are preserved, the GAN method may have some limitations in accurately capturing patterns around the most extreme values. While not critical, this indicates areas where improvement may be warranted in the GAN methodology.

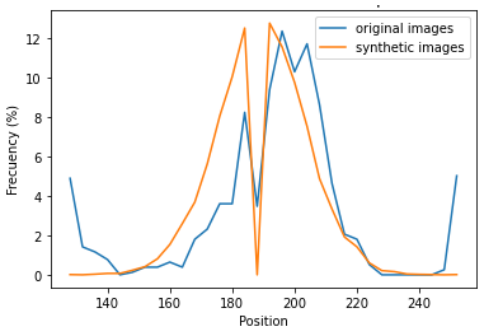


(A) Histogram of the position of the peak of gray/white colors for both original and synthetic images

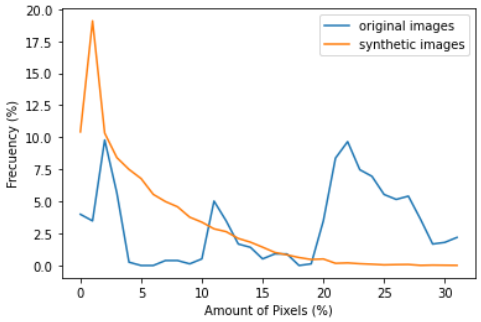


(B) Histogram of the number of dark pixels (First Decile) for both original and synthetic images

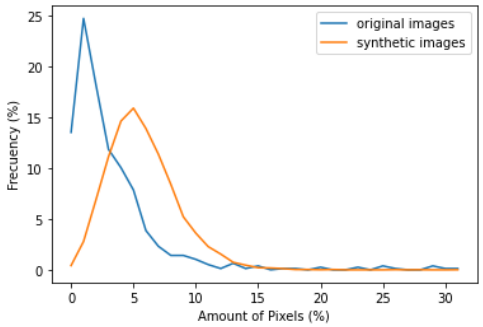


(C) Histogram of the number of white pixels (Last Decile) for both original and synthetic images

FIGURE 6.13: Comparison of the different aspects of the histograms of both original and synthetic images

### Image Quality Metrics

Previous studies on the synthetic generation of EL images of PV cells have typically overlooked the crucial aspect of ensuring data quality by employing objective metrics. The Inception Score (IS) and the Fréchet Inception Distance (FID) emerge as key metrics for assessing the quality of synthetic images. Below, we elaborate on both metrics and present their results.

### Inception Score

The Inception Score, introduced in 2016 [195], is utilized for evaluating the quality of generated artificial images. It relies on a pretrained InceptionV3 model [196] applied to the generated images. This score is maximized under two conditions: the entropy of the label distribution is minimized, indicating uniformity, and the images exhibit diversity across all possible labels.

For our analysis, we employed a custom Python implementation based on TensorFlow. Three datasets were compared: the original dataset, the synthetic dataset, and a dataset comprising only noise. Each dataset was split into 10 subsets, and the IS was computed for each subset to calculate the mean and standard deviation. This approach reduces memory costs and randomization effects.

The mean IS for the original dataset was 2.1440 with a standard deviation of 0.0559, while for the synthetic dataset, it was 2.3418 with a standard deviation of

0.4079. The noise dataset yielded a mean IS of 1.0506 with a standard deviation of 0.0026. Although neither dataset achieved exceptional results with this metric, they outperformed the noise dataset. Notably, the similarity between the IS values of both datasets suggests a high degree of similarity. This underscores the quality of the synthetic dataset while highlighting areas for improvement.

#### Fréchet Inception Distance

The Fréchet Inception Distance, introduced in 2017 [197], compares the distribution of synthetic data with that of original data, assessing the similarity between the two datasets.

Similarly, a custom implementation based on Python and TensorFlow was employed for comparison across the same three datasets. Each dataset was divided into two halves, shuffled, and compared five times to mitigate randomization effects. The results indicated minimal distances between each dataset with itself. Additionally, the distance between the original and synthetic datasets was notably lower than that between either dataset and the noise dataset. This indicates a substantial similarity between the original and synthetic datasets, suggesting that differences primarily arise from new patterns of shadows and defects generated through the combination of different shadows in the original images, facilitated by the generative capacity of DCGAN models.

| Metric | Mean Score | Std. |
|---|---|---|
| IS (O) | 2.144 | 0.055 |
| IS (S) | 2.341 | 0.407 |
| IS (N) | 1.050 | 0.002 |
| FID (O-O) | 0.431 | 0.095 |
| FID (S-S) | 0.150 | 0.025 |
| FID (N-N) | 2.511 | 0.016 |
| FID (O-S) | 15.80 | 0.075 |
| FID (O-N) | 293.8 | 0.366 |
| FID (S-N) | 296.7 | 0.735 |

TABLE 6.4: Metrics for ensuring the quality of the synthetic dataset. Original: O, Synthetic: S, Noise: N. Extracted from [59].

### 6.1.7 Summary

This experiment resulted in the creation of a synthetic dataset which helped to reduce the problem of data scarcity and imbalance of the data (Objective S01). The synthetic images were proved to be similar to the original images by analyzing their histogram and by several similarity metrics. The labeling of the synthetic dataset was performed using a Random Forest Algorithm.

## 6.2 Feature Regressor

The work explained in this section resulted in a publication in the Journal Q2 Solar Energy [162].

### 6.2.1 Objective

This section presents the first proposal for solving the problem of estimating the output power of the PV cells using their EL images (Objective SO3) which is the next step after preparing the data.

The models in this work do not use the images directly, they work with various features that were extracted from the data. Another issue explored in this section is the effect of improving the performance of the models by solving the unbalance of the data (Objective SO2).

### 6.2.2 Structure

The structure of this section is as follows: first, it introduces the dataset used in this study. Next, it introduces the methodology used to balance the data. After that, outlines the developed models. Finally, it delves into the results attained by these models and offers an analysis of the effects of the unbalance in the data.

### 6.2.3 Data

The models were trained only with the Polycrystalline Dataset (Section 5.2 and some data from the Synthetic Dataset (Section 6.1).

### 6.2.4 Feature Extraction

The two methods for extracting features have been applied in this work: The manual extraction with every feature and the Resnet Extraction. The synthetic images have been also processed to obtain their features.

### 6.2.5 Balacing of the Data

As depicted in Fig. 6.14a, the distribution of cells based on their maximum power is not evenly balanced. This disparity is inherent to the problem itself. It is typically easier to encounter cells in a somewhat eroded state or exhibiting minor defects, compared to cells that are completely broken or in perfect condition.

As observed in other studies [62], [185], [186], dataset imbalance is a prevalent issue in machine learning that necessitates tailored strategies for resolution. To address this challenge, synthetic images were introduced. The process employed can be summarized in the following steps:

- The original dataset is segmented into four distinct subgroups based on their power levels: Group 0 ($x < 0.7$), Group 1 ($0.7 \leq x < 0.8$), Group 2 ($0.8 \leq x \leq 0.9$), and Group 3 ($x > 0.9$) (refer to Fig. 6.14b).
- For each group, synthetic images with power values falling within the same range as the others within the group are incorporated until all groups reach the size of the largest group.

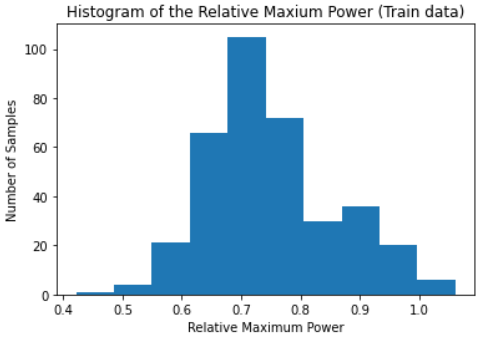


(A) Distribution of the power

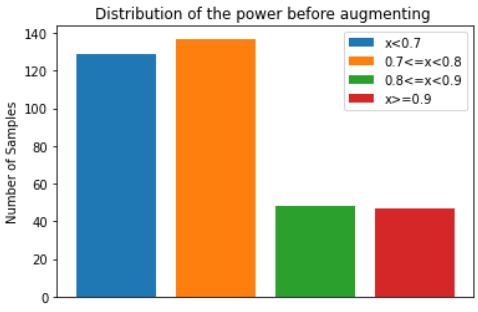


(B) Distribution of the groups before the augmentation

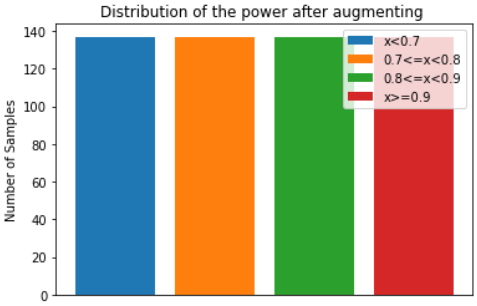


(C) Distribution of the groups after the augmentation

FIGURE 6.14: Histogram of the distribution of the images before and after the balancing. Extracted from [162].

This approach aids in achieving a more balanced dataset (refer to Fig. 6.14c). Various combinations of groups and sizes were experimented with, revealing that utilizing four groups at the maximum size yielded the most favorable outcomes in our evaluations. It's important to note that this balancing technique was solely applied to the data that was used to train the models.

### 6.2.6 Models

This section introduces several models developed to identify the most suitable approach for addressing the problem at hand and the process used to optimize their performance

#### Traditional Methods

This section presents a baseline method for predicting power from a single EL image. Various traditional techniques commonly employed for regression problems [198] were considered. Among the multitude of available techniques, Random Forest [199] and Gradient Boosting [200] were selected based on their promising performance in preliminary tests and their relatively low computational requirements.

The algorithms were trained with features extracted from the EL images. The implementation used can be found in the Sklearn [201] library for both of the methods.

**Hyperparameter Tuning:** Tuning hyperparameters is crucial in machine learning problems as it can significantly enhance model performance. This process becomes particularly vital in models with a high number of parameters, as finding the right

adjustments can be complex. Various algorithms have been developed to automate this task. In this study, GridSearchCV from the Sklearn library [201] was utilized. GridSearch conducts an exhaustive search over specified parameters, evaluating results based on the metrics of the model. The optimization results for Random Forest (RF) can be found in Table 6.5, and for Gradient Boosting (GB) in Table 6.6.

TABLE 6.5: Best hyperparameters found for Random Forest: n_estimators $\in$ [100, 1000], max_depth $\in$ [2, *None*] , min_samples_leaf $\in$ [1, 10] ,min_samples_leaf$\in$ [1, 10],min_weight_fraction_leaf $\in$ [0, 0.8]. Extracted from [162].

| n_estimators | max_depth | min_samples_leaf | min_samples_leaf | min_weight_fraction_leaf |
|---|---|---|---|---|
| 750 | None | 1 | 3 | 0 |

TABLE 6.6: Best hyperparameters found for Gradient Boosting: n_estimators $\in$ [100, 500], max_depth $\in$ [2, *None*] , learning_rate $\in$ [0.01, 0.001]. Extracted from [162].

| n_estimators | max_depth | learning_rate |
|---|---|---|
| 275 | None | 0.08 |

**Recurrent Neural Networks**

Two methods based on Recurrent Neural Networks (RNN) were tested. These networks are characterized by nodes that can form cycles, allowing them to demonstrate temporal dynamic behavior. One of the methods utilizes Long Short-Term Memory (LSTM) [202], while the other is based on Gated Recurrent Unit (GRU) [203] [204]. The implementation was carried out using TensorFlow [129].

**Optimization** The optimization of hyperparameters is a highly intricate process in the design of deep learning models. Manual tuning is impractical due to the vast number of parameters and their possible values. To address this challenge, the Keras-Tuner library [205] was selected.

This library offers different optimizers, including the Bayesian Optimization Tuner [206]. This algorithm leverages past evaluation results when selecting the hyperparameter to evaluate next, thereby improving the search within the most promising regions of the search space. It also disregards less promising areas, reducing the iterations required to find the optimal set of parameters.

Several parameters were chosen for optimization: the learning rate, batch size, number of hidden layers, and number of nodes in each layer (with an increment of 16 nodes each time). The optimization process was conducted for 32 iterations. Adam was used as the optimizer. The best results can be found in Table 6.7.

TABLE 6.7: Best hyperparameters found for Recurrent Neural Networks: num_layers $\in$ [2, 3, 4, 5, 6], num_units $\in$ [16, 32, 64, 125, 256, 512], batch_size $\in$ [16, 32, 64, 80, 96, 112, 128], learning_rate $\in$ [0.001, 0.00001]. Extracted from [162].

| RNN | num_layers | num_units | batch_size | learning_rate |
|---|---|---|---|---|
| LSTM | 6 | 512 | 16 | 0.000219 |
| GRU | 2 | 16 | 16 | 0.001 |

**Architecture** The architecture of the best model according to the tuning process can be found in Fig. 6.15.

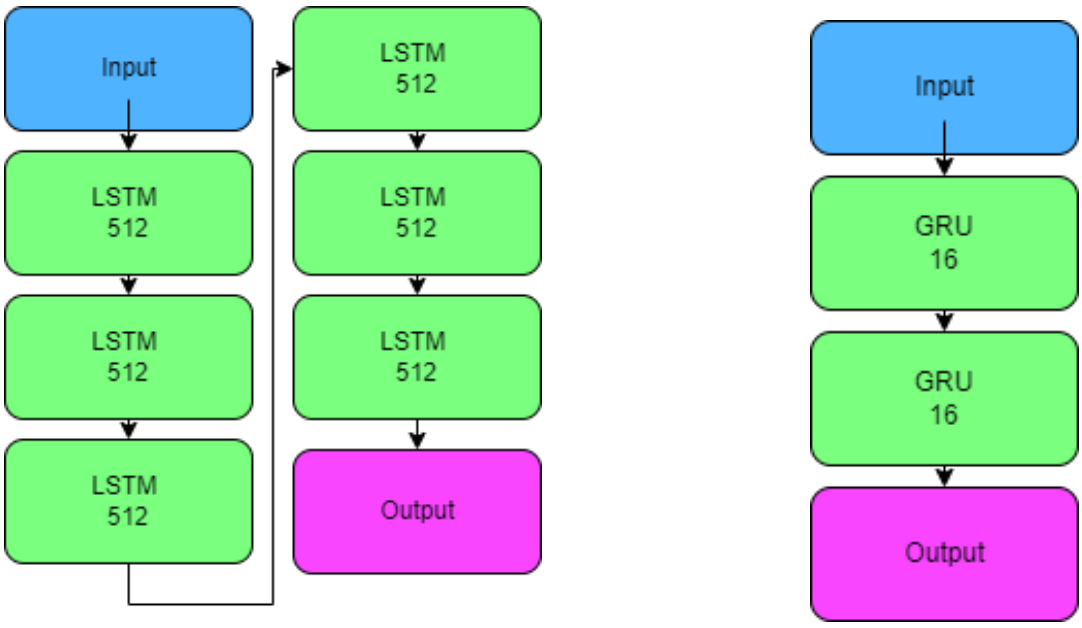


(A) LSTM network (B) GRU network

FIGURE 6.15: Final Architectures of the Recurrent Networks. Extracted from [162].

### Convolutional Neural Networks

This section introduces a CNN-based approach for predicting the power of a cell based on its EL image. CNNs are well-suited for image-related tasks as they can effectively perform feature extraction using their convolutional layers. The implementation of these models is carried out using TensorFlow.

**Architecture** The architecture of the neural network was selected through a manual process. The networks were trained for 500 epochs, and the best-performing model from each option was deemed the final one. The investigation revealed that the optimal architecture comprised two convolutional layers with 64 and 128 units respectively, followed by a dense layer with 256 units (refer to Fig. 6.16).

This architecture was determined after conducting a trial-and-error process with various architectures, aiming to minimize validation error. Due to hardware limitations during experimentation, automatic optimization methods were not feasible.

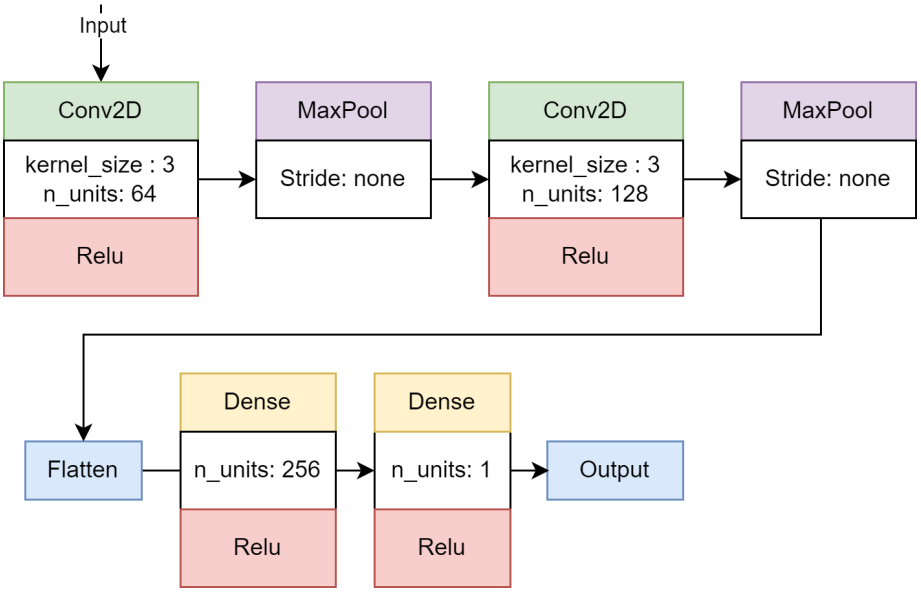


FIGURE 6.16: Final Architecture for the Convolutional Network, Extracted from [162].

**Optimization** Bayesian Tuner from Keras-Tuner was also applied in the experiments involving CNNs, optimizing parameters such as the learning rate and batch size. The optimization process was executed for 32 iterations, utilizing Adam as the optimizer. The best results obtained from these experiments can be found in Table 6.8.

TABLE 6.8: Best hyperparameters found for Convolutional Neural Networks: batch_size $\in [16, 32, 64, 80, 96, 112, 128]$, learning_rate $\in [0.001, 0.00001]$. Extracted from [162]

| batch_size | learning_rate |
|---|---|
| 16 | 0.00005 |

### 6.2.7 Results

This section evaluates the performance of various methods for predicting the power of a cell by comparing different approaches based on their performance metrics. Each experiment was repeated five times using the parameters identified during hyperparameter optimizations. This approach ensured the stability and quality of the results for each method.

#### Training only with original images

The results of the experiments using only the original dataset are provided in Table 6.9.

TABLE 6.9: Results using the polycrystalline dataset. Extracted from [162].

| Metric | MAE | | | MSE | | |
|---|---|---|---|---|---|---|
| Data | Train | Validate | Test | Train | Validate | Test |
| GB | 0.00222 | 0.03674 | 0.03667 ± 0.00148 | 4.67e-05 | 0.00224 | 0.00290 ± 0.00006 |
| RF | 0.01432 | 0.03821 | 0.03721 ± 0.00179 | 0.00287 | 0.00227 | **0.00285 ± 0.00002** |
| LSTM | 0.03682 | 0.04602 | 0.04397 ± 0.00386 | 0.00257 | 0.00343 | 0.00354 ± 0.00027 |
| GRU | 0.03805 | 0.04615 | 0.04637 ± 0.00402 | 0.00258 | 0.00343 | 0.00386 ± 0.00008 |
| CNN | 0.01181 | 0.03328 | **0.03630 ± 0.00160** | 0.00039 | 0.00202 | 0.00301 ± 0.00005 |

The results demonstrate that CNN exhibits superior performance in terms of MAE, while RF outperforms others when considering MSE. However, methods based on Recurrent Networks show considerably poorer performance compared to other approaches. Despite encountering the challenge of unbalanced data, notably good results were achieved across all methods. These findings will be further elaborated and discussed in subsequent analyses.

### Training with original + synthetic images

The results of the experiments balancing the original dataset with synthetic images are presented in Table 6.10.

TABLE 6.10: Results using the balanced dataset. Extracted from [162].

| Metric | MAE | | | MSE | | |
|---|---|---|---|---|---|---|
| Data | Train | Validate | Test | Train | Validate | Test |
| GB | 0.00233 | 0.03647 | 0.03708 ± 0.00316 | 8.62e-05 | 0.00206 | **0.00282 ± 0.0006** |
| RF | 0.00980 | 0.03712 | 0.03747 ± 0.00394 | 0.00980 | 0.002155 | 0.002935 ± 0.0001 |
| LSTM | 0.01998 | 0.04497 | 0.04068 ± 0.00340 | 0.00114 | 0.00332 | 0.00349 ± 0.00008 |
| GRU | 0.02582 | 0.04601 | 0.04870 ± 0.00439 | 0.00149 | 0.00357 | 0.00430 ± 0.00004 |
| CNN | 0.01071 | 0.03255 | **0.03407 ± 0.00255** | 0.00034 | 0.00192 | 0.00284 ± 0.00005 |

The results of the experiments with both the original dataset and the balanced dataset show similarities. In methods utilizing features, there is a slight increase in both errors, while in CNN, which operates directly on images, there is a slight decrease in errors. From these findings, two conclusions can be drawn: either manual feature extraction is insufficient for this problem, or the imbalance in the original dataset does not significantly impact the performance of the models. To validate the first hypothesis, we will further investigate the feature extraction methods outlined in the methodology section.

### Using Resnet

For this experiment, only the two most promising feature-based methods from the previous section are considered. (GB and RF). The results of both methods are compared using both the original dataset and the balanced dataset.

TABLE 6.11: Results of using Resnet for feature extraction (R): Original Dataset, (S): Balanced Dataset. Extracted from [162].

| Metric | MAE | | | MSE | | |
|---|---|---|---|---|---|---|
| Data | Train | Validate | Test | Train | Validate | Test |
| GB (R) | 0.001000 | 0.032786 | **0.034277 ± 0.00293** | 1.63e-05 | 0.003078 | **0.002271 ± 0.0001** |
| RF (R) | 0.009926 | 0.035272 | 0.034684 ± 0.00251 | 0.000202 | 0.003469 | 0.002332 ± 0.0001 |
| GB (S) | 0.001957 | 0.032993 | **0.034143 ± 0.00307** | 5.12e-05 | 0.003183 | **0.002116 ± 0.0001** |
| RF (S) | 0.009926 | 0.034884 | 0.034559 ± 0.00248 | 0.000202 | 0.003444 | 0.002319 ± 0.0001 |

As depicted in Table 6.11, both Gradient Boosting (GB) and Random Forest (RF) exhibit superior performance with this feature extraction method. Their results even surpass those of CNN in terms of Mean Squared Error (MSE), albeit slightly underperforming in terms of Mean Absolute Error (MAE).

GB is considered the best model for two primary reasons: First, MSE is deemed a more suitable metric than MAE in this problem, as it places greater emphasis on outliers. This property of MSE is beneficial for dealing with problems characterized by data imbalance. Second, the computational cost of GB [207] is considerably lower than that of CNN [208], even after utilizing ResNet for feature extraction.

Fig. 6.17 presents a summary of all the experiments.

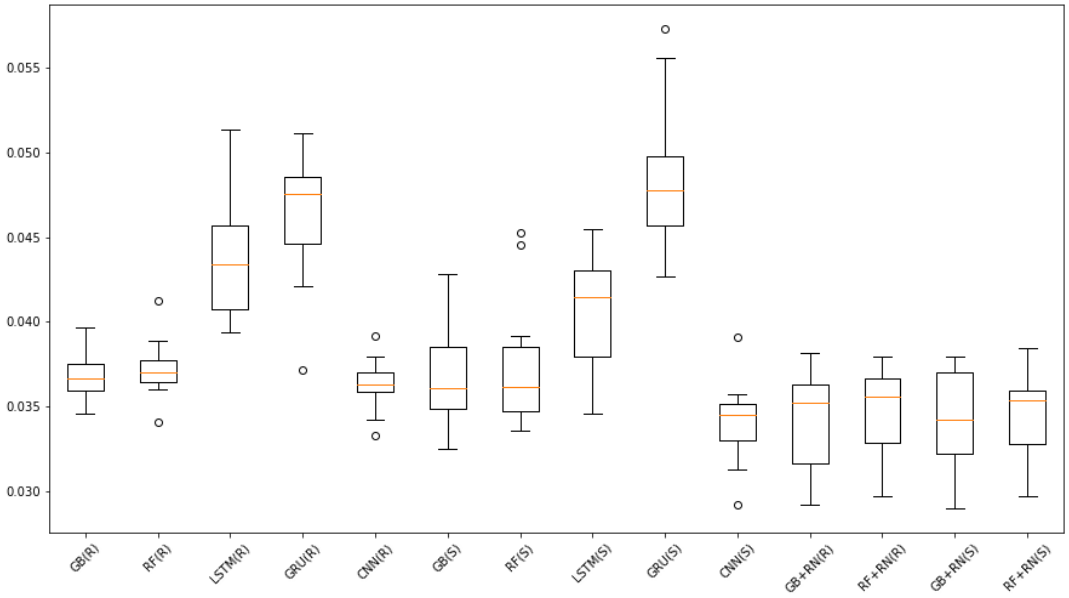


FIGURE 6.17: Box Diagram of the Experiments. Extracted from [162].

It is also notable that the utilization of synthetic images for balancing the dataset does not significantly alter the performance of the models; however, it does not worsen their performance either. From this observation, it can be inferred that the problem of dataset imbalance does not detrimentally affect the models' performance. Moreover, this reaffirms the quality of the synthetic images.

Fig. 6.18 illustrates the relationship between the actual values and predictions. It is observed that the majority of samples exhibit a distance within the range of $[-0.1, 0.1]$, with only a few outliers at the extreme ends. This indicates that the method is not biased toward specific values and demonstrates a balanced prediction distribution across the dataset.

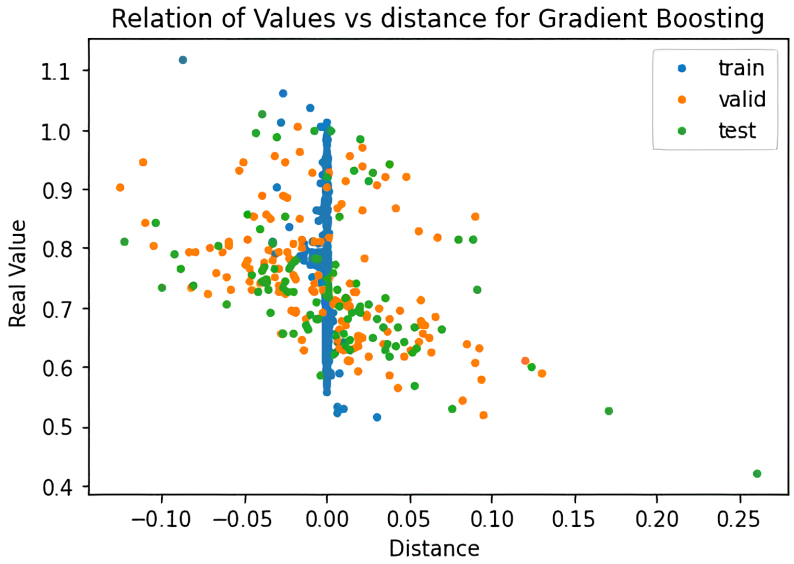


FIGURE 6.18: Relation between the values and error. Extracted from [162].

### 6.2.8 Summary

This experiment resulted in the comparison of various models (Objective S01), resulting in CNN and Gradient Boosting being the ones with better results. This work has also explored various feature extraction methods, with the use of a Resnet as a extractor the best one. Finally, it has proven that the effects of unbalance in the data are not critical in this problem.

## 6.3 Fuzzy Classifier

The work explained in this section resulted in two papers: One presented in the congress **VI ICSC-CITIES 2024** in the article [189], another work is still in publication process [209].

### 6.3.1 Objective

The following step after obtaining a working model was to test other technologies and approaches (Objective S04).

This section elucidates a different way of analyzing the condition of photovoltaic cells, changing the proposal of estimating the output power into a classification. Moreover, a Fuzzy Logic model is proposed for it, which is capable of solving the problem by analyzing the distribution of the intensity of the pixels of the EL Images. The FL also provides easy-to-understand rules for humans and its requirements are considerably lower than other methods such as Neural Networks.

### 6.3.2 Structure

This section is organized as follows: initially, it introduces the dataset utilized in this study. Subsequently, it describes the developed models. Finally, it details the results achieved by these models and provides a comparative analysis with several other learning methods.

### 6.3.3 Data

The FL model was trained originally only using the Polycrystalline dataset but the work performed to extend the article included the inclusion of the Monocrystalline dataset using the second labeling method that was presented in Chapter 5.2. The images that presented Series Resistance problems were not included in the experiments.

### 6.3.4 Feature Extraction

FL models have an important limitation since they are not capable of dealing directly with images. As explained before, several features have been extracted from the images to make them suitable for these algorithms.

Only three manual features have been chosen for these FL models, that will be work as their inputs: The proportion of white pixels, the proportion of gray pixels, and the proportion of black pixels. More information can be found in Chapter 5.2.

### 6.3.5 Model

This section introduces several FL Models employing the Mandami Inference System. Each model has been trained with a different dataset: One model for the Polycrystalline and another for the Monocrystalline. As previously outlined, the primary aim of this study is to categorize PV cells based on their performance criteria. FL models offer notable advantages for this task, as they generate interpretable rules directly comprehensible to humans. Additionally, FL models do not necessitate high-end computational resources.

The Mandami Inference System was chosen among the other kinds of inference systems since it shows a high expressive power while providing rules that are easily understandable by humans.

The models presented herein were developed using the Fuzzy Logic Designer tool in Matlab. Design parameters were fine-tuned through a combination of expert knowledge and iterative refinement, optimizing the accuracy of the model outputs.

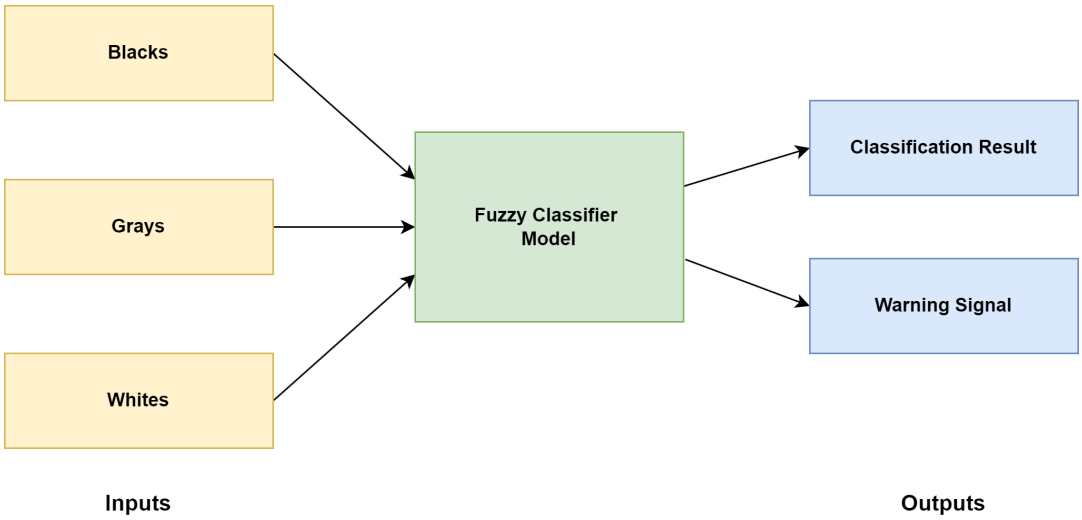


FIGURE 6.19: Structure of the designed Fuzzy Logic model with its three inputs (Black, Grays, Whites) and the 2 outputs (Classification Results and Warning Signal). Extracted from [209].

The models retain the same basic structure (see Fig. 6.19) using the extracted features as inputs and providing two outputs: The results of the classification and an output that works as a warning about inputs that are not logical in this context (proportions not adding 100% or really high values in an input such as grays 100%).

### Membership Functions

Each input (Blacks, Grays, and Whites) is characterized by three membership functions corresponding to the proportion of pixels of that type in the image: Low, Medium, and High. These functions were meticulously designed through a manual process using the knowledge of experts and aiming to enhance the performance of each model on its respective training dataset. The membership functions have varied on the dataset used (refer to Fig. 6.20).

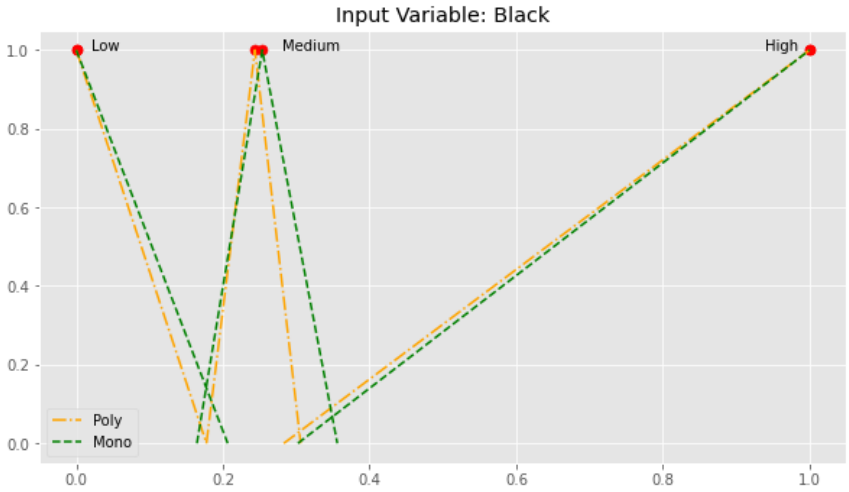


(A) Membership functions of the input variable: Proportion of Black pixels

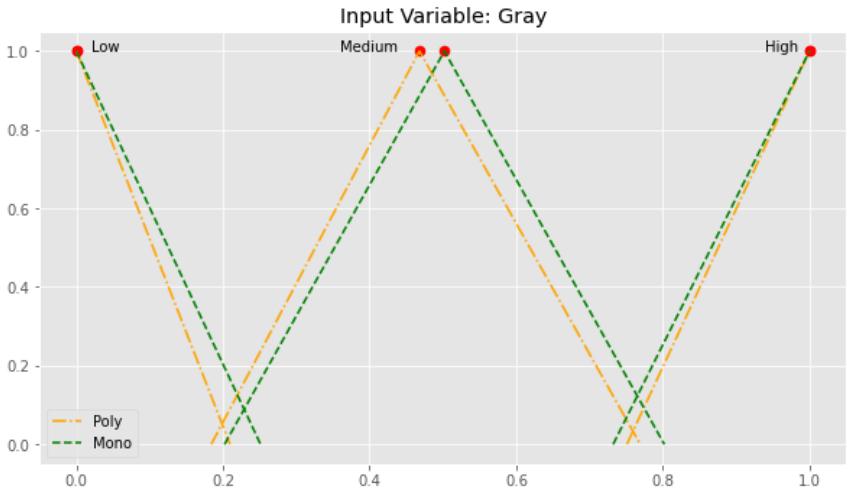


(B) Membership functions of the input variable: Proportion of Gray pixels

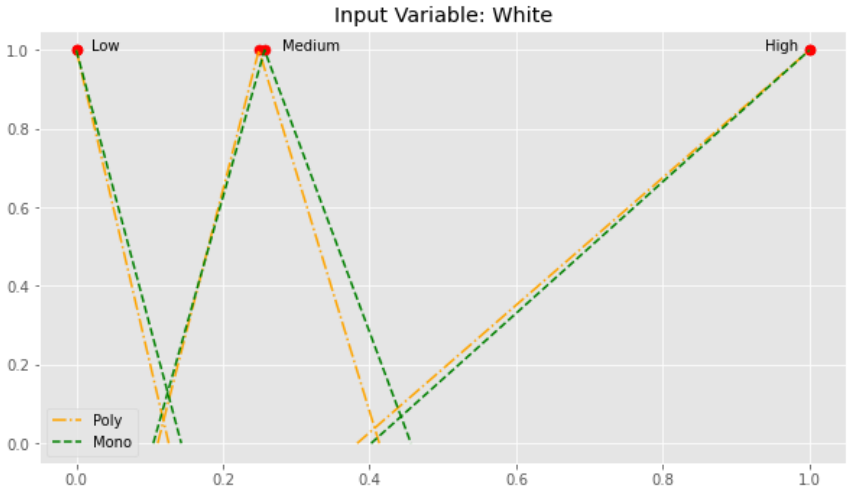


(C) Membership functions of the input variable: Proportion of White pixels

FIGURE 6.20: The membership functions for the three different inputs of the Fuzzy Logic Model. Green Values shows the values for the Monocrystalline dataset and Green Values of the Polycrystalline dataset. Extracted from [209].

The classification output is also represented by three distinct membership functions, each associated with the amount of power produced by the cell and its performance (see Fig. 6.21): High (Class 0, cells with good performance), Medium (Class 1, cells that do not meet expected performance), and Low (Class 2, cells with extremely low performance). These membership functions are consistent across both models.

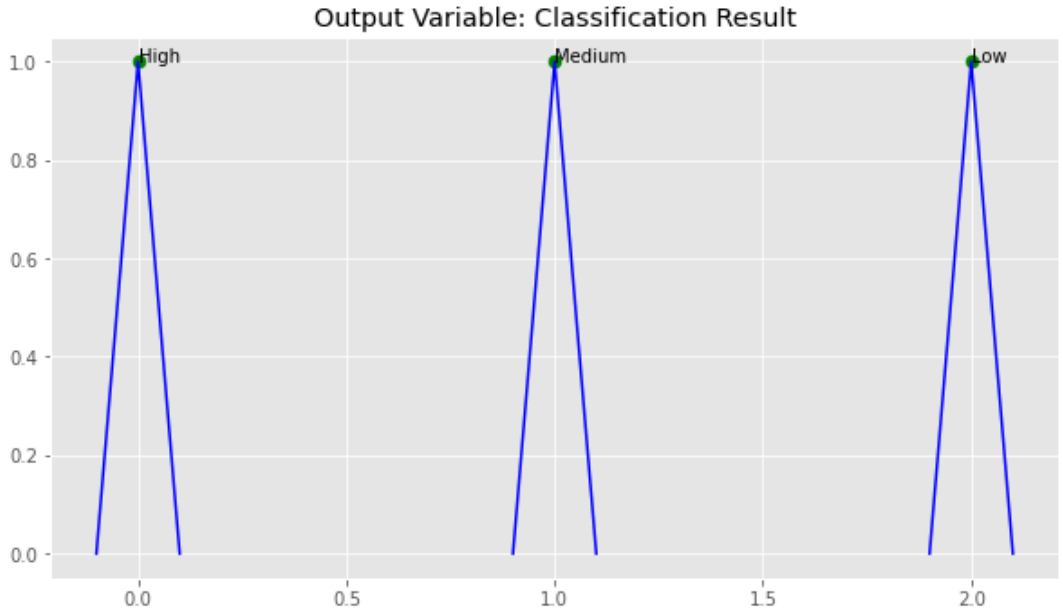


FIGURE 6.21: Membership functions obtained for the classification output of the Fuzzy Model. Extracted from [209].

The Warning output is represented by a pair of membership functions: Negative and Positive (Refer to Fig. 6.22).

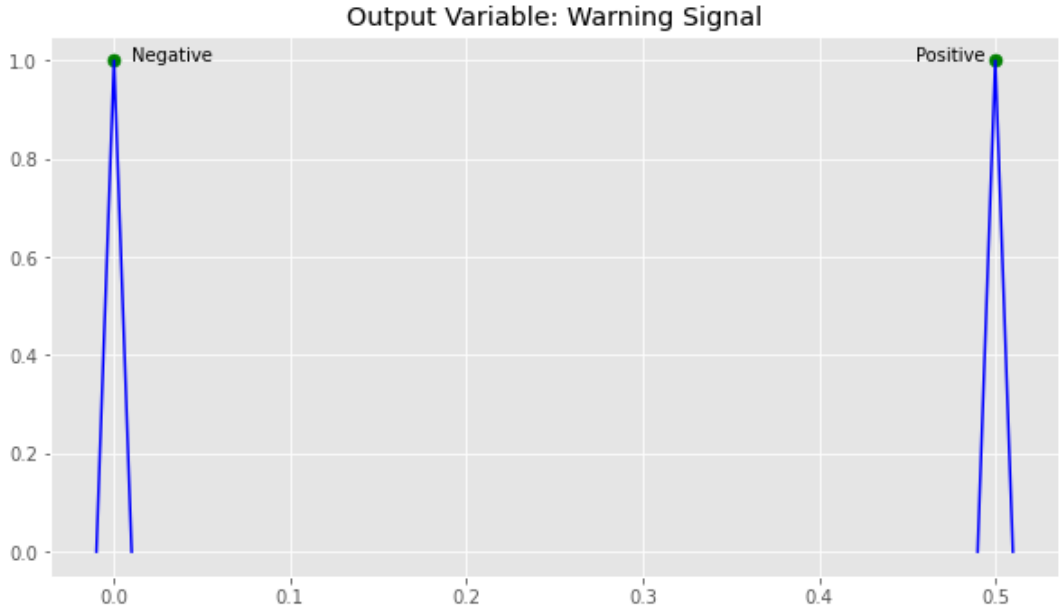


FIGURE 6.22: Membership function obtained for the Warning Output designed to detect invalid combinations of inputs. Extracted from [209].

**Ruleset of the models**

The rules were devised based on the expertise of professionals in the field, who comprehended the impact of defects on cell performance and the nuances of the I-V curve's output power. This knowledge was utilized to formulate rules for categorizing images into their respective classes, aiming to enhance the accuracy of classification within the training set.

It's worth noting that the warning output is not factored into the training metrics, as its purpose is to flag incorrect values in the inputs. The process of determining the optimal parameters was entirely manual, a departure from other algorithms like Machine Learning methods.

As mentioned earlier, neither of the two models incorporated the validation set into their training processes, ensuring potential biases are minimized during testing.

| Rule | Black | Gray | White | Classification Output | Warning Signal |
|---|---|---|---|---|---|
| 1 | L | L | L | L (0) | + |
| 2 | L | L | M | H (2) | - |
| 3 | L | L | H | H (2) | - |
| 4 | L | M | L | H (2) | - |
| 5 | L | M | M | H (2) | - |
| 6 | L | M | H | H (2) | - |
| 7 | L | H | L | M (1) | - |
| 8 | L | H | M | H (2) | - |
| 9 | L | H | H | H (2) | + |
| 10 | M | L | L | L (0) | + |
| 11 | M | L | M | M (1) | - |
| 12 | M | L | H | M (1) | - |
| 13 | M | M | L | M (1) | - |
| 14 | M | M | M | M (1) | - |
| 15 | M | M | H | M (1) | + |
| 16 | M | H | L | L (0) | - |
| 17 | M | H | M | L (0) | + |
| 18 | M | H | H | L (0) | + |
| 19 | H | L | L | L (0) | - |
| 20 | H | L | M | L (0) | - |
| 21 | H | L | H | L (0) | - |
| 22 | H | M | L | L (0) | - |
| 23 | H | M | M | L (0) | - |
| 24 | H | M | H | L (0) | - |
| 25 | H | H | L | L (0) | + |
| 26 | H | H | M | L (0) | - |
| 27 | H | H | H | L (0) | + |

TABLE 6.12: Fuzzy Ruleset of both models. Black, Gray, and White are the inputs. Classification output and Warning Signal the outputs. H: High; M: Medium; L: Low; +: Positive; -: Negative. Extracted from [209].

Figure 6.23 illustrates a 3D surface diagram depicting the relationship between the classification output and two inputs: Black and Gray. This diagram visually represents how the input values correlate with the output. For instance, lower values of Blacks correspond to an output of Class 0, while Class 1 is associated with Blacks ranging between 20

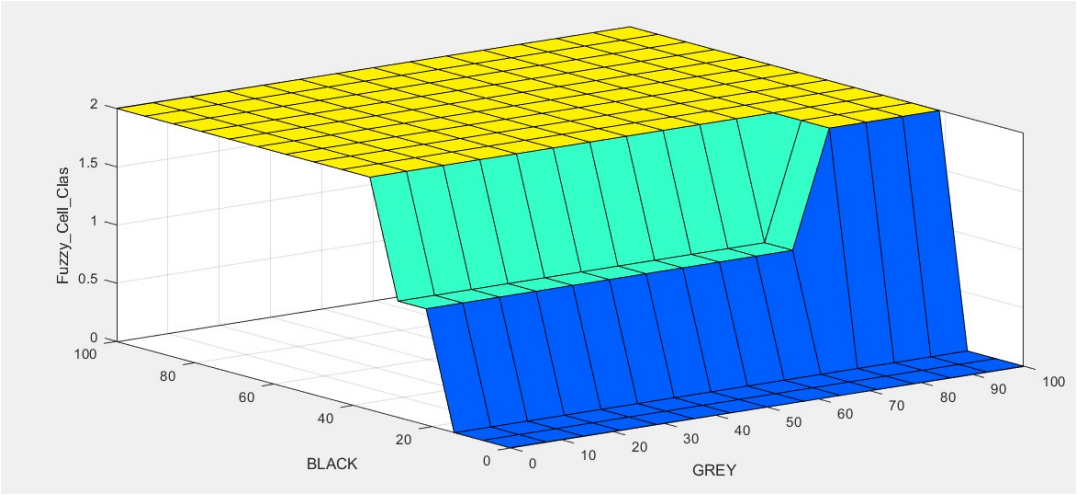


FIGURE 6.23: 3D surface diagram illustrating the impact of inputs Black and Gray on the output. Extracted from [209].

### 6.3.6 Results

This section presents the performance evaluation of the models on the validation sets, along with a comparative analysis against alternative methods created using the Classification Learner tool in Matlab.

The model achieved an accuracy of 99.11% on the Validation set of the Polycrystalline dataset. Figure 6.24 illustrates the classification results, including the confusion matrix and accuracy for each class. The results indicate high accuracy across all classes, although Class 1 exhibits a slightly lower accuracy. Notably, classification errors only occur between adjacent classes, with no instances of misclassifying an image from Class 0 as Class 2 or vice versa.

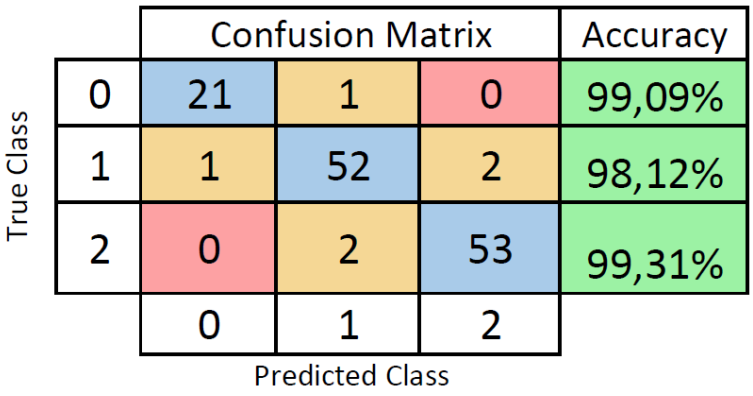


FIGURE 6.24: Confusion Matrix and Accuracy of the classification of the FL model for Polycrystalline cells on the Validation Set. Extracted from [209].

The results on the validation set of the Monocrystalline model (Fig. 6.25) show a slightly lower accuracy compared to the previous case, achieving an accuracy of 98%. Similar to the Polycrystalline dataset, there are no miss-classifications between Classes 0 and 2.

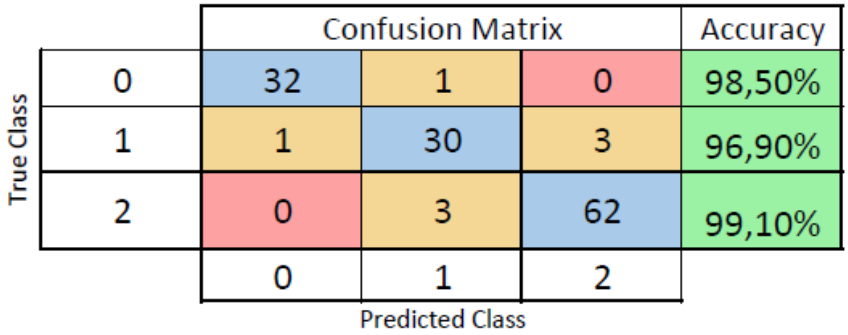


FIGURE 6.25: Confusion Matrix and Accuracy of the classification of the FL model for Monocrystalline cells on the Validation Set. Extracted from [209].

A variety of algorithms were chosen for comparative analysis with the method presented in this study, all of which are available in the Classification Learner application of Matlab. These algorithms include Decision Trees, Discriminant Analysis, Logistic Regression Classifiers, Naive Bayes Classifiers, Support Vector Machines, Nearest Neighbor Classifiers, and Ensemble Classifiers. Notably, Decision Trees and Ensemble Classifiers showed the highest results across both Polycrystalline and Monocrystalline datasets.

Refer to Table 6.13 for a comprehensive presentation of the results of the selected algorithms. While they exhibited commendable classification capabilities, their performance still falls behind the proposed method, as evidenced by the observed accuracy metric. This highlights the importance of incorporating fuzzy logic to address the complexities of the problem effectively.

TABLE 6.13: Accuracy of the proposed FL models versus the best-performing ML tested method. Extracted from [209].

| | Fuzzy Model | Ensemble Classifiers | Decision Trees |
|---|---|---|---|
| Polycrystalline | *99,11%* | 98,32% | 96,45% |
| Monocrystalline | *98,12%* | 96,27% | 97,17% |

### 6.3.7 Summary

This experiment resulted in the creation of a Fuzzy Logic classifier (Objective S04) capable of solving the problem. The classification approach reduces the complexity of the problem but it also reduces the amount of information. However, the Fuzzy Logic provides additional information about how the logic was used to perform the classifications.

## 6.4 ANFIS Regressor

The work explained in this section resulted in two articles: One was presented in the congress **VI ICSC-CITIES 2024** in the article [210], and another one is still in publication process [73].

### 6.4.1 Objective

As in the previous experiment, another alternative to the original proposal has been considered (Objective S04), in this case using a combination of Deep Learning and Fuzzy Logic which reduces the limitations of Fuzzy Logic while still provides the an understable knowledge.

Two different models are created, a basic one using only the features obtained by the images and an improved model that uses an additional input based on the results of the FL classifiers that were explained in Section 6.3.

### 6.4.2 Structure

.

This section is organized as follows: initially, it introduces the dataset utilized in this study and the methodology employed for extracting information from images. Subsequently, it describes the developed models. Finally, it details the results achieved by these models and provides a comparative analysis with several other learning methods.

### 6.4.3 Data

The ANFIS models were trained only using the Polycrystalline dataset using the second labeling method that was presented in Chapter 5.2. The images that presented Series Resistance problems were not included in the experiments.

The data is divided into three different sets: Training, Validation, and Testing. Only training and validation are used in the training phase.

### 6.4.4 Feature Extraction

ANFIS algorithms are incapable of processing directly images. As in Section 6.3, it is necessary to obtain the most important characteristic that effectively represents those images.

The process to obtain these features is the same as in Section 5.2, the pixels of each image are divided into three groups and the proportion of pixels in each group is computed for every image. This provides three features: The proportion of black pixels, the proportion of white pixels and the proportion of gray pixels.

### 6.4.5 Models

The models were implemented using the Neuro-Fuzzy Designer application in Matlab, providing a user-friendly platform for model development, optimization, and visualization. Through this tool, architects could efficiently create, fine-tune,

and analyze models using diagrams and graphical representations. They were designed using the Takegi-Sugeno inference system.

The architectural design of the models was meticulously executed to optimize the performance metrics, particularly focusing on Mean Absolute Error (MAE), Mean Square Error (MSE), and Root Mean Square Error (RMSE) during training and tuning. This iterative process involved extensive experimentation with critical parameters like training epochs and the count and type of input membership functions. The objective was to strike a delicate balance that mitigates overfitting while achieving an optimal number of rules, all within computational constraints.

The models have been trained using data from two sets: Training and Validation. The testing set is not taken into account in the construction and tuning of the models. The optimization process encompasses the integration of backpropagation for the input membership functions and least squares for the outputs, with the overarching goal of minimizing the RSME for the output.

Optimization of input membership functions was carried out methodically, combining manual selection with automatic adjustment. In the manual phase, deliberate decisions were made regarding the shape and count of membership functions for each input. Concurrently, during network training, an automatic process fine-tuned the intervals' size and intersections. Various shapes, including Phi-Shaped, Trapezoidal, Triangular, Simple Gaussian, and Double Gaussian, underwent thorough testing. Notably, the Double Gaussian function demonstrated superior performance compared to others.

#### ANFIS model

This section presents the details of the basic model, its architecture, the evolution of the metrics during the training phase, and the obtained membership functions and rulesets.

**Model and Architecture** The model comprised three inputs, each corresponding to one of the extracted features. The determination of the number of functions for each input involved a manual exploration. It was found that the optimal configuration consisted of 2 functions for the Blacks feature, 4 functions for the Grays feature, and 5 functions for the Whites feature. This meticulous optimization process aimed to strike a delicate balance, mitigating the risk of overfitting while maintaining a manageable number of rules without imposing undue computational burdens.

The finalized model encompasses a total of 40 if-then rules, derived from the integration of unique input membership functions. These functions consist of 2 for Blacks, 4 for Grays, and 5 for Whites, collectively yielding 40 rules. The architectural configuration of the model is visually depicted in Fig. 6.26.

**Training** The training was conducted over 1000 epochs. Fig. 6.27 illustrates the progression of the RMSE throughout the training process. Notably, around epoch 600, the validation error reaches its lowest point (0.0911). However, beyond this epoch, the error consistently rises, indicating a clear instance of overfitting.

Fig. 6.28 illustrates the membership functions of the inputs that were obtained after the manual tunning and the training process

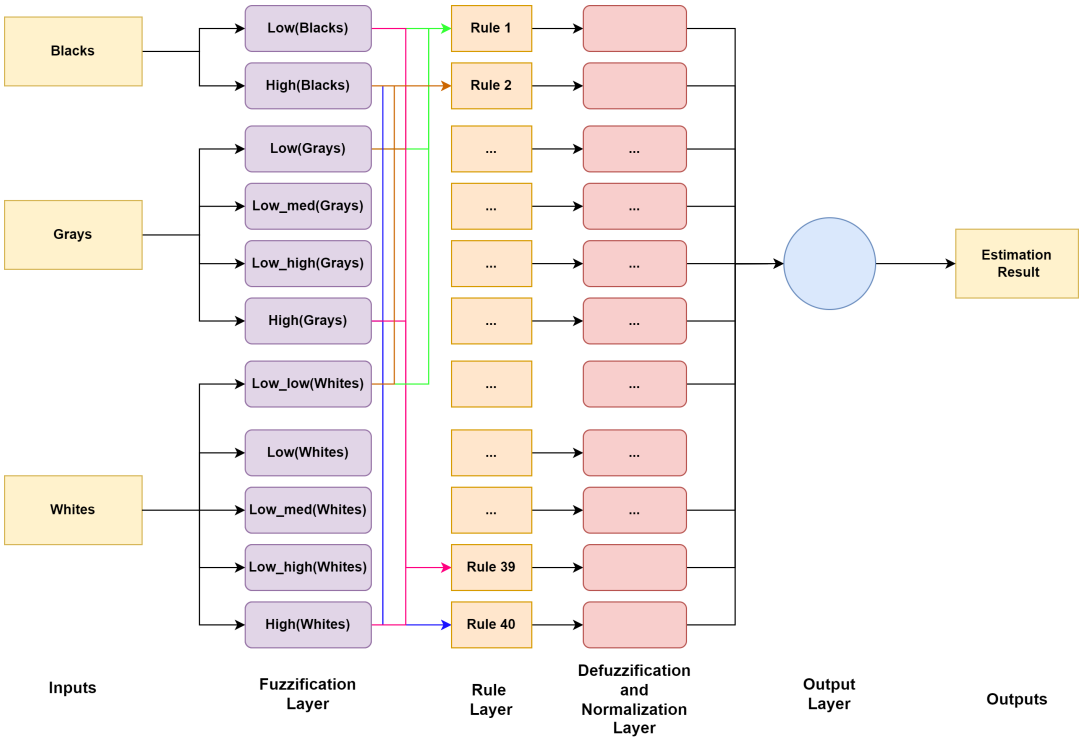


FIGURE 6.26: Architecture of the model. Black, Grays, and Whites are the inputs. Estimation Result is the output. Extracted from [73].

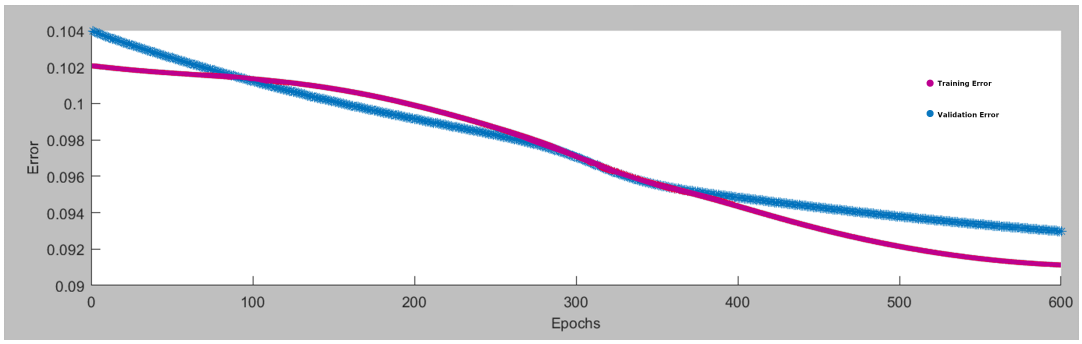


FIGURE 6.27: Changes in training and validation errors throughout the training process. Extracted from [73]

**Rules** As detailed earlier, the rules are automatically acquired in the course of the training process. Table 6.14 provides a comprehensive overview of the 40 rules governing the system, outlining each conceivable combination of inputs.

3D surface graphs elucidate the correlations between input features and outputs, providing a graphical depiction of the internal logic within the Fuzzy models. In Fig. 6.29, the impact of Whites and Grays on power estimation is showcased. This visualization underscores how alterations in both variables significantly affect the system's output.

### Improved Model

This section presents the details of the improved model, its architecture, the evolution of the metrics during the training phase, and the obtained membership functions and rulesets.

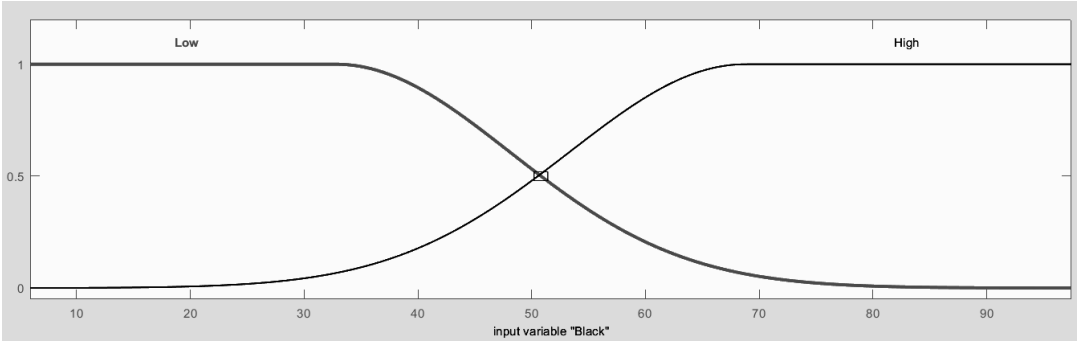


(A) Membership functions after training for input: Blacks

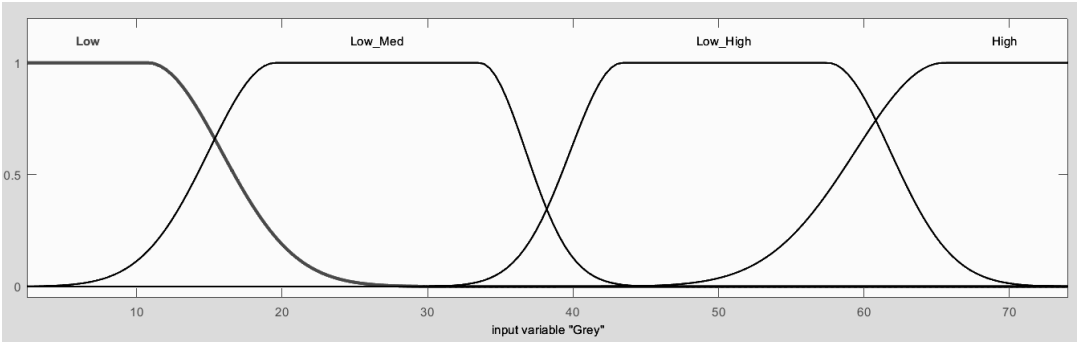


(B) Membership functions after training for input: Grays

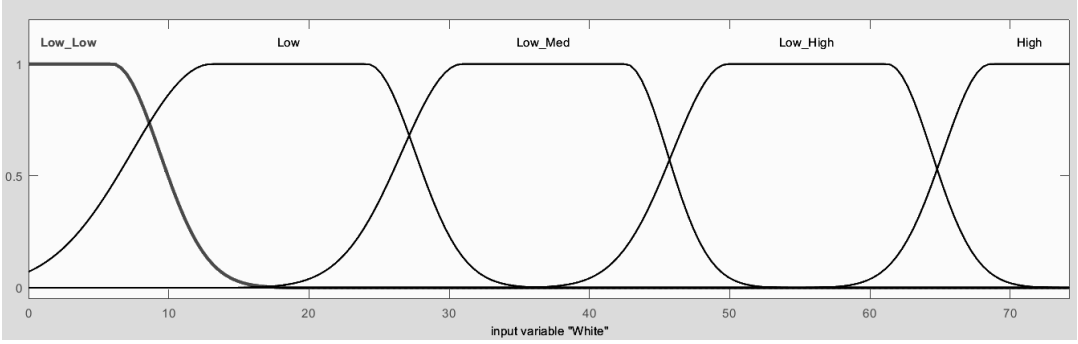


(C) Membership functions after training for input: Whites

FIGURE 6.28: The membership functions for the three different inputs of the ANFIS model. A combination of manual optimization and the automatic training process was performed to obtain them. Extracted from [73].

The main improvement of this method is that it has an additional input. This new input called "Fuzzy Class" is obtained from the classifier presented in Section 6.3. This new input helps the estimator to improve its prediction. Details about the FL model can be found in its section.

**Model and Architecture** .

The number and shape of membership functions for the original inputs (Blacks, Grays, Whites) have been retained in the extended model. The Fuzzy Classification input is characterized by three Double Gaussian membership functions. Fig. 6.30 illustrates the ANFIS model's architecture, featuring 4 inputs, 14 membership functions, 120 rules resulting from the combination of all membership functions ($2 \times 4 \times 5 \times 3 = 120$), and a single output.

TABLE 6.14: Fuzzy Rules of the model. Black, Gray, and White are the inputs. Estimation is the output. H: High; M: Medium; L: Low; LH: Low High; LM: Low Medium; LH: Low High. Extracted from [73]

| Rule | Black | Gray | White | Estimation Output | Rule | Black | Gray | White | Estimation Output |
|---|---|---|---|---|---|---|---|---|---|
| 1 | L | L | LL | | 21 | H | L | LL | |
| 2 | L | L | L | | 22 | H | L | L | |
| 3 | L | L | LM | | 23 | H | L | LM | |
| 4 | L | L | LH | | 24 | H | L | LH | |
| 5 | L | L | H | | 25 | H | L | H | |
| 6 | L | LM | LL | | 26 | H | LM | LL | |
| 7 | L | LM | L | | 27 | H | LM | L | |
| 8 | L | LM | LM | | 28 | H | LM | LM | |
| 9 | L | LM | LH | | 29 | H | LM | LH | |
| 10 | L | LM | H | | 30 | H | LM | H | |
| 11 | L | LH | LL | | 31 | H | LH | LL | |
| 12 | L | LH | L | | 32 | H | LH | L | |
| 13 | L | LH | LM | | 33 | H | LH | LM | |
| 14 | L | LH | LH | | 34 | H | LH | LH | |
| 15 | L | LH | H | | 35 | H | LH | H | |
| 16 | L | H | LL | | 36 | H | H | LL | |
| 17 | L | H | L | | 37 | H | H | L | |
| 18 | L | H | LM | | 38 | H | H | LM | |
| 19 | L | H | LH | | 39 | H | H | LH | |
| 20 | L | H | H | | 40 | H | H | H | |

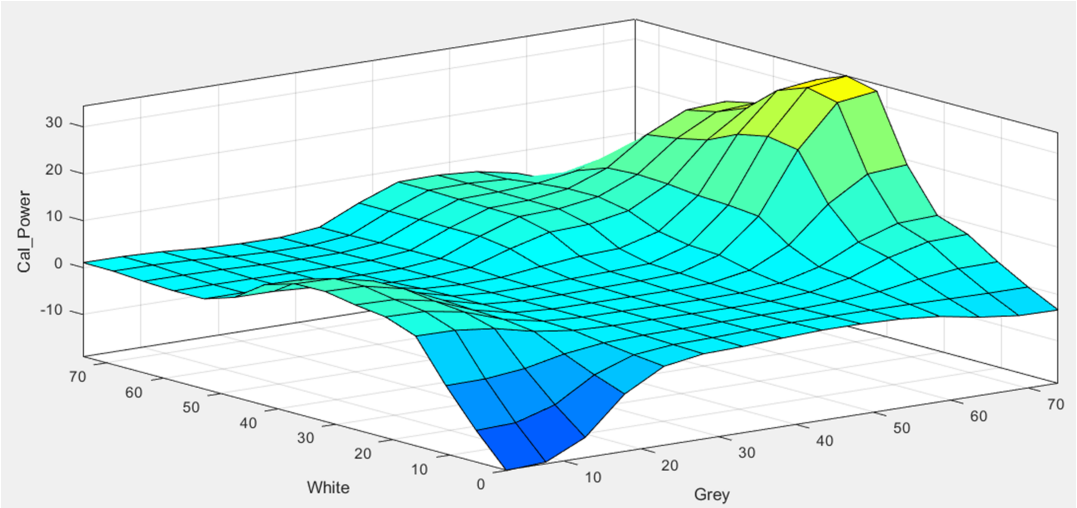


FIGURE 6.29: 3D surface diagram illustrating the impact of inputs White and Gray on the output.

**Training** The model undergoes the same training process as the original one. Fig. 6.31 illustrates the dynamic evolution of errors throughout the training phase, attaining its minimum in the validation set during the final epoch with an RMSE of 0.0874.

Figure 6.32 depicts the membership functions of this extended model. As observed, the functions for Blacks, Whites, and Grays closely resemble those of the original model.

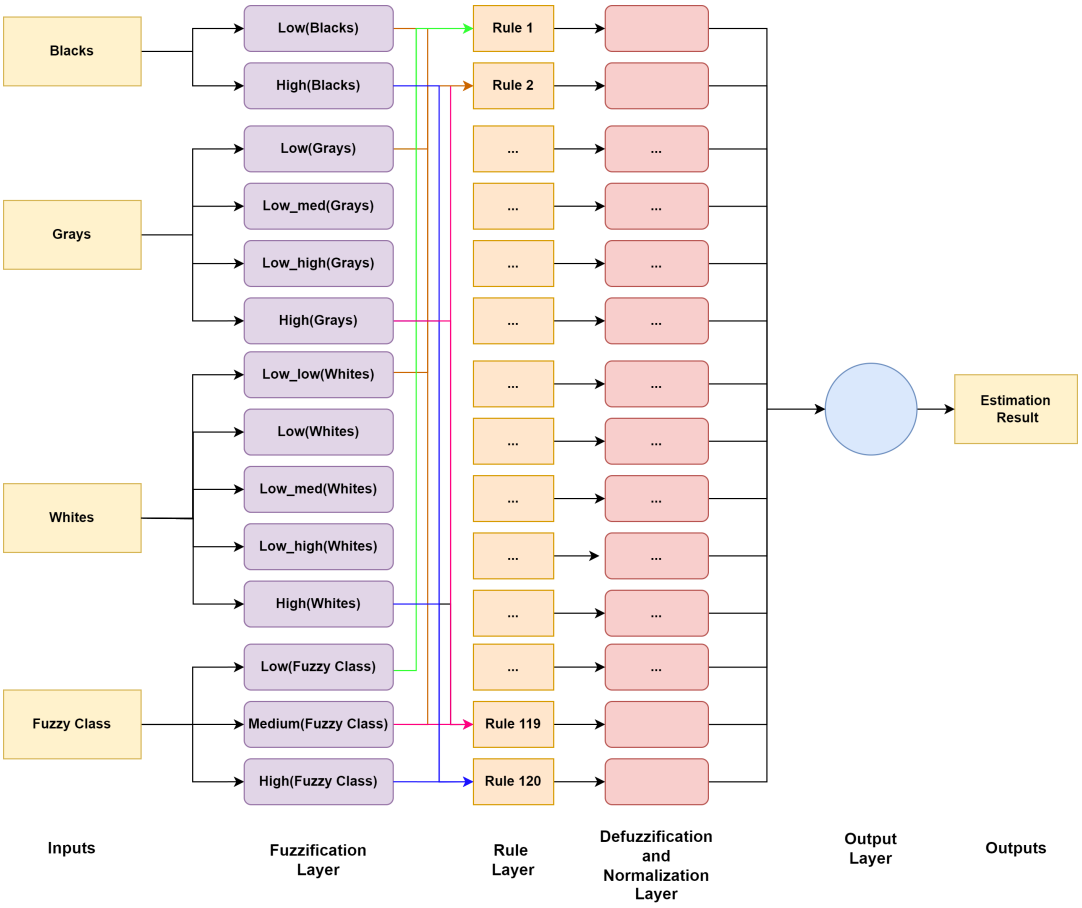


FIGURE 6.30: Architecture of the model. Black, Grays, Whites, and Fuzzy Class are the inputs. Estimation result is the output. Extracted from [73].

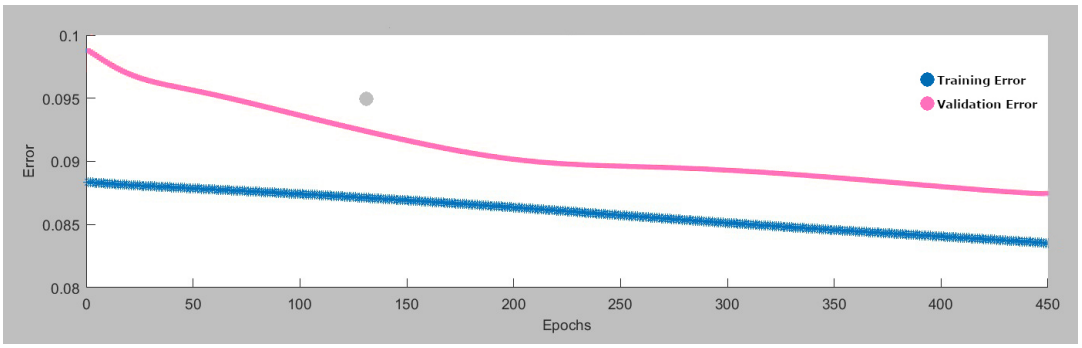


FIGURE 6.31: Changes in training and validation errors throughout the training process

**Rules** Table 6.15 and Table 6.16 present the 120 obtained during the training phase, for each combination of the inputs.

In Fig. 6.33, the 3D diagrams of the surface of the rules are presented. Specifically, Fig. 6.33a illustrates the relationship between the output, Cell Class, and Whites, while Fig. 6.33b displays the relationship between the output, Grays, and Blacks.

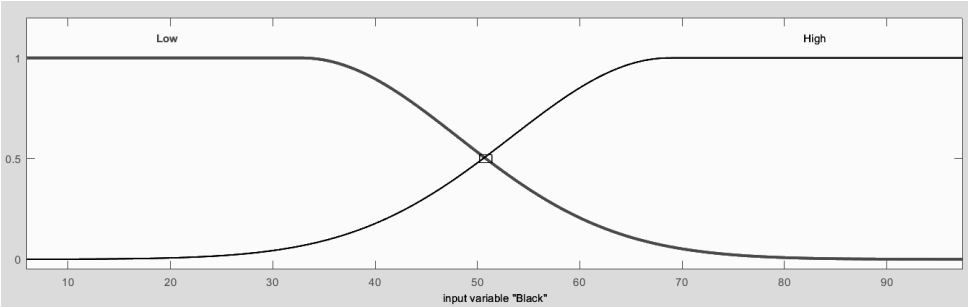


(A) Membership Function of the input: Blacks

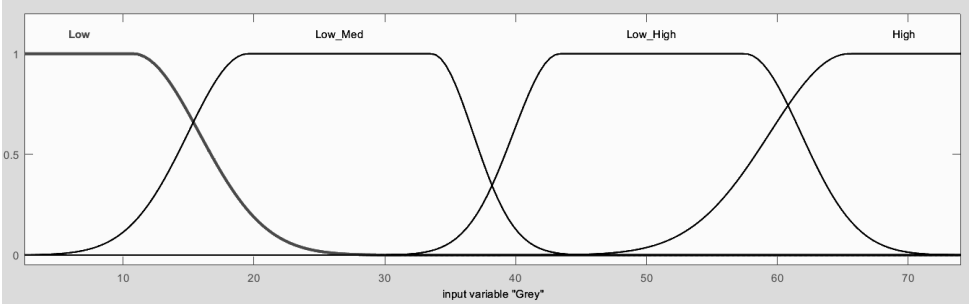


(B) Membership Function of the input: Grays

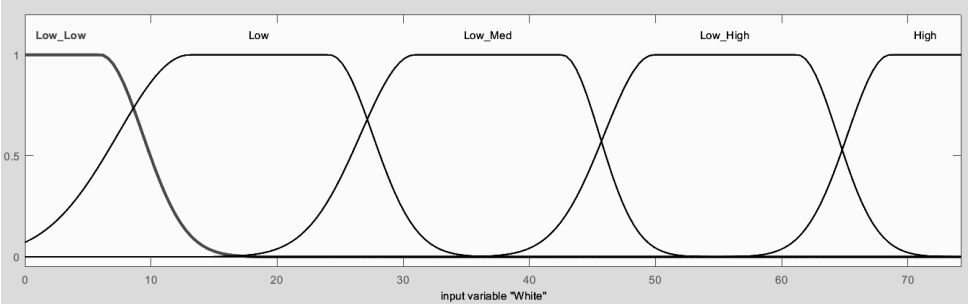


(C) Membership Function of the input: Whites

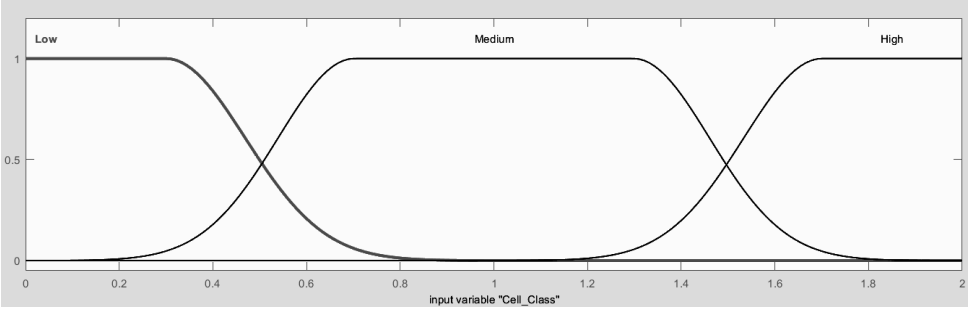


(D) Membership Function of the input: Fuzzy Class.

FIGURE 6.32: The membership functions for the four different inputs of the improved ANFIS model. A combination of manual optimization and the automatic training process was performed to obtain them. Extracted from [73].

### 6.4.6 Results

This section addresses the capabilities of the developed models, examining their performance and identifying potential weaknesses. Initially, the performance of models is evaluated across the different sets. After that, a comparative analysis is conducted to assess how the model performs in comparison to other ML models.

TABLE 6.15: Fuzzy Rules 1-60 of the model. Black, Gray, and White are the inputs. Estimation is the output. H: High; M: Medium; L: Low; LL: Low Low; LM: Low Medium; LH: Low High. Extracted from [73].

| Rule | Black | Gray | White | Fuzzy Class | Estimation Output | Rule | Black | Gray | White | Fuzzy Class | Estimation Output |
|---|---|---|---|---|---|---|---|---|---|---|---|
| 1 | L | L | LL | 0 | | 31 | L | LH | LL | 0 | |
| 2 | L | L | LL | 1 | | 32 | L | LH | LL | 1 | |
| 3 | L | L | LL | 2 | | 33 | L | LH | LL | 2 | |
| 4 | L | L | L | 0 | | 34 | L | LH | L | 0 | |
| 5 | L | L | L | 1 | | 35 | L | LH | L | 1 | |
| 6 | L | L | L | 2 | | 36 | L | LH | L | 2 | |
| 7 | L | L | LM | 0 | | 37 | L | LH | LM | 0 | |
| 8 | L | L | LM | 1 | | 38 | L | LH | LM | 1 | |
| 9 | L | L | LM | 2 | | 39 | L | LH | LM | 2 | |
| 10 | L | L | LH | 0 | | 40 | L | LH | LH | 0 | |
| 11 | L | L | LH | 1 | | 41 | L | LH | LH | 1 | |
| 12 | L | L | LH | 2 | | 42 | L | LH | LH | 2 | |
| 13 | L | L | H | 0 | | 43 | L | LH | H | 0 | |
| 14 | L | L | H | 1 | | 44 | L | LH | H | 1 | |
| 15 | L | L | H | 2 | | 45 | L | H | H | 2 | |
| 16 | L | LM | LL | 0 | | 46 | L | H | LL | 0 | |
| 17 | L | LM | LL | 1 | | 47 | L | H | LL | 1 | |
| 18 | L | LM | LL | 2 | | 48 | L | H | LL | 2 | |
| 19 | L | LM | L | 0 | | 49 | L | H | L | 0 | |
| 20 | L | LM | L | 1 | | 50 | L | H | L | 1 | |
| 21 | L | LM | L | 2 | | 51 | L | H | L | 2 | |
| 22 | L | LM | LM | 0 | | 52 | L | H | LM | 0 | |
| 23 | L | LM | LM | 1 | | 53 | L | H | LM | 1 | |
| 24 | L | LM | LM | 2 | | 54 | L | H | LM | 2 | |
| 25 | L | LM | LH | 0 | | 55 | L | H | LH | 0 | |
| 26 | L | LM | LH | 1 | | 56 | L | H | LH | 1 | |
| 27 | L | LM | LH | 2 | | 57 | L | H | LH | 2 | |
| 28 | L | LM | H | 0 | | 58 | L | H | H | 0 | |
| 29 | L | LM | H | 1 | | 59 | L | H | H | 1 | |
| 30 | L | LM | H | 2 | | 60 | L | H | H | 2 | |

**Results in the different sets for the proposed models** Table 6.17 provides an overview of the performance metrics of the models, illustrating their consistency across the three datasets. It is evident that both models exhibit low errors, with the improved model consistently outperforming the basic model across all datasets. A slight decrease in performance is observed in the testing set, which is anticipated as this data was not utilized during the model training phase.

Fig. 6.34 illustrates the output diagram for the testing set, revealing the close correspondence between actual and predicted values in the majority of cases. Notably, the enhanced model exhibits even smaller deviations, confirming the commendable performance of both models. Furthermore, the occurrence of outliers with significant deviations from their labels is minimal, with the majority closely aligning with the actual values.

**Comparison of the performance of the models with other ML algorithms** While the results underscore the effectiveness of both methods in achieving low error rates, a critical evaluation involves comparing their performance against alternative approaches. Given the absence of prior works specifically addressing the prediction of a cell's output power using EL images, direct comparisons are intricate. Nonetheless, Table 6.18 offers a comparative analysis between the proposed ANFIS models and traditional ML methods. These ML methods were implemented using Python,

TABLE 6.16: Fuzzy Rules 60-120 of the model. Black, Gray, and White are the inputs. Estimation is the output. H: High; M: Medium; L: Low; LL: Low Low; LM: Low Medium; LH: Low High. Extracted from [73].

| Rule | Black | Gray | White | Fuzzy Class | Estimation Output | Rule | Black | Gray | White | Fuzzy Class | Estimation Output |
|---|---|---|---|---|---|---|---|---|---|---|---|
| 61 | H | L | LL | 0 | | 91 | H | LH | LL | 0 | |
| 62 | H | L | LL | 1 | | 92 | H | LH | LL | 1 | |
| 63 | H | L | LL | 2 | | 93 | H | LH | LL | 2 | |
| 64 | H | L | L | 0 | | 94 | H | LH | L | 0 | |
| 65 | H | L | L | 1 | | 95 | H | LH | L | 1 | |
| 66 | H | L | L | 2 | | 96 | H | LH | L | 2 | |
| 67 | H | L | LM | 0 | | 97 | H | LH | LM | 0 | |
| 68 | H | L | LM | 1 | | 98 | H | LH | LM | 1 | |
| 69 | H | L | LM | 2 | | 99 | H | LH | LM | 2 | |
| 70 | H | L | LH | 0 | | 100 | H | LH | LH | 0 | |
| 71 | H | L | LH | 1 | | 101 | H | LH | LH | 1 | |
| 72 | H | L | LH | 2 | | 102 | H | LH | LH | 2 | |
| 73 | H | L | H | 0 | | 103 | H | LH | H | 0 | |
| 74 | H | L | H | 1 | | 104 | H | LH | H | 1 | |
| 75 | H | L | H | 2 | | 105 | H | H | H | 2 | |
| 76 | H | LM | LL | 0 | | 106 | H | H | LL | 0 | |
| 77 | H | LM | LL | 1 | | 107 | H | H | LL | 1 | |
| 78 | H | LM | LL | 2 | | 108 | H | H | LL | 2 | |
| 79 | H | LM | L | 0 | | 109 | H | H | L | 0 | |
| 80 | H | LM | L | 1 | | 110 | H | H | L | 1 | |
| 81 | H | LM | L | 2 | | 111 | H | H | L | 2 | |
| 82 | H | LM | LM | 0 | | 112 | H | H | LM | 0 | |
| 83 | H | LM | LM | 1 | | 113 | H | H | LM | 1 | |
| 84 | H | LM | LM | 2 | | 114 | H | H | LM | 2 | |
| 85 | H | LM | LH | 0 | | 115 | H | H | LH | 0 | |
| 86 | H | LM | LH | 1 | | 116 | H | H | LH | 1 | |
| 87 | H | LM | LH | 2 | | 117 | H | H | LH | 2 | |
| 88 | H | LM | H | 0 | | 118 | H | H | H | 0 | |
| 89 | H | LM | H | 1 | | 119 | H | H | H | 1 | |
| 90 | H | LM | H | 2 | | 120 | H | H | H | 2 | |

TABLE 6.17: Results based on the model across different sets, presenting various metrics: Mean Absolute Error (MAE), Mean Squared Error (MSE), and Root Square Mean Error (RSME). Extracted from [73].

| | Original Model | | | Improved Model | | |
|---|---|---|---|---|---|---|
| Metric | Training | Validation | Testing | Training | Validation | Testing |
| MSE | 0.00871 | 0.00830 | 0.00940 | 0.00697 | 0.00763 | 0.00732 |
| MAE | 0.05878 | 0.06416 | 0.06474 | 0.04854 | 0.04942 | 0.05352 |
| RSME | 0.09297 | 0.09112 | 0.09695 | 0.08350 | 0.08740 | 0.08560 |

leveraging the Sklearn library, which provides several easy-to-configure models ready to be trained.

The tabulated results highlight the substantial superiority of ANFIS models over Linear Regression and Support Vector Machines, particularly evident in the significantly lower errors across various metrics. Although Gradient Boosting exhibits comparable performance in terms of MAE, ANFIS outperforms it in both MSE and RMSE. The notable improvement in performance is underscored by the enhanced ANFIS model, surpassing all other methods in every metric. Notably, ANFIS distinguishes itself by providing more robust outcomes through the transparent presentation of the rule set employed for inference.

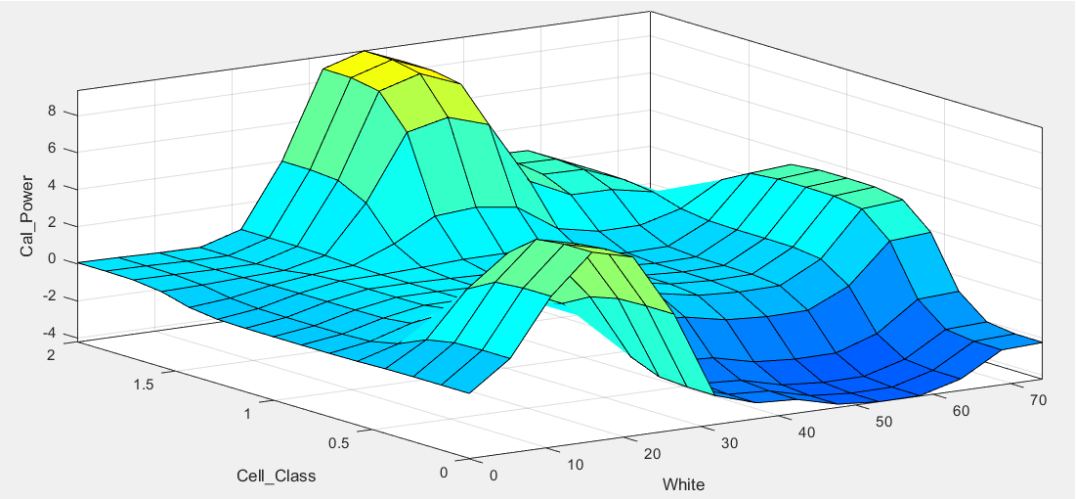


(A) 3D surface diagram illustrating the impact of inputs White and Cell Class on the output.

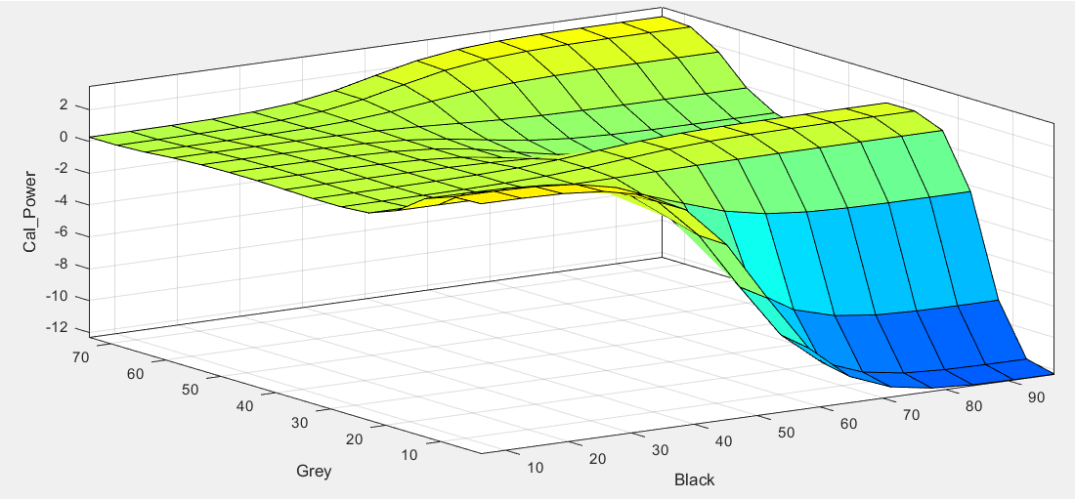


(B) 3D surface diagram illustrating the impact of inputs Gray and Black on the output.

FIGURE 6.33: 3D surface diagrams illustrating the effects of inputs on the output. Extracted from [73].

TABLE 6.18: Comparison between various traditional ML models and the proposed ANFIS methods, presenting various metrics. Mean Absolute Error (MAE), Mean Squared Error (MSE), and Root Square Mean Error (RSME), Linear Regression (LR), Support Vector Machines (SVM), Gradient Boosting Regressor(GBR). Extracted from [73].

| Metric | Original ANFIS | ANFIS Improved | LR | SVM | GBR |
|---|---|---|---|---|---|
| MSE | 0.00940 | **0.00732** | 0.02153 | 0.01291 | 0.01058 |
| MAE | 0.0647 | **0.05352** | 0.09169 | 0.06830 | 0.05933 |
| RSME | 0.09695 | **0.08560** | 0.14673 | 0.11362 | 0.10285 |

While the ANFIS system demonstrates promising results, it is important to acknowledge its limitations. Presently, its inability to operate in real-time applications beyond the cell level raises practical concerns. Extensive testing across diverse PV cell types is imperative to evaluate and enhance its generalization capabilities.

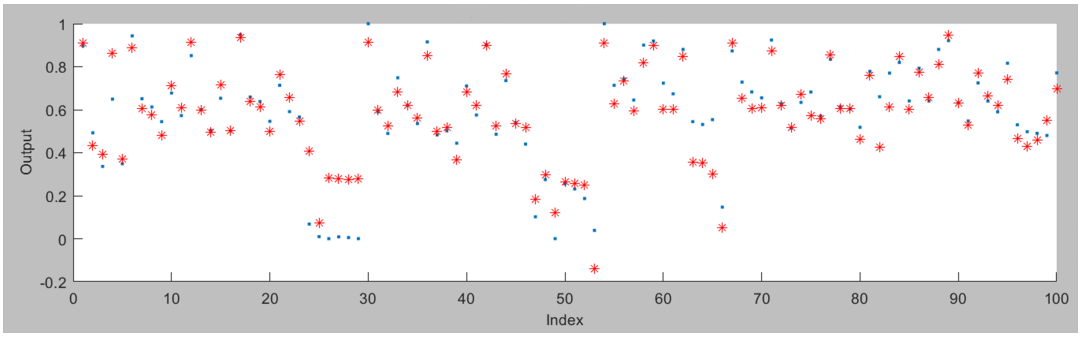


(A) Results of the Original Model in the Testing set.

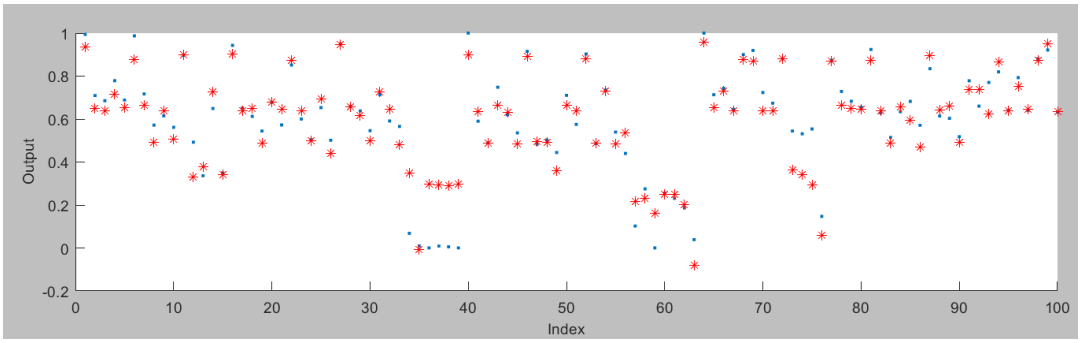


(B) Results of the Improved Model in the Testing set

FIGURE 6.34: Diagramas of the predictions from the models and the original values across the testing set. Blue dots correspond to the original data, while red stars indicate the output from the models. Extracted from [73].

Moreover, it is essential to recognize that the training process of ANFIS demands more computational resources compared to traditional ML methods, although it still maintains a notable advantage in speed over deep learning methods.

### 6.4.7 Summary

This experiment has resulted in the creation of an ANFIS estimator capable of solving the problem (Objective SO4). The ANFIS exhibits a good performance while providing understandable rules.

## 6.5 Detection of Connection Failures

The work explained in this section has resulted in an article that is still in the publication process [182].

### 6.5.1 Objective

While performing the measurements and previous experiment it was observed that some cells presented an anomalous behavior, since their energetic production was adjusted to their EL image, since they did not provide a good performance even if their EL image did not present any kind of defect. An undetected defect was reducing the performance of the cells. This problem appeared in around 1% of the samples.

This section presents a Spatial Frequency Analysis of the EL images of PV cells using a Two-dimensional discrete analysis with a Biorthogonal Filter, applied to the detection of connection failures in the Busbar of Poly-Si Photovoltaic Cells Using Two-Dimensional Wavelet Analysis of Electroluminescence Images. This analysis is complemented with a continuous analysis using a Cauchy Wavelet.

This analysis provides additional information about defects related with series resistance that are not directly visible in EL images (Objective S05).

### 6.5.2 Structure

This section is organized as follows: initially, it introduces the dataset utilized in this study and the problem. Subsequently, it describes the techniques used in the analysis.

### 6.5.3 Data

The analysis has been conducted using both Polycrystalline and Monocrystalline PV cells.

### 6.5.4 Problem

While performing the measurements and first experiments for the works presented in previous sections, it was noted that certain PV cells exhibited EL images devoid of significant defects (Fig. 6.35, yet their corresponding IV curves yielded notably lower MPP values compared to other PV cells under identical conditions 6.36.

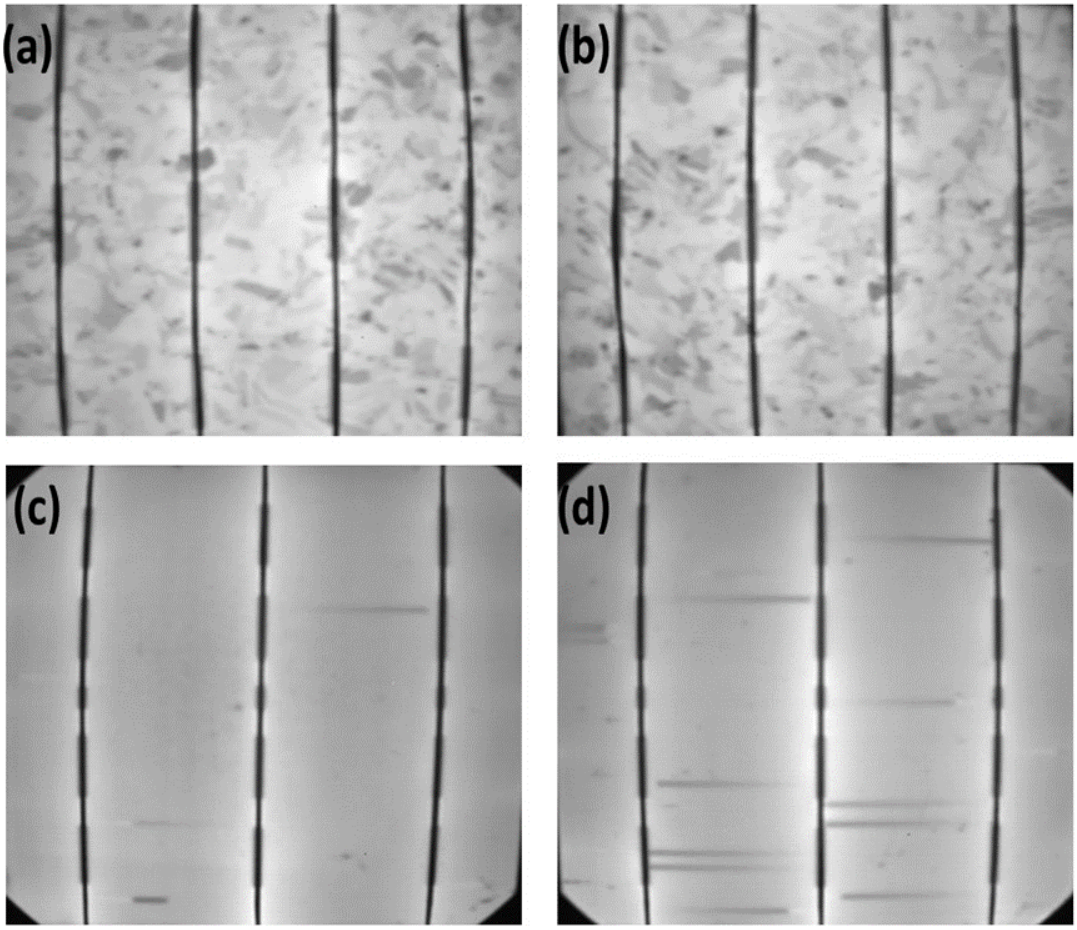


FIGURE 6.35: EL image of four different crystalline silicon cells, PS1 (a), PS2 (b), MS1 (c) and MS2 (d). Extracted from [182].

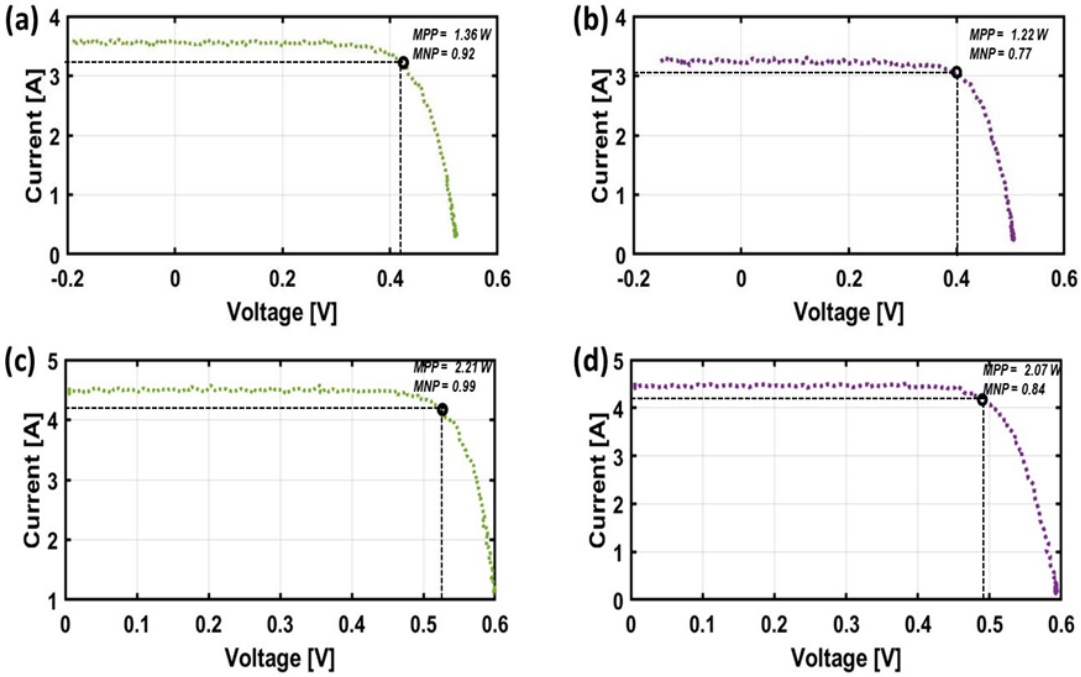


FIGURE 6.36: I-V curve of PS1 cell applying minimum irradiance (1.27 A) (a), PS2 cell applying minimum irradiance (b), MS1 cell applying intermediate irradiance (1.53 A) (c), MS2 cell applying intermediate irradiance (d). Extracted from [182].

The histograms of the EL images also showed that there was not a clear difference between the cells of each type since their shape is extremely similar. (Fig. 6.37). This showed an important limitation of the EL images since they did not provide directly enough information to identify these underperforming PV cells.

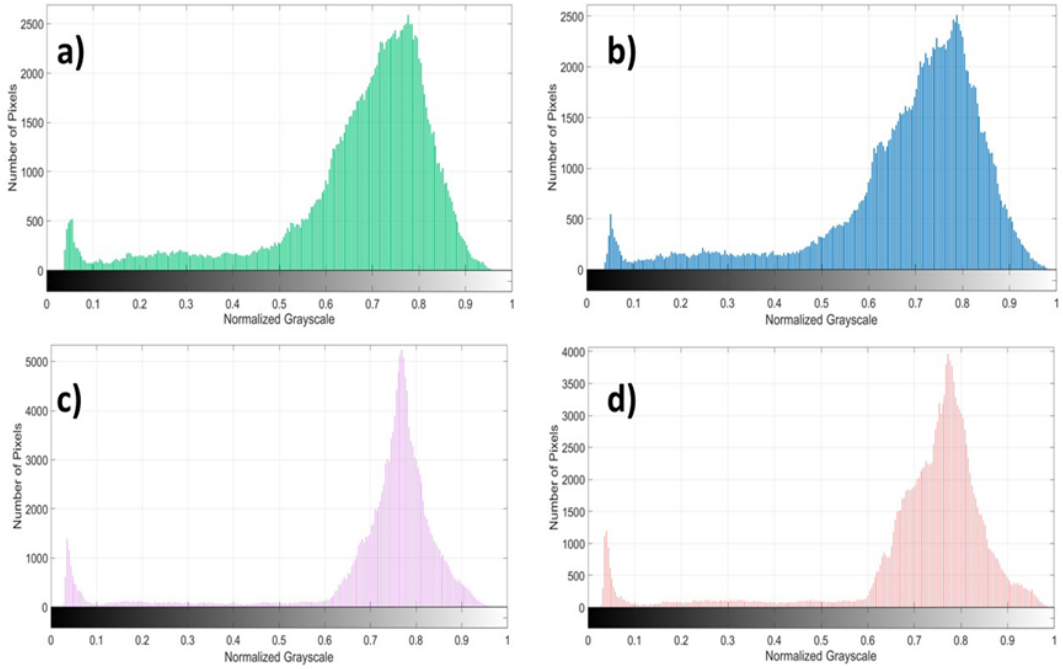


FIGURE 6.37: a) Histogram of the EL image of the PS1 cell (dark green bars) , b) histogram of the EL image of the PS2 cell (dark blue bars) , c) histogram of the EL image of the MS1 cell (light purple bars) and d) the histogram of MS2 (light red bars) . Extracted from [182].

### 6.5.5 3D diagrams of the EL images

Since the usual algorithm was not enough, a different way to analyze the image was considered: a 3D diagram of each image using the mesh function available in Matlab. This method provides a color scale according to the surface illumination. Whereby, the dark blue color indicates the lowest level of illumination and the dark red the highest.

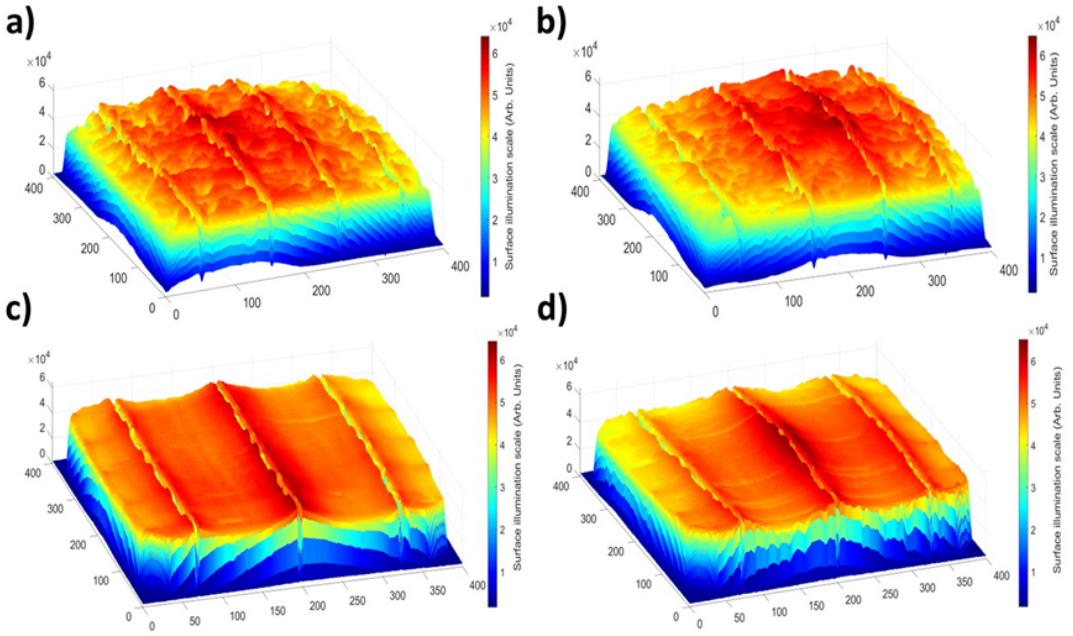


FIGURE 6.38: 3D diagram of the EL image of PS1 (a), PS2 (b), MS1 cell (c) and MS2 cell (d). Extracted from [182].

In Fig. 6.38a, we present a 3D representation of the EL image of the PS1 cell. As anticipated from the EL image histogram and the normalized maximum power analysis, this cell showcases favorable surface illumination, with the central region emitting the highest intensity of light according to the surface illumination scale. Nevertheless, toward the periphery, an intermediate level of illumination is noticeable, with the right segment of the cell exhibiting comparatively lower energy generation. Fig.6.38b illustrates the 3D diagram of the PS2 cell, revealing that the central region exhibits the highest illumination. However, in the left portion of the cell surrounding the first busbar, a region with diminished illumination is observed, as indicated by the surface illumination scale. The diminished energy output in this region may correlate with the normalized low power readings compared to the PS1 cell. Further examination of Fig. 6.38b indicates a reduced current flow on that specific busbar compared to others.

Similarly, Fig. 6.38(c, d) depict the 3D diagrams of cells MS31 and MS2, demonstrating comparable trends. The MS1 cell exhibits uniform and elevated surface illumination, except for the lower surface illumination observed at the right extremity of the cell, as indicated by the color scale. Conversely, the MS2 cell displays predominantly high surface illumination, except for the edges where there are regions of reduced light emission. Analysis of these 3D diagrams suggests that certain structural factors may be impeding the surface illumination of the cells during the EL tests.

### 6.5.6 2D discrete wavelet analysis

The analysis of EL images in the spatial domain was extended into the frequency domain using the two-dimensional discrete wavelet transform. This method allows for the segmentation of color change rates among different image pixels based on the

selected filtering level. Specifically, we applied a Biorthogonal (Bior) wavelet filter of order 4.4 to decompose the images into two levels.

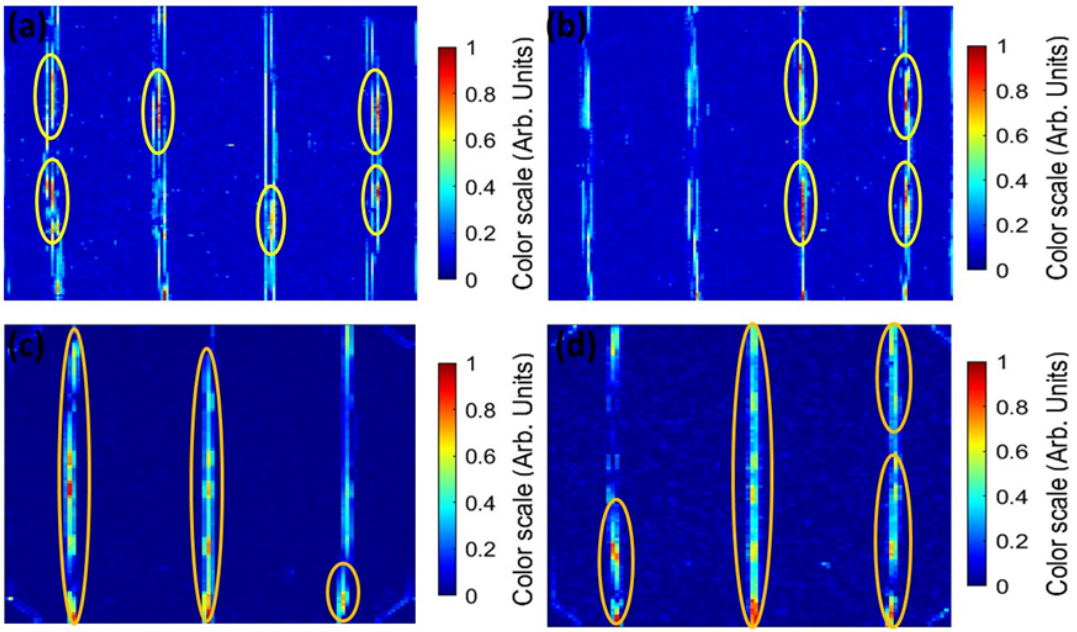


FIGURE 6.39: Second-level vertical detail coefficients of the EL image of PS1cell (a), coefficients of the EL image of the PS2 cell (b), coefficients of the EL image of the MS1 cell (c) and MS2 cell (d). Extracted from [182].

In Fig. 6.39a, the second-level vertical detail coefficients derived from the discrete wavelet transform of the EL image of the PS1 cell are depicted. Notably, several dark red areas are discernible above four of the busbars. These areas represent the energy density emitted by the current flowing through the respective busbars at the time of EL image capture, directly correlating with cell illumination. Fig. 6.39 b highlights that the first busbar, from left to right, exhibits minimal to no red-colored areas (as indicated by yellow marks). The associated vertical detail wavelet coefficients appear white, suggesting a lower energy density compared to other busbars. This elucidates the observed lower surface illumination surrounding this busbar in Fig. 6.39b. Further examination revealed defective soldering between the cell and the conductor, which can increase the series resistance of the cell and impede the current flow through that particular busbar.

Figs. 6.39(c, d) present the 2D DWT of the EL images for two monocrystalline cells, each equipped with three busbars. In Fig. 6.39 c, a notable reduction in energy density is observed in the last busbar on the right side of the MS1 cell, resulting in diminished surface illumination around that area, as depicted in Fig. 6.39c. Fig. 6.39d displays a similar phenomenon, but in the first busbar of the MS2 cell, affecting the surface illumination in that region of the cell. Upon closer physical inspection, welding defects between the cell and the busbar were discovered, contributing to the observed phenomenon in the 2D wavelet analysis conducted.

### 6.5.7 2D continuous wavelet analysis

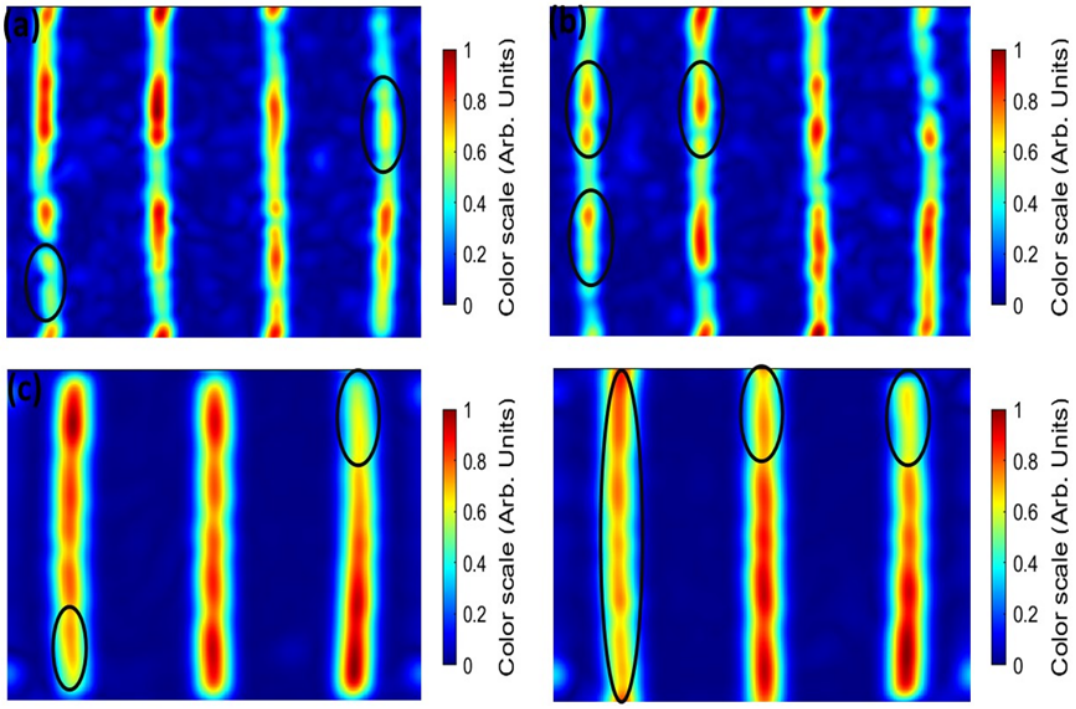


FIGURE 6.40: Coefficients of the 2D continuous wavelet transformation of the EL image of PS1 cell (a), 2D CWT coefficients of the EL image of PS2 cell (b), 2D CWT coefficients of the EL image of MS1 cell (c) and 2D CWT coefficients of the EL image of MS2 cell (d). Extracted from [182].

To extend the analysis into the frequency domain, the 2D Continuous Wavelet Transform (2D CWT) was applied to the EL images of PS1, PS2, MS1, and MS2 cells across various current levels. The Cauchy anisotropic mother wavelet was chosen for its sensitivity to wave orientation and image features. Additionally, its extended support compared to isotropic (non-directional) wavelets enables the capture of finer details during the transformation process. Given its complex nature, only the wavelet modulus is depicted graphically.

Fig. 6.40a illustrates the graphical representation of the wavelet modulus of the PS1 cell's EL image, with an orientation angle of  radians (180ř) and a two-level decomposition scale. At this orientation, the mother wavelet facilitates the observation of the squared magnitude wavelet coefficients on scale 2, corresponding to the energy generated by current flow through the cell's busbars during the EL test. The 3D plot, along with its color scale, reveals lower current flowing through the rightmost busbar compared to the others, resulting in reduced illumination around that area (refer to Fig. 6.38).

This observation mirrors the previously identified behavior in the 2D Discrete Wavelet Transform representation. The phenomenon can be attributed to a potential electrical contact failure between the electrode and the cell during the welding process, leading to increased series resistance over time and ultimately restricting current flow across that region of the cell. Fig. 6.40b showcases the 2D CWT spatial

frequency representation of the PS2 cell's EL image, analyzed with the same parameters ( radians angle and scale 2). This figure reveals a similar situation for the first busbar on the far left of the cell. The 2D wavelet coefficients exhibit a lighter yellow color (marked with black indicators), indicating lower current flow through the busbar compared to others based on the color scale. This translates to reduced illumination in that specific region of the cell, as observed in Figure 10b.

Fig. 6.40(c, d) depicts the 2D DWT of monocrystalline cells with four busbars, MS1 and MS2, respectively. The spectral energy density of the MS1 and MS2 cells exhibits variations on certain busbars (areas marked with black ovals). These variations manifest as reduced surface illumination and lower peak power output, replicating the issues observed in the discrete wavelet analysis and other analyzed cells.

### 6.5.8 Summary

This experiment has provided an analysis of the EL images using various techniques (Objective S05. The analysis based on Wavelet Transform has provided information about the energetic distribution of the cell and how some cell presents defects in their busbar bar that augment the series resistance of the cells which reduces their performance.

## 6.6 Convolutional Mixture of Experts

The work explained in this Section has resulted in an article that is still in the publication process. [17].

### 6.6.1 Objective

The final objective of the thesis is to improve the estimation in order to include various kinds of PV cells (Objective S06).

The section introduces an innovative approach for assessing the performance state of a PV cell based on its EL image. The method involves training models by integrating EL images with information derived from the I-V curves of the PV cells. This approach is applied across cells of different technologies, including Monocrystalline and Polycrystalline cells, with an analysis conducted to evaluate the impact of these technologies on the performance of various Machine Learning models. Additionally, a Mixture of Experts model is introduced, which leverages pretrained convolutional models to enhance the performance of simpler models.

### 6.6.2 Structure

The paper follows the following structure: it begins by presenting the utilized data, followed by an explanation of the models employed. Finally, it details the obtained results.

### 6.6.3 Data

All the seven presented original datasets (Section 5.2 are taken into consideration in this work: Polycrystalline, Polycrystalline balanced, Monocrystalline 3 busbar, Monocrystalline 4 busbar, Monocrystalline complete, Mono+Poly and Mono+Poly balanced.

### 6.6.4 Feature Extraction

Feature extraction has been needed in the case of the traditional methods, all the extracted features from the manual approach have been considered (Section 5.2. CNNs have used the images directly.

### 6.6.5 Models

Various AI methods have been employed to assess the performance differences for each dataset. Each method has been optimized to fulfill its specific task while maintaining a capacity for generalization.

The datasets utilized have been partitioned into three distinct sets: Training (60%), Validation (20%), and Test (20%). Only the Training Dataset and Validation set are utilized during the training process.

#### CNN model

Convolutional Neural Networks are currently considered the state-of-the-art method for processing images [211], including within the field of photovoltaics [11]. CNNs

are capable of directly processing input images without the need for prior feature extraction. The experiments related with CNNs were conducted in Python, utilizing the Tensorflow library [129].

**Preprocessing** The images, additionally to the steps explained in Section 5.2 undergo a reduction of their size based on a scale factor, which serves as a hyperparameter. This reduction aims to mitigate algorithmic costs arising from hardware limitations.

**Architecture** The design of the model architecture was conducted manually, adjusting the complexity based on training process metrics. The final architecture comprises 13 layers, incorporating Convolutional 2D, Max Pooling, Flatten, and Dense layers. Figure 6.41 illustrates this architecture. This design process utilized the Mono + Poly dataset as the input dataset, as it encompasses samples from various types of PV cells.

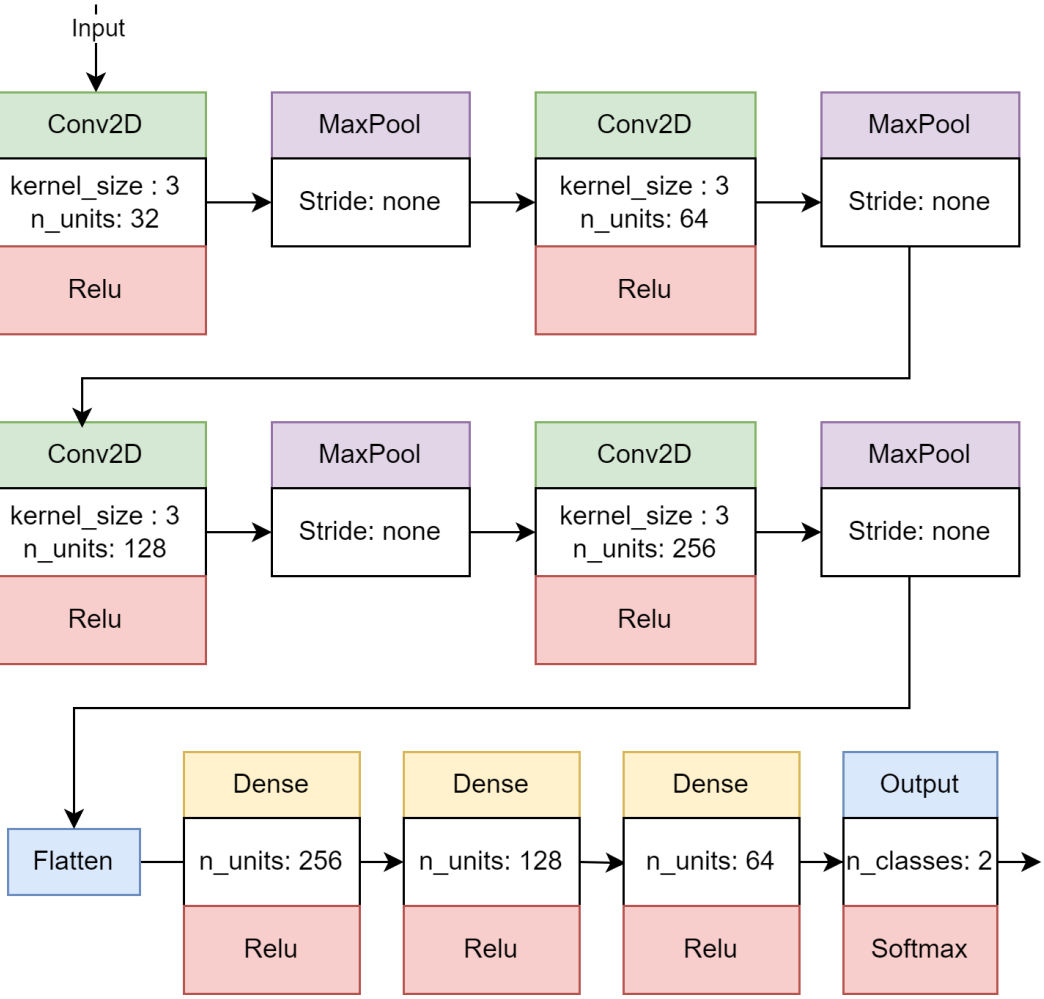


FIGURE 6.41: Architecture of the CNN model. Extracted from [17].

**Hyperparameter Optimization** Neural Networks, including CNNs, suffer from a significant drawback as they heavily rely on their hyperparameters. However, the vast number of possible configurations makes manually finding the best configuration nearly impossible. To address this challenge, the Keras Tuner library [205] has

been utilized. This library offers various methods to optimize the hyperparameters of NN models. The chosen algorithm, Bayesian Optimization Tuner [206], leverages information from previous trials to inform the selection of subsequent values, thereby improving the exploitation of the search space. This optimization process was conducted using the Mono + Poly dataset as the input dataset for the same reasons mentioned previously.

TABLE 6.19: Optimal Hyperparameters found for Convolutional Neural Networks: batch_size $\in$ [8, 16, 32, 64], learning_rate $\in$ [0.01, 0.0001],scale_factor in [0.5, 1],optimizer: Adam, Nadam, SGD. Extracted from [17].

| model | batch_size | learning_rate | scale_factor | optimizer |
|---|---|---|---|---|
| Mono | 8 | 0.00025 | 0.66 | Adam |
| Mono-3 | 8 | 0.0005 | 0.66 | Adam |
| Mono-4 | 8 | 0.00025 | 0.66 | Adam |
| Poly-Complete | 8 | 0.00025 | 0.66 | Adam |
| Poly-Reduced | 8 | 0.00025 | 0.66 | Adam |
| Mono + Poly | 8 | 0.001 | 0.66 | Adam |
| Mono + Poly Balanced | 8 | 0.001 | 0.66 | Adam |

**Training** The seven distinct datasets were utilized to train seven separate networks, employing the architecture and hyperparameters detailed in previous sections.

The training process spanned 500 epochs, with the model achieving the lowest MAE being saved as the final model. Figure 6.42 depicts the evolution of MAE in both the training and validation sets for each model. The discrepancy in performance across the various datasets will be discussed further in the results section.

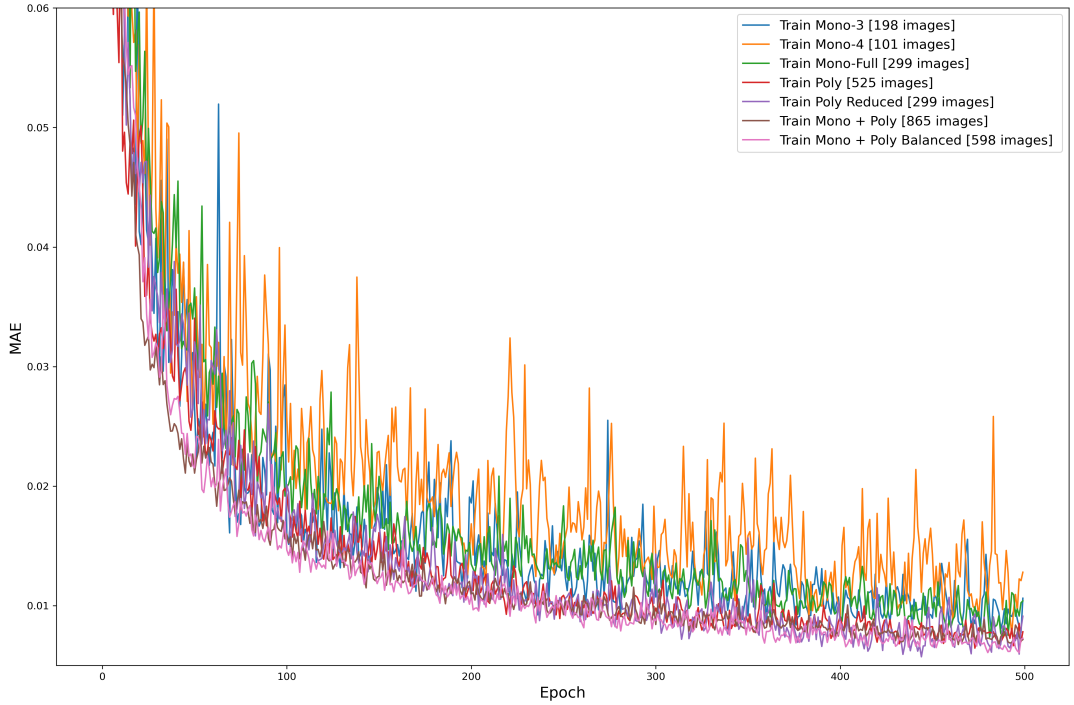


(A) Training set.

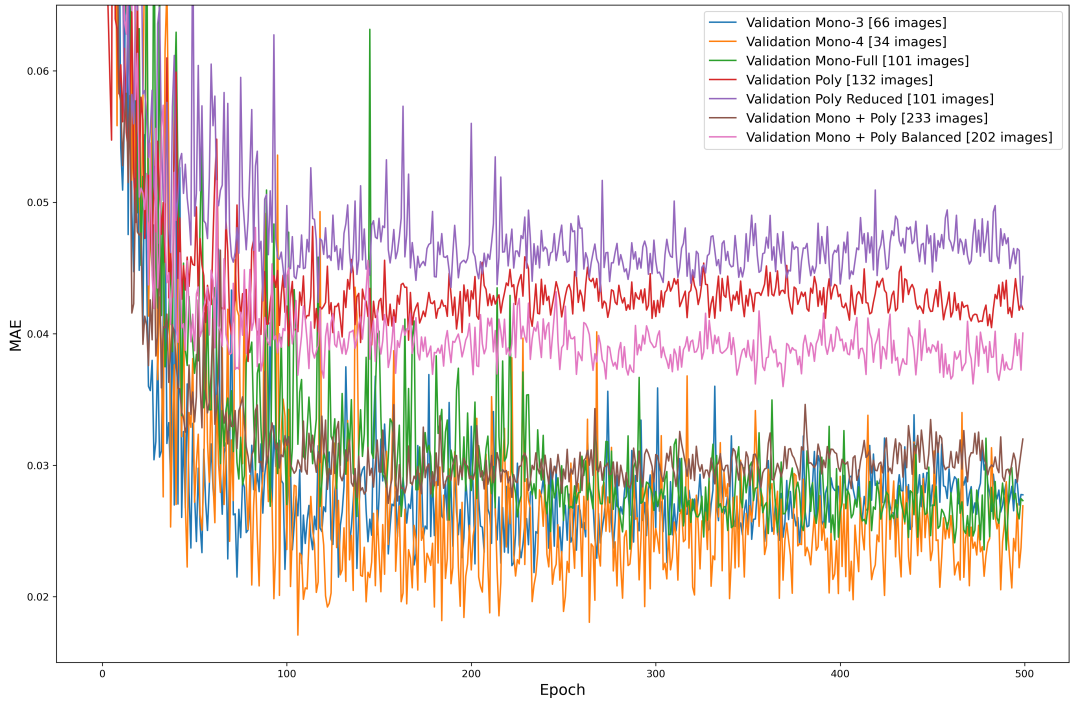


(B) Validation set.

FIGURE 6.42: Evolution of the Mean Absolute Error in the training process of the CNN models. Extracted from [17].

### Feature-Based Methods

Traditional machine learning methods have been widely applied for regression tasks across various fields [198], owing to their low computational demands and

satisfactory performance. The following algorithms have been implemented in Matlab utilizing the Regression Learner application: Bagged Trees, Gaussian Process Regression, Support Vector Machine, and Neural Networks.

**Model Selection and Hyperparameter Optimization** The process of selecting the best models was conducted using the Mono+Poly Dataset, which encompasses samples from every type of PV represented. All the algorithms described were trained with their hyperparameters optimized using a Bayesian Optimizer, conveniently available directly within the application. Table 6.20 presents the results of the top 5 models along with their hyperparameters. Notably, Exponential GPR emerged as the best algorithm in terms of both MAE and MSE.

TABLE 6.20: Results of various Machine Learning methods in the Mono+Poly dataset. GPR: Gaussian Process Regression. SVM: Support Vector Machines. NN: Neural Network. MAE: Mean Absolute Error. MSE: Mean Squared Error. Extracted from [17].

| | Validation | Hyperparameters |
|---|---|---|
| Bagged Trees | MAE 0.0729<br>MSE 0.0110 | Minimum leaf size : 8<br>Number of learners: 30 |
| Rational Quadratic GPR | MAE 0.0718<br>MSE 0.0100 | Basis Function: Constant<br>Kernel Function : Rational Quadratic |
| **Exponential GPR** | **MAE 0.0698**<br>**MSE 0.0095** | **Basis Function: Constant**<br>**Kernel Function : Exponential** |
| Medium Gaussian SVM | MAE 0.0822<br>MSE 0.0119 | Kernel Function : Gaussian<br>Kernal Scale: 3.9 |
| Trilayered NN | MAE 0.0856<br>MSE 0.0148 | Number of layers: 3<br>Size of the layers : [10, 10, 10]<br>Activation Function: Relu |

**Feature Selection** Parameter selection is a crucial step in identifying the optimal configuration of input features. Table 6.21 presents all the features after applying the F-test algorithm [212] to rank them based on their relevance. Table 6.22 displays the performance of the chosen model with varying numbers of features. Interestingly, it demonstrates how removing features enhances performance, with eleven features yielding the best results. Moving forward, only these eleven features will be considered in the experiments.

TABLE 6.21: F-type-based raking of the features. Extracted from [17].

| Feature | Blacks | Grays | Mean | Kurtosis | Peak 0 Height | Roughness | Variance | Median |
|---|---|---|---|---|---|---|---|---|
| F-Type Score | 440.83 | 405.62 | 302.85 | 245.48 | 190.62 | 189.67 | 138.90 | 60.22 |
| Feature | Peak 1 Width | Whites | Mode | Peaks Distance | Peak 1 Height | Peak 0 Width | Peaks Number | - - |
| F-Type Score | 29.47 | 21.88 | 21.06 | 18.73 | 13.96 | 6.71 | 1.61 | - - |

TABLE 6.22: Results in the Validation set of the GPR-Exponential method using Feature Selection to remove different amounts of features. Extracted from [17].

| Number of Features | 15 | 13 | **11** | 9 |
|---|---|---|---|---|
| MAE | 0.0698 | 0.0678 | **0.0652** | 0.0680 |
| MSE | 0.00950 | 0.00907 | **0.00830** | 0.00901 |

### Convolutional Hierarchical Mixture of Experts

The Mixture of Experts [213] is a machine learning technique employed to partition a problem into distinct subproblems. This approach proves highly beneficial for the discussed problem, as each type of PV cell can be viewed as a separate subproblem. Among the various Mixture of Experts frameworks, the Hierarchical Mixture of Experts [214] is utilized. Given that the models employed are Convolutional Networks, the proposed model is referred to as Convolutional Hierarchical Mixture of Experts (CHME).

**Preprocessing** The images are processed, as in the case of the simple CNN models. This model uses directly the images since it is based on convolutional models.

**Architecture** This approach entails a Tree-Structured architecture (refer to Fig. 6.43). At the highest level, a Discriminator model is situated, which discerns the type of input. Subsequently, at the next level, a distinct regression model is selected based on the discriminator model's decision. The architecture of the discriminator model was meticulously chosen through a manual process, iterating on the architecture to optimize model performance. The final architecture is depicted in Fig. 6.44. The CNN models maintain their respective architectures and hyperparameters.

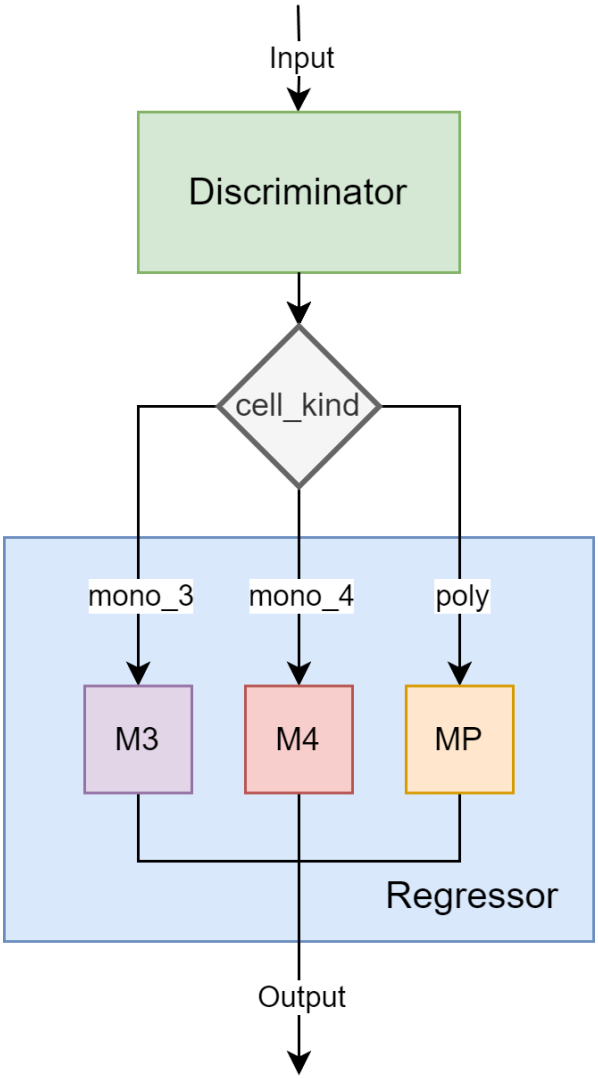


FIGURE 6.43: Architecture of the Convolutional Hierarchical Mixture of Experts. Cell_kind represents the output of the discriminator network. M3 represents a Convolutional network trained only with the Mono3 dataset. M4 represents a Convolutional network trained only with the Mono4 dataset. MP represents a Convolutional network trained only with the Poly dataset. Extracted from [17].

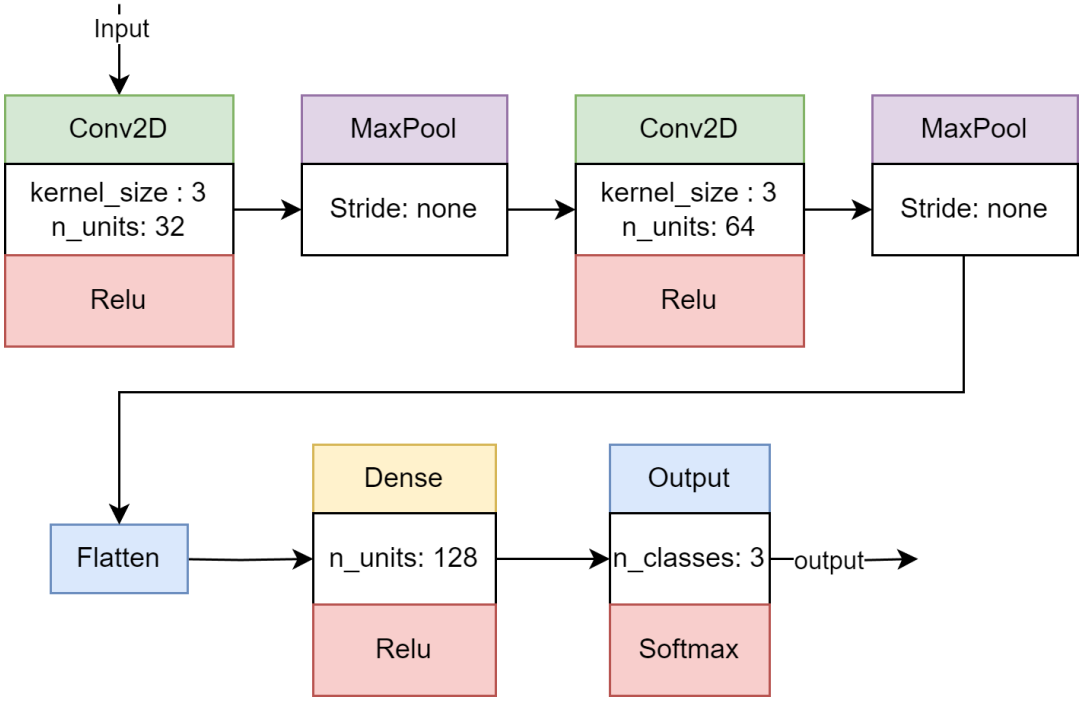


FIGURE 6.44: Architecture of the Discriminator Model. Extracted from [17].

**Hyperparameter Optimization** The parameter optimization process for the networks was also executed using Keras Tuner. Table 6.23 provides an overview of the hyperparameters for all networks, with the regression networks retaining their original hyperparameters.

TABLE 6.23: Optimal Hyperparameters found for Convolutional Neural Networks: batch_size $\in$ [8, 16, 32, 64], learning_rate $\in$ [0.01, 0.00001],scale_factor in [0.5, 1],optimizer: Adam, Nadam, SGD. Extracted from [17].

| model | batch_size | learning_rate | scale_factor | optimizer |
|---|---|---|---|---|
| Discriminator | 8 | 0.00001 | 0.66 | Adam |
| M3 | 8 | 0.0005 | 0.66 | Adam |
| M4 | 8 | 0.00025 | 0.66 | Adam |
| MP | 8 | 0.00025 | 0.66 | Adam |

**Training** The training of the four networks was conducted individually. Detailed training procedures for M3, M4, and MP can be found in Section 6.6.5. The discriminator network underwent training for 20 epochs utilizing Binary Cross Entropy [215] as the loss function, with accuracy serving as an additional metric. The evolution of both metrics throughout the training process is depicted in Fig. 6.45. Notably, the model demonstrates the capability to classify various types of PV cells with 100% accuracy and high confidence, as evidenced by its low Binary Cross Entropy. Interestingly, the training process necessitates fewer epochs compared to the regressor models. Furthermore, the absence of overfitting is apparent, as indicated by the close alignment between training and validation values in the final epochs.

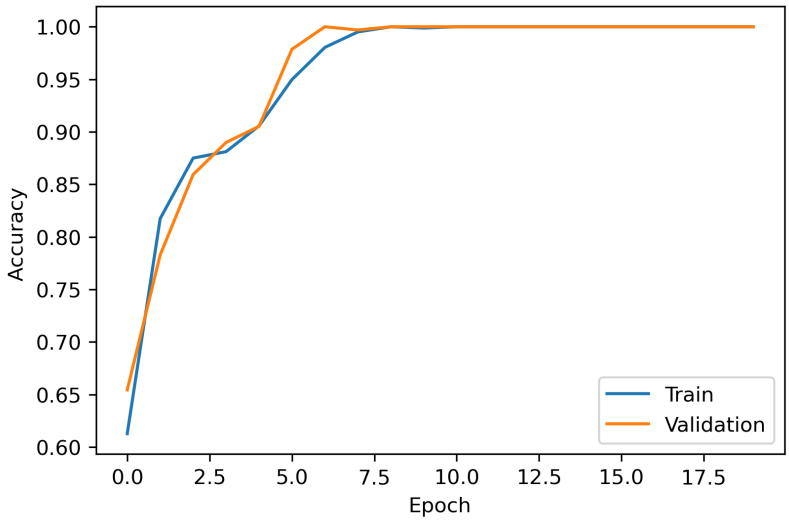


(A) Evolution of the Accuracy.

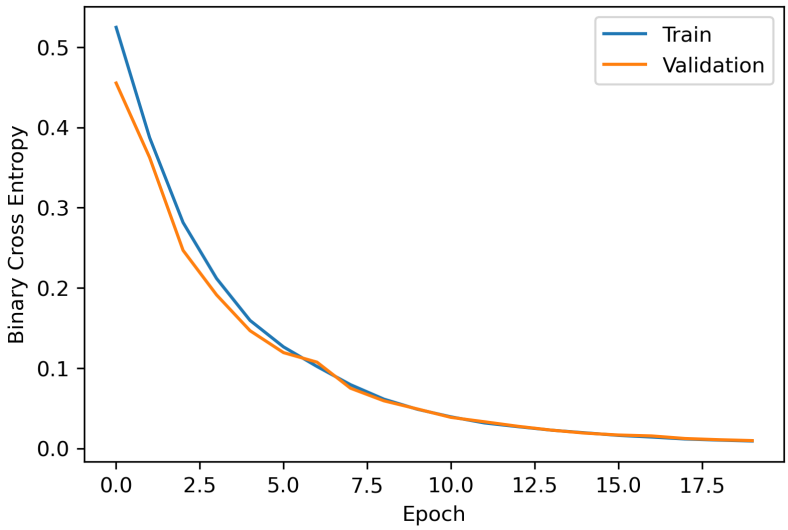


(B) Evolution of the Binary Cross Entropy.

FIGURE 6.45: Evolution of the metrics in the discriminator network during its training process. Extracted from [17].

### 6.6.6 Results

This section evaluates the performance of the proposed models across each dataset. Firstly, the CNN models will be evaluated, followed by an assessment of the feature-based methods. Finally, the CNN-based ensemble of experts will be compared with the other methodologies.

#### Comparison of the CNN models trained with different datasets

The experiments were structured according to the methodology outlined previously. Each model underwent testing with diverse datasets, ensuring that no sample used in the training or validation sets appeared in these tests. The results (Table 6.24) reveal several noteworthy observations.

- As evident from the results, the performance on the Test sets closely mirrors that of the Validation sets, affirming the models' capacity for generalization.
- The Mono Complete model exhibits proficiency in handling Monocrystalline cells from the dataset, achieving an MAE of 0.0194. This underscores its ability to discern crucial patterns during training for processing such images effectively. However, its performance diminishes notably when confronted with Polycrystalline images, evident from the elevated MAE of 0.2169 in the Poly dataset. This discrepancy suggests a lack of adaptability in predicting output power for Polycrystalline PV cells.
- The Mono-3 model demonstrates proficiency in processing images of Monocrystalline cells with 3 busbars, yielding an MAE of 0.0211. However, its performance diminishes notably when presented with images of Mono-4 cells, as reflected in the higher MAE of 0.1283. While not optimal for handling every Monocrystalline PV cell type in the dataset, it still delivers acceptable performance, as evidenced by its MAE of 0.0758 in the Mono Complete dataset. Interestingly, its performance with the Polycrystalline dataset mirrors that of the previous model.
- The Mono-4 model exhibits a behavior akin to its predecessor, demonstrating commendable performance for Mono-4 cells with an MAE of 0.0216, and acceptable performance for Mono-3 cells with an MAE of 0.1190. While capable of handling various Mono PV cell types, it may not yield optimal outcomes. Its performance with Polycrystalline cells remains consistent with that of the preceding models.
- The Poly Complete model demonstrates impressive performance in its test set, achieving an MAE of 0.0337. However, this result falls short of the Mono Complete model's performance. This discrepancy could be attributed to the greater irregularities in the surface of Polycrystalline PV cells, as depicted in Fig. 4.1. Conversely, when applied to the Mono-Complete dataset, the model's performance is subpar, as it struggles to handle Monocrystalline cells due to their distinct patterns (MAE = 0.2228). This trend persists across both Mono-3 (MAE = 0.2030) and Mono-4 (MAE = 0.2628) PV cell types.
- The performance of Poly Reduced closely mirrors that of the Complete model, with an MAE of 0.0339. In the Mono datasets, its performance is akin to that of the Complete model, with MAEs of 0.2167 for Mono Complete, 0.1919 for Mono-3, and 0.2690 for Mono-4.
- The combination of Monocrystalline and Polycrystalline achieves an MAE of 0.0288. For Monocrystalline cells, the model achieves an MAE of 0.0265, with 0.0259 for Mono-3 and 0.0281 for Mono-4. In the Polycrystalline dataset, the model achieves an MAE of 0.0288. The consistent performance across all datasets suggests that combining both datasets in training allows the network to learn the various patterns necessary to handle all available types of PV cells.
- The results of the Mono+Poly balanced dataset are similar to the non-balanced dataset, with a Test MAE of 0.298. For Monocrystalline cells, the MAE is 0.0312, with 0.0295 for Mono-3 and 0.0351 for Mono-4. The MAE for Polycrystalline cells is 0.0288. These results closely resemble those of the previous model, albeit slightly lower due to the reduced number of Polycrystalline cell samples during the training phase.

TABLE 6.24: Results of CNN-based models. Extracted from [17].

| | Validation | Test | Mono Complete | Mono Busbar-3 | Mono Busbar-4 | Poly | Mono + Poly |
|---|---|---|---|---|---|---|---|
| Mono Complete | MAE 0.0207<br>MSE 0.0010 | MAE 0.0194<br>MSE 0.0006 | MAE 0.0194<br>MSE 0.0006 | MAE 0.0221<br>MSE 0.0009 | MAE 0.0255<br>MSE 0.0010 | MAE 0.2159<br>MSE 0.0639 | MAE 0.1195<br>MSE 0.0340 |
| Mono Busbar-3 | MAE 0.0184<br>MSE 0.0008 | MAE 0.0214<br>MSE 0.0008 | MAE 0.0758<br>MSE 0.0124 | MAE 0.0211<br>MSE 0.0008 | MAE 0.1283<br>MSE 0.0239 | MAE 0.1668<br>MSE 0.0439 | MAE 0.1488<br>MSE 0.0307 |
| Mono Busbar-4 | MAE 0.0216<br>MSE 0.0008 | MAE 0.0215<br>MSE 0.0007 | MAE 0.0753<br>MSE 0.0122 | MAE 0.1190<br>MSE 0.0223 | MAE 0.0215<br>MSE 0.0007 | MAE 0.2351<br>MSE 0.0786 | MAE 0.1913<br>MSE 0.0586 |
| Poly Complete | MAE 0.0313<br>MSE 0.0019 | MAE 0.0337<br>MSE 0.0022 | MAE 0.2228<br>MSE 0.0728 | MAE 0.2030<br>MSE 0.0617 | MAE 0.2628<br>MSE 0.0960 | MAE 0.0341<br>MSE 0.0024 | MAE 0.1211<br>MSE 0.0351 |
| Poly Reduced | MAE 0.0435<br>MSE 0.0042 | MAE 0.0339<br>MSE 0.0021 | MAE 0.2167<br>MSE 0.0700 | MAE 0.1919<br>MSE 0.0551 | MAE 0.2688<br>MSE 0.1014 | MAE 0.0339<br>MSE 0.0021 | MAE 0.1290<br>MSE 0.0345 |
| Mono and Poly | MAE 0.0281<br>MSE 0.0015 | MAE 0.0288<br>MSE 0.0015 | MAE 0.0265<br>MSE 0.0012 | MAE 0.0259<br>MSE 0.0011 | MAE 0.0281<br>MSE 0.0013 | MAE 0.0301<br>MSE 0.0018 | MAE 0.0288<br>MSE 0.0015 |
| Mono and Poly Balanced | MAE 0.0246<br>MSE 0.0012 | MAE 0.0298<br>MSE 0.0018 | MAE 0.0312<br>MSE 0.0016 | MAE 0.0285<br>MSE 0.0012 | MAE 0.0351<br>MSE 0.0019 | MAE 0.0305<br>MSE 0.0019 | MAE 0.0298<br>MSE 0.0018 |

As evidenced, the efficacy of the models diminishes when applied to alternative types of PV cells. This phenomenon can be attributed to the structural divergences among the various cell types. As depicted in Fig. 4.1, variations in the number of busbars significantly alter the fundamental architecture of the cell. Additionally, the surface characteristics of Monocrystalline and Polycrystalline cells differ markedly, with Monocrystalline cells exhibiting greater homogeneity compared to Polycrystalline cells.

### Comparison of the feature-based models trained with different datasets

The primary aim of the feature-based models is to mitigate the impact of cell structure on the generalization capabilities of the models. As elucidated earlier, these features are derived from a thorough analysis of the most pertinent characteristics of the images and their histograms. The models have undergone training and testing using identical samples as in the preceding section. Table 6.22 provides an overview of the outcomes derived from these experiments.

TABLE 6.25: Results of the best feature-based method. Extracted from [17].

| | Validation | Test | Mono Complete | Mono Busbar-3 | Mono Busbar-4 | Poly | Mono + Poly |
|---|---|---|---|---|---|---|---|
| Mono Complete | MAE 0.0662<br>MSE 0.0081 | MAE 0.0648<br>MSE 0.0071 | MAE 0.0648<br>MSE 0.0071 | MAE 0.0699<br>MSE 0.0081 | MAE 0.0531<br>MSE 0.0037 | MAE 0.2114<br>MSE 0.0634 | MAE 0.1724<br>MSE 0.0476 |
| Mono Busbar-3 | MAE 0.0651<br>MSE 0.0075 | MAE 0.0581<br>MSE 0.0058 | MAE 0.0591<br>MSE 0.0068 | MAE 0.0581<br>MSE 0.0055 | MAE 0.0604<br>MSE 0.0053 | MAE 0.2092<br>MSE 0.0639 | MAE 0.1771<br>MSE 0.0532 |
| Mono Busbar-4 | MAE 0.0668<br>MSE 0.0044 | MAE 0.0458<br>MSE 0.0036 | MAE 0.0654<br>MSE 0.0076 | MAE 0.0853<br>MSE 0.0124 | MAE 0.0458<br>MSE 0.0036 | MAE 0.2151<br>MSE 0.0706 | MAE 0.1846<br>MSE 0.0526 |
| Poly Complete | MAE 0.0540<br>MSE 0.0056 | MAE 0.0521<br>MSE 0.0051 | MAE 0.1881<br>MSE 0.0536 | MAE 0.1406<br>MSE 0.0330 | MAE 0.2515<br>MSE 0.0813 | MAE 0.0540<br>MSE 0.0056 | MAE 0.1534<br>MSE 0.0416 |
| Poly Reduced | MAE 0.0524<br>MSE 0.0058 | MAE 0.0530<br>MSE 0.0059 | MAE 0.1897<br>MSE 0.0543 | MAE 0.2523<br>MSE 0.0806 | MAE 0.2688<br>MSE 0.1014 | MAE 0.0524<br>MSE 0.0058 | MAE 0.1442<br>MSE 0.0375 |
| Mono and Poly | MAE 0.0698<br>MSE 0.0095 | MAE 0.0748<br>MSE 0.0108 | MAE 0.0864<br>MSE 0.0119 | MAE 0.0777<br>MSE 0.0093 | MAE 0.1000<br>MSE 0.0162 | MAE 0.0698<br>MSE 0.0095 | MAE 0.0748<br>MSE 0.0108 |
| Mono and Poly Balanced | MAE 0.0778<br>MSE 0.0113 | MAE 0.0681<br>MSE 0.0092 | MAE 0.0677<br>MSE 0.0083 | MAE 0.0664<br>MSE 0.0078 | MAE 0.0712<br>MSE 0.0095 | MAE 0.0686<br>MSE 0.0103 | MAE 0.0681<br>MSE 0.0092 |

Overall, it is evident that the feature-based models generally yield inferior results compared to the CNN models. Nonetheless, the obtained results still demonstrate

satisfactory performance, with a mean MAE of 0.06. Notably, there is a significant disparity observed between the performance of the Mono-3 and Mono-4 models, indicating the efficacy of the patterns learned during their training phase for classifying other types of PV cells. This underscores the capability of feature-based regression to mitigate the influence of PV cell structure on performance. However, a noticeable distinction persists between the Mono and Poly models, highlighting the inability of the feature-based approach to completely mitigate the impact of PV cell surface characteristics.

#### Convolutional Hierarchical Mixture of Experts

As demonstrated, achieving satisfactory performance necessitates training models with images representing all types of PV cells. While employing an abstraction method like feature extraction somewhat alleviates this reliance, it also significantly diminishes model performance. The inherent specialization of the models poses a challenge, as they struggle to handle other types of PV cells effectively. However, this characteristic can be harnessed to develop a more sophisticated model capable of better handling diverse PV types. This can be accomplished by training the model with a combination of images representing various PV cell configurations.

The Convolutional Hierarchical Mixture of Experts (CHME) model is structured around training specialized networks with their corresponding datasets while maintaining a tripartite division into Train, Validation, and Test sets. Evaluation across all Test sets derived from the utilized datasets (Mono-3, Mono-4, and Poly Complete) yielded an MAE of 0.0262 and an MSE of 0.0012. These metrics exhibit a slight improvement over the results achieved by the Mono+Poly model as documented in Table 6.24. Fig. 6.46 depicts the Box Plot model comprising all CNN-based models alongside the CHME model, showcasing fewer outliers in comparison to the Mono+Poly and Mono+Poly balanced models, with generally reduced values (excluding one instance), thereby reinforcing its superior performance. The CHME model excels in attaining the optimal performance from each individual model, leveraging them only when the discriminator deems them appropriate. Moreover, it offers several notable advantages, including the capability to assimilate new data without necessitating complete model retraining. In such scenarios, only the discriminator network necessitates retraining, a process shown to be efficient, along with the corresponding network. Introducing a novel PV cell type would require the creation of a new network.

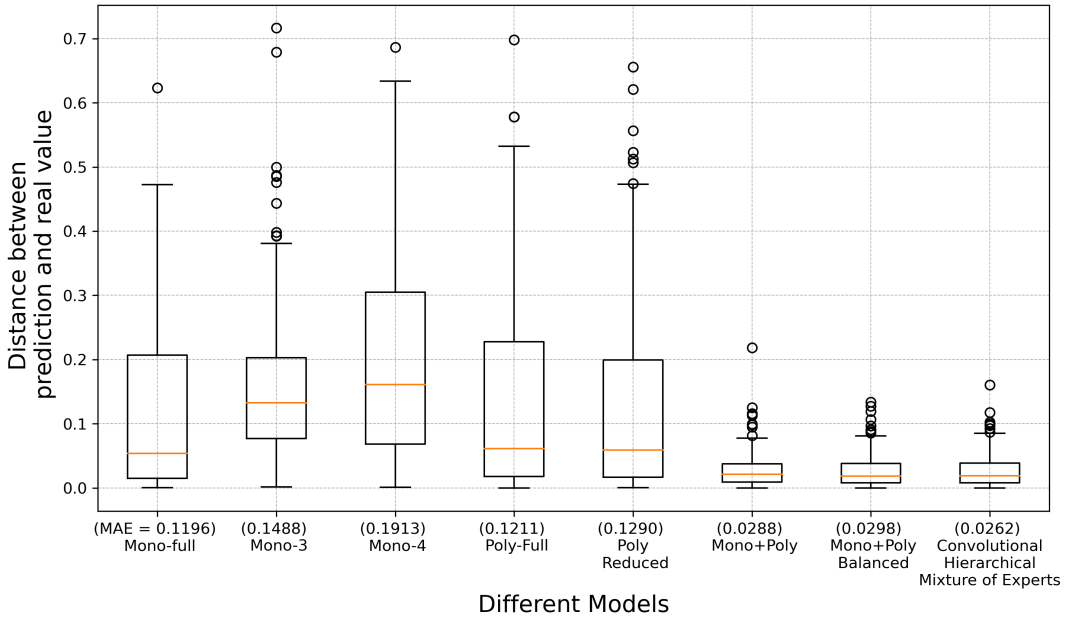


FIGURE 6.46: Box Plot comparing the distance between predictions and real values of all the CNN-based models and the CHME model. The Mean Absolute Error for each model is also provided. Extracted from [17].

### 6.6.7 Summary

The experiment has led to the development of multiple models aimed at determining the optimal approach for assessing the performance of different types of PV cells based on their electroluminescence images. It has been noted that these models are highly specialized, as they are designed to handle specific PV cell technologies used during their training. By leveraging this specialization, it becomes feasible to create a unified model known as the Convolutional Mixture of Experts, which can achieve superior performance compared to a single model trained on diverse types of PV cells.

# Chapter 7

# Discussion

This chapter explains the conclusions obtained from the experiments that have been performed and explained in Chapter 6. This analysis is divided into three different issues: The imbalance in the data that was observed while gathering the data, observing how it affects to the problem. The problem of the Series Resistance Problem that was observed is also discussed. Finally, the performance of the various models proposed are compared.

## 7.1 Effects of the Unbalance in the data

The issue of the unbalance in the data was observed during the gathering of the data (Chapter 5.2), it was observed that a high percentage of labels of the data were between 0.6 and 0.8, giving a low presence to the other values of the domain.

The creation of synthetic data (Chapter 6.1 ) was conceived to solve this issue, providing new examples of underrepresented values. These images have been shown as similar to the original ones performing an analysis or the histogram and with similarity metrics such as Inspection Score (IS) and Fréchet Inception Distance (FID).

Although the synthetic images were proved to be of high quality, it has been seen in the experiments of the feature-based regressor (Chapter 6.2 how their inclusion does not have a critical improvement in the performance of the models. The best model (Gradient Boosting) was found to provide an MSE of 0.00265 while using only the original data versus an MSE of 0.00282. This showed two important facts: It was possible to create a model that provides good performance for the problem (This will be detailed in Section 7.3) and that improvement after including the synthetic data was quite limited.

There are several reasons for the lack of improvement. First of all, these models are quite capable of solving the problem since they provide low error metrics, so it seems that the issue of the unbalance of the data does not impede them from performing well. Another reason of the lack of improvement is that GAN creates data based on the the input data [14], trying to find the patterns to replicate them as exactly as possible. This proves that this kind of method is not suitable for generating new patterns, creating synthetic data too similar to the original, which does not provide new information in the training processes of the models.

The lack of improvement showed that it was not necessary to consider the issue of the unbalance in the following experiments, for this reason, the other models do not use the synthetic dataset. However, it is planned to return to this issue in the future, to try other technologies capable of generating data.

## 7.2 Effects of the Series Resistance Problem

The issue of unexpected values of output power was observed during the recollection of the data (Chapter 5.2). It was seen how cells that did not present any defects or shadows presented unusually low values. After performing the analysis presented in Chapter 6.5, it was concluded that this problem was caused because those PV cells present a higher Series Resistance than the usual values which reduces their performance.

The Wavelet analysis performed provides a new way to analyze the images, since it can detect problems that are not directly visible in the EL image. It has been seen how both CTW analysis and DTW analysis also provided information about Power Spectral Density in each busbar bar. The cells with low MPP exhibited busbars with low density since few electrons are being emitted in those areas.

It was also discovered that the Series Resistance Problem in our datasets were provoked by some incorrect weldings between the PV cells and their busbar bars. This kind of defects was presented in the cells since their manufacture since some new cells also presented this problem.

However, this problem is not extremely critical, since it is only presented in few cells . At that point of the research, it was decided that it was not feasible to include this new problematic in the models trying to solve the problem since it would need to change completely the planning of the experiments. However, it will be important to return to this issue in the future, trying to add information about the resistance to the models in order to improve their performance.

## 7.3 Comparison of the result of the different models

The estimation of the output power of the PV cells was the main objective of the thesis, and all the specific objectives have been chosen to complete it. Two different approaches have been tackled: Considering the problem as a Classification (Chapter 6.3) and as a Regression (Chapters 6.2,6.4,6.6).

### 7.3.1 Classification Approach

The Fuzzy classification was the only algorithm proposed to solve this approach. Of the two proposed models, the Polycrystalline showed an accuracy of 99% and the Monocrystalline an accuracy of 98%. Their results are clearly higher than other tested Machine Learning methods such as Ensemble Classifiers or Decision Trees. This model also has provided several understandable rules that can be used by workers to perform a manual visual inspection of the rules.

It is important to remark that the classification approach reduces severely the complexity of the problem. The amount of information provided by the classification is quite limited in comparison with the information provided a by full estimation of the output power. However, this model is still useful due to its good results and its transparent logic.

### 7.3.2 Regression Approach

The regression Approach was the main focus of the research. The first models that tackled it were the Feature-based models which used manually-configured features obtained from the images to estimate the output power. The best model presented an MAE of 0.0341 and an MSE of 0.0021. It showed that it was possible to solve the problem with a good performance since an MAE of 0.0341 presents an error of around 3.4%, which is an acceptable low value in our context. This model, however, was only tested in the Polycrystalline dataset, since it was the only one available at that moment.

The second wave of models proposed was based on the ANFIS concept combining the capacities of Neural Networks and the transparent logic from Fuzzy Models. It was also based on the manually configured features but limited to three features. The best model obtained an MAE of 0.0535 and an MSE of 0.0073. It could be considered that its performance is considerably low than the previous one, however, it is important to take into account that that model used the first proposal of labelling (See Chapter 5.2). The first proposal had the values extremely focused on certain values, which reduced the real domain of the problem. This model and the following ones use the second proposal, which provides a better-distributed output. This model also provided important information that can be useful for manual inspection or to find new patterns of error in the cells. Similarly to the previous case, only the Polycrystalline set was used.

The last proposed wave of models was based on Convolutional Neural Networks (Chapter 6.6), analyzing the performance of the models depending on the data that was used to train them. The results showed that the models were not capable of obtaining good results with kinds of PV cells different from the ones used in the training process. For example, a model trained only with the Monocrystalline dataset obtained an MAE of 0.0194 in its testing set but it performed an MAE of 0.2159 in the Polycrystalline dataset. This behavior was presented with all the different kinds

of PV cells, showing that it was necessary to train a model in one kind of technology to obtain good results with that technology. The Mixture of Experts approach presented in the same Chapter which combines models trained with each kind of PV cells was able to obtain an MAE of 0.0262 in the Mono+ Poly Dataset. This showed how this model was capable of solving the problem for each of the presented technologies of PV cells, and it had the advantage that it was easily retrainable if new technologies of PV cells were included.

The CNN approach has been found as the best-performing method, however, the other approaches are not useless. The feature-based method provides good performance with a low computer cost in comparison with the approaches that are based on Neural Networks. The ANFIS approach still does not provide a performance at the level of the CNN approach but it provides the basis of its logic with understandable rules. These rules can be used to analyze directly how shadows and defects impact in the production of the PV cells. It is also less computer-demanding than the CNN approach.

Table 7.1 provides a comparison of the time for training for each one of the models. Although the number of samples is not exactly the same in every model it shows how the convolutional models need a considerable amount of time in comparison to the models that use only features. Fuzzy logic does not include a number since the training needs to be done manually, with the knowledment of the experts. ANFIS need a considerable higher time than other feature based models since it uses neural networks but it is still extremely fast compared to CNN.

TABLE 7.1: Comparison of the time needed to train each model. Every experiment was conducted in the same computer.

| model | Random forest | Gradient Boosting | Fuzzy Logic | ANFIS | CNN |
|---|---|---|---|---|---|
| Time | 1 seg | 2 segs | Manual | 120 seg | 120 mins |

# Chapter 8

# Conclusions

In this thesis, we have addressed the issue of estimating the performance of PV cells of various types using their EL images. Some other issues have been tackled along the main objective such as the analysis of the effects of the unbalance in the data and the analysis of the Series Resistance problem that was found. Several solutions have been tested to find the most suitable method for solving the problem.

This chapter contains the main conclusions that have been derived from the research and its main contributions to the field. It also provides some ideas for future work that could be done to obtain better models to solve the problem. Finally, it presents a list of the main achievements and attributions obtained during the thesis.

## 8.1 Conclusions

In this thesis, it has been proved that it is possible to create Artificial Intelligence models trained with EL images and information about the energetic production of PV cells to estimate the production of other PV cells. The results have shown that the better-performing method is the CNN-based, however, this method requires a high amount of data and is extremely computer-demanding needing even a GPU for the training process. Other tested methods have other advantages despite their lower performance that could be useful in certain situations.

The tested methods have an important limitation since they are only capable of working with technologies of PV that have been used in the training process. The approach of creating a Mixture of Experts partially deals with this issue, simplifying the retraining when new kinds of PV cells are added but the problem itself remains the same. However, the model is still vulnerable to the lack of data and has a high computational cost.

The analysis of the unbalance of the data has proved that the unbalance is not a critical issue in our problem and its effect is minimal in the performance of the models. The analysis of the resistance series problem that was observed in some cells showed that it was caused by bad welding between the busbars and the PV cell, this analysis performed with wavelet Transforms provided more information about the the current distribution in the busbar bars than the original EL image.

Another important contribution of this thesis are the datasets that have been created during this thesis. These datasets are important since there are not other datasets in the bibliography that relate the EL image of a PV cell with its energetic

production. The datasets are available for anyone who requests them and include various types of PV cells.

## 8.2 Future Directions

This research still has potential for improvement on several fronts. Firstly, addressing the challenge of incorporating new types of PV cells not encountered during the training phase remains a non-trivial task. While complex, resolving this issue would enhance the versatility of the models.

The issue of unusual power values stemming from series resistance in certain cells has been acknowledged. Currently, it is not factored into the models, and a new approach is required. This involves extracting not only the MPP from the curves but also the resistance value. Models can then be trained to estimate resistance in new cells.

Furthermore, there is a need for more focused attention on the creation of synthetic data. Although our data exhibits similarity to real-world scenarios, this similarity also presents a challenge, as it doesn't introduce enough new information to significantly enhance model performance. Exploring novel techniques to diversify synthetic data and improve its impact on the models is crucial.

The logical next would be addressing this issue in a PV module. It would not be a problem to programally segment a whole module into the various PV that it possesses but it is necessary to determine the way that the performance of each cell impacts the performance of the whole module.

Other interesting possibilities would be the inclusion of new kinds of PV cells, the further optimization of the models using metaheuristics, or improving the system to make it suitable to work a Real Time which is extremely important to apply it in real installations.

## 8.3 Achievements and Attributions

Below is a compilation of contributions to international journals and conferences affiliated with this thesis.

### 8.3.1 Journal Publications

- **JCR Q2** Mateo Romero, H.F.; González Rebollo, M.Á.; Cardeñoso-Payo, V.; Alonso Gómez, V.; Redondo Plaza, A.; Moyo, R.T.; Hernández-Callejo, L. *Applications of Artificial Intelligence to Photovoltaic Systems: A Review*. Appl. Sci. 2022, 12, 10056. https://doi.org/10.3390/app121910056 [11]
- **JCR Q2** Mateo Romero, H.F.; Hernández-Callejo, L.; Rebollo, M.Á.G.; Cardeñoso-Payo, V.; Gómez, V.A.; Bello, H.J.; Moyo, R.T.; Aragonés, J.I.M. *Synthetic Dataset of Electroluminescence Images of Photovoltaic Cells by Deep Convolutional Generative Adversarial Networks*. Sustainability 2023, 15, 7175. https://doi.org/10.3390/su15097175 [59]
- **JCR Q2** Héctor Felipe Mateo Romero, Luis Hernández-Callejo, Miguel Ángel González Rebollo, Valentín Cardeñoso-Payo, Victor Alonso Gómez, Jose Ignacio Morales Aragonés, Ranganai Tawanda Moyo, *Optimized estimator of the*

*output power of PV cells using EL images and IV curves*, Solar Energy, Volume 265, 2023, 112089, ISSN 0038-092X https://doi.org/10.1016/j.solener.2023.112089 [162]

- **Accepted article in process of publication** Héctor Felipe Mateo Romero,Mario Carbonó deal Rosa, Luis Hernández-Callejo, Miguel Ángel González Rebollo, Valentín Cardeñoso-Payo, Victor Alonso Gómez, Sara Gallardo Saavedra, Jose Ignacio Morales Aragonés. *Enhancing Photovoltaic Cell Classification through Mamdani Fuzzy Logic: A Comparative Study with Machine Learning Approaches Employing Electroluminescence Images* [209]
- **Article in process of publication** Héctor Felipe Mateo Romero,Mario Carbonó deal Rosa, Luis Hernández-Callejo, Miguel Ángel González Rebollo, Valentín Cardeñoso-Payo, Victor Alonso Gómez, Óscar Martinez-Sacristán,Sara Gallardo Saavedra , Adalberto José Ospino Castro. *Enhancing Photovoltaic Cell Performance Evaluation: An Adaptive Neural Fuzzy Inference Modeling Approach.* [73]
- **Article in process of publication** Héctor Felipe Mateo Romero, Luis Hernández-Callejo, Miguel Ángel González Rebollo, Valentín Cardeñoso-Payo, Victor Alonso Gómez, Leonardo Cardinale Villalobos, Jose Ignacio Morales Aragonés,Sara Gallardo Saavedra,Abel Méndez Porras,Mario Carbonò dela Rosa. *Analyzing the effect of different technologies of Photovoltaics cells for predicting the output power from their Electroluminiscence images using Machine Learning.* [17]
- **Article in process of publication** Mario Eduardo Carbonó dela Rosa, Héctor Felipe Mateo-Romero, Luis Hernandez-Callejo, Victor Alonso-Gómezd, Victor Ndeti Ngungu, Rocío Nava, José Ignacio Morales Aragonés, Alberto Redondo Plaza, Miguel Ángel González-Rebollo and Valentín Cardeñoso-Payo *Detection of Connection Failures in the Busbar of Poly-Si Photovoltaic Cells Using Two-Dimensional Wavelet Analysis of Electroluminescence Images.* [182]

### 8.3.2 Conference Publications

- Mateo-Romero, H.F. et al. (2022). *Photovoltaic Cells Defects Classification by Means of Artificial Intelligence and Electroluminescence Images.* In: Nesmachnow, S., Hernández Callejo, L. (eds) Smart Cities. ICSC-Cities 2021. Communications in Computer and Information Science, vol 1555. Springer, Cham. https://doi.org/10.1007/978-3-030-96753-6_3 [216]
- Mateo-Romero, H.F. et al. (2023). *Synthetic Dataset of Electroluminescence Images of Photovoltaic Cells by Deep Convolutional Generative Adversarial Networks. In: Nesmachnow, S., Hernández Callejo,* L. (eds) Smart Cities. ICSC-CITIES 2022. Communications in Computer and Information Science, vol 1706. Springer, Cham. https://doi.org/10.1007/978-3-031-28454-0_1 [60]
- Mateo-Romero, H.F. et al. (2024). *Estimation of the Performance of Photovoltaic Cells by Means of an Adaptative Neural Fuzzy Inference Model*. In: Nesmachnow, S., Hernández Callejo, L. (eds) Smart Cities. ICSC-Cities 2023. Communications in Computer and Information Science, vol 1938. Springer, Cham. https://doi.org/10.1007/978-3-031-52517-9_12 [210]
- Mateo-Romero, H.F. et al. (2024). *Enhancing Solar Cell Classification Using Mamdani Fuzzy Logic Over Electroluminescence Images: A Comparative Analysis with Machine Learning Methods*. In: Nesmachnow, S., Hernández Callejo, L. (eds)

Smart Cities. ICSC-Cities 2023. Communications in Computer and Information Science, vol 1938. Springer, Cham.
https://doi.org/10.1007/978-3-031-52517-9_11 [189]

### 8.3.3 Attendances and Participation in Conferences and Workshops

- **International Conference (Online Assistance)** . ICSC-CITIES 2021. IV Ibero-American Congress of Smart Cities CANCUN CENTER, Cancún, México. 29 Nov. to 1 Decem. 2021. http://2021.icsc-cities.com/index.html
- **International Conference (Presential Assistance)**. ICSC-CITIES 2022. V Ibero-American Congress of Smart Cities Campus Balzay, Cuenca, Ecuador. 28-30 Nov. 2022. http://2022.icsc-cities.com/index.html
- **International Conference (Presential Assistance)**. ICSC-CITIES 2023. VI Ibero-American Congress of Smart Cities Mexico City and Cuernavaca, Mexico. 13-17 Nov. 2023. http://2023.icsc-cities.com/index.html
- **National Workshop (Presential Assistance)**. "Jornada: Reto de las energías renovables, eficiencia energética y biodiversidad en el mundo agropecuario" 2022. Campus Duques de Soria, Soria, Spain. 11 July. 2022. http://2023.icsc-cities.com/index.html
- **International Workshop (Online Assistance)**. "Jornadas Agenda Urbana" 2023. Tecnologico of Costa Rica, San Carlos, Costa Rica. 17 October. 2022. http://2023.icsc-cities.com/index.html

### 8.3.4 Research Stays

- **International Stay (3 Months)**
  - **Start Date**: 02/09/2023
  - **End Date**: 05/12/2023
  - **Financing Entity:** "Erasmus+ Prácticas" Program Universidad de Valladolid
  - **Host Institution:** Campus de San Carlos Técnologico de Costa Rica, San Carlos, Costa Rica.
  - **Summary:** The objective of the stay was to create an Artificial Intelligence model based on Machine Learning capable of calculating the performance of photovoltaic cells regardless of the cell type. In contrast to other works found in the literature, this method was trained with different types of photovoltaic cells to create a model that can identify the energy production of a cell based on its electroluminescence (EL) image.
- **National Stay (3 Months)**
  - **Start Date**: 01/05/2024
  - **End Date**: 31/07/2024
  - **Financing Entity:** Predoctoral short-term fellowship 2024 from the Univerdad de Valladolid (Movilidad doctorandos ayudas para estancias breves en el desarrollo de tesis doctoralesConvocatoria 2024)

  - **Host Institution:** Facultad de Informática. Universidad de Murcia, España.
  - **Summary:** The objective of the stay was to create an Artificial Intelligence model based on Machine Learning capable of calculating the performance of photovoltaic cells regardless of the cell type. In contrast to other works found in the literature, this method was trained with different types of photovoltaic cells to create a model that can identify the energy production of a cell based on its electroluminescence (EL) image.

- **International Stay (5 days)**
  - **Start Date**: 30/05/2022
  - **End Date**: 03/06/2022
  - **Financing Entity:** Erasmus+ K107 Grants for Research Stays of 5 days outside the European Union)
  - **Host Institution:** Universum College, Kosovo.
  - **Summary:** The objective of the stay was to meet experts of the field in the country, learn about how they use certain Artificial Intelligence Techniques and create contacts.

- **International Stay (5 days)**
  - **Start Date**: 12/12/2023
  - **End Date**: 16/12/2023
  - **Financing Entity:** Erasmus+ K131 Grants for Research Stays of 5 days in the European Union)
  - **Host Institution:** Instituto Politenico de Bragança, Bragança, Portugal.
  - **Summary:** The objective of the stay was to engage with experts in the field within the country, gain insights into their utilization of specific Artificial Intelligence techniques, and tech the students of the university about the topic of the thesis.

- **International Stay (5 days)**
  - **Start Date**: 15/05/2023
  - **End Date**: 19/05/2023
  - **Financing Entity:** Erasmus+ K107 Grants for Research Stays of 5 days outside the European Union)
  - **Host Institution:** University Donja Gorica, Montenegro.
  - **Summary:** The objective of the stay was to engage with experts in the field within the country, gain insights into their utilization of specific Artificial Intelligence techniques, and establish professional connections.

### 8.3.5 Attributions

- **One of the best articles** at VI Ibero-American Congress of Smart Cities Mexico City and Cuernavaca, Mexico. 13-17 Nov. 2023: Estimation of the Performance of Photovoltaic Cells by Means of an Adaptative Neural Fuzzy Inference Model. http://2023.icsc-cities.com/index.html

### 8.3.6 Funding

The research carried out during this thesis has been facilitated by the following research projects and grants:

- **Title:** Predoctoral Research Contracts 2020 from the Universidad de Valladolid
  - **Beneficiary:** Héctor Felipe Mateo Romero
  - **Start Date:** 01/11/2021
  - **End Date:** 31/10/2025
  - **Financing Entity**: Universidad de Valladolid (Spain)
- Title: Doctor-PV
  - **Beneficiary:** Miguel Ángel Gonzalez Rebollo and Óscar Martínez Sacristán
  - **Project Number:** RTC-2017-6712-3
  - **Start Date:** 01/07/2018
  - **End Date:** 31/12/2021
  - **Financing Entity**: Ministerio de Economia, Industria y Competitividad
- **Title:** *Ayudas a la investigation desarrollada en el curso 2021-2022*
  - **Beneficiary:** Héctor Felipe Mateo Romero
  - **Start Date:** 01/11/2021
  - **End Date:** 30/07/2022
  - **Financing Entity**: Catedra Ciencia e Innovacion Caja Rural de Soria (Spain)
- **Title:** *Grant to attend to congresses during the development of the thesis (AYUDAS MOVILIDAD DOCTORADO 2022)*
  - **Beneficiary:** Héctor Felipe Mateo Romero
  - **Start Date:** 28/11/2022
  - **End Date:** 30/11/2022
  - **Financing Entity**: Universidad de Valladolid (Spain)
- **Title:** *Erasmus+ Practicas grant for international stays in companies or universities*
  - **Beneficiary:** Héctor Felipe Mateo Romero
  - **Start Date:** 02/09/2023
  - **End Date:** 05/12/2023
  - **Financing Entity**: Universidad de Valladolid (Spain)

- **Title:** *Grant to attend to congresses during the development of the thesis (AYUDAS MOVILIDAD DOCTORADO 2023)*
  - **Beneficiary:** Héctor Felipe Mateo Romero
  - **Start Date:** 13/11/2023
  - **End Date:** 17/11/2023
  - **Financing Entity**: Universidad de Valladolid (Spain)
- **Title:** *Erasmus + K107 Grants for 1 week stays outside the European Union 2021-2022*
  - **Beneficiary:** Héctor Felipe Mateo Romero
  - **Start Date:** 30/05/2022
  - **End Date:** 03/06/2022
  - **Financing Entity**: Universidad de Valladolid (Spain)
- **Title:** *Erasmus + K131 Grants for 1 week stays in the European Union 2022-2023*
  - **Beneficiary:** Héctor Felipe Mateo Romero
  - **Start Date:** 12/12/2022
  - **End Date:** 19/12/2022
  - **Financing Entity**: Universidad de Valladolid (Spain)
- **Title:** *Erasmus + K107 Grants for 1 week stays outside the European Union 2022-2023*
  - **Beneficiary:** Héctor Felipe Mateo Romero
  - **Start Date:** 15/05/2023
  - **End Date:** 19/05/2023
  - **Financing Entity**: Universidad de Valladolid (Spain)

### 8.3.7 Datasets

The following datasets have been created and are available to the public at previous request:

- **Dataset of Polycrystalline Cells**: Composed of 785 EL images of Polycrystalline cells with 4 busbars. Information about their production with the two different labeling methods is also provided.
- **Dataset of Monocrystalline Cells with 3 busbars**: Composed of 398 EL images of Monocrystalline cells with 3 busbars. Information about their production with the two different labeling methods is also provided.
- **Dataset of Monocrystalline Cells with 4 busbars**: Composed of 168 EL images of Monocrystalline cells with 4 busbars. Information about their production with the two different labeling methods is also provided.

- **Synthetic dataset of Polycrystalline Cells**: Composed of 10000 EL images of Polycrystalline cells with 4 busbars. Information about their production with the first labeling method is also provided.

# Bibliography


[1] H. Ritchie, P. Rosado, and M. Roser, "Energy production and consumption", *Our World in Data*, 2020. [Online]. Available: https://ourworldindata.org/energy-production-consumption.

[2] IEA, *Net Zero by 2050*. International Energy Agency, 2021.

[3] IRENA, *Renewable capacity statistics 2023*. International Renewable Energy Agency, 2023.

[4] A. S. Al-Ezzi and M. N. M. Ansari, "Photovoltaic solar cells: A review", *Applied System Innovation*, vol. 5, no. 4, 2022, ISSN: 2571-5577. DOI: 10.3390/asi5040067. [Online]. Available: https://www.mdpi.com/2571-5577/5/4/67.

[5] W. Chen, X. Li, Q. Ji, X. Pei, Z. Wang, and F. He, "A dynamic and combined maintenance strategy for photovoltaic power plants considering the dependencies and availability of components", *ELECTRICAL ENGINEERING*, vol. 104, no. 6, pp. 3779–3792, Dec. 2022, ISSN: 0948-7921. DOI: 10.1007/s00202-022-01576-7.

[6] F. Spertino, E. Chiodo, A. Ciocia, G. Malgaroli, and A. Ratclif, "Maintenance activity, reliability, availability, and related energy losses in ten operating photovoltaic systems up to 1.8 mw", *IEEE TRANSACTIONS ON INDUSTRY APPLICATIONS*, vol. 57, no. 1, pp. 83–93, Jan. 2021, 19th IEEE International Conference on Environment and Electrical Engineering (EEEIC) / 3rd IEEE Industrial and Commercial Power Systems Europe Conference (I and CPS Europe), Univ Genoa, Genova, ITALY, JUN 10-14, 2019, ISSN: 0093-9994. DOI: 10.1109/TIA.2020.3031547.

[7] S. Canada, L. Moore, H. Post, and J. Strachan, "Operation and maintenance field experience for off-grid residential photovoltaic systems", *Progress in Photovoltaics: Research and Applications*, vol. 13, pp. 67–74, Jan. 2005. DOI: 10.1002/pip.573.

[8] L. Pratt, D. Govender, and R. Klein, "Defect detection and quantification in electroluminescence images of solar pv modules using u-net semantic segmentation", *Renewable Energy*, vol. 178, pp. 1211–1222, 2021, ISSN: 0960-1481. DOI: https://doi.org/10.1016/j.renene.2021.06.086. [Online]. Available: https://www.sciencedirect.com/science/article/pii/S0960148121009526.

[9] T. Hussain, M. Hussain, H. Al-Aqrabi, T. Alsboui, and R. Hill, "A review on defect detection of electroluminescence-based photovoltaic cell surface images using computer vision", *Energies*, vol. 16, no. 10, 2023, ISSN: 1996-1073. DOI: 10.3390/en16104012. [Online]. Available: https://www.mdpi.com/1996-1073/16/10/4012.

[10] D.-M. Tsai, S.-C. Wu, and W.-C. Li, "Defect detection of solar cells in electroluminescence images using fourier image reconstruction", *Renewable Energy*, 2012. DOI: 10.1016/j.solmat.2011.12.007. [Online]. Available: www.elsevier.com/locate/solmat.

[11] H. F. Mateo Romero, M. A. Gonzalez Rebollo, V. Cardenoso Payo, *et al.*, "Applications of artificial intelligence to photovoltaic systems: A review", *Applied Sciences*, vol. 12, no. 19, 2022, ISSN: 2076-3417. DOI: 10.3390/app121910056.

[12] M. Hoffmann, J. Hepp, B. Doll, *et al.*, "Module-power prediction from pl measurements using deep learning", *Conference Record of the IEEE Photovoltaic Specialists Conference*, pp. 827–830, Jun. 2021, ISSN: 01608371. DOI: 10.1109/PVSC43889.2021.9519005.

[13] M. Hoffmann, C. Buerhop-Lutz, L. Reeb, *et al.*, "Deep-learning-based pipeline for module power prediction from electroluminescense measurements", *Progress in Photovoltaics: Research and Applications*, vol. 29, pp. 920–935, 8 Aug. 2021, ISSN: 1099-159X. DOI: 10.1002/PIP.3416.

[14] I. J. Goodfellow, J. Pouget-Abadie, M. Mirza, *et al.*, *Generative adversarial networks*, 2014. arXiv: 1406.2661 [stat.ML].

[15] M. Thirugnanasambandam, S. Iniyan, and R. Goic, "A review of solar thermal technologies", *Renewable and Sustainable Energy Reviews*, vol. 14, no. 1, pp. 312–322, 2010, ISSN: 1364-0321. DOI: https://doi.org/10.1016/j.rser.2009.07.014. [Online]. Available: https://www.sciencedirect.com/science/article/pii/S1364032109001750.

[16] B. Parida, S. Iniyan, and R. Goic, "A review of solar photovoltaic technologies", *Renewable and Sustainable Energy Reviews*, vol. 15, no. 3, pp. 1625–1636, 2011, ISSN: 1364-0321. DOI: https://doi.org/10.1016/j.rser.2010.11.032. [Online]. Available: https://www.sciencedirect.com/science/article/pii/S1364032110004016.

[17] H. F. Mateo-Romero, L. Hernández-Callejo, M. Á. González-Rebollo, *et al.*, "Analyzing the effect of different technologies of photovoltaics cells for predicting the output power from their electroluminiscence images using machine learning.", *(In Review) Engineering Applications of Artificial Intelligence*, 2024.

[18] M. Köntges, S. Kurtz, C. Packard, *et al.*, "Review of failures of photovoltaic modules", IEA International Energy Agency, Tech. Rep., 2014.

[19] S. Gallardo-Saavedra, L. Hernández-Callejo, and O. Duque-Perez, "Technological review of the instrumentation used in aerial thermographic inspection of photovoltaic plants", *Renewable and Sustainable Energy Reviews*, vol. 93, pp. 566–579, 2018, ISSN: 1364-0321. DOI: https://doi.org/10.1016/j.rser.2018.05.027. [Online]. Available: https://www.sciencedirect.com/science/article/pii/S1364032118303708.

[20] L. Koester, S. Lindig, A. Louwen, A. Astigarraga, G. Manzolini, and D. Moser, "Review of photovoltaic module degradation, field inspection techniques and techno-economic assessment", *Renewable and Sustainable Energy Reviews*, vol. 165, p. 112 616, 2022, ISSN: 1364-0321. DOI: https://doi.org/10.1016/j.rser.2022.112616. [Online]. Available: https://www.sciencedirect.com/science/article/pii/S136403212200510X.

[21] T. Trupke, B. Mitchell, J. Weber, W. McMillan, R. Bardos, and R. Kroeze, "Photoluminescence imaging for photovoltaic applications", *Energy Procedia*, vol. 15, pp. 135–146, 2012, International Conference on Materials for Advanced Technologies 2011, Symposium O, ISSN: 1876-6102. DOI: https://doi.org/10.1016/j.egypro.2012.02.016. [Online]. Available: https://www.sciencedirect.com/science/article/pii/S1876610212003529.

[22] V. Vapnik, "Statistical learning theory", *Wiley*, 1998.

[23] C. Cortes and V. Vapnik, "Support-vector networks", *Machine learning*, vol. 20, no. 3, pp. 273–297, 1995.

[24] C. J. Burges, "Tutorial on support vector machines for pattern recognition", *Data mining and knowledge discovery*, vol. 2, no. 2, pp. 121–167, 1998.
[25] T. Joachims, "Text categorization with support vector machines: Learning with many relevant features", *Machine learning: ECML-98*, pp. 137–142, 1998.
[26] C. Cortes and V. Vapnik, "Support vector networks", *Machine learning*, vol. 20, no. 3, pp. 273–297, 1999.
[27] M. P. Brown, W. N. Grundy, D. Lin, *et al.*, "Support vector machines in bioinformatics", *Journal of computational biology*, vol. 7, no. 3-4, pp. 601–614, 2000.
[28] H. Drucker, C. J. Burges, L. Kaufman, A. J. Smola, and V. N. Vapnik, "Support vector regression machines", *Advances in neural information processing systems*, pp. 155–161, 1997.
[29] J. Shawe-Taylor and N. Cristianini, "Support vector machines for classification and regression", *Neural networks*, vol. 10, no. 5, pp. 757–760, 2000.
[30] B. E. Boser, I. M. Guyon, and V. N. Vapnik, "A training algorithm for optimal margin classifiers", *Proceedings of the fifth annual workshop on Computational learning theory*, pp. 144–152, 1992.
[31] V. N. Vapnik, "The nature of statistical learning theory", *Springer Science & Business Media*, 1995.
[32] A. J. Smola and B. Schölkopf, "Tutorial on support vector regression", *Statistics and computing*, vol. 14, no. 3, pp. 199–222, 2004.
[33] K. Crammer and Y. Singer, "Algorithmic methods of multiclass classification", *Journal of Machine Learning Research*, vol. 2, no. Dec, pp. 113–141, 2002.
[34] C. E. Rasmussen and C. K. Williams, "Gaussian processes for machine learning", *MIT Press*, 2006.
[35] C. K. Williams and C. E. Rasmussen, "Gaussian processes for machine learning", *IEEE Signal Processing Magazine*, vol. 20, no. 3, pp. 102–104, 2003.
[36] B. Shahriari, K. Swersky, Z. Wang, and R. P. Adams, "Taking the human out of the loop: A review of bayesian optimization", *Proceedings of the IEEE*, vol. 104, no. 1, pp. 148–175, 2016.
[37] N. A. C. Cressie, *Statistics for spatial data*. Wiley, 1993.
[38] A. G. Wilson and R. P. Adams, "Gaussian process regression networks", in *Proceedings of the 31st International Conference on Machine Learning (ICML-14)*, 2014, pp. III–1278.
[39] L. Breiman, "Random forests", *Machine learning*, vol. 45, no. 1, pp. 5–32, 2001.
[40] A. Liaw and M. Wiener, "Classification and regression by randomforest", *R news*, vol. 2, no. 3, pp. 18–22, 2002.
[41] I. Ghorbel and M. A. Omri, "Application of random forest algorithm for financial risk forecasting", *International Journal of Business Information Systems*, vol. 20, no. 1, pp. 101–117, 2015.
[42] J. H. Friedman, "Greedy function approximation: A gradient boosting machine", *Annals of Statistics*, vol. 29, no. 5, pp. 1189–1232, 2001.
[43] T. Chen and C. Guestrin, "Xgboost: A scalable tree boosting system", *Proceedings of the 22nd ACM SIGKDD International Conference on Knowledge Discovery and Data Mining*, pp. 785–794, 2016.
[44] R. Caruana and A. Niculescu-Mizil, "Empirical comparison of supervised learning algorithms", *Proceedings of the 23rd International Conference on Machine Learning*, pp. 161–168, 2006.
[45] G. Chen and C. Guestrin, "Lightgbm: A highly efficient gradient boosting decision tree", *Advances in Neural Information Processing Systems*, vol. 30, pp. 3149–3157, 2017.

[46] R. E. Schapire and Y. Freund, "Boosting: Foundations and algorithms", *MIT Press*, 2012.
[47] Y. LeCun, L. Bottou, Y. Bengio, and P. Haffner, "Gradient-based learning applied to document recognition", *Proceedings of the IEEE*, vol. 86, no. 11, pp. 2278–2324, 1998.
[48] Y. LeCun, L. Bottou, Y. Bengio, and P. Haffner, "Backpropagation applied to handwritten zip code recognition", *Neural Computation*, vol. 1, no. 4, pp. 541–551, 1990.
[49] S. E. Umbaugh, "A tutorial on multilayer perceptrons for neuro-image processing", *IEEE Signal Processing Magazine*, vol. 11, no. 3, pp. 21–30, 1994.
[50] C. C. Aggarwal, *Neural Networks and Deep Learning: A Textbook*. Springer, 2018.
[51] D. E. Rumelhart, G. E. Hinton, and R. J. Williams, "Learning representations by back-propagating errors", *Nature*, vol. 323, no. 6088, pp. 533–536, 1986.
[52] J. L. Elman, "Finding structure in time", *Cognitive Science*, vol. 14, no. 2, pp. 179–211, 1990.
[53] I. Sutskever, O. Vinyals, and Q. V. Le, "Sequence to sequence learning with neural networks", *Advances in neural information processing systems*, vol. 27, pp. 3104–3112, 2014.
[54] A. Graves, A.-r. Mohamed, and G. Hinton, "Speech recognition with deep recurrent neural networks", *IEEE International Conference on Acoustics, Speech and Signal Processing*, pp. 6645–6649, 2013.
[55] S. Hochreiter and J. Schmidhuber, "Long short-term memory", *Neural computation*, vol. 9, no. 8, pp. 1735–1780, 1997.
[56] A. Krizhevsky, I. Sutskever, and G. E. Hinton, "Imagenet classification with deep convolutional neural networks", *Advances in neural information processing systems*, vol. 25, pp. 1097–1105, 2012.
[57] K. Simonyan and A. Zisserman, "Very deep convolutional networks for large-scale image recognition", *arXiv preprint arXiv:1409.1556*, 2014.
[58] G. Litjens, T. Kooi, B. E. Bejnordi, *et al.*, "A survey on deep learning in medical image analysis", *Medical image analysis*, vol. 42, pp. 60–88, 2017.
[59] H. F. Mateo-Romero, L. Hernandez-Callejo, M. A. G. Rebollo, *et al.*, "Synthetic dataset of electroluminescence images of photovoltaic cells by deep convolutional generative adversarial networks", *Sustainability*, vol. 15, no. 9, p. 7175, Apr. 2023, ISSN: 2071-1050. DOI: 10.3390/su15097175.
[60] H. F. M. Romero, M. A. G. Rebollo, V. Cardeñoso-Payo, *et al.*, "Synthetic dataset of electroluminescence images of photovoltaic cells by deep convolutional generative adversarial networks", in *Smart Cities*, S. Nesmachnow and L. Hernández Callejo, Eds., Cham: Springer Nature Switzerland, 2023, pp. 3–16, ISBN: 978-3-031-28454-0.
[61] I. J. Goodfellow, J. Pouget-Abadie, M. Mirza, *et al.*, "Generative Adversarial Networks", *arxiv*, Jun. 2014. DOI: 10.48550/arXiv.1406.2661. [Online]. Available: https://arxiv.org/abs/1406.2661.
[62] J. H. Xue and D. M. Titterington, "Do unbalanced data have a negative effect on LDA?", *Pattern Recognition*, vol. 41, no. 5, pp. 1558–1571, 2008, ISSN: 00313203. DOI: 10.1016/J.PATCOG.2007.11.008.
[63] T. Karras, S. Laine, and T. Aila, "A style-based generator architecture for generative adversarial networks", *IEEE/CVF Conference on Computer Vision and Pattern Recognition (CVPR)*, 2019.
[64] Z. Pan, W. Yu, X. Yi, A. Khan, F. Yuan, and Y. Zheng, "Recent progress on generative adversarial networks (gans): A survey", *IEEE Access*, vol. 7, pp. 36 322–36 333, 2019. DOI: 10.1109/ACCESS.2019.2905015.

[65] A. Radford, L. Metz, and S. Chintala, "Unsupervised Representation Learning with Deep Convolutional Generative Adversarial Networks", *arxiv*, Nov. 2015. [Online]. Available: http://arxiv.org/abs/1511.06434.

[66] L. A. Zadeh, "Fuzzy sets", *Information and Control*, vol. 8, no. 3, pp. 338–353, 1965.

[67] S. Shapiro and T. Kouri Kissel, "Classical Logic", in *The Stanford Encyclopedia of Philosophy*, E. N. Zalta, Ed., Spring 2021, Metaphysics Research Lab, Stanford University, 2021.

[68] E. H. Mamdani, "Applications of fuzzy algorithms for control of a simple dynamic plant", *Proceedings of the IEEE*, vol. 121, pp. 1585–1588, 12 1974, ISSN: 00203270. DOI: 10.1049/PIEE.1974.0328.

[69] T. Takagi and M. Sugeno, "Fuzzy identification of systems and its applications to modeling and control", *IEEE Transactions on Systems, Man, and Cybernetics*, vol. SMC-15, no. 1, pp. 116–132, 1985. DOI: 10.1109/TSMC.1985.6313399.

[70] J.-S. R. Jang, "Anfis: Adaptive-network-based fuzzy inference system", *IEEE Transactions on Systems, Man, and Cybernetics*, vol. 23, no. 3, pp. 665–685, 1993.

[71] J.-S. Jang, "Anfis: Adaptive-network-based fuzzy inference system", *IEEE Transactions on Systems, Man, and Cybernetics*, vol. 23, no. 3, pp. 665–685, 1993. DOI: 10.1109/21.256541.

[72] D. Karaboga and E. Kaya, "Adaptive network based fuzzy inference system (anfis) training approaches: A comprehensive survey", *ARTIFICIAL INTELLIGENCE REVIEW*, vol. 52, no. 4, pp. 2263–2293, Dec. 2019, ISSN: 0269-2821. DOI: 10.1007/s10462-017-9610-2.

[73] H. F. Mateo-Romero, M. E. C. d. Rosa, L. Hernández-Callejo, *et al.*, "Enhancing photovoltaic cell performance evaluation: An adaptive neural fuzzy inference modeling approach", *[Still in review] Progress in Artificial Intelligence*, 2024.

[74] J.-S. R. Jang, C.-T. Sun, and E. Mizutani, "Adaptive-network-based fuzzy inference system", *IEEE Transactions on Systems, Man, and Cybernetics*, vol. 23, no. 3, pp. 665–685, 1993.

[75] J.-S. R. Jang, C.-T. Sun, and E. Mizutani, "Fuzzy modeling using generalized neural networks and kalman filter algorithm", *Proceedings of the IEEE*, vol. 82, no. 3, pp. 450–462, 1994.

[76] S. Mallat, "A theory for multiresolution signal decomposition: The wavelet representation", *IEEE Transactions on Pattern Analysis & Machine Intelligence*, vol. 11, no. 7, pp. 674–693, 1989.

[77] I. Daubechies, *Ten lectures on wavelets*. SIAM, 1992.

[78] V. Strela and A. Walden, "Signal and image denoising via wavelet thresholding: Orthogonal and biorthogonal, scalar and multiple wavelet transforms", Mar. 2001.

[79] Anutam and Rajni, "Comparative analysis of filters and wavelet based thresholding methods for image denoising", pp. 137–148, 2014. DOI: 10.5121/csit.2014.4515.

[80] S. Karasu and Z. Saraç, "The effects on classifier performance of 2d discrete wavelet transform analysis and whale optimization algorithm for recognition of power quality disturbances", *Cognitive Systems Research*, vol. 75, pp. 1–15, 2022, ISSN: 1389-0417. DOI: https://doi.org/10.1016/j.cogsys.2022.05.001. [Online]. Available: https://www.sciencedirect.com/science/article/pii/S1389041722000183.

[81] J. Azpiroz-Leehan and J.-F. Lerallut, "Selection of biorthogonal filters for image compression of mr images using wavelet packets", *Medical Engineering and Physics*, vol. 22, no. 5, pp. 335–343, 2000, ISSN: 1350-4533. DOI: https://doi.org/10.1016/S1350-4533(00)00042-4. [Online]. Available: https://www.sciencedirect.com/science/article/pii/S1350453300000424.

[82] A. W. Jayawardena, A. P. C. Xu, and A. W. K. Li, "Rainfall data simulation by hidden markov model and discrete wavelet transformation", *Stochastic Environmental Research and Risk Assessment*, ISSN: 1436-3259. DOI: 10.1007/s00477-008-0264-0.

[83] J.-P. Antoine and R. Murenzi, "Two-dimensional directional wavelets and the scale-angle representation", *Signal Processing*, vol. 52, no. 3, pp. 259–281, 1996, ISSN: 0165-1684. DOI: https://doi.org/10.1016/0165-1684(96)00065-5. [Online]. Available: https://www.sciencedirect.com/science/article/pii/0165168496000655.

[84] L. C. Wu, L. Z. H. Chuang, D. J. Doong, and C. C. Kao, "Ocean remotely sensed image analysis using two-dimensional continuous wavelet transforms", *International Journal of Remote Sensing*, vol. 32, pp. 8779–8798, 23 Dec. 2011, ISSN: 13665901. DOI: 10.1080/01431161.2010.534511. [Online]. Available: https://www.tandfonline.com/doi/abs/10.1080/01431161.2010.534511.

[85] T. T. Yetayew and T. G. Workineh, "A comprehensive review and evaluation of classical mppt techniques for a photovoltaic system", *Lecture Notes of the Institute for Computer Sciences, Social-Informatics and Telecommunications Engineering, LNICST*, vol. 384, pp. 259–272, 2021, ISSN: 1867822X. DOI: 10.1007/978-3-030-80621-7_19/FIGURES/11. [Online]. Available: https://link.springer.com/chapter/10.1007/978-3-030-80621-7_19.

[86] H. Pallathadka, E. H. Ramirez-Asis, T. P. Loli-Poma, K. Kaliyaperumal, R. J. M. Ventayen, and M. Naved, "Applications of artificial intelligence in business management, e-commerce and finance", *Materials Today: Proceedings*, Jul. 2021, ISSN: 2214-7853. DOI: 10.1016/J.MATPR.2021.06.419.

[87] A. Alshahrani, S. Omer, Y. Su, E. Mohamed, and S. Alotaibi, "The technical challenges facing the integration of small-scale and large-scale pv systems into the grid: A critical review", *Electronics (Switzerland)*, vol. 8, 12 Dec. 2019, ISSN: 20799292. DOI: 10.3390/ELECTRONICS8121443.

[88] L. R. Valer, A. R. Manito, T. B. Ribeiro, R. Zilles, and J. T. Pinho, "Issues in pv systems applied to rural electrification in brazil", *Renewable and Sustainable Energy Reviews*, vol. 78, pp. 1033–1043, Oct. 2017, ISSN: 1364-0321. DOI: 10.1016/J.RSER.2017.05.016.

[89] L. B. Bosman, W. D. Leon-Salas, W. Hutzel, and E. A. Soto, "Pv system predictive maintenance: Challenges, current approaches, and opportunities", *Energies 2020, Vol. 13, Page 1398*, vol. 13, p. 1398, 6 Mar. 2020, ISSN: 1996-1073. DOI: 10.3390/EN13061398. [Online]. Available: https://www.mdpi.com/1996-1073/13/6/1398/htm%20https://www.mdpi.com/1996-1073/13/6/1398.

[90] A. O. Baba, G. Liu, and X. Chen, "Classification and Evaluation Review of Maximum Power Point Tracking Methods", *Sustainable Futures*, vol. 2, p. 100 020, Jan. 2020, ISSN: 2666-1888. DOI: 10.1016/J.SFTR.2020.100020.

[91] M. A. Eltawil and Z. Zhao, "MPPT techniques for photovoltaic applications", *Renewable and Sustainable Energy Reviews*, vol. 25, pp. 793–813, Sep. 2013, ISSN: 1364-0321. DOI: 10.1016/J.RSER.2013.05.022.

[92] A. M. A. Mahmoud, H. M. Mashaly, S. A. Kandil, H. E. Khashab, and M. N. F. Nashed, "Fuzzy logic implementation for photovoltaic maximum power tracking", *IECON 2000: 26TH ANNUAL CONFERENCE OF THE IEEE INDUSTRIAL ELECTRONICS SOCIETY, VOLS 1-4: 21ST CENTURY TECHNOLOGIES AND INDUSTRIAL OPPORTUNITIES*, pp. 735–740, 2000, 26th Annual Conference of the IEEE-Industrial-Electronics-Society, NAGOYA, JAPAN, OCT 22-28, 2000, ISSN: 1553-572X.

[93] X. Qiao, B. Wu, Z. Deng, and Y. You, "Mppt of photovoltaic generation system using fuzzy/pid control", *Electric Power Automation Equipment*, vol. 28, pp. 92–95, Oct. 2008.

[94] J. Hui and X. Sun, "Mppt strategy of pv system based on adaptive fuzzy pid algorithm", *LIFE SYSTEM MODELING AND INTELLIGENT COMPUTING, PT I*, vol. 97, K. Li, S. Ma, and G. W. Irwin, Eds., pp. 220–228, 2010, International Conference on Life System Modeling and Simulation/International Conference on Intelligent Computing for Sustainable Energy and Environment, Wuxi, PEOPLES R CHINA, SEP 17-20, 2010, ISSN: 1865-0929.

[95] T. L. Kottas, A. D. Karlis, and Y. S. Boutalis, "Fuzzy cognitive networks for maximum power point tracking in photovoltaic arrays", *FUZZY COGNITIVE MAPS: ADVANCES IN THEORY, METHODOLOLOGIES, TOOLS AND APPLICATIONS*, vol. 247, G. M, Ed., pp. 231–257, 2010, ISSN: 1434-9922.

[96] M. Adly, H. El-Sherif, and M. Ibrahim, "Maximum power point tracker for a pv cell using a fuzzy agent adapted by the fractional open circuit voltage technique", *IEEE INTERNATIONAL CONFERENCE ON FUZZY SYSTEMS (FUZZ 2011)*, pp. 1918–1922, 2011, IEEE International Conference on Fuzzy Systems (FUZZ 2011), Taipei, TAIWAN, JUN 27-30, 2011, ISSN: 1098-7584.

[97] G. Felix Benjamín, G. Nápoles, R. Falcon, W. Froelich, K. Vanhoof, and R. Bello, "A review on methods and software for fuzzy cognitive maps", *Artificial Intelligence Review*, vol. 52, Oct. 2019. DOI: 10.1007/s10462-017-9575-1.

[98] O. F. Kececioglu, A. Gani, and M. Sekkeli, "Design and hardware implementation based on hybrid structure for mppt of pv system using an interval type-2 tsk fuzzy logic controller", *Energies 2020, Vol. 13, Page 1842*, vol. 13, p. 1842, 7 Apr. 2020, ISSN: 19961073. DOI: 10.3390/EN13071842. [Online]. Available: https://www.mdpi.com/1996-1073/13/7/1842/htm%20https://www.mdpi.com/1996-1073/13/7/1842.

[99] N. Altin, "Single phase grid interactive pv system with mppt capability based on type-2 fuzzy logic systems", *2012 International Conference on Renewable Energy Research and Applications, ICRERA 2012*, 2012. DOI: 10.1109/ICRERA.2012.6477335.

[100] N. Altin, "Interval type-2 fuzzy logic controller based maximum power point tracking in photovoltaic systems", *Advances in Electrical and Computer Engineering*, vol. 13, pp. 65–70, 3 2013. DOI: 10.4316/AECE.2013.03011.

[101] P. Verma, R. Garg, and P. Mahajan, "Asymmetrical interval type-2 fuzzy logic control based mppt tuning for pv system under partial shading condition", *ISA Transactions*, vol. 100, pp. 251–263, May 2020, ISSN: 0019-0578. DOI: 10.1016/J.ISATRA.2020.01.009.

[102] M. Allouche, K. Dahech, and M. Chaabane, "Multiobjective maximum power tracking control of photovoltaic systems: T-s fuzzy model-based approach", *Soft Computing*, vol. 22, pp. 2121–2132, 7 Apr. 2018. DOI: 10.1007/S00500-017-2691-7.

[103] H. Zayani, M. Allouche, M. Kharrat, and M. Chaabane, "T-s fuzzy maximum power point tracking control of photovoltaic conversion system", *16th International Conference on Sciences and Techniques of Automatic Control and Computer Engineering, STA 2015*, pp. 534–539, Jul. 2016. DOI: 10.1109/STA.2015.7505123.

[104] M. Dahmane, J. Bosche, A. El-Hajjaji, and M. Davarifar, "T-s implementation of an mppt algorithm for photovoltaic conversion system using poles placement and h performances", *2013 3rd International Conference on Systems and Control, ICSC 2013*, pp. 1116–1121, 2013. DOI: 10.1109/ICOSC.2013.6750994.

[105] S. Azali and M. Sheikhan, "Intelligent control of photovoltaic system using bpso-gsa-optimized neural network and fuzzy-based pid for maximum power point tracking", *Applied Intelligence*, vol. 44, pp. 88–110, 1 Jan. 2016. DOI: 10.1007/S10489-015-0686-6.

[106] S. Duman, N. Yorukeren, and I. H. Altas, "A novel mppt algorithm based on optimized artificial neural network by using fpsogsa for standalone photovoltaic energy systems", *Neural Computing and Applications*, vol. 29, pp. 257–278, 1 Jan. 2018. DOI: 10.1007/S00521-016-2447-9.

[107] R. Sarkar, J. R. Kumar, R. Sridhar, and S. Vidyasagar, "A new hybrid bat-anfis-based power tracking technique for partial shaded photovoltaic systems", *International Journal of Fuzzy Systems*, vol. 23, pp. 1313–1325, 5 Jul. 2021. DOI: 10.1007/S40815-020-01037-Y.

[108] Naveen and A. K. Dahiya, "Implementation and comparison of perturb observe, ann and anfis based mppt techniques", *Proceedings of the International Conference on Inventive Research in Computing Applications, ICIRCA 2018*, pp. 1–5, Dec. 2018. DOI: 10.1109/ICIRCA.2018.8597271.

[109] A. Arora and P. Gaur, "Comparison of ann and anfis based mppt controller for grid connected pv systems", *12th IEEE International Conference Electronics, Energy, Environment, Communication, Computer, Control: (E3-C3), INDICON 2015*, Mar. 2016. DOI: 10.1109/INDICON.2015.7443568.

[110] S. Padmanaban, N. Priyadarshi, M. S. Bhaskar, J. B. Holm-Nielsen, V. K. Ramachandaramurthy, and E. Hossain, "A hybrid anfis-abc based mppt controller for pv system with anti-islanding grid protection: Experimental realization", *IEEE Access*, vol. 7, pp. 103 377–103 389, 2019, ISSN: 21693536. DOI: 10.1109/ACCESS.2019.2931547.

[111] A. A. Kulaksiz and R. Akkaya, "Training data optimization for anns using genetic algorithms to enhance mppt efficiency of a stand-alone pv system", *Turkish Journal of Electrical Engineering and Computer Sciences*, vol. 20, pp. 241–254, 2 Mar. 2012. DOI: 10.3906/ELK-1101-1051.

[112] C. Larbes, S. M. A. Cheikh, T. Obeidi, and A. Zerguerras, "Genetic algorithms optimized fuzzy logic control for the maximum power point tracking in photovoltaic system", *Renewable Energy*, vol. 34, pp. 2093–2100, 10 Oct. 2009, ISSN: 0960-1481. DOI: 10.1016/J.RENENE.2009.01.006.

[113] A. A. Kulaksiz and R. Akkaya, "A genetic algorithm optimized ann-based mppt algorithm for a stand-alone pv system with induction motor drive", *Solar Energy*, vol. 86, pp. 2366–2375, 9 Sep. 2012, ISSN: 0038-092X. DOI: 10.1016/J.SOLENER.2012.05.006.

[114] M. Azab, "Optimal power point tracking for stand-alone pv system using particle swarm optimization", *IEEE International Symposium on Industrial Electronics*, pp. 969–973, 2010. DOI: 10.1109/ISIE.2010.5637061. [Online]. Available: https://www.researchgate.net/publication/251965535_Optimal_

power_point_tracking_for_stand-alone_PV_system_using_particle_swarm_optimization.

[115] M. Alshareef, Z. Lin, M. Ma, and W. Cao, "Accelerated particle swarm optimization for photovoltaic maximum power point tracking under partial shading conditions", *Energies 2019, Vol. 12, Page 623*, vol. 12, p. 623, 4 Feb. 2019, ISSN: 19961073. DOI: 10.3390/EN12040623. [Online]. Available: https://www.mdpi.com/1996-1073/12/4/623/.

[116] K. Sundareswaran, S. Peddapati, and S. Palani, "Mppt of pv systems under partial shaded conditions through a colony of flashing fireflies", *IEEE Transactions on Energy Conversion*, vol. 29, pp. 463–472, 2 2014, ISSN: 08858969. DOI: 10.1109/TEC.2014.2298237.

[117] A. S. Oshaba, E. S. Ali, and S. M. A. Elazim, "Pi controller design using abc algorithm for mppt of pv system supplying dc motor pump load", *Neural Computing and Applications*, vol. 28, pp. 353–364, 2 Feb. 2017, ISSN: 09410643. DOI: 10.1007/s00521-015-2067-9.

[118] A. soufyane Benyoucef, A. Chouder, K. Kara, S. Silvestre, and O. A. Sahed, "Artificial bee colony based algorithm for maximum power point tracking (mppt) for pv systems operating under partial shaded conditions", *Applied Soft Computing Journal*, vol. 32, pp. 38–48, Jul. 2015, ISSN: 15684946. DOI: 10.1016/j.asoc.2015.03.047.

[119] B. Bilal, "Implementation of artificial bee colony algorithm on maximum power point tracking for pv modules", *2013 - 8th International Symposium on Advanced Topics in Electrical Engineering, ATEE 2013*, 2013. DOI: 10.1109/ATEE.2013.6563495.

[120] H. S. Moreira, J. L. de S Silva, E. Y. P. G. C. S., Sako, M. V. G. dos Reis, and M. G. Villalva, "Comparison of swarm optimization methods for mppt in partially shaded photovoltaic systems", *2019 2ND INTERNATIONAL CONFERENCE ON SMART ENERGY SYSTEMS AND TECHNOLOGIES (SEST 2019)*, 2019, 2nd International Conference on Smart Energy Systems and Technologies (SEST), Porto, PORTUGAL, SEP 09-11, 2019.

[121] M. Habibi and A. Yazdizadeh, "New mppt controller design for pv arrays using neural networks (zanjan city case study)", *ADVANCES IN NEURAL NETWORKS - ISNN 2009, PT 2, PROCEEDINGS*, vol. 5552, W. Yu, H. B. He, and N. Zhng, Eds., pp. 1050–1058, 2009, 6th International Symposium on Neural Networks, Wuhan, PEOPLES R CHINA, MAY 26-29, 2009, ISSN: 0302-9743.

[122] O. Veligorskyi, R. Chakirov, and Y. Vagapov, "Artificial neural network-based maximum power point tracker for the photovoltaic application", *Proceedings of the 2015 1st International Conference on Industrial Networks and Intelligent Systems, INISCom 2015*, pp. 133–138, Jul. 2015. DOI: 10.4108/icst.iniscom.2015.258313.

[123] A. M. Farayola, A. N. Hasan, and A. Ali, "Efficient photovoltaic mppt system using coarse gaussian support vector machine and artificial neural network techniques", *International Journal of Innovative Computing, Information and Control*, vol. 14, pp. 323–339, 1 Feb. 2018. DOI: 10.24507/IJICIC.14.01.323.

[124] S. D. Al-Majidi, M. F. Abbod, and H. S. Al-Raweshidy, "A particle swarm optimisation-trained feedforward neural network for predicting the maximum power point of a photovoltaic array", *Engineering Applications of Artificial Intelligence*, vol. 92, Jun. 2020. DOI: 10.1016/J.ENGAPPAI.2020.103688.

[125] B. Babes, A. Boutaghane, and N. Hamouda, "A novel nature-inspired maximum power point tracking (mppt) controller based on aco-ann algorithm for

photovoltaic (pv) system fed arc welding machines", *Neural Computing and Applications*, 2021. DOI: 10.1007/S00521-021-06393-W.

[126] N. Pachaivannan, R. Subburam, M. Padmanaban, and A. Subramanian, "Certain investigations of anfis assisted cpho algorithm tuned mppt controller for pv arrays under partial shading conditions", *Journal of Ambient Intelligence and Humanized Computing*, vol. 12, pp. 9923–9938, 10 Oct. 2021. DOI: 10.1007/S12652-020-02738-W.

[127] D. Mlakic and S. Nikolovski, "Anfis as a method for determinating mppt in the photovoltaic system simulated in matlab/simulink", *2016 39th International Convention on Information and Communication Technology, Electronics and Microelectronics, MIPRO 2016 - Proceedings*, pp. 1082–1086, Jul. 2016. DOI: 10.1109/MIPRO.2016.7522301.

[128] L. Avila, M. D. Paula, M. Trimboli, and I. Carlucho, "Deep reinforcement learning approach for mppt control of partially shaded pv systems in smart grids", *Applied Soft Computing*, vol. 97, Dec. 2020. DOI: 10.1016/J.ASOC.2020.106711.

[129] Martín Abadi, Ashish Agarwal, Paul Barham, *et al.*, *TensorFlow: Large-scale machine learning on heterogeneous systems*, Software available from tensorflow.org, 2015. [Online]. Available: https://www.tensorflow.org/.

[130] S. Sobri, S. Koohi-Kamali, and N. A. Rahim, "Solar photovoltaic generation forecasting methods: A review", *Energy Conversion and Management*, vol. 156, pp. 459–497, Jan. 2018, ISSN: 0196-8904. DOI: 10.1016/J.ENCONMAN.2017.11.019.

[131] T. Senjyu, H. Takara, K. Uezato, and T. Funabashi, "One-hour-ahead load forecasting using neural network", *IEEE Transactions on Power Systems*, vol. 17, pp. 113–118, 1 Feb. 2002, ISSN: 08858950. DOI: 10.1109/59.982201.

[132] D. Caputo, F. Grimaccia, M. Mussetta, and R. E. Zich, "Photovoltaic plants predictive model by means of ann trained by a hybrid evolutionary algorithm", *2010 INTERNATIONAL JOINT CONFERENCE ON NEURAL NETWORKS IJCNN 2010*, 2010, World Congress on Computational Intelligence (WCCI 2010), Barcelona, SPAIN, 2010, ISSN: 2161-4393.

[133] M. Rana, I. Koprinska, and V. G. Agelidis, "Forecasting solar power generated by grid connected pv systems using ensembles of neural networks", *Proceedings of the International Joint Conference on Neural Networks*, vol. 2015-September, Sep. 2015. DOI: 10.1109/IJCNN.2015.7280574.

[134] R. M. Ehsan, S. P. Simon, and P. R. Venkateswaran, "Day-ahead forecasting of solar photovoltaic output power using multilayer perceptron", *Neural Computing and Applications 2016 28:12*, vol. 28, pp. 3981–3992, 12 Apr. 2016, ISSN: 1433-3058. DOI: 10.1007/S00521-016-2310-Z. [Online]. Available: https://link.springer.com/article/10.1007/s00521-016-2310-z.

[135] Z. Li, C. Zang, P. Zeng, H. Yu, and H. Li, "Day-ahead hourly photovoltaic generation forecasting using extreme learning machine", *2015 IEEE INTERNATIONAL CONFERENCE ON CYBER TECHNOLOGY IN AUTOMATION, CONTROL, AND INTELLIGENT SYSTEMS (CYBER)*, pp. 779–783, 2015, IEEE International Conference on Cyber Technology in Automation, Control, and Intelligent Systems (CYBER), Shenyang, PEOPLES R CHINA, JUN 09-12, 2015, ISSN: 2379-7711.

[136] D. M. Quan, E. Ogliari, F. Grimaccia, S. Leva, and M. Mussetta, "Hybrid model for hourly forecast of photovoltaic and wind power", *IEEE International Conference on Fuzzy Systems*, 2013. DOI: 10.1109/FUZZ-IEEE.2013.6622453.

[137] J. F. Torres, A. Troncoso, I. Koprinska, Z. Wang, and F. M. Alvarez, "Big data solar power forecasting based on deep learning and multiple data sources", *Expert Systems*, vol. 36, 4 2019. DOI: 10.1111/EXSY.12394.

[138] I. Koprinska, D. Wu, and Z. Wang, "Convolutional neural networks for energy time series forecasting", *2018 INTERNATIONAL JOINT CONFERENCE ON NEURAL NETWORKS (IJCNN)*, 2018, International Joint Conference on Neural Networks (IJCNN), Rio de Janeiro, BRAZIL, JUL 08-13, 2018, ISSN: 2161-4393.

[139] T. Zhang, C. Lv, F. Ma, K. Zhao, H. Wang, and G. M. O'Hare, "A photovoltaic power forecasting model based on dendritic neuron networks with the aid of wavelet transform", *Neurocomputing*, vol. 397, pp. 438–446, Jul. 2020. DOI: 10.1016/J.NEUCOM.2019.08.105.

[140] P. Mandal, S. T. S. Madhira, A. U. haque, J. Meng, and R. L. Pineda, "Forecasting power output of solar photovoltaic system using wavelet transform and artificial intelligence techniques", *Procedia Computer Science*, vol. 12, pp. 332–337, 2012, ISSN: 18770509. DOI: 10.1016/j.procs.2012.09.080.

[141] Y. Wen, D. AlHakeem, P. Mandal, *et al.*, "Performance evaluation of probabilistic methods based on bootstrap and quantile regression to quantify pv power point forecast uncertainty", *IEEE Transactions on Neural Networks and Learning Systems*, vol. 31, pp. 1134–1144, 4 Apr. 2020. DOI: 10.1109/TNNLS.2019.2918795.

[142] G. Capizzi, C. Napoli, and F. Bonanno, "Innovative second-generation wavelets construction with recurrent neural networks for solar radiation forecasting", *IEEE Transactions on Neural Networks and Learning Systems*, vol. 23, pp. 1805–1815, 11 2012, ISSN: 2162237X. DOI: 10.1109/TNNLS.2012.2216546.

[143] A. Alzahrani, P. Shamsi, C. Dagli, and M. Ferdowsi, "Solar irradiance forecasting using deep neural networks", *Procedia Computer Science*, vol. 114, pp. 304–313, 2017, ISSN: 18770509. DOI: 10.1016/j.procs.2017.09.045.

[144] M. Abdel-Nasser and K. Mahmoud, "Accurate photovoltaic power forecasting models using deep lstm-rnn", *Neural Computing and Applications*, vol. 31, pp. 2727–2740, 7 Jul. 2019, ISSN: 09410643. DOI: 10.1007/s00521-017-3225-z.

[145] X. Yao, Z. Wang, and H. Zhang, "A novel photovoltaic power forecasting model based on echo state network", *Neurocomputing*, vol. 325, pp. 182–189, Jan. 2019. DOI: 10.1016/J.NEUCOM.2018.10.022.

[146] R. D. Leone, M. Pietrini, and A. Giovannelli, "Photovoltaic energy production forecast using support vector regression", *Neural Computing and Applications 2015 26:8*, vol. 26, pp. 1955–1962, 8 Mar. 2015, ISSN: 1433-3058. DOI: 10.1007/S00521-015-1842-Y. [Online]. Available: https://link.springer.com/article/10.1007/s00521-015-1842-y.

[147] B. Wolff, E. Lorenz, and O. Kramer, "Statistical learning for short-term photovoltaic power predictions", *Studies in Computational Intelligence*, vol. 645, pp. 31–45, 2016. DOI: 10.1007/978-3-319-31858-5_3.

[148] R. Nageem and R. Jayabarathi, "Predicting the power output of a grid-connected solar panel using multi-input support vector regression", *Procedia Computer Science*, vol. 115, pp. 723–730, 2017. DOI: 10.1016/J.PROCS.2017.09.143.

[149] M. R. Chen, J. H. Chen, G. Q. Zeng, K. D. Lu, and X. F. Jiang, "An improved artificial bee colony algorithm combined with extremal optimization and boltzmann selection probability", *Swarm and Evolutionary Computation*, vol. 49, pp. 158–177, Sep. 2019. DOI: 10.1016/J.SWEVO.2019.06.005.

[150] M. G. Villalva, J. R. Gazoli, and E. R. Filho, "Comprehensive approach to modeling and simulation of photovoltaic arrays", *IEEE Transactions on Power*

*Electronics*, vol. 24, pp. 1198–1208, 5 2009, ISSN: 08858993. DOI: 10.1109/TPEL.2009.2013862.

[151] Y. Liang, X. Wang, H. Zhao, T. Han, Z. Wei, and Y. Li, "A covariance matrix adaptation evolution strategy variant and its engineering application", *Applied Soft Computing Journal*, vol. 83, Oct. 2019, Parameter estimation. DOI: 10.1016/J.ASOC.2019.105680.

[152] W. Long, T. Wu, J. Jiao, M. Tang, and M. Xu, "Refraction-learning-based whale optimization algorithm for high-dimensional problems and parameter estimation of pv model", *Engineering Applications of Artificial Intelligence*, vol. 89, Mar. 2020. DOI: 10.1016/J.ENGAPPAI.2019.103457.

[153] Y. Zhang, M. Ma, and Z. Jin, "Backtracking search algorithm with competitive learning for identification of unknown parameters of photovoltaic systems", *Expert Systems with Applications*, vol. 160, Dec. 2020. DOI: 10.1016/J.ESWA.2020.113750.

[154] A. Saxena, A. Sharma, and S. Shekhawat, "Parameter extraction of solar cell using intelligent grey wolf optimizer", *Evolutionary Intelligence*, 2020. DOI: 10.1007/S12065-020-00499-1.

[155] H. Rezk, J. Arfaoui, and M. R. Gomaa, "Optimal parameter estimation of solar pv panel based on hybrid particle swarm and grey wolf optimization algorithms", *International Journal of Interactive Multimedia and Artificial Intelligence*, vol. 6, pp. 145–155, 6 2021. DOI: 10.9781/IJIMAI.2020.12.001.

[156] M. Li, C. Li, Z. Huang, J. Huang, G. Wang, and P. X. Liu, "Spiral-based chaotic chicken swarm optimization algorithm for parameters identification of photovoltaic models", *Soft Computing*, vol. 25, pp. 12 875–12 898, 20 Oct. 2021. DOI: 10.1007/S00500-021-06010-X.

[157] X. Yang and W. Gong, "Opposition-based jaya with population reduction for parameter estimation of photovoltaic solar cells and modules", *Applied Soft Computing*, vol. 104, Jun. 2021. DOI: 10.1016/J.ASOC.2021.107218.

[158] M. A. E. Sattar, A. A. Sumaiti, H. Ali, and A. A. Diab, "Marine predators algorithm for parameters estimation of photovoltaic modules considering various weather conditions", *Neural Computing and Applications*, vol. 33, pp. 11 799–11 819, 18 Sep. 2021. DOI: 10.1007/S00521-021-05822-0.

[159] S. Yang, N. Max, S. Xie, L. Li, and T. Zhao, "Photovoltaic cell model parameter optimization using micro-charge field effect p systems", *Engineering Applications of Artificial Intelligence*, vol. 104, Sep. 2021. DOI: 10.1016/J.ENGAPPAI.2021.104374.

[160] M. U. Siddiqui and M. Abido, "Parameter estimation for five- and seven-parameter photovoltaic electrical models using evolutionary algorithms", *Applied Soft Computing Journal*, vol. 13, pp. 4608–4621, 12 2013, ISSN: 15684946. DOI: 10.1016/j.asoc.2013.07.005.

[161] MATLAB, *version 7.10.0 (R2010a)*. Natick, Massachusetts: The MathWorks Inc., 2010.

[162] H. F. M. Romero, L. Hernandez-Callejo, M. A. G. Rebollo, *et al.*, "Optimized estimator of the output power of pv cells using el images and iv curves", *Solar Energy*, vol. 265, p. 112 089, 2023, ISSN: 0038-092X. DOI: https://doi.org/10.1016/j.solener.2023.112089.

[163] B. Nian, Z. Fu, L. Wang, and X. Cao, "Automatic detection of defects in solar modules: Image processing in detecting", *2010 6th International Conference on Wireless Communications, Networking and Mobile Computing, WiCOM 2010*, 2010, <br/>. DOI: 10.1109/WICOM.2010.5600703.

[164] S. A. Anwar and M. Z. Abdullah, "Micro-crack detection of multicrystalline solar cells featuring shape analysis and support vector machines", *Proceedings - 2012 IEEE International Conference on Control System, Computing and Engineering, ICCSCE 2012*, pp. 143–148, 2012. DOI: 10.1109/ICCSCE.2012.6487131.

[165] S. Deitsch, C. Buerhop-Lutz, E. Sovetkin, *et al.*, "Segmentation of photovoltaic module cells in uncalibrated electroluminescence images", *Machine Vision and Applications*, vol. 32, 4 Jun. 2018. DOI: 10.1007/s00138-021-01191-9. [Online]. Available: http://arxiv.org/abs/1806.06530%20http://dx.doi.org/10.1007/s00138-021-01191-9.

[166] A. M. Karimi, J. S. Fada, J. Liu, J. L. Braid, M. Koyuturk, and R. H. French, "Feature extraction, supervised and unsupervised machine learning classification of pv cell electroluminescence images", *2018 IEEE 7th World Conference on Photovoltaic Energy Conversion, WCPEC 2018 - A Joint Conference of 45th IEEE PVSC, 28th PVSEC and 34th EU PVSEC*, pp. 418–424, Nov. 2018. DOI: 10.1109/PVSC.2018.8547739.

[167] A. Bartler, L. Mauch, B. Yang, M. Reuter, and L. Stoicescu, "Automated detection of solar cell defects with deep learning", *European Signal Processing Conference*, vol. 2018-September, pp. 2035–2039, Nov. 2018, ISSN: 22195491. DOI: 10.23919/EUSIPCO.2018.8553025.

[168] A. M. Karimi, J. S. Fada, M. A. Hossain, *et al.*, "Automated pipeline for photovoltaic module electroluminescence image processing and degradation feature classification", *IEEE Journal of Photovoltaics*, vol. 9, pp. 1324–1335, 5 Sep. 2019, ISSN: 21563403. DOI: 10.1109/JPHOTOV.2019.2920732.

[169] Z. Ying, M. Li, W. Tong, and C. Haiyong, "Automatic detection of photovoltaic module cells using multi-channel convolutional neural network", *Proceedings 2018 Chinese Automation Congress, CAC 2018*, pp. 3571–3576, Jan. 2019. DOI: 10.1109/CAC.2018.8623258. [Online]. Available: https://www.researchgate.net/publication/331426567_Automatic_Detection_of_Photovoltaic_Module_Cells_using_Multi-Channel_Convolutional_Neural_Network.

[170] M. W. Akram, G. Li, Y. Jin, *et al.*, "Cnn based automatic detection of photovoltaic cell defects in electroluminescence images", *Energy*, vol. 189, p. 116 319, Dec. 2019, ISSN: 0360-5442. DOI: 10.1016/J.ENERGY.2019.116319.

[171] J. Balzategui, L. Eciolaza, and N. Arana-Arexolaleiba, "Defect detection on Polycrystalline solar cells using Electroluminescence and Fully Convolutional Neural Networks", *Proceedings of the 2020 IEEE/SICE International Symposium on System Integration, SII 2020*, pp. 949–953, Jan. 2020. DOI: 10.1109/SII46433.2020.9026211.

[172] N. Mathias, F. Shaikh, C. Thakur, S. Shetty, P. Dumane, and D. S. Chavan, "Detection of micro-cracks in electroluminescence images of photovoltaic modules", *SSRN Electronic Journal*, Apr. 2020, ISSN: 1556-5068. DOI: 10.2139/SSRN.3563821. [Online]. Available: https://papers.ssrn.com/abstract=3563821.

[173] B. Su, H. Chen, P. Chen, G. Bian, K. Liu, and W. Liu, "Deep learning-based solar-cell manufacturing defect detection with complementary attention network", *IEEE Transactions on Industrial Informatics*, vol. 17, pp. 4084–4095, 6 Jun. 2021, ISSN: 19410050. DOI: 10.1109/TII.2020.3008021.

[174] M. Y. Demirci, N. Beli, and A. Gümüçü, "Efficient deep feature extraction and classification for identifying defective photovoltaic module cells in Electroluminescence images", *Expert Systems with Applications*, vol. 175, Aug. 2021, ISSN: 09574174. DOI: 10.1016/j.eswa.2021.114810.

[175] B. Su, H. Chen, P. Chen, G. Bian, K. Liu, and W. Liu, "Deep Learning-Based Solar-Cell Manufacturing Defect Detection with Complementary Attention Network", *IEEE Transactions on Industrial Informatics*, vol. 17, no. 6, pp. 4084–4095, Jun. 2021, ISSN: 19410050. DOI: 10.1109/TII.2020.3008021.

[176] C. Shou, L. Hong, W. Ding, *et al.*, "Defect Detection with Generative Adversarial Networks for Electroluminescence Images of Solar Cells", in *2020 35th Youth Academic Annual Conference of Chinese Association of Automation (YAC)*, IEEE, Oct. 2020, pp. 312–317, ISBN: 978-1-7281-7684-0. DOI: 10.1109/YAC51587.2020.9337676. [Online]. Available: https://ieeexplore.ieee.org/document/9337676/.

[177] Z. Luo, S. Y. Cheng, and Q. Y. Zheng, "GAN-Based Augmentation for Improving CNN Performance of Classification of Defective Photovoltaic Module Cells in Electroluminescence Images", *IOP Conference Series: Earth and Environmental Science*, vol. 354, no. 1, p. 012 106, Oct. 2019, ISSN: 1755-1307. DOI: 10.1088/1755-1315/354/1/012106. [Online]. Available: https://iopscience.iop.org/article/10.1088/1755-1315/354/1/012106.

[178] A. Creswell, T. White, V. Dumoulin, K. Arulkumaran, B. Sengupta, and A. A. Bharath, "Generative Adversarial Networks: An Overview", *IEEE Signal Processing Magazine*, vol. 35, no. 1, pp. 53–65, Oct. 2017, ISSN: 1053-5888. DOI: 10.1109/MSP.2017.2765202. [Online]. Available: http://arxiv.org/abs/1710.07035.

[179] J. Schreiber, M. Jessulat, and B. Sick, "Generative Adversarial Networks for Operational Scenario Planning of Renewable Energy Farms: A Study on Wind and Photovoltaic", in *Artificial Neural Networks and Machine Learning ICANN 2019: Image Processing: 28th International Conference on Artificial Neural Networks, Munich, Germany, September 1719, 2019, Proceedings, Part III*, 2019, pp. 550–564. DOI: 10.1007/978-3-030-30508-6_44. [Online]. Available: http://link.springer.com/10.1007/978-3-030-30508-6%7B%5C_%7D44.

[180] M. Li, J. Fioresi, N. K. Pannaci, and K. O. Davis, "Improving the accuracy of pixel-level defect classification of electroluminescence images", in *2021 IEEE 48th Photovoltaic Specialists Conference (PVSC)*, 2021, pp. 1458–1459. DOI: 10.1109/PVSC43889.2021.9518567.

[181] J. I. Morales-Aragonés, V. A. Gómez, S. Gallardo-Saavedra, A. Redondo-Plaza, D. Fernández-Martínez, and L. Hernández-Callejo, "Low-cost three-quadrant single solar cell i-v tracer", *Applied Sciences*, vol. 12, no. 13, 2022, ISSN: 2076-3417. DOI: 10.3390/app12136623.

[182] M. E. C. dela Rosa, H. F. M. Romero, L. H. Callejo, *et al.*, "Detection of connection failures in the busbar of poly-si photovoltaic cells using two-dimensional wavelet analysis of electroluminescence images", *[Still in review] Computers and Electrical Engineering*, 2024.

[183] European Network of Excellence in Knowledge Discovery in Databases (Eurika), "CRISP-DM: Cross-Industry Standard Process for Data Mining", European Network of Excellence in Knowledge Discovery in Databases (Eurika), Tech. Rep., 1999.

[184] D. T. Campbell and J. C. Stanley, *Experimental and Quasi-Experimental Designs for Research*. Boston: Houghton Mifflin, 1963.

[185] B. Zhou, M. Ha, and C. Wang, "An improved algorithm of unbalanced data svm", in *FUZZY INFORMATION AND ENGINEERING 2010, VOL 1*, B. Cao, G. Wang, S. Guo, and S. Chen, Eds., ser. Advances in Intelligent and Soft Computing, 5th Annual Conference on Fuzzy Information and Engineering, Huludao, PEOPLES R CHINA, SEP 23-27, 2010, Liaoning Technol Univ;

China Operat Res Soc, Fuzzy Informat & Engn Branch; Int Inst Gen Syst Studies, Fuzzy Informat & Engn Branch, vol. 78, 2010, pp. 549+, ISBN: 978-3-642-14879-8.

[186] W. Gan, J. Geng, Y. Wang, *et al.*, "Effects of Unbalanced Data on Radiometric Transforming Model Fitting for Relative Radiometric Normalization", *International Geoscience and Remote Sensing Symposium (IGARSS)*, pp. 2316–2319, Sep. 2020. DOI: 10.1109/IGARSS39084.2020.9324679.

[187] N. Chaki, S. H. Shaikh, and K. Saeed, *Exploring Image Binarization Techniques (Studies in Computational Intelligence, 560)*. Springer, 2014.

[188] K. He, X. Zhang, S. Ren, and J. Sun, "Deep residual learning for image recognition", *2016 IEEE Conference on Computer Vision and Pattern Recognition (CVPR)*, pp. 770–778, 2016.

[189] H. F. Mateo-Romero, M. E. C. d. Rosa, L. Hernández-Callejo, *et al.*, "Enhancing solar cell classification using mamdani fuzzy logic overăelectroluminescence images: A comparative analysis withămachine learning methods", in *Smart Cities*, S. Nesmachnow and L. Hernández Callejo, Eds., Cham: Springer Nature Switzerland, 2024, pp. 159–173, ISBN: 978-3-031-52517-9.

[190] J. Deng, W. Dong, R. Socher, L.-J. Li, K. Li, and L. Fei-Fei, "Imagenet: A large-scale hierarchical image database", in *2009 IEEE Conference on Computer Vision and Pattern Recognition*, 2009, pp. 248–255. DOI: 10.1109/CVPR.2009.5206848.

[191] M. Oquab, L. Bottou, I. Laptev, and J. Sivic, "Learning and transferring mid-level image representations using convolutional neural networks", in *2014 IEEE Conference on Computer Vision and Pattern Recognition*, 2014, pp. 1717–1724. DOI: 10.1109/CVPR.2014.222.

[192] F. Zhuang, Z. Qi, K. Duan, *et al.*, "A comprehensive survey on transfer learning", *Proceedings of the IEEE*, vol. 109, no. 1, pp. 43–76, 2020.

[193] S. Ioffe and C. Szegedy, "Batch Normalization: Accelerating Deep Network Training by Reducing Internal Covariate Shift", *arxiv*, Feb. 2015. DOI: 10.5555/3045118.3045167. [Online]. Available: http://arxiv.org/abs/1502.03167.

[194] B. Xu, N. Wang, T. Chen, and M. Li, "Empirical Evaluation of Rectified Activations in Convolutional Network", *arxiv*, May 2015. [Online]. Available: http://arxiv.org/abs/1505.00853.

[195] T. Salimans, I. Goodfellow, W. Zaremba, *et al.*, "Improved techniques for training gans", in *Advances in Neural Information Processing Systems*, D. Lee, M. Sugiyama, U. Luxburg, I. Guyon, and R. Garnett, Eds., vol. 29, Curran Associates, Inc., 2016. [Online]. Available: https://proceedings.neurips.cc/paper/2016/file/8a3363abe792db2d8761d6403605aeb7-Paper.pdf.

[196] C. Szegedy, V. Vanhoucke, S. Ioffe, J. Shlens, and Z. Wojna, "Rethinking the inception architecture for computer vision", in *2016 IEEE Conference on Computer Vision and Pattern Recognition (CVPR)*, 2016, pp. 2818–2826. DOI: 10.1109/CVPR.2016.308.

[197] M. Heusel, H. Ramsauer, T. Unterthiner, B. Nessler, and S. Hochreiter, *Gans trained by a two time-scale update rule converge to a local nash equilibrium*, 2017. DOI: 10.48550/ARXIV.1706.08500. [Online]. Available: https://arxiv.org/abs/1706.08500.

[198] A. Gron, *Hands-On Machine Learning with Scikit-Learn and TensorFlow: Concepts, Tools, and Techniques to Build Intelligent Systems*, 1st. O'Reilly Media, Inc., 2017, ISBN: 1491962291.

[199] L. Breiman, "Random forests", *Machine Learning 2001 45:1*, vol. 45, pp. 5–32, 1 Oct. 2001, ISSN: 1573-0565. DOI: 10.1023/A:1010933404324. [Online]. Available: https://link.springer.com/article/10.1023/A:1010933404324.

[200] J. H. Friedman, "Greedy function approximation: A gradient boosting machine.", *The Annals of Statistics*, vol. 29, no. 5, pp. 1189–1232, 2001. DOI: 10.1214/aos/1013203451.

[201] F. Pedregosa, G. Varoquaux, A. Gramfort, *et al.*, "Scikit-learn: Machine learning in Python", *Journal of Machine Learning Research*, vol. 12, pp. 2825–2830, 2011.

[202] S. Hochreiter and J. Schmidhuber, "Long short-term memory", *Neural computation*, vol. 9, no. 8, pp. 1735–1780, 1997.

[203] K. Cho, B. Van Merriënboer, D. Bahdanau, and Y. Bengio, "On the properties of neural machine translation: Encoder-decoder approaches", *arXiv preprint arXiv:1409.1259*, 2014.

[204] Y. Yu, X. Si, C. Hu, and J. Zhang, "A Review of Recurrent Neural Networks: LSTM Cells and Network Architectures", *Neural Computation*, vol. 31, no. 7, pp. 1235–1270, Jul. 2019, ISSN: 0899-7667. DOI: 10.1162/neco_a_01199. eprint: https://direct.mit.edu/neco/article-pdf/31/7/1235/1053200/neco_a_01199.pdf. [Online]. Available: https://doi.org/10.1162/neco%5C_a%5C_01199.

[205] T. O'Malley, E. Bursztein, J. Long, F. Chollet, H. Jin, L. Invernizzi, *et al.*, *Keras Tuner*, https://github.com/keras-team/keras-tuner, 2019.

[206] R. Garnett, *Bayesian Optimization*. Cambridge University Press, 2022.

[207] S. Peter, F. Diego, F. A. Hamprecht, and B. Nadler, "Cost efficient gradient boosting", *Advances in neural information processing systems*, vol. 30, 2017. [Online]. Available: http://github.com/svenpeter42/LightGBM-CEGB..

[208] J. Cong and B. Xiao, "Minimizing computation in convolutional neural networks", in *International conference on artificial neural networks*, Springer, LNCS 8681, 2014, pp. 281–290.

[209] H. F. Mateo-Romero, M. E. C. d. Rosa, L. Hernández-Callejo, *et al.*, "Enhancing photovoltaic cell classification through mamdani fuzzy logic: A comparative study with machine learning approaches employing electroluminescence images", *[Still in review] Applied Science*, 2024.

[210] H. F. Mateo-Romero, M. E. C. d. l. Rosa, L. Hernández-Callejo, *et al.*, "Estimation of the performance of photovoltaic cells by means of an adaptative neural fuzzy inference model", in *Smart Cities*, S. Nesmachnow and L. Hernández Callejo, Eds., Cham: Springer Nature Switzerland, 2024, pp. 174–188, ISBN: 978-3-031-52517-9.

[211] L. Alzubaidi, J. Zhang, A. J. Humaidi, *et al.*, "Review of deep learning: Concepts, cnn architectures, challenges, applications, future directions", *J Big Data*, vol. 8, p. 53, 2021. DOI: 10.1186/s40537-021-00444-8. [Online]. Available: https://doi.org/10.1186/s40537-021-00444-8.

[212] N. Pudjihartono, T. Fadason, A. W. Kempa-Liehr, and J. M. O'Sullivan, "A review of feature selection methods for machine learning-based disease risk prediction", *Frontiers in Bioinformatics*, vol. 2, 2022, ISSN: 2673-7647. DOI: 10.3389/fbinf.2022.927312. [Online]. Available: https://www.frontiersin.org/articles/10.3389/fbinf.2022.927312.

[213] S. Masoudnia, R. Ebrahimpour, S. Masoudnia, and R. Ebrahimpour, "Mixture of experts: A literature survey", *Artif Intell Rev*, vol. 42, pp. 275–293, 2014. DOI: 10.1007/s10462-012-9338-y.

[214] M. Jordan and R. Jacobs, "Hierarchical mixtures of experts and the em algorithm", in *Proceedings of 1993 International Conference on Neural Networks (IJCNN-93-Nagoya, Japan)*, vol. 2, 1993, 1339–1344 vol.2. DOI: 10.1109/IJCNN.1993.716791.

[215] Z. Zhang and M. R. Sabuncu, "Generalized cross entropy loss for training deep neural networks with noisy labels", *CoRR*, vol. abs/1805.07836, 2018. arXiv: 1805.07836. [Online]. Available: http://arxiv.org/abs/1805.07836.

[216] H. F. Mateo-Romero, Á. Pérez-Romero, L. Hernández-Callejo, *et al.*, "Photovoltaic cells defects classification by means of artificial intelligence and electroluminescence images", in *Smart Cities*, S. Nesmachnow and L. Hernández Callejo, Eds., Cham: Springer International Publishing, 2022, pp. 31–41, ISBN: 978-3-030-96753-6.